



This work is protected by copyright and other intellectual property rights and duplication or sale of all or part is not permitted, except that material may be duplicated by you for research, private study, criticism/review or educational purposes. Electronic or print copies are for your own personal, non-commercial use and shall not be passed to any other individual. No quotation may be published without proper acknowledgement. For any other use, or to quote extensively from the work, permission must be obtained from the copyright holder/s.





# The impact of ionized outflows on the surrounding interstellar medium in disc galaxies

Ameerah Aboalsawd Hammadi Al-Sadooni  
M.Sci. Physics Babylon university

Doctor of Philosophy

Department of Physics, University of Keele.

October 2018

# Abstract

The aim of this thesis was to study the evolution of spiral galaxies by quantifying the impact of the ionized outflows in spiral galaxies on the surrounding interstellar medium. This project was based on optical Fabry-Pérot and long-slit observations with the instrument RSS (Robert Stobie Spectrograph) at the 10 m Southern African Large Telescope (SALT). I focussed on two types of nearby spirals, the first of which is a face-on spiral galaxy (NGC 300) in order to study the kinematics of outflows from H II regions, and their impact on their surroundings as well as the present-day chemical abundances across these areas. I used the CLOUDY model to compare with my results in order to quantify the conditions in these areas.

The second object was the Seyfert 2 galaxy NGC 4945, which shows high activity in the centre (AGN and starburst). I studied the physical properties of the ionized ejected material, their kinematics and morphology. I presented a first kinematic map for the central area based on Fabry-Pérot observations of H $\alpha$  and [N II]. The shapes of emission lines in this area were analysed to estimate the physical conditions in the areas of interest.

The final chapter shows preliminary results of an on-going optical and radio survey for a sample of 36 Southern edge-on disc galaxies in order to study the disc-halo interface by tracing extended ionized extraplanar gas.

My results from the previous three projects show that the outflows from H II regions and AGN and/or starburst play an important role in re-shaping the surrounding ISM by forming filaments or shells. The kinematics of the surrounding gas are affected by the outflows also. My results suggest that the ionized ejected material from the centre of NGC 4945 forms a bi-conal structure, and I constructed a model for the shape of the bi-cone according to my results.

# Acknowledgements

Firstly, I consider myself extremely lucky to have had Jacco Van Loon as my supervisor. Throughout the last four years he has guided me to progress as a researcher by allowing me to explore my own ideas and enhance my research skills. His deep knowledge of the subject, unlimited patience and faith in me were my motivations to overcome the difficulties and continue my work during the hard times.

I am grateful to the astrophysical group at Keele University for offering me the opportunity to study at this prestigious institute and providing all the needed assets. I would like to thank Dr Barry Smalley and Prof Aneurin Evans for providing me support during my work.

My special thanks to the Staff of the South African Large Telescope team, in particular (Ted Williams, Petri Vaisanen) and their Ph.D. student Wendyam Blaise Tapsoba. I spent a great and rewarding time at SALT. I learned so many new skills there, and through their knowledge and experience I managed to reduce my data. Big thank goes to Encarni Romero for her advice and support during the preparation of the different proposals with SALT. I thank my husband Ali Abed, my children Abbas, Fatimah, Sarah for being there for me when I needed them and for being away when I did not. I am grateful to my sisters Azhar and Majeda Al-Sadooni for encouraging me during the moments of weakness and their love and support. I would like to thank the following people how helped me along the way: Prof Fadel Al-Sadooni, Lorna Temple, Huda Abid, Yousef Al-Sadooni, Shazma Abdulbari, and Tina Hadi.

Finally, I would like to acknowledge the Ministry of Higher Education and Scientific Research, Iraq for providing the financial support which made this work possible.

July 2018

# Contents

<b>Abstract</b> . . . . .	<b>iii</b>
<b>Acknowledgements</b> . . . . .	<b>iv</b>
<b>1 Introduction</b> . . . . .	<b>1</b>
1.1 Background . . . . .	1
1.1.1 Formation and evolution of galaxies . . . . .	1
1.1.2 Galaxy color–magnitude diagram . . . . .	4
1.1.3 Spiral galaxies . . . . .	5
1.1.4 Galactic outflows . . . . .	6
1.2 The interstellar medium . . . . .	10
1.2.1 Disc–halo interaction . . . . .	12
1.2.1.1 Ionized extraplanar gas . . . . .	12
1.2.1.2 Extraplanar dust . . . . .	13
1.2.2 Diffuse nebulae . . . . .	13
1.2.3 Mechanisms of heating and cooling . . . . .	16
1.3 Optical emission lines . . . . .	17
1.3.1 Emission lines from low excitation regions and electron density .	19
1.3.2 Dust extinction . . . . .	21
1.4 Case Studies . . . . .	24
1.4.1 NGC 4945 . . . . .	24
1.4.2 NGC 300 . . . . .	29
1.5 Aims and outline . . . . .	32
<b>2 Observations and data analysis</b> . . . . .	<b>33</b>
2.1 SALT . . . . .	33
2.2 The long-slit spectroscopy . . . . .	35
2.2.1 Long-slit data reduction . . . . .	37
2.3 Fabry-Pérot spectral imaging . . . . .	43
2.3.1 Fabry-Pérot reduction . . . . .	49
2.3.2 Mask . . . . .	49
2.3.3 Ghost . . . . .	49
2.3.4 Flat field . . . . .	51
2.3.5 Flux calibration and scaling . . . . .	51
2.3.6 Wavelength calibration . . . . .	54
2.3.7 Sky-lines subtraction . . . . .	59
2.3.8 Kinematics map . . . . .	60
2.3.8.1 Line profile . . . . .	60
2.3.8.2 Intensity of the line emission, continuum, velocity, ve- locity dispersion maps . . . . .	61

2.4	CLOUDY model . . . . .	62
2.4.1	Chemical composition . . . . .	62
2.4.2	Geometry . . . . .	62
2.4.3	Velocity structure . . . . .	63
2.4.4	Overview . . . . .	63
2.4.4.1	Continua . . . . .	63
2.4.4.2	Geometry . . . . .	66
2.4.4.3	Application . . . . .	69
<b>3</b>	<b>Outflows from diffuse nebulae in the face-on spiral galaxy NGC 300</b>	<b>70</b>
3.1	Introduction . . . . .	70
3.2	Fabry-Pérot observations . . . . .	71
3.2.1	Results of Fabry-Pérot mode . . . . .	75
3.2.2	Long-slit observations . . . . .	79
3.2.3	Spectral analysis . . . . .	81
3.3	Discussion . . . . .	89
3.3.1	Archival properties of selected objects . . . . .	89
3.3.2	Intensity maps and the kinematics of $H\alpha$ and $H\beta$ . . . . .	90
3.3.2.1	A comparison of optical observation in different spectral windows . . . . .	90
3.3.2.2	The dust distribution . . . . .	95
3.3.2.3	The kinematics of $H\alpha$ and $H\beta$ . . . . .	97
3.3.2.4	Signatures of shocks . . . . .	98
3.3.3	The emission line ratios and the diagnostic diagrams . . . . .	101
3.3.4	Analysis of the largest objects A44 and A155 . . . . .	104
3.3.5	Photoionization modelling . . . . .	107
3.3.6	Calculation of abundance from the ratios of emission lines . . . . .	114
3.3.7	The centre of NGC 300 . . . . .	121
3.4	Conclusions . . . . .	121
<b>4</b>	<b>The kinematics of the gas surrounding the active nucleus of NGC 4945124</b>	
4.1	Introduction . . . . .	124
4.2	Observations . . . . .	125
4.3	Flux calibration for Fabry-Pérot observations . . . . .	128
4.4	Results of Fabry-Pérot observations . . . . .	130
4.4.1	Ionized gas distribution in the nucleus . . . . .	135
4.4.1.1	$H\alpha$ emission . . . . .	135
4.4.1.2	[N II] emission . . . . .	136
4.4.1.3	The Ratio of [N II]/ $H\alpha$ . . . . .	136
4.4.1.4	The estimated mass of the ionized energetic outflows . . . . .	137
4.5	Long-slit observation and reduction . . . . .	139
4.6	Results and data analysis . . . . .	141

4.6.1	The kinematics and physical properties along the cone . . . . .	141
4.6.2	The kinematics and physical properties across the cone . . . . .	150
4.7	Discussion . . . . .	159
4.7.1	Morphological and kinematical evidence . . . . .	159
4.7.2	Physical evidence . . . . .	162
4.7.3	Signatures of the second part of the bi-cone . . . . .	165
4.8	Conclusions . . . . .	168
<b>5</b>	<b>The disc–halo interaction in edge-on galaxies . . . . .</b>	<b>170</b>
5.1	Introduction . . . . .	170
5.2	Observation and data reduction . . . . .	173
5.3	Results . . . . .	177
5.3.1	Morphological structures of the ionized emission . . . . .	182
5.3.1.1	NGC 4672 . . . . .	182
5.3.1.2	ESO 202-G35 . . . . .	182
5.3.1.3	ESO 575-G61 . . . . .	183
5.3.1.4	ESO 505-G03 . . . . .	183
5.3.1.5	ESO 506-G02 . . . . .	184
5.3.1.6	ESO 321-G10 . . . . .	184
5.3.1.7	ESO 033-G22 . . . . .	184
5.3.1.8	ESO 311-G12 . . . . .	184
5.3.1.9	IC 1963 . . . . .	185
5.4	Discussion . . . . .	185
<b>6</b>	<b>Conclusion and future work . . . . .</b>	<b>189</b>
6.1	Outflows from H II regions in NGC 300 . . . . .	189
6.2	Outflows from the centre of NGC 4945 . . . . .	191
6.3	The distribution of ionized gas in edge-on disc galaxies . . . . .	193
6.4	General conclusion . . . . .	193
6.5	Future work . . . . .	195
6.5.1	Upcoming observations for the cone structure in NGC 4945 . . . . .	195
6.5.2	Upcoming observations for the optical and radio survey . . . . .	196
	<b>Appendices . . . . .</b>	<b>197</b>
<b>A</b>	<b>Charts . . . . .</b>	<b>197</b>
<b>B</b>	<b>Spectra of different objects in NGC 300 . . . . .</b>	<b>206</b>
<b>C</b>	<b>Profiles were marked onto the object B in Figure 3.15. . . . .</b>	<b>211</b>
<b>D</b>	<b>An example of input file used in CLOUDY model . . . . .</b>	<b>214</b>
<b>E</b>	<b>Table for the full sample of galaxies included in the optical and radio survey . . . . .</b>	<b>215</b>
	<b>Bibliography . . . . .</b>	<b>217</b>

# List of Figures

1.1	The principal processes that drive to the formation and evolution of galaxies (Falcón-Barroso & Knapen 2013). . . . .	3
1.2	Galaxy color–magnitude diagram . . . . .	4
1.3	short name . . . . .	5
1.4	Example of bi-polar galactic winds, seen in UGC 100043, from the CALIFA survey. The white contour shows the limit of the observed [N II]6584 emission line, and the white dashed lines present the shape of the bi-conical structure created by ionized outflows with opening angle $\approx 80^\circ$ . Adopted from López-Cobá et al. (2017). . . . .	7
1.5	Illustration of the assumed configuration of the Strömgren sphere. . . . .	15
1.6	The main recombination and collisionally excited emission lines in the spectra of H II regions( adopted from Vogel 2017). . . . .	18
1.7	The partial energy-level diagram of the $2p^3$ and $3p^3$ ground configuration of [O II] and [S II]. . . . .	19
1.8	The intensity of [S II] and [O II] versus $n_e(10^4/T)^{1/2}$ . Adapted from Osterbrock (1974). . . . .	21
1.9	Energy-level diagram of the $2p^3$ ground configuration [O III] and [N II]. The solid lines represent emission in infrared and ultraviolet, and the optical lines are shown with dashed lines. Adapted from Osterbrock (2006). . . . .	22
1.10	An image of NGC 4945 taken at optical wavelengths . . . . .	24
1.11	The nucleus of NGC 4945. Left and middle panel: $H\alpha$ + [N II] and J continuum images from IRAC2-FP image, the contour represents $H_2$ from IRAC2-FP image (step = $0.3 \times 10^{-4}$ erg cm $^{-2}$ s $^{-1}$ sr $^{-1}$ from 0.4 to 2.8). Right panel: L-band image ( $3.5 \mu\text{m}$ ) superimposed by $B_{r\gamma}$ contours from the IRAC2-FP image (step = $0.25 \times 10^{-4}$ erg cm $^{-2}$ s $^{-1}$ sr $^{-1}$ from 0.7 to 2). Adopted from Moorwood et al. (1996). . . . .	27
1.12	IRAC $4.5 \mu\text{m}$ and $8.0 \mu\text{m}$ images of NGC 4945 tracing PAH and hot dust emission. The intensity scalings are inverse hyperbolic sine in both panels. North is top and East is left (McCormick, Veilleux & Rupke 2013). . . . .	28
1.13	Color composite image of NGC 300 from NASA/JPL-Caltech/OCIW <a href="http://www.galex.caltech.edu/media/glx2005-01r_img01.html">http://www.galex.caltech.edu/media/glx2005-01r_img01.html</a> . . . . .	29
1.14	The rotation curve of NGC 300 from two different works based on ATCA and VLA observations (Muñoz-Mateos et al. 2007). . . . .	31
1.15	The optical rotation curve of NGC 300 based on Fabry-Pérot observation (Muñoz-Mateos et al. 2007). . . . .	31
2.1	The Southern African Large Telescope, image taken by the author. . . . .	33

2.2	The toilet seat diagram of SALT, objects have values of Hour Angle and Declination in the annular regions that can be observed by SALT. . . .	34
2.3	The schematic represents the important optical components of the long-slit spectroscopy mode of RSS in SALT. . . . .	36
2.4	An example of received data of the long-slit from SALT. Notice the curved telluric emission lines, and the two data gaps between the three CCDs. X-axis represents observed wavelengths and the y-axis shows the position on the sky. . . . .	37
2.5	The long slit frame after filtering cosmic ray events. . . . .	39
2.6	An example of arc lamp calibration that was observed after the object observation in the same setting. . . . .	40
2.7	An example of arc lamp spectrum which was used to identify lines of the arc-line calibration spectra which were created by <i>PYSALT SALTSPEC</i> package. . . . .	41
2.8	The long-slit frame after transforming the identified arc lamp frame solution. Notice the telluric emission lines are now straight, but the CCD gaps have become curved. . . . .	42
2.9	The final frame after removing sky lines. . . . .	43
2.10	Representative diagram of a data cube of Fabry-Pérot. The data cube produces three dimensional information (two spatial, one wavelength), therefore, all pixels have the same position in the successive scans of the cube, and the emission line profile. . . . .	44
2.11	The major components of the interferometer: Collimating lens, Fabry-Pérot etalon, and focusing lens. . . . .	46
2.12	The transmission profile of Fabry-Pérot: The red line shows the FP transmission profile with high finesse ( $\mathcal{F} = 10$ ), and the blue one represents the FP transmission profile with low finesse ( $\mathcal{F} = 2$ ) . . . . .	47
2.13	The left panel shows the deghosted frame and the right panel represents the ghost frame. The green circles show examples of the treated areas. . . . .	51
2.14	The top panel shows the normalised magnitude of the chosen stars in each FP scan, while the bottom panel displays the scale factors. Scan number 7 was chosen as reference. . . . .	52
2.15	The OH sky-lines emission in the range between 6000 Å to 6680 Å (Osterbrock et al. 1996). . . . .	55
2.16	The extraction method of sky-lines. . . . .	56
2.17	The geometry of the interference pattern produced via FP étalon from monochromatic light, shows the relation between the incident angle of the light beam, the radius of the formed rings and the focal length of the camera (Moiseev 2002). . . . .	58
2.18	The fits of the night-sky lines wavelength as a function of $r$ and $z$ . . . .	59

2.19	Top left: the raw FP image has the object and sky-lines. Top right: the fitted sky-lines to those recorded in the previous panel, 6580 Å corresponds to the centre of the the FP scan. Bottom left: the model scan of the fitted sky-lines. Bottom right: the final scan after subtracting the model of sky-lines. . . . .	60
2.20	shows several of the continua that enter in the calculations of the CLOUDY model (Ferland 1996). . . . .	64
2.21	Incident (dashed) and reflected (solid) continua produced by the CLOUDY model (Ferland 1996). . . . .	65
2.22	Representative diagram of the two limiting geometries (open & closed) that can be considered in the CLOUDY model (Ferland 1996). . . . .	66
3.1	An image of NGC 300 illustrating the summary of observations used in this chapter. Two FP fields are located at (RA: $00^h 55^m 08^s$ , Dec: $-37^\circ 41' 50''$ ) and (RA: $00^h 54^m 45^s$ , Dec: $-37^\circ 37' 0''$ ) respectively. Five long-slit positions (LS1, LS2, LS3, LS4, LS5) were oriented with PA = $44^\circ$ , $155^\circ$ , $119^\circ$ , $111^\circ$ , $68^\circ$ respectively. The base image is a combination of visible-light and ultraviolet images, the red and yellow colours represent visible light observed using the Carnegie Institution of Washington's 100-inch telescope at Las Campanas Observatory, and the blue colour represents ultraviolet observations from NASA's Galaxy Evolution Explorer. <a href="https://en.wikipedia.org/wiki/NGC_300">https://en.wikipedia.org/wiki/NGC_300</a> . . . . .	71
3.2	Total intensity maps of the observed field (RA: $00^h:55^m:08^s$ , Dec: $-37^\circ:41':50''$ ) in NGC 300 showing H $\alpha$ (upper panels) and H $\beta$ (lower panels). The intensity is in arbitrary units, and the centre of the galaxy is marked with a black cross. The bar in the left bottom corner represents 1 kpc. . . . .	76
3.3	Total intensity map in the observed field (RA: $00^h:55^m:08^s$ , Dec: $-37^\circ:41':50''$ ) in NGC 300 showing H $\alpha$ . The intensity is in arbitrary units, and the centre of the galaxy is marked with a black cross. The red arrows identify 14 objects in the field (K1–K14). . . . .	77
3.4	After fitting the data cube of H $\alpha$ of the first field, from top left to bottom right: (a) the maximum intensity of the H $\alpha$ profile, (b) continuum, (c) velocity and (d) velocity dispersion. The intensity is in arbitrary units. . . . .	78
3.5	As Figure 3.4, but for H $\beta$ . . . . .	79
3.6	As Figure 3.4, but for the second field. . . . .	80
3.7	zoom into the red rectangular area in Figure 3.6. . . . .	81
3.8	Zoomed-in maps of object A: (a) intensity of H $\alpha$ , (b) intensity of continuum emission, (c) H $\alpha$ velocity and (d) H $\alpha$ velocity dispersion; (e) and (f) show the H $\beta$ velocity and velocity dispersion respectively. The intensity is in arbitrary units. The bar to the left bottom corner in panels (a) and (e) represents 1 kpc. . . . .	83
3.9	As Figure 3.8, but for object B. . . . .	84

3.10	The long-slit frames of the blue and red side of the spectra at PA = 155° (left panel) and PA = 44° (right panel): the interesting objects and emission lines are marked on the frames. . . . .	85
3.11	The major identified components in objects A and B which were collected through Vizier. WR* = Wolf–Rayet star, SNR = supernova remnant, V* = Variable star, As* = association of stars, H II = star-formation region, CL = cluster of stars. The background image taken at optical wavelength. . . . .	89
3.12	Maps of complex A: (a) U-band (near & far ultra-violet), (b) infrared emission at 8 μm; X-axis and Y-axis represent the RA and Dec respectively. Superposed contours onto the maps represent Hα emission (Roussel et al. 2005). (c) shows the ratio of Hα/Hβ (present study), (d) and (e) represent Hα and Hβ emission (present study). (f) Shows a radio image (Payne et al. 2004). . . . .	93
3.13	As Figure 3.12, but for object B. . . . .	94
3.14	The ratio of Hα/Hβ. Pixels that do not have both Hα and Hβ emission are excluded from the map. . . . .	95
3.15	Bottom right: A map showing the total intensity in Hα for object B. The other panels display examples of Hα profiles in various regions in object B, which are marked onto the map. Notice panels (5) and (6) have signatures of splitting in the profiles. Panel (12) shows an example of a single profile. The other panels marked on the map are shown in Appendix C (Figures C.1, C.2, C.3). . . . .	99
3.16	The Hα profile in object B with two peaks and model fit of two Gaussian components. The spectrum is an average of 49 pixels that are marked with a white box in Figure 3.15. . . . .	100
3.17	Diagnostic diagram to distinguish between H II regions, SNRs and planetary nebulae (PNe) derived from the ratios of Hα to forbidden lines [S II] and [N II], adapted from Camps-Fariña et al. (2016). . . . .	102
3.18	Diagnostic diagram showing the positions across object A (PA = 155°, 44°) with superimposed empirical boundaries of H II regions, PNe, and SNRs. The boundaries of the theoretical shock regime are from Phillips & Cuesta (1999); Hartigan, Raymond & Hartmann (1987). Note that the ratios used follow [O III] = [O III]4959 Å + 5007 Å, [S II] = [S II]6717 Å + 6731 Å, and [N II] = [N II] 6548 Å + 6583 Å. . . . .	103

3.19	The top panels show the morphology of the $H\alpha$ emission line. Left-middle panel: ratios of $H\alpha$ (blue), $[S II]\lambda 6717+6731$ (green), $[N II]\lambda 6583$ (red) and $[O III]\lambda 5007$ (black) to $H\beta$ along the slit through object A in NGC 300. Right-middle, ratios $[N II]/H\alpha$ , $[S II]/[S II]$ , $[O III]/H\alpha$ and $[S II]/H\alpha$ . The bottom panels represent velocity (left) and velocity dispersion (right), and the long-slit was oriented with $PA = 155^\circ$ . The solid line in the bottom panels represents the average value. . . . .	106
3.20	As Figure 3.19, but now the long-slit was oriented with $PA = 44^\circ$ . . . . .	107
3.21	Distribution of 18 objects in diagnostic BPT diagrams compared to the predicted models (black and red asterisks). The red and green lines represent the Kewley (Kewley et al. 2001) and Kauffmann (Kauffmann et al. 2003) curves respectively. The triangle symbols represent the objects in the first FP field, and the circles represent the objects in the second FP field. . . . .	108
3.22	A comparison between the two methods used to determine the $12+\log(O/H)$ ; the red line is a linear fit to the results. The green line represents one-to-one correlation. . . . .	115
3.23	Trends of $\log(N/O)$ with oxygen abundance. The black dashed line represents the solar values. . . . .	116
3.24	Upper panel: Observed trends of oxygen abundance as a function of the normalized galactocentric radius ( $R/R_{25}$ ). The continuous green line represents the linear fitting of the H II regions sample from Stasińska et al. (2013), and the black line shows the linear fitting of the sample of interest. Lower panel: Trends of $\log(N/O)$ with the normalized galactocentric radius ( $R/R_{25}$ ). The black dashed line represents the solar values. The labels are as in Figure 3.23. . . . .	118
3.25	The relation between the intensity of $H\alpha$ and the index N2 ( $\log([N II]/H\alpha)$ ). The red line represents the fitted model. . . . .	121
3.26	The upper panel displays the blue side and the bottom one shows the red side of the spectra of the centre of NGC 300. The observed lines are marked. The spectra was extracted from LS3. . . . .	122
4.1	An image of NGC 4945 illustrating the summary of observations used in this chapter. The FP field is located at (RA: $13^h 27^m 30^s.0$ , Dec: $-49^\circ 28' 4''.5$ ). Four long-slit positions are labelled LS1, LS2, LS3 and LS4. The base image is a combination of images taken in five bands (B, V, R, $H\alpha$ and $[S II]$ ) with the 2.2-metre MPG/ESO telescope at La Silla. <a href="http://www.eso.org/public/images/eso0931a/">http://www.eso.org/public/images/eso0931a/</a> . . . . .	125

- 4.2 Total intensity maps of the observed field (RA:  $13^h 05^m 27^s.30$  and Dec:  $-49^\circ 28' 04''.5$ ) in NGC 4945, showing  $H\alpha$  (upper panels). Lower panels show the intensity maps of  $[N II]6583$ . The centre of the galaxy is marked with a black cross symbol in panels (b) and (d), and the intensity is in arbitrary units. The North and East of the galaxy are marked to the top left corner in (a) and (c), and the black bar represents 1 kpc. . . . 131
- 4.3 Total intensity maps of the observed field (RA:  $13^h 05^m 27''.3$  and Dec:  $-49^\circ 28' 04''.0$ ) in NGC 4945, showing  $[S II]$  (upper panels). Lower panels show the intensity maps of  $H\beta$ . The centre of the galaxy is marked with a black cross symbol in panels (b) and (d), the intensity is in arbitrary units, and the black bar represents 1 kpc. . . . . 132
- 4.4 After fitting the data cube of  $H\alpha$ , from top left to bottom right: (a) the continuum, (b) maximum intensity of the  $H\alpha$  profile, (c) velocity dispersion and (d) velocity in the centre of NGC 4945 and its surroundings. The cross represents the centre of the galaxy in all panels, and the N and E represent the North and East. The accepted values of the fitting parameters have intensities with a  $S/N > 5$ . . . . . 133
- 4.5 After fitting  $[N II]6583$ , from top left to bottom right: (a) the continuum, (b) maximum intensity of the  $H\alpha$  profile, (c) velocity dispersion and (d) velocity in the centre of NGC 4945 and its surroundings. The cross represents the centre of the galaxy in all panels, and the N and E represent the North and East. The accepted values of the fitting parameters have intensities with a  $S/N$  is  $> 8$ . . . . . 134
- 4.6 The ratio of  $[N II]/H\alpha$ . Pixels that do not have both  $[N II]$  and  $H\alpha$  emission are excluded from the map. The centre of the galaxy is marked with a red cross symbol. . . . . 137
- 4.7 Two images of NGC 4945: (left panel) the long-slit position (LS1) in a perpendicular direction to the disc through the nucleus, and (right panel) zoom into the black rectangular area ( $0.53' \times 0.5'$ ). The black cross symbol represents the centre of the galaxy. . . . . 140
- 4.8 Two images of NGC 4945: (left panel) two different long-slit positions crossed the cone structures parallel to the disc, with two different offsets:  $0'.23$  (LS2) and  $0'.4$  (LS3) respectively, and (right panel) zoom into the black rectangular area. The black cross symbol represents the centre of the galaxy. . . . . 141
- 4.9 The spatial and kinematic maps of the  $[N II]$  doublet and  $H\alpha$  (left panel),  $[S II]$  doublet (middle panel), and  $H\beta$  (right panel) along the slit (LS1). The wavelength axis is transformed into heliocentric Doppler velocity for the  $[N II]6583$  line,  $[S II]6716$  and  $H\beta$  lines respectively. The long-slit was oriented with  $PA = -45^\circ$  (perpendicular to the disc of NGC 4945). 143

- 4.10 Red part (6540–6760 Å) spectra in subsequent subdivisions along the interesting part of LS1. The labels in the top left corners represent the central position of the structures, and the labels in the top right corners are the spatial width of the structures. . . . . 146
- 4.11 Left and middle panels show optical emission lines at a distance of 0'07 to the NW from the centre of NGC 4945. The right panel displays H $\alpha$  and [N II] at a distance of 0'33. The resolution is 0.75 Å and the long-slit (LS1) was oriented with PA = -45° (perpendicular to the disc of NGC 4945). . . . . 148
- 4.12 Panel (a): spatial and kinematic map of [N II] and H $\alpha$  lines along the slit position (LS2). The wavelength axis was transformed into heliocentric Doppler velocity for the [N II]6583 line. (b) [S II] lines. (c) Ratio map of [S II]6716/[S II]6732. (d) Zoom into the red rectangular area in (a). (e) and (f) show the ratios of [N II]/H $\alpha$  and [N II]/[S II] respectively. The slit (LS2) was oriented with PA = 45° and shifted 0'23 from the centre of the galaxy (parallel to the disc of NGC 4945). The North and East directions are as right panel of Figure 4.8. . . . . 151
- 4.13 Left: spectrum of [N II], H $\alpha$  and fitted profiles; Right: spectrum of [S II] lines and fitted profile for three areas: Centre ( $\Delta = 23''$ ), area-1 ( $\Delta = 15''$ ) and area-2 ( $\Delta = 28''$ ), which are labelled in Figure 4.12. The long-slit (LS2) was oriented with PA = 45°, with a shift of 0'23 towards NW. . . 152
- 4.14 Panel (a): the spatial and kinematic maps of [N II] and H $\alpha$  lines along the slit position (LS3). The wavelength axis is transformed into heliocentric Doppler velocity for the [N II]6583 line; (b) presents [S II] lines; (c) ratio map of [S II]6716/[S II]6732; (d) zoom into the red rectangular area in (a). (e) and (f) ratio of [N II]/H $\alpha$  and [N II]/[S II] respectively. The long-slit (LS3) was oriented with PA = 45° and shifted 0'4 from the centre of the galaxy (parallel to the disc of NGC 4945). The North and East directions are as right panel of Figure 4.8. . . . . 156
- 4.15 Left: spectrum of [N II], H $\alpha$  and fitted profiles; middle: spectrum of [S II] lines and fitted profiles; Right: spectrum of H $\beta$  and [O III] lines and fitted profiles; for three areas (area-3 ( $\Delta = 24''$ ), area-4 ( $\Delta = 24''$ ) and area-5 ( $\Delta = 32''$ )), which are labelled in Figure 4.14. The long-slit (LS3) was oriented with PA = 45°, with a shift of 0'4 towards NW. . . . . 157
- 4.16 Three kinematic maps of [N II]6583 from successive regions along the vertex of the cone: (a) at 470 pc, (b) at 940 pc and (d) at 270 pc from the centre of NGC 4945. These three areas are from three different long-slit setting (LS3, LS4, LS2) respectively. Panel (c) shows the position of the three long-slit positions. (e) and (f) show intensity maps of the ejected cone by H $\alpha$  and [N II]6583 respectively. The black cross symbol in (c) represents the centre of the galaxy. . . . . 161

4.17	Distribution of nine objects covering different positions on the cone in the diagnostic BPT diagrams. The red line represents the Kewley curve which is used to distinguish between starburst regions and AGN (Kewley et al. 2001), and the green one represents the Kauffmann curve to separate between objects that have ionizing source power between AGN and starburst, such as weak AGN, post-AGB, or shocks by planetary nebulae (Kauffmann et al. 2003). . . . .	163
4.18	As Figure 4.17, but for $[\text{S II}]/\text{H}\alpha$ . . . . .	164
4.19	Panel a shows the position of LS5, and b zooms into the black rectangular area. Panel c represents the spatial and kinematic maps of $[\text{N II}]6583$ and $\text{H}\alpha$ . The wavelength axis is transformed into heliocentric Doppler velocity for the $[\text{N II}]6583$ line. Panel d shows the distribution of four areas (S1, S2, S3 and S4) covering different positions on the second part of the bi-cone in the diagnostic BPT diagrams. The red line represents the Kewley curve (Kewley et al. 2001), and the green one represents the Kauffmann curve (Kauffmann et al. 2003). . . . .	167
4.20	A simple model of NGC 4945 showing the emerging cone from the centre of the galaxy with inclination $80^\circ$ w.r.t. the line of sight, and opening angle = $140^\circ$ . The V-shaped structured which is suggested to be filled with gas, is shown with a yellow cone having opening angle = $80^\circ$ . The unobserved part of the bi-cone is shown in the model, which has the same dimensions and structures of the observed part. . . . .	168
5.1	A schematic diagram showing the positions (wavelengths) of the scans of FP covering the emission profile and continuum in ESO 575-G61. <i>Scans</i> - 2 to -5 span the emission line and <i>scan</i> - 1 and <i>scan</i> - 6 are used to determine the continuum. . . . .	174
5.2	Maps show the $\text{H}\alpha$ emission (left panels), continuum (middle panels), $\text{H}\alpha/\text{Continuum}$ (right panels) in NGC 4672, ESO 202-35 and ESO 575-G61. . . . .	178
5.3	as Figure 5.2, but now ESO 505-G03, ESO 506-G02 and ESO 321-G10.	179
5.4	as Figure 5.2, but now ESO 033-G22, ESO 311-G12 and IC 1963. . . .	180
5.5	Maps show the ratio of the tracing blue-shifted emission to red-shifted emission in the sample of galaxies. . . . .	181
5.6	shows the correlation between the average of $\text{H}\alpha/\text{C}$ against the morphological type in the sample of galaxies. . . . .	187
A.1	A chart showing the long-slit position on NGC 300 oriented with PA = $155^\circ$ and with the centre of the slit (LS1 in Figure 3.1) at (RA: $00^h 55^m 12^s$ , Dec: $-37^\circ 41' 20''$ ). . . . .	197
A.2	As Figure A.1, but for PA = $44^\circ$ and the centre of the slit (LS2 in Figure 3.1) at (RA: $00^h 55^m 13^s$ , Dec: $-37^\circ 41' 36''$ ). . . . .	198

A.3	As Figure A.1, but for PA = 111° and the centre of the slit (LS3 in Figure 3.1) at (RA: 00 <sup>h</sup> 54 <sup>m</sup> 44 <sup>s</sup> , Dec: -37° 40' 22"). . . . .	199
A.4	As Figure A.1, but for PA = 68° and the centre of the slit (LS4 in Figure 3.1) at (RA: 00 <sup>h</sup> 54 <sup>m</sup> 40 <sup>s</sup> , Dec: -37° 39' 17"). . . . .	200
A.5	As Figure A.1, but for PA = 119° and the centre of the slit (LS5 in Figure 3.1) at (RA: 00 <sup>h</sup> 54 <sup>m</sup> 40 <sup>s</sup> , Dec: -37° 39' 15"). . . . .	201
A.6	A chart showing the long-slit position on NGC 4945 oriented with PA = -45° and with the centre of the slit (LS1 in Figure 4.1) at (RA: 13 <sup>h</sup> 5 <sup>m</sup> 17 <sup>s</sup> , Dec: -49° 28' 4"4). . . . .	202
A.7	As Figure A.6, but for PA = 45° and the centre of the slit (LS2 in Figure 4.1) at (RA: 13 <sup>h</sup> 5 <sup>m</sup> 26 <sup>s</sup> , Dec: -49° 27' 40"4). . . . .	203
A.8	As Figure A.6, but for PA = 45° and with the centre of the slit (LS3 in Figure 4.1) at (RA: 13 <sup>h</sup> 5 <sup>m</sup> 26 <sup>s</sup> , Dec: -49° 27' 54"4). . . . .	204
A.9	As Figure A.6, but for PA = 49° and the centre of the slit (LS4 in Figure 4.1) at (RA: 13 <sup>h</sup> 5 <sup>m</sup> 34 <sup>s</sup> , Dec: -49° 25' 59"4). . . . .	205
B.1	Optical emission lines from object A. The left panel displays Hβ and forbidden [O III]λλ4959,5007; the middle panel covers Hα and forbidden [N II]λλ6549,6583; the right panel shows forbidden [S II]λλ6717,6731 lines. The resolution is 0.75 Å and the long-slit was oriented with PA = 44°. . . . .	206
B.2	As Figure B.1, but now the long-slit was oriented with PA = 155°. . . . .	207
B.3	As Figure B.2, but for object F. . . . .	207
B.4	As Figure B.3, but for object E. . . . .	208
B.5	Optical emission lines from object B-1. The left panel displays Hβ and forbidden [O III]λλ4959,5007; The middle panel covers Hα and forbidden [N II]λλ6549,6583; the right panel shows forbidden [S II]λλ6717,6731. The resolution is 0.75 Å and the long-slit was oriented with PA = 44°. . . . .	208
B.6	As Figure B.5, but for object B-2. . . . .	209
B.7	As Figure B.6, but for object D. . . . .	209
B.8	As Figure B.7, but for object R. . . . .	210
C.1	The Hα profiles in various regions in object B, which are marked onto the map in the bottom right panel in Figure 3.15. . . . .	211
C.2	Continuation of Figure C.1. . . . .	212
C.3	Continuation of Figure C.1. . . . .	213

# List of Tables

1.1	Physical properties of the different components of the gas in the Galaxy (Lequeux 2005). . . . .	12
1.2	Examples of $H\alpha$ luminosities and SFR in some H II regions. . . . .	16
1.3	The main parameters of NGC 4945. . . . .	25
1.4	Properties of the NGC 300. . . . .	25
2.1	An example of the main parameters of the input task <i>qphot</i> used in <i>PYRAF</i> for Fabry-Pérot scans. . . . .	52
3.1	The main parameters of NGC 300 observations of $H\alpha$ and $H\beta$ , with Fabry-Pérot MR and LR mode respectively. . . . .	73
3.2	Étalon configuration wavelengths for the FP $H\alpha$ and $H\beta$ observations of NGC 300. . . . .	74
3.3	Summary of the spectroscopic (long-slit) observations of NGC 300. . . . .	82
3.4	Emission line parameters from the spectra of objects of interest in NGC 300. . . . .	87
3.5	Same as Table 3.4, but now emission line ratios. . . . .	88
3.6	The kinematic parameters of object B, average spectrum of 49 pixels which are marked in a white box in Figure 1.5. . . . .	100
3.7	Abundance ratio in the Orion nebula (NGC 1976) and Sun. . . . .	110
3.8	The estimated temperature and observed line ratios in 18 objects in NGC 300 and as predicted from the models. . . . .	113
3.9	The metallicities of the objects in NGC 300. . . . .	115
4.1	The main parameters of NGC 4945 observations with Fabry-Pérot mode (LR). . . . .	127
4.2	Étalon configuration wavelengths for the Fabry-Pérot $H\alpha$ , $H\beta$ , [N II], and [S II] observations of NGC 4945. . . . .	128
4.3	The physical properties of the outflows from the centre of NGC 4945. . . . .	139
4.4	Summary of the spectroscopic (long-slit) observations of NGC 4945. . . . .	142
4.5	Emission line ratios, velocities and FWHMs at a distance of 0'.07 and 0'.33 from the centre of NGC 4945. Note that the [N II] line used is the red one (6583 Å). . . . .	149
4.6	Emission line ratios, velocities and FWHMs of three objects (red rectangle centre, area-1, area-2) along LS2 in NGC 4945. . . . .	153
4.7	Emission line ratios, velocities and FWHMs for three objects (area-3, area-4 and area-5) along LS3 in NGC 4945. . . . .	158
5.1	Basic information about the nine edge-on galaxies from the sample, observed in the first stage of the survey, the position angle (PA) is measured from the North. . . . .	172

5.2	The main parameters of the H $\alpha$ observations, using the Fabry-Pérot LR mode. . . . .	175
5.3	Étalon configuration wavelength for the Fabry-Pérot H $\alpha$ observations of the sample of galaxies with LR. . . . .	176
D.1	An example of an input file used in Chapter 2.4.4.3. . . . .	214
E.1	Basic information for 36 disc galaxies included in the optical and radio survey. . . . .	215
E.2	Continuation to Table E.1. . . . .	216

# Chapter 1

## Introduction

### 1.1 Background

The gas in the interstellar medium (ISM) and intergalactic medium (IGM) comprises of a collection of atoms, ions, free electrons, dust grains, and molecules. These materials appear with different physical properties, various gas phases and variable morphological structures due to local influences of different events happening in the disc of the galaxy. These events could be supernova explosions, star formation regions and active galactic nuclei. All these vigorous phenomena have mechanical and/or radiative feedback onto the surrounding ISM.

Galactic winds (GWs) are a common phenomenon in galaxies hosting active galactic nuclei (AGNs) or star formation (SF) regions. The origin of the GWs and their feedback on the surroundings have been the subject of numerous studies, however it is still an open question that requires more investigation. Stellar winds driven by massive star formation have a huge impact on the baryonic component of the galaxy in particular as well as the universe in general, through regulating matter and energy between a galaxy and its environment and contributing to formation and evolution of galaxies.

#### 1.1.1 Formation and evolution of galaxies

The formation and evolution of galaxies are highly complicated processes, which are both internally and environmentally driven. These physical processes were fast soon after the Big Bang, and then became slower with the expansion of the universe (Kormendy & Kennicutt 2004). The classical scenario of the galaxy formation suggests that fluctuations of non-baryonic matter (dark matter), which was created after the start of

the Big Bang, expanded with the universe, and gravity caused them to grow, separate, collapse, and as a consequence form galactic halos. The virialised halo attracted baryonic gas, which settled into the potential well and experienced shock heating, reaching the virial temperature. The hot gas, nevertheless, radiated away energy to cool, and its density confined the timescale required for the cooling process. This cooled gas was the first seed that formed a disc. Consequently, smaller fragments appeared within the preliminary disc, creating clouds consisting of molecular hydrogen, and then collapsed to form stars, planets, and black holes (Toomre 1977; Kauffmann, White & Guiderdoni 1993; Sparre & Springel 2017). The latter were produced after the massive stars died.

Figure 1.1 outlines the major processes of galaxy evolution (Falcón-Barroso & Knapen 2013). These processes are divided into fast evolution occurring on the free timescale (see Figure 1.1 in the top two corners); and slow processes that require time scales of many galactic rotation periods (lower two corners in Figure 1.1). The prior processes can happen for one galaxy (right side) or group of galaxies (left side). The processes in the middle have an important role in all types of evolution. The feedback from radiation, stellar winds, AGNs and supernovae explosions within the galaxy has a deciding contribution to regulating structures and kinematics of the ISM, and might cause new events of star formation.

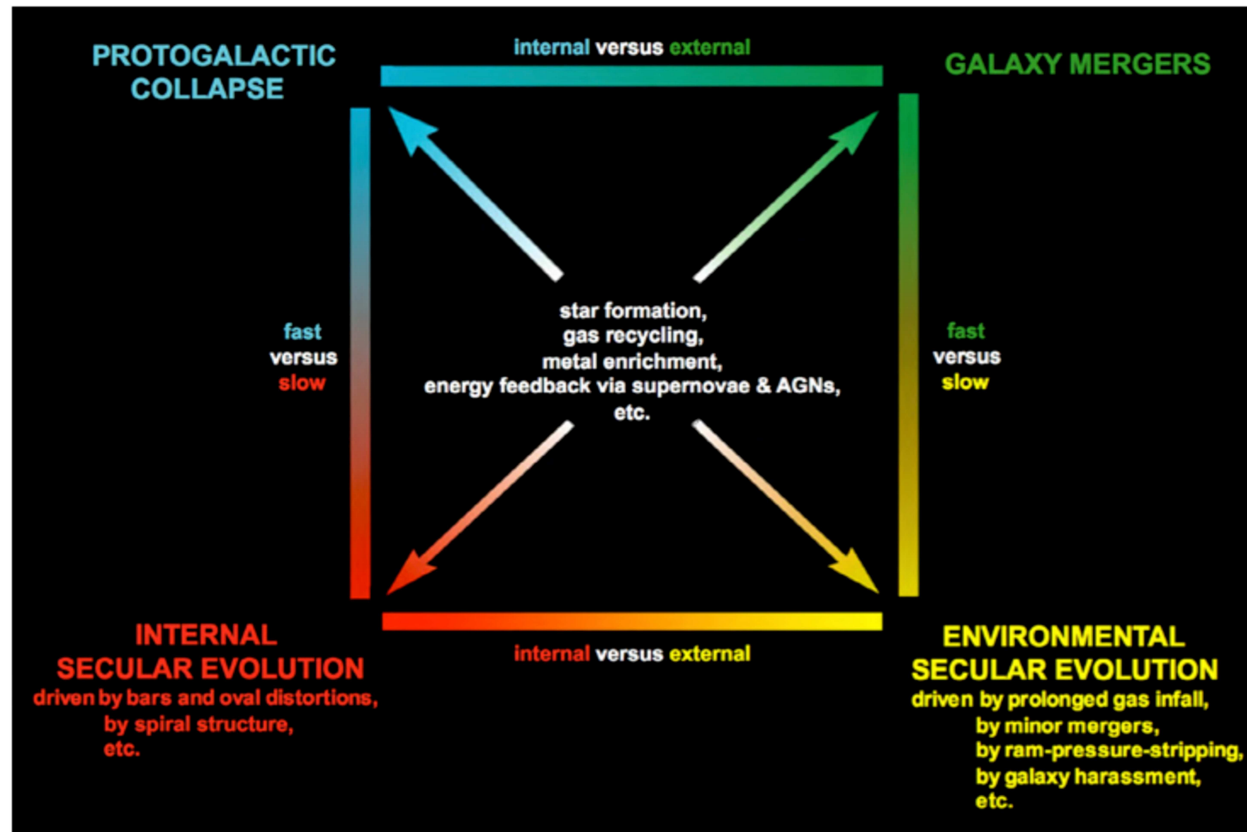


Figure 1.1: The principal processes that drive to the formation and evolution of galaxies (Falcón-Barroso & Knapen 2013).

### 1.1.2 Galaxy color–magnitude diagram

The galaxies in the universe fall into one of three categories according to the galaxy color-magnitude diagram (Bell et al. 2004), blue cloud, red sequence and green valley. Figure 1.2 shows the correlation between absolute magnitude and luminosity of the galaxies. The blue cloud category comprises of star-forming, later type and disc dominated galaxies, while the red sequence comprises of elliptical, early type, non-star-forming and bulge dominated galaxies full in the red sequence. The galaxies in-between blue cloud and red sequence represent the green valley category. It includes two different galaxies populations later type galaxies with quenched SF process due to the lack of gas to maintain SF processes for few billions years. The second population is early type galaxies; their gas runs out quickly as a result of a high activity of AGN and/or mergers with other galaxies (Schawinski et al. 2014). Both the Milky way and M31 are located in the green valley because of their low SFR as a result of exhausting gas (Mutch, Croton & Poole 2011).

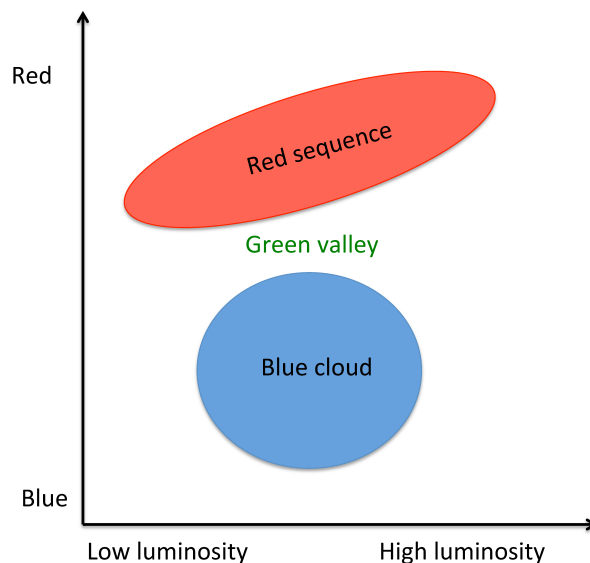


Figure 1.2: Galaxy color–magnitude diagram, adopted from (<https://www.revolvy.com/page>).

### 1.1.3 Spiral galaxies

Spiral galaxies represent about two thirds of the massive galaxies according to Galaxy Zoo (Lintott et al. 2008) and have a complex morphology compared to that of ellipticals. A crucial difference between spirals and ellipticals is that the spirals have active star formation while the ellipticals are more likely quenched (Kennicutt 1998). Typically, spirals exhibit a distinctive disc, which contributes about 90% of the total luminosity of the Galaxy and has a considerable gas content in a rotationally-supported thin disc, which is occupied by the spiral arms, bar, and bulge. The latter is very prominent in the earliest types and it is likely very faint or totally absent in the later types. The level of complexity of the spiral structures is a defining property of their discs.

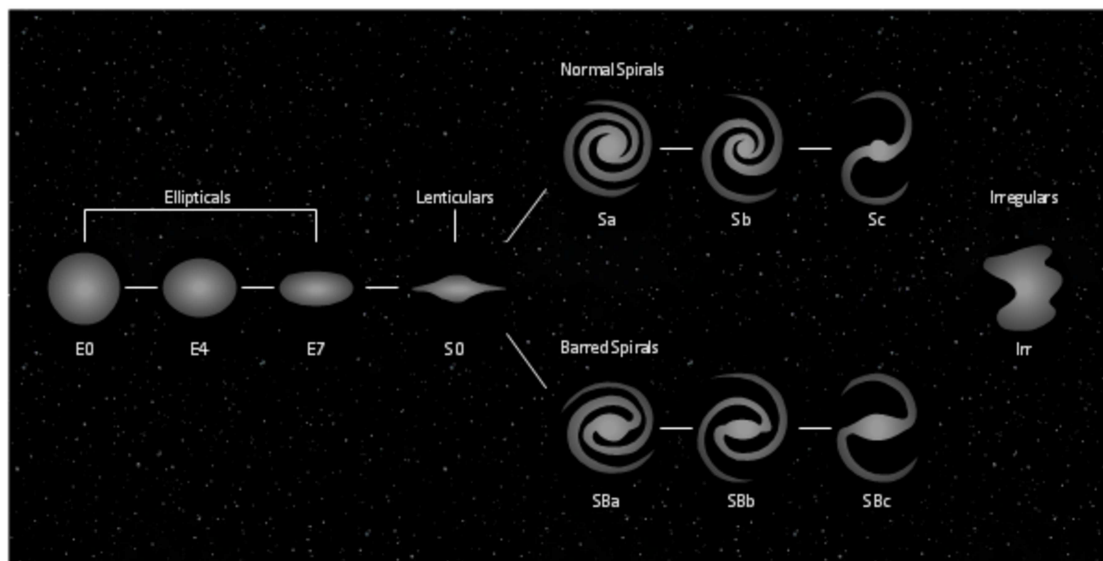


Figure 1.3: Hubble tuning-fork diagram (<https://conceptdraw.com/a2353c3/preview>).

Disc galaxies occupy the right side of the Hubble tuning-fork diagram, as shown in Figure 1.3. According to the morphology of the spiral galaxies, they are divided into two major types, barred and non-barred galaxies depending on the presence or absence of a bar structure in the central area of the disc (Hubble 1926). Each type is subdivided

into three subclasses: a, b and c. Three criteria are taken into account to distinguish between these subclasses: the size of the central bulge, the pitch angle; and the ratio of the resolved H II regions, stars, and dust lanes in the spiral arms. According to these criteria, Sa galaxies have a prominent bulge, tightly wound arms with faint H II regions, whereas galaxies without a bulge, or which display a weak one with pronounced H II regions and open arms are classified as Sc galaxies. An additional subclass, d, is reserved for flocculent discs that lack clearly defined spiral structure but are instead densely populated by dust and H II complexes.

The spiral galaxies have a variety of inclinations ( $i$ ) in the universe, representing a great opportunity to study their structures. Face-on systems ( $i=0$ ) display the structure of the spiral arms, as well as their components (stars, H II regions, dust, and molecular clouds) clearly. On the other hand, the vertical structures (thin, thick disc, and halo) are best seen in an edge-on system ( $i = 90^\circ$ ), which presents an opportunity to study the extraplanar material in isolation without the interfering effect of gas from the disc. This is why edge-on and face-on galaxies have been selected to be the subject of this thesis.

#### 1.1.4 Galactic outflows

Galactic wind is a fundamental mechanism by which matter and energy are recycled in galaxies, so it can play an important role in the formation and evolution processes of galaxies. Since its first detection in the centre of M82, several scenarios have been explored to identify the energy sources that are powering these winds, and their feedback on the ambient ISM.

AGN and/or starbursts are the more widely accepted sources that drive galactic winds (Heckman, Armus & Miley 1990; Veilleux et al. 2003; Tüllmann et al. 2006; Wild et al. 2014; López-Cobá et al. 2017). Figure 1.4 shows galactic winds from the centre of the edge-on spiral galaxy UGC 10043; the image is extracted from an integral field spectroscopy (CALIFA) survey (López-Cobá et al. 2017).

GWs are complex phenomena having diverse phases of gas that move at differ-

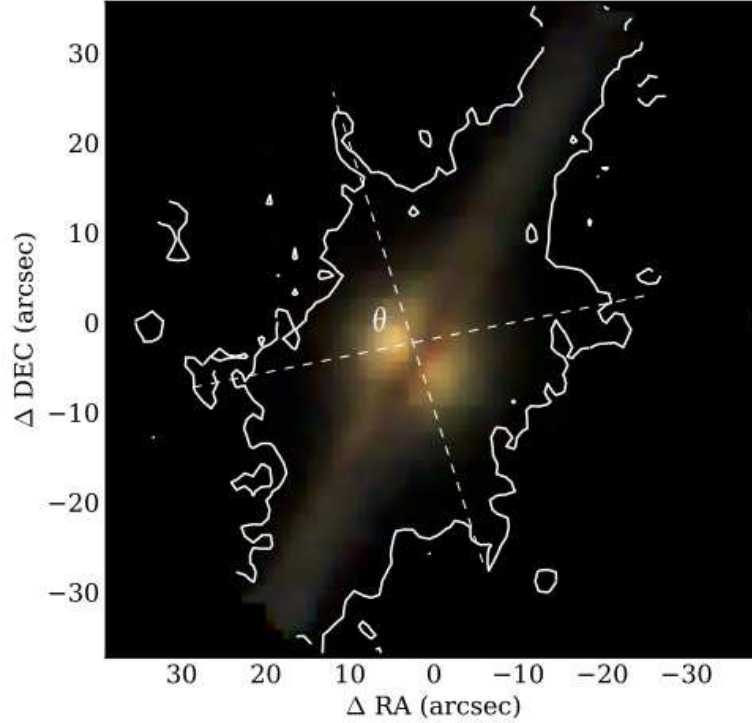


Figure 1.4: Example of bi-polar galactic winds, seen in UGC 100043, from the CALIFA survey. The white contour shows the limit of the observed  $[\text{N II}]\lambda 6584$  emission line, and the white dashed lines present the shape of the bi-conical structure created by ionized outflows with opening angle  $\approx 80^\circ$ . Adopted from López-Cobá et al. (2017).

ent velocities. The dynamical evolution and morphological structures of superwinds happening in a disc galaxy were described through a numerical simulation of M82 by Tomisaka & Ikeuchi (1988). In general, the combined effect of the supernovae explosions and stellar winds in highly active galaxies (starburst and/or AGN) forms a partially evacuated bubble in the nuclear regions, having a size of a few hundreds pc and which is filled with hot ejecta ( $10^8$  K). Then, the bubble expands at a high speed on the order of several thousands of  $\text{km s}^{-1}$ , sweeps up its surrounding ISM, and enters a radiative phase. This occurs when the radiative cooling time of the shocked material becomes shorter than the expansion time scale of the wind. A cooled shell is created at the interface of the interaction; Chevalier & Clegg (1985) suggested that the super-

winds results when the kinetic energy of the ejected material is efficiently thermalized. The expansion of the bubble is high in the direction towards the halo with its lower pressure and density. At a certain scale height the cooled shell breaks and allows the hot gas to expand freely with velocities of a few hundred  $\text{km s}^{-1}$ , reaching 1–2 kpc from the midplane in the form of bipolar winds. This will enter blow-out phase from the transition between bubble and galactic winds (Castor, McCray & Weaver 1975; Weaver et al. 1977).

Large scale outflows or GWs are commonly observed in nearby spiral galaxies and even in the high-redshift universe (Frye, Broadhurst & Benítez 2002). The kinematics and morphology of ionised outflowing gas provide insights into the evolution of spiral galaxies, which need a mechanism to sustain SF. The galactic fountain likely plays an important role in recycling gas within the environment of the galaxy. An ionized outflow of gas could be driven by Active Galactic Nucleus (AGN) activity (King & Pounds 2015; Hopkins et al. 2008), or powered by starburst-driven winds (Veilleux, Cecil & Bland-Hawthorn 2005; Heckman, Armus & Miley 1990), resulting in strong feedback onto the surroundings that could suppress or enhance the SF process in galaxies with low mass by heating the ISM and reducing the cold gas that is fundamental to the SF process (Hopkins, Quataert & Murray 2012; Cazzoli et al. 2014).

Warm and hot gas and plasma in the GWs are investigated by tracing lines and continuum emission in a wide range of the electromagnetic spectrum. The ejected materials are affected by hot OB stars, which cause them to be excited and will cause radiative shocks at the interface of the energetic wind and the interstellar matter of the disc. Emission lines in the optical range, (e.g. [S II], [N II],  $\text{H}\beta$ , and  $\text{H}\alpha$ ), and their ratios can be powerful tracers to investigate the properties of the GWs, in particular the excitation by shocks, which represents evidence of the galactic winds (Martín-Fernández et al. 2016; Matsubayashi et al. 2009), and a diagnostic to distinguish shocked regions by AGN from starburst regions. Essentially, in shocked areas the forbidden/recombination line ratios are larger than those in H II regions (López-Cobá et al. 2016). Electron density ( $n_e$ ) is one of the fundamental conditions that characterises the ionization state of the ionized gaseous nebulae. A precise estimation

of  $n_e$  reveals valuable information about the chemical abundances and masses of the ionized gas (Bae et al. 2017). The powerful method to calculate the  $n_e$  in an ionized gaseous nebula is by observing the impact of the collisional de-excitation on forbidden emission lines for a given nebula, like the ratio of the [S II] doublet which is sensitive to electron density in the nebula (Osterbrock 1989). In addition, they can uncover detailed information about the properties of the GWs like the kinetic energies, masses, and excitation sources (Martín-Fernández et al. 2016; Matsubayashi et al. 2009).

Optical and X-ray observations usually provide evidence that verifies the existence of galactic winds, such as morphological evidence of super-winds on large scales from a few kpc to tens of kpc, which are ejected in the form of a perpendicular cone onto the stellar disc, and finally kinematic signatures appearing as a double-peak in the emission line profiles of the ionized gas. Some galaxies have a highly energetic core, as a result of the existence of a black hole and/or active star formation regions, such as Seyfert and starburst galaxies. The morphology and kinematics of the ionized gas that is surrounding these nuclei are the subject of many studies (e.g., M82: Shopbell & Bland-Hawthorn 1998; NGC 253: Sugai, Davies & Ward 2003; NGC 5728 & NGC 7679: Davies et al. 2016; UGC 10043: López-Cobá et al. 2016). Their galactic winds display asymmetric and complex structures. The nucleus of NGC 4388 shows ionized gas in the form of two cones extending to a distance of  $\sim 1.5$  kpc or more on either side of the disc (Corbin, Baldwin & Wilson 1988). Another example is NGC 3079; its inner central region shows evidence of a super-bubble and outflows. This is confined within 5.1 kpc above and below the mid-plane (Robitaille et al. 2007).

Face-on galaxies provide a complementary view (to edge-on galaxies) of the distribution of the ionized outflows, by tracing its emission lines across the face of the galaxy. Massive stars have an additional impact on the surrounding interstellar medium: a high quantity of outflowing gas could be blown by the winds of these stars. Their strong radiation-driven winds could reach the halo of the host galaxy, or farther into the intergalactic medium, and that could explain the existence of heavy elements in the halo (Garnett 2002). Likewise, H II regions have been used to trace the current chemical composition of the interstellar medium in different parts of the galaxy (Bresolin et al.

2009a; Peimbert 1975).

Most external and internal galactic processes that happen in or around a rotating disc led to the creation of a prominent extraplanar layer. Its extent is confined by the impacts of these processes. The external processes can be an interaction between a galaxy and its environment, such as the accretion of cold or hot gases from an intergalactic medium (Sancisi et al. 2008a; Kereš et al. 2005; Oort 1970) or stripped material from satellite galaxies (Moore, Lake & Katz 1998). Meanwhile internal processes like star formation, supernova explosions, and outflows from an AGN have local impacts, resulting in different forms of extraplanar material such as galactic fountains (Fraternali & Binney 2006), chimneys, and galactic winds (Breitschwerdt, McKenzie & Voelk 1991).

Detailed dynamical analysis of these processes and their feedback on the surrounding ISM will uncover locally the origin of the ionization sources of the extended diffuse ionized gas. This will help to create more optimal models in order to elucidate the mechanism through which matter, energy and momentum are exchanged between the disc and halo. In general, the extraplanar gas could be a local phenomenon, which is directly impacted by star formation activity.

## 1.2 The interstellar medium

The ISM has different phases of gas (composition is dominated by hydrogen), which needs a variety of tracers to probe. Depending on the temperature, ionization states, and densities of the gas, the ISM can be classified into three main categories. These are: Neutral atomic medium (H I), ionized medium (H II), and molecular gas (H<sub>2</sub>) (McKee & Ostriker 1977; Kulkarni & Heiles 1987; Wolfire 2010).

- Neutral atomic medium: The neutral medium is observed to be either cold neutral gas or warm neutral gas based on its temperature. It is about 100 K in cold H I clouds, and can be  $\sim 8000$  K in the areas between cold H I clouds (Wolfire et al. 2003; Wolfire, Hollenbach & McKee 2010), and an effective tracer

of this phase is the 21 cm radio emission line. It enables us to investigate a wide range of galactic processes which include the interaction of disc galaxies and their halos (Fraternali et al. 2005; Barbieri et al. 2005; Lockman et al. 2008), the feedback of massive stars on the surrounding ISM (McClure-Griffiths et al. 2002), and the formation of cold clouds (Gibson et al. 2000).

- Molecular gas: This gas is found in the form of giant molecular clouds with a temperature of 10 K, and a density of  $\geq 1000 \text{ cm}^{-3}$ . The interstellar molecular gas is commonly traced by line emission from low rotational levels of CO (Paron et al. 2017).
- Ionized atomic medium: This represents the main medium that is the main focus of this thesis. The ionized atomic gas has a temperature of about 8000 K, and a density of up to  $0.1 \text{ cm}^{-3}$ . Ionized gas is present in the form of filaments with a complex structure, which extends to a scale height from few hundreds pc to few kpc away from the midplane of the galaxy. Ionized gas can be observed for example in  $\text{H}\alpha$  emission and in the UV and optical windows.
- Dust: The last essential component of the ISM is the interstellar dust which consists of solid particles, mainly Fe, Si, C,  $\text{H}_2\text{O}$  and ice. The dust particles have a typical radius of  $0.001 \mu\text{m}$  to  $0.1 \mu\text{m}$ . Two main sources are responsible for the generation of dust: supernovae explosions (Martínez-González, Wunsch & Palouš 2017; Matsuura et al. 2015) and evolved stars producing stellar winds (Ferreras 2015; Zhang et al. 2016). It can be observed either by attenuation (interstellar extinction) or by re-emission of the absorbed energy as infrared radiation.

Table 1.1 shows the physical properties of the environment of these components including: density, temperature, and mass (Lequeux 2005).

Table 1.1: Physical properties of the different components of the gas in the Galaxy (Lequeux 2005).

Phase		Density $\text{cm}^{-3}$	Temperature K	Total mass $M_{\odot}$	Thermal pressure $P/K = nT \text{ cm}^{-3} \text{ K}$
Atomic (HI)	Cold	$\simeq 25$	$\simeq 100$	$1.5 \times 10^9$	2500
	Warm	$\simeq 0.25$	$\simeq 8000$	$1.5 \times 10^9$	2000
Molecular		$\geq 1000$	$\leq 100$	$1 \times 10^9$	100 000
Ionized	H II region	$\simeq 1-10^4$	$\simeq 10\ 000$	$5 \times 10^7$	$1 \times 10^4 - 1 \times 10^8$
	Diffuse	$\simeq 0.03$	$\simeq 8000$	$1 \times 10^9$	240
	Hot	$\simeq 6 \times 10^{-3}$	$\simeq 5 \times 10^5$	$1 \times 10^8$	3000
Stellar mass				$6.1 \pm 1 \times 10^{10}$	
Dark matter				$10^{12}$ (Battaglia et al. 2005)	

## 1.2.1 Disc–halo interaction

The disc-halo interactions in disc galaxies play an important role in their evolution. Part of the outflowing gas is ejected from the disc as winds and can modify halo structures. This ejected gas creates a fountain that represents a mechanism by which gas is recycled between the disc and the environment. In addition, the ISM that is shocked by the ejected gas can enhance cooling of the hot gas of the halo, which then precipitates back onto the disc under gravity. This layer (between the disc and halo) can be traced in different spectral windows. In the next paragraphs I will focus on ionized gas that is the core topic of this thesis.

### 1.2.1.1 Ionized extraplanar gas

Different wavelength observations of nearby spiral galaxies have uncovered an ionized extraplanar gas in the multi-phase gaseous halos. These diffuse ionized layers ( $T \geq 10^4$  K and  $n_e \sim 0.1 \text{ cm}^{-3}$ ) appear in clumpy or filamentary morphologies (Rossa & Dettmar 2000), and need a photoionization power that coincides with the energy of the emitted photons from O and B stars in the disc. The presence of ionized extraplanar gas is positively correlated with active events in the disc, like H II regions and AGN (Veilleux et al. 2003). Examination of the rotational velocity profiles indicates that this layer could be of disc origin (Heald et al. 2007). Strickland et al. (2004) suggested that the presence of ionized extraplanar gas is always combined with the presence of X-ray extraplanar emission of similar vertical extent. In recent years, studies have suggested different scenarios relevant to the origin of the extraplanar gas. One could be that supernovae and stellar winds swept up ionized gas from the disc in the form of a fountain, which then falls back to the disc after losing its angular momentum and cooling down (Fraternali & Binney 2006). Accretion in a hot or cold model from

the intergalactic medium (IGM) is another possible scenario (Kereš et al. 2005), or the stripping of gas from satellites or nearby galaxies (Sancisi et al. 2008b; Abramson et al. 2011).

In this thesis, the focus will be on tracing this layer for different reasons; it plays an important role in recycling gas within the environment of the host galaxy, hence it sustains star formation with gas that is needed for new star-formation events. This layer transfers metals from the disc by outflows to the halo and even to the IGM, resulting in a change of the chemical composition of the galaxy. Results of the outflows' impact onto the surroundings could change the physical properties of the ISM and even trigger new star formation events. All these processes contribute to the evolution of spiral galaxies.

### 1.2.1.2 Extraplanar dust

The outflow energy which is provided by stellar winds from the thin disc in spiral galaxies does not have the ability to destroy dust grains totally, where two ways are responsible for destroying dust, grain–grain collisions and particle–grain collisions due to shocks (Jones, Tielens & Hollenbach 1996; Aoyama et al. 2017). Optical images of edge-on spiral galaxies show large numbers of dusty clouds which occupy the thick disc to a height of  $\sim 2$  kpc (Howk & Savage 1999a; Rossa & Dettmar 2003). As well as this, infrared observation reveals emission from regular grains and PAHs (polycyclic aromatic hydrocarbons) from those clouds (Lagache et al. 2000). Dusty extraplanar material is common in spiral galaxies: there is strong evidence that the Milky Way has extraplanar dust from many studies of the warm gas halo (Sembach & Savage 1996) and warm ionized halo (Howk & Savage 1999b; Odegard et al. 2007). The properties of the halo dust can contribute to the understanding the gas' dynamical history, like the ejecting mechanism and the correction of the observed colors of objects.

### 1.2.2 Diffuse nebulae

One of the most prominent areas in the disc of spiral galaxies is H II regions, which is an excellent laboratory to study the impact of the ionized outflows onto the surrounding ISM from physical and chemical aspects. It uncovers the greatest detail of how stars create elements by nuclear processes in their centre, as the ionizing stars are mainly O stars having recently formed. The surrounding ionized gas acts as repository of the heavy elements that enrich the ISM. As well as this, it considerably affects the kinematics of the interstellar gas and the physical properties of the environment. So the outflows from these regions can regulate and recycle each of the matter, energy, and momentum of the gas into the disc and the environment of the host galaxy.

Diffuse nebulae (H II regions) are one of the main types of gaseous nebulae, which are formed from the impact of the massive star formation ( $M \geq 8 M_{\odot}$ ) on the surrounding ISM. This results in the gas being ionized by supersonic winds, ultraviolet radiation, and supernova explosions. Due to the recent formation of these stars, they have effective temperatures throughout H II regions in the range from  $3 \times 10^4$  to  $5 \times 10^4$  K. In these regions, the hydrogen is entirely ionized and other elements are, generally, in the first or second ionization state. The typical density in H II regions is of the order of  $10$  to  $10^4 \text{ cm}^{-3}$ . Noticeably, the hot ionized gas expands outwardly into the cooler area having neutral gas (H I), hence the density declines as the nebula and the ionized volume increases. The mass of H II regions is typically in the range of  $10^2$ - $10^4 M_{\odot}$ .

H II regions have approximately a spherical shape around OB stars (see Figure 1.5). Under steady conditions, the gas in H II regions is in an equilibrium state between photoionization<sup>1</sup> and recombination<sup>2</sup>. This means that the total number of photoionizations per unit time ( $Q_*$ ) inside the sphere must be equal to the total number of recombining hydrogen (electron & proton) per unit time per unit volume ( $R_{rec}$ ), where  $Q_*$  is the number of escaped ionizing photons from the star per unit time:

$$Q_* = R_{rec} \frac{4}{3} \pi r^3 \quad (1.1)$$

The recombination process includes interaction between two particles having relative velocities  $v$ , a particular volume density and a cross section  $\sigma_{rec}$  for the interaction. Thus,  $R_{rec}$  can be given by the following equation:

$$R_{rec} = n_p n_e \sigma_{rec} v \quad (1.2)$$

where  $\sigma_{rec} v = \alpha(T)$  is the recombination coefficient that can be determined from quantum mechanics.

$$n_p n_e \alpha(T) = \alpha(T) n_e^2 = \alpha(T) x^2 n^2 \quad (1.3)$$

$x$  = fraction of photoionized gas.

$n_p$  = proton density.

$n_e$  = electron density.

By using equation 1.1 and equation 1.3 and assuming that all hydrogen is ionized ( $x = 1$ ), the radius of an H II region will be:

$$r_{strom} = \left( \frac{3Q_*}{4\pi\alpha n^2} \right)^{1/3} \quad (1.4)$$

---

<sup>1</sup>Hydrogen atoms are ionized by emitted stellar photons with energy higher than 13.6 eV.

<sup>2</sup>This is the inverse process of photoionization, whereby free electrons are captured by ions.

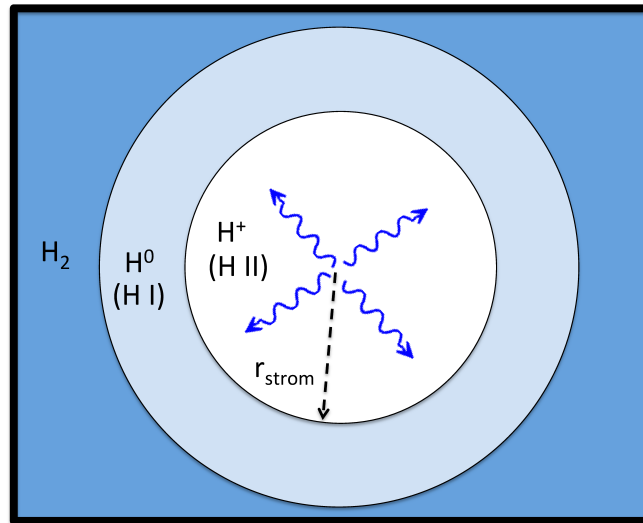


Figure 1.5: Illustration of the assumed configuration of the Strömgen sphere.

This is called the Strömgen radius. Its value is 0.2 pc for  $H\ II$  regions that have been created by a main-sequence star (O5V) through case B recombination (temperature =  $10^4$  &  $n_e = 100\text{ cm}^{-3}$  from Osterbrock 2006). Some examples of  $H\ II$  regions, their luminosities,  $Q_*$  and star formation rate (SFR) are listed in Table 1.2.

Table 1.2: Examples of H $\alpha$  luminosities and SFR in some H II regions.

Object	L(H $\alpha$ ) (erg s $^{-1}$ )	Q(H $^0$ (s $^{-1}$ ))	SFR (M $_{\odot}$ yr $^{-1}$ )
NGC 1976	$5.0 \times 10^{36}$	$3.7 \times 10^{48}$	$3.9 \times 10^{-5}$
SMC	$4.8 \times 10^{39}$	$3.5 \times 10^{51}$	$3.8 \times 10^{-2}$
LMC	$2.7 \times 10^{40}$	$2.0 \times 10^{52}$	$2.1 \times 10^{-1}$
H237(in M 101)	$1.2 \times 10^{39}$	$8.8 \times 10^{50}$	$9.3 \times 10^{-3}$
NGC 5455 (in M 101)	$1.1 \times 10^{40}$	$8.0 \times 10^{51}$	$8.3 \times 10^{-2}$
NGC 5461 (in M 101)	$2.5 \times 10^{40}$	$1.8 \times 10^{52}$	$2.0 \times 10^{-1}$

### 1.2.3 Mechanisms of heating and cooling

There are different heating mechanisms in the ISM, such as heating via X-rays, low energy cosmic rays, ejected photoelectric heating (from grains and by the photoionization of atoms or molecules), chemical, etc. However, the phase of the gas determines which mechanism dominates. In H II regions, the dominant heating mechanism is the photoionization process as a result of UV emission from the massive stars.

The heating rate in H II regions represents the rate of energy that is received from the central ionizing stars. The best way to understand how to estimate this value is by illustrating an example for a specific case. Consider an O star in the centre of an H II region with an effective temperature of  $T_e = 20\,000$  K which produces a blackbody distribution peak at 4.8 eV. All photons with energy larger than the binding energy of hydrogen (13.6 eV) can ionize the hydrogen atoms and then are totally absorbed within the Strömngren sphere. The liberated electrons (photoelectron) will have energy equal to the difference between the energy of the ionizing photon and the ionization potential energy that is required to ionize the hydrogen atom ( $h\nu - 13.6$  eV). Then the total heating rate over the entire Strömngren sphere will be:

$$\Gamma_{heating}^{tot} = \int_{h\nu=13.6 \text{ eV}}^{\infty} (h\nu - 13.6 \text{ eV}) \frac{L_{\nu}(T = 20\,000 \text{ K})}{h\nu} d\nu \quad (1.5)$$

where  $L_{\nu}$  is luminosity per unit frequency.

When the density of the gas is high enough, the liberated electrons directly collide with the previously existing particles within the H II region (electrons, protons and ions) resulting in the distribution of the kinetic energy of the liberated electrons through all particles according to the Maxwell–Boltzmann distribution. Most of the radiation leaves the H II region without scattering due to the high mean free path

of the Thomson scattering compared to  $r_{strom}$ . This suggests that the particles are in thermodynamic equilibrium (following a Maxwell–Boltzmann energy distribution), while there is no thermal equilibrium between these particles and radiation. Therefore, the produced radiation from the gas with  $10^4$  K will not have a spectrum of a blackbody. The radiated emission from H II regions mainly occurs at specific wavelengths. The recombination process of the hydrogen atom normally ends in the ground state, but it will be either in one step or passing through some excited level. The last step usually introduces one emission line of the Lyman series. In each step, the recombining atom generates emission lines at discrete wavelengths and the difference between the photoelectron kinetic energy and the binding energy of the atom will radiate as a continuum. Quantum mechanics will decide the probabilities of the end states of the recombining or decaying atom.

The process of recombination and decay of the hydrogen atom is repeated continuously until the original recombined state is divided into many lower energy levels and one Lyman- $\alpha$  photon. The latter will follow successive absorption and re-emission until arriving at the boundary of the H II region, where it may be absorbed by a dust grain and then re-emitted from the dust as infrared thermal radiation. This is a cooling mechanism by which the H II region loses energy that is gained from the central star continuously.

The hydrogen line emission resulting from the recombination process is another cooling mechanism, but the collisionally excited lines of metals (C, N, O, S & Fe) provide a more efficient cooling mechanism. In general, the excited energy of metals at relatively low energies is almost equal to the electron kinetic energy ( $kT = 1$  eV at  $T_e = 10\,000$  K). Each collision between the electron and metal ion (collisional excitation) will reduce the kinetic energy of the electron, and the excited ion can decay radiatively to a lower energy level. In this process, emission line photons will transport thermal energy away from the H II region. The probability of another ion reabsorbing the emitted photon is very low due to the low abundance of the metals in these areas. Once again, the excited metal ion can collide with another electron and collisional de-excitation occurs with no emitted photon but the kinetic energy is returned to the gas.

The observations in this thesis are focused on both recombination and collisionally excited (metal) emission lines that are present in H II regions and AGN. Figure 1.6 shows the important emission lines in typical spectra of H II regions (Vogel 2017).

### 1.3 Optical emission lines

There are two types of optical emission lines: permitted (recombination lines) and forbidden lines (collisionally excited lines). They are found in the spectrum of nebulae,

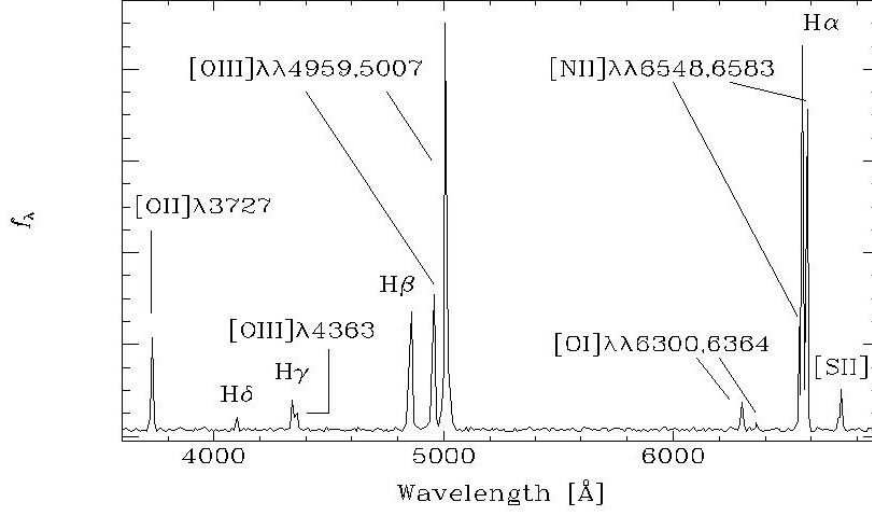


Figure 1.6: The main recombination and collisionally excited emission lines in the spectra of H II regions( adopted from Vogel 2017).

AGN, and the solar corona. The following points summarise the main properties of the emission lines used throughout this thesis:

- Permitted lines: The main permitted emission lines adopted in this work are  $H\alpha$  and  $H\beta$ , which are part of the Balmer series. These two lines are produced as a result of the transitions of an electron from a higher main energy level ( $n = 3$  for  $H\alpha$  and  $n = 4$  for  $H\beta$ ) to the second main energy level ( $n = 2$ ). These two lines are recombination lines, which appear in the energetic regions like AGN or H II regions, where electrons are in a continuous process of being free from and recombined with hydrogen nuclei, and can be created in high and low density environments.
- Forbidden emission lines: Metal emission lines are common in real nebulae, like  $[S II]\lambda\lambda 6716, 6732$ ,  $[O III]\lambda\lambda 4959, 5007$  and  $[N II]\lambda\lambda 6548, 6583$ . Their radiation can escape from the nebulae and cool it. In metals, there are special energy levels that can be split into fine structure states (metastable states). The probability of the de-excitation transitions between these levels is very low, between 10 and 100  $\text{sec}^{-1}$ . These metastable states have excitation potentials of about 1 eV. So, it is possible for the outer bound electrons of the metal ions to be excited to upper levels after they collide with free electrons produced from the photoionization of hydrogen atoms, with kinetic energy of  $\sim 1$  eV at  $T_e = 10\,000$  K. The excited electron can sit for a relatively long time in the fine

structure state, thus it can be de-excited simultaneously to emit a forbidden line photon.

### 1.3.1 Emission lines from low excitation regions and electron density

The electron configuration of the first-ionised sulphur  $S^+$  is  $1s^2 2s^2 2p^6 3s^2 3p^3$ , and their ionization energy is  $\sim 10.36$  eV.  $S^+$  has 5 electrons in the outer shell, 2 electrons in the 3s sub-shell and 3 electrons in the 3p sub-shell. These three electrons hold three of the six possible configurations within 3p sub-shells, thus they can move between them to produce the emission lines of the [S II] $\lambda\lambda 6716, 6732$  doublet. The different quantum states of [S II] are determined by these three electrons (their positions and spin). The energy-level diagram of [S II], and [O II], is shown in Figure 1.7.

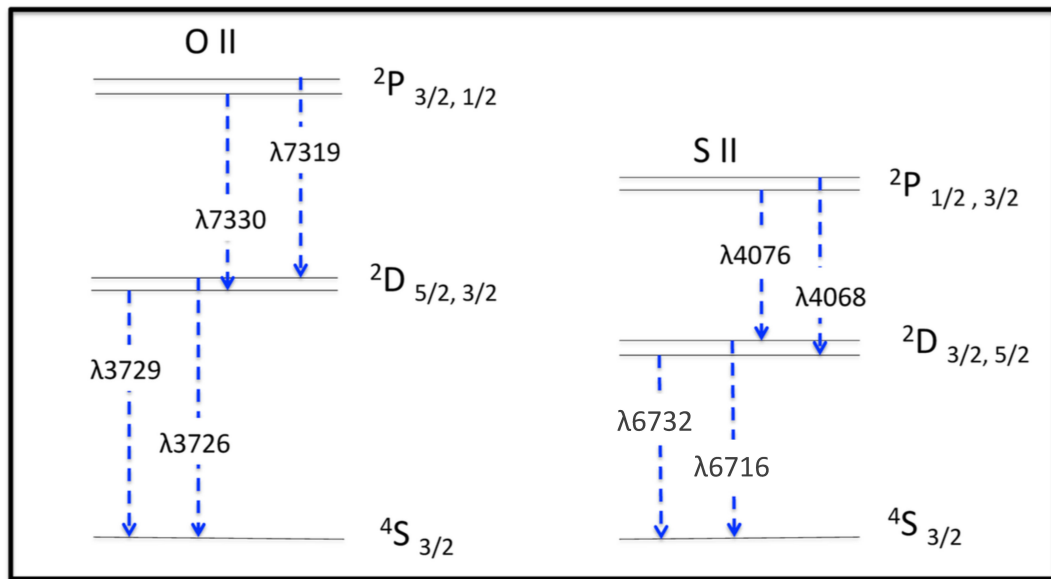


Figure 1.7: The partial energy-level diagram of the  $2p^3$  and  $3p^3$  ground configuration of [O II] and [S II].

$n_e$  is one of the fundamental criteria that characterises the ionization state of the ionized gaseous nebulae. A precise estimation of  $n_e$  reveals valuable information about the chemical abundances and masses of the ionized gas. A powerful method to calculate  $n_e$  in ionized gaseous nebulae is by observing the impact of the collisional

de-excitation of forbidden emission lines for a given nebula. This can be achieved by comparing the intensities of two emission lines, which are emitted from different levels, and having similar excitation energies. Thus, if the radiative transition probabilities are very different in these two levels, the populations will vary with density.

The best examples in the optical range are the ratios of the two doublets [O II] $\lambda$ 3729/ $\lambda$ 3726 and [S II] $\lambda$ 6716/ $\lambda$ 6732. Both of them satisfy all the previous conditions, therefore they appear in similar ionization regions, and yield comparable values of intensity. There is a critical density for each forbidden transition. At larger values, the rate of the collisional de-excitation exceeds the rate of the radiative de-excitation (no emitted photons). However, the lower this value and the higher the low density limit ( $1 \text{ cm}^{-3}$ ) all collisional excitations are followed by the emission of a photon, when the ratio of [S II] $\lambda$ 6716/ $\lambda$ 6732 is sensitive to the  $n_e$ . Nevertheless, at higher ionization regimes ( $n_e \simeq 10^4 \text{ cm}^{-3}$ ), other density-tracers such as [Cl II] $\lambda$ 5517/ $\lambda$ 5537 and [Ar IV] $\lambda$ 4711/ $\lambda$ 4740 are more useful than [O II] and [S II], which are suppressed at high plasma densities.

The density diagnostic ratio of [S II] is used throughout this thesis, so it will be explained in detail. As mentioned before, at low density regimes, a photon is created as a result of each collisional excitation, therefore the intensity ratio of [S II] doublet is determined by comparing the strength of the  $\lambda$ 6716 and  $\lambda$ 6732 transition, from the ground level  $4S_{3/2}$  to  $2D_{5/2}$  and  $2D_{3/2}$  respectively. Figure 1.8 shows the correlation between the ratio of the [S II] doublet versus  $n_e$  (Osterbrock 1974). The values of the  $n_e$  can be determine by using equation (1.8) (McCall 1984; López-Cobá et al. 2017).

$$\frac{I([\text{S II}]\lambda 6716)}{I([\text{S II}]\lambda 6732)} = 1.49 \frac{1 + 3.77x}{1 + 12.8x} \quad (1.6)$$

$$x = 10^{-4} n_e T^{-1/2} \quad (1.7)$$

where:

$x$  = density parameter.

$T$  = temperature of the electron in units of  $10^4 \text{ K}$ .

[O III] and [N II] have emission lines that emit from levels with different high excitation energies, the partial energy-level diagram of these two ions is shown in Figure 1.9. The [N II]5755 emits from the  $1S$  level, and [N II]6548 and [N II]6583 emit from the  $1D$  level. Meanwhile, the line occurs only by an electric-quadruple transition ( $3P_0-1D_2$ ) and has small transition probability compared to the latter transitions. The electron temperature determines the excitation ratio of  $1S$  and  $1D$  levels, hence the relative intensity of these emission lines can be used to measure  $n_e$ .

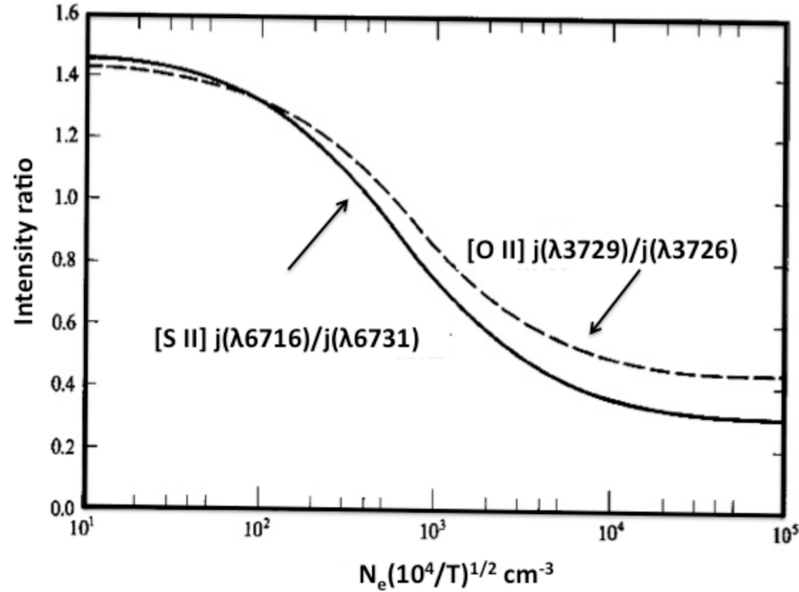


Figure 1.8: The intensity of [S II] and [O II] versus  $n_e(10^4/T)^{1/2}$ . Adapted from Osterbrock (1974).

### 1.3.2 Dust extinction

Dust grains can remove part of the stellar energy in the optical and ultraviolet and limit our understanding of how galaxies evolve with time. Dust grains cause extinction which is due to absorption and scattering. Typically, dust can absorb optical and ultraviolet, scatter optical and X-ray and emits infra-red radiation. Dust dims and reddens the emitted light from a galaxy and this leads to biases in the measurements of the galaxy including stellar populations in local (Bell & de Jong 2001) and high redshifted galaxies (Glazebrook et al. 1999) and the stellar initial mass function.

The highest reddening happens in the UV and reduces toward longer wavelengths. The dust correction is determined by using the nebular colour-excess computed from the Balmer decrement. As mentioned before, in the interstellar medium, the Balmer emission lines occur from the recombination process and following cascade of electrons to the second level of the hydrogen atom ( $n = 2$ ). The simple structure of the hydrogen atom represents an efficient way to estimate the transition rate and the ratios of the emission lines as a function of the electron density and temperature of the plasma. Two common cases are considered when examining the Balmer line emission. The case A recombination model arises when the photon of the Lyman continuum series faces an optically thin nebula. While, in case B, the nebula is optically thick to the Lyman

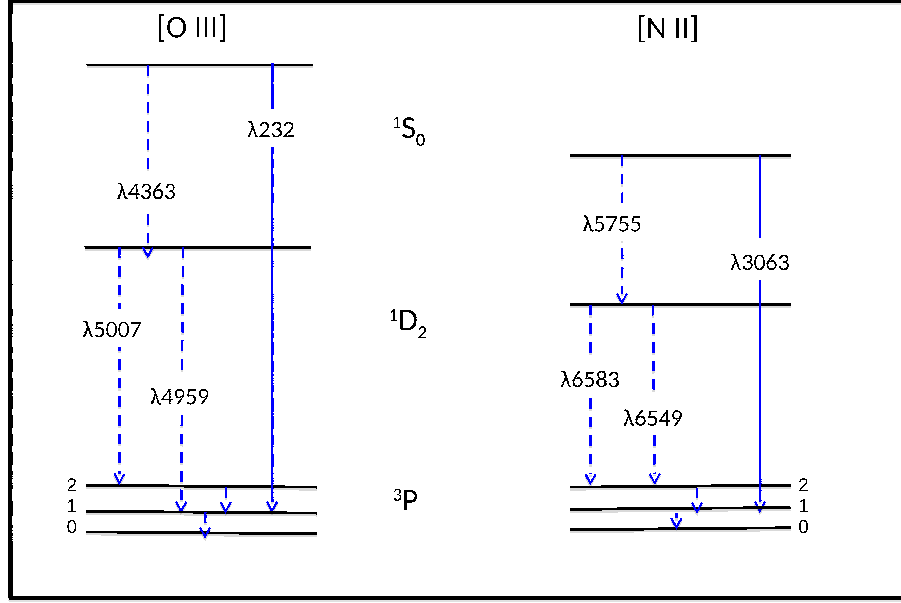


Figure 1.9: Energy-level diagram of the  $2p^3$  ground configuration [O III] and [N II]. The solid lines represent emission in infrared and ultraviolet, and the optical lines are shown with dashed lines. Adapted from Osterbrock (2006).

continuum and higher series of the hydrogen atom. Generally, case B recombination is used to calculate the intrinsic line ratio, where the assumed electron density and temperature are typical for H II regions:  $10^2 \text{ cm}^{-3}$  and 10 000 K. Osterbrock (1989) suggested using intrinsic line ratios subject to these conditions of the B model:

$$\begin{aligned} (H\alpha/H\beta)_{\text{int}} &= 2.85 \\ (H\gamma/H\beta)_{\text{int}} &= 0.469 \\ (H\delta/H\beta)_{\text{int}} &= 0.260 \end{aligned}$$

These ratios are highly sensitive to temperature and less sensitive to electron density. Dopita & Sutherland (2003) found a small variation in  $H\alpha/H\beta$  of only 0.05, when the electron density changes from  $10^2$  to  $10^6 \text{ cm}^{-3}$ . On the other hand this ratio varies by 0.29 when the temperature rises from 5000 to 20 000 K. Nevertheless, the effects of these discrepancies are often negligible. The intrinsic luminosity is given by:

$$F_{\text{int}}(\lambda) = F_{\text{obs}}(\lambda)10^{0.4A_\lambda} \quad (1.8)$$

where  $A_\lambda$  = the extinction in unit of magnitude at the specific wavelength  $\lambda$ .

The colour excess  $E(B - V)$  is given by :

$$E(B - V) = E(B - V)_{obs} - E(B - V)_{int} \quad (1.9)$$

where  $E(B - V)$  = the difference between the observed and estimated  $(B - V)$  colour without dust attenuation.

The dust extinction in galaxies can be determined by tracing Balmer decrements  $F(H\alpha)/F(H\beta)$ . The relation between the colour excess of the nebular emission line and the Balmer decrement can be given by this equation (Domínguez et al. 2013):

$$E(B - V) = \frac{E(H\beta - H\alpha)}{k(\lambda_{H\beta}) - k(\lambda_{H\alpha})} = \frac{2.5}{k(\lambda_{H\beta}) - k(\lambda_{H\alpha})} \log_{10} \left[ \frac{(H\alpha/H\beta)_{obs}}{(H\alpha/H\beta)_{int}} \right] \quad (1.10)$$

The colour excess was determined under typical gas conditions in star-forming galaxies. In other words, the case B recombination model is used in the analysis of this thesis. Hence:

$$E(B - V) = 1.97 \times \log_{10} \left[ \frac{(H\alpha/H\beta)_{obs}}{2.86} \right] \quad (1.11)$$

where:

$k$  = the opacity.

## 1.4 Case Studies

### 1.4.1 NGC 4945

NGC 4945 is the third brightest extragalactic source in the IRAS Point Source Catalog, the third nearest far-infrared galaxy (FIRG) after M82 and NGC 253, and a prominent hard X-ray source (Done, Madejski & Smith 1996). This galaxy is located in the Southern hemisphere at a distance of 6.75 Mpc (Whiteoak & Gardner 1977). It is a member of the Centaurus group, an edge-on spiral galaxy ( $i = 78^\circ$ ; Ables et al. 1987), and classified as SB(s)cd or SAB(s)cd (de Vaucouleurs 1964) (see Figure 1.10). The important parameters of NGC 4945 are listed in Table 1.3.

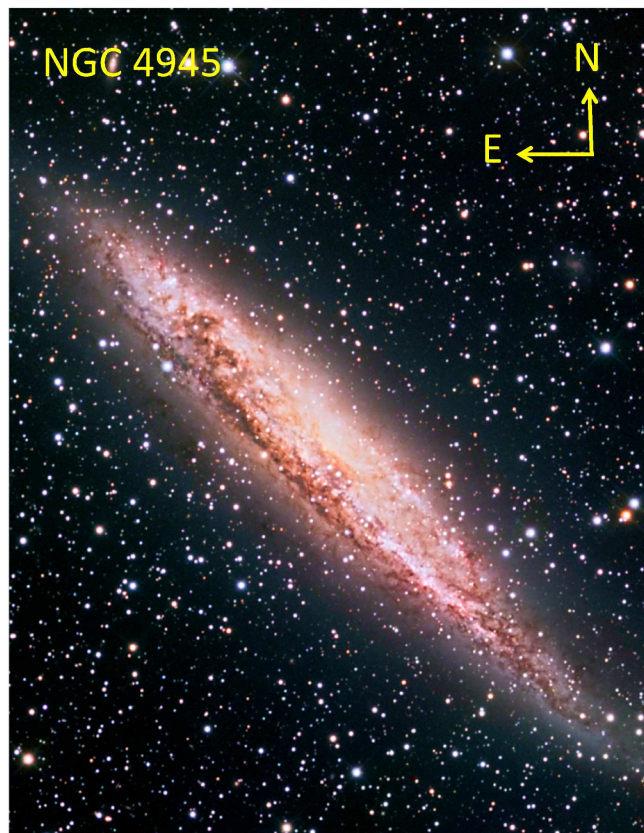


Figure 1.10: An image of NGC 4945 taken at optical wavelengths (<http://www.astrosurf.com/antilhue/ngc4945rc.htm>).

Table 1.3: The main parameters of NGC 4945.

Morphological type	SA(s)d	(Corwin, de Vaucouleurs & de Vaucouleurs 1978)
Centre position	RA (2000) = $13^h 05^m 27^s.4$ Dec (2000) = $-49^\circ 28' 05''$	
Inclination angle (degree)	$78 \pm 3$	(Dahlem et al. 1993)
Systemic velocity ( $\text{km s}^{-1}$ )	555	(Ables et al. 1987)
Distance (Mpc)	6.75	(Whiteoak & Gardner 1977)
Diameter $D_{25m}$	$23'3$	(Lauberts & Valentijn 1989)
Baryonic mass (stellar plus H I) ( $M_\odot$ )	$5.2 \times 10^{10}$	(Bell & de Jong 2001)
SFR ( $M_\odot \text{ yr}^{-1}$ )	$2-8$	(Lenc & Tingay 2009a)
Position angle (degree)	$43 \pm 2$	(Dahlem et al. 1993)
$L_{IR}$ ( $10^{10} L_\odot$ )	2.49	(McCormick, Veilleux & Rupke 2013)

Table 1.4: Properties of the NGC 300.

Parameter	Value	Ref.
Morphological type	SB(s)d	(Gieren et al. 2005a)
Centre position	RA (2000) = $00^h:54^m:53^s$ Dec (2000) = $-37^\circ:41':02''.6$	
Inclination angle	$39.8^\circ$	(Westmeier, Braun & Koribalski 2011)
Distance (Mpc)	1.9	(Gieren et al. 2005b)
Diameter $R_{25}$	$9'.8$ (5.3 kpc)	(Carignan 1985)
Radial velocity ( $\text{km s}^{-1}$ )	$136 \pm 2$	(Westmeier, Braun & Koribalski 2011)
HI mass ( $M_\odot$ )	$1.5 \times 10^9$	
Gas mass <sup>1</sup> ( $M_\odot$ )	$(1.9 \pm 0.2) \times 10^9$	(Westmeier, Braun & Koribalski 2011)
Stellar mass <sup>1</sup> $M_\odot$	$(1.0 \pm 0.1) \times 10^9$	(Westmeier, Braun & Koribalski 2011)
Total mass <sup>2</sup> ( $M_\odot$ )	$\sim 0.02$ stellar mass of MW $(2.9 \pm 0.2) \times 10^9$ $\sim 0.001 \times$ total mass of MW	(Westmeier, Braun & Koribalski 2011)
Metallicity ( $Z_\odot$ )	0.5–0.6	(Bresolin et al. 2009b)

<sup>1</sup> = across tilted ring area ( $0.9 < r < 18.4$  kpc).

<sup>2</sup> = within  $r < 18.4$  kpc.

The central part of NGC 4945 was imaged with ALMA, and shows a lopsidedness that is likely similar to what exists in the central molecular area of the Milky Way. As well as this it displays a thick, bar-like structure extended to 300 pc away from the centre. Two spiral arms are seen at the West and East tips of the bar, which turn to the Northeast and Southwest respectively (Henkel et al. 2018).

The nucleus of the NGC 4945 shows a wide range of activity from radio to hard X-ray wavelengths, representative of both starburst and AGN activity (Roy et al. 2010; Schurch, Roberts & Warwick 2002; Cunningham & Whiteoak 2005).

The infrared properties of its nucleus coincide with starburst activity: a starburst ring with 100 pc scale is distinguished by tracing Pa $\alpha$  emission (in infra-red wavelengths at 1.875  $\mu$ m). On the other hand, H<sub>2</sub> observation detects walls of a conical structure which is created by supernova-driven winds, while the presence of high and variable hard X-ray emission could be related to the presence of an AGN (Marconi et al. 2000).

NGC 4945 hosts one of the closest and highly obscured AGN (Sadler et al. 1995; Pérez-Beaupuits et al. 2011), with a mass  $\approx 10^6 M_{\odot}$  (Guainazzi et al. 2000; Tully et al. 2008; Mouhcine et al. 2005). In general, this non-interacting galaxy could be in a transition stage from starburst to Seyfert galaxy according to speculation by the latter authors, who adopted the starburst model of Kruegel, Tutukov & Loose (1983). A dense radio emitter with high temperature produces bright synchrotron emission, which is another strong indicator of an AGN (Sadler et al. 1995; Tully et al. 2008; Mouhcine et al. 2005). This galaxy has a central star forming disc (400 pc) (Moorwood & Oliva 1994) with an electron temperature of about  $5400 \pm 600$  K, which is similar to what is found near the nucleus of the Milky Way, and the derived SFR of this central source is  $4.35 \pm 0.25 M_{\odot} \text{ yr}^{-1}$  (Bendo et al. 2016).

Even though NGC 4945 has a partially obscured nucleus, its small inclination and an outflow from the nucleus enable spectroscopic studies to verify morphological evidence of the mass loss from the active nucleus. A conical structure extends out of the nucleus in the direction perpendicular to the disc, traced at IR, optical, and X-ray wavelengths (Nakai 1989a; Heckman, Armus & Miley 1990; Marconi et al. 1994; Moorwood et al. 1996; Schurch, Roberts & Warwick 2002; Rossa & Dettmar 2003; McCormick, Veilleux & Rupke 2013). Figure 1.11 shows the outflows from the centre of NGC 4945 (Moorwood et al. 1996). Optical images reveal a wide cone of radiation that spreads out from the relatively obscured nucleus. The emergence of a radial filament is strong evidence of the loss of material from the nucleus in the form of ionized gas (Nakai 1989b). The origin of the optical outflowing filament may be star formation (supernovae, stellar winds, and superwinds) (Whiteoak & Gardner 1979), or possibly non-thermal excitation (AGN) (Moorwood & Glass 1984). Heckman, Armus & Miley (1990) suggested, that the cone-like structure in H $\alpha$ + [N II] is produced by a superwind driven by shock-heated gas, and this bubble in NGC 4945 is limb-brightened on its outer edges. Furthermore, the same authors studied the kinematics of the emission lines and detected a split in the lines of H $\alpha$  and [N II] that appears in a region about 300 pc

away from the nucleus, and extends to about 500 pc northwest (NW); the velocity

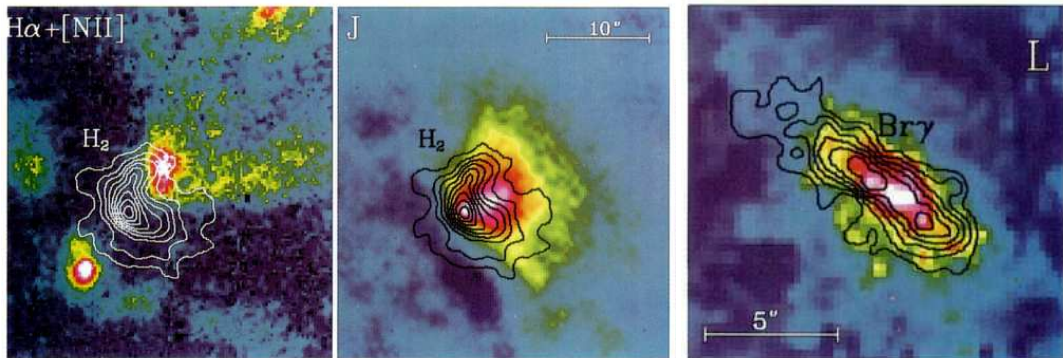


Figure 1.11: The nucleus of NGC 4945. Left and middle panel:  $H\alpha + [N II]$  and J continuum images from IRAC2-FP image, the contour represents  $H_2$  from IRAC2-FP image (step =  $0.3 \times 10^{-4} \text{ erg cm}^{-2} \text{ s}^{-1} \text{ sr}^{-1}$  from 0.4 to 2.8). Right panel: L-band image ( $3.5 \mu\text{m}$ ) superimposed by  $Br\gamma$  contours from the IRAC2-FP image (step =  $0.25 \times 10^{-4} \text{ erg cm}^{-2} \text{ s}^{-1} \text{ sr}^{-1}$  from 0.7 to 2). Adopted from Moorwood et al. (1996).

separation of the split lines is  $\sim 600 \text{ km s}^{-1}$  around the central area, and reduces to nearly  $300 \text{ km s}^{-1}$  near the edges of the bubble with full width at half maximum (FWHM) of each split component ranging from  $200 \text{ km s}^{-1}$  to  $400 \text{ km s}^{-1}$ ; the strong component is redshifted relative to the systemic velocity by  $50 \pm 50 \text{ km s}^{-1}$ , while the fainter component is blueshifted from the systemic velocity by  $250 \text{ km s}^{-1}$  to about  $550 \text{ km s}^{-1}$ . A study by Lípari, Tsvetanov & Macchetto (1997) added valuable information regarding the kinematics, extinction, and physical conditions in the active nucleus and surroundings in NGC 4945. Estimates from optical long-slit observations indicate that a blue asymmetry arises in the forbidden  $[N II]$  and  $[S II]$  lines in the nucleus of NGC 4945, and the FWHM of the blueshifted component of these two lines is  $\sim 700 \text{ km s}^{-1}$  with  $\Delta \sim 200 \text{ km s}^{-1}$  (Lípari, Tsvetanov & Macchetto 1997). These values (FWHM and velocity) are different from those suggested by (Heckman, Armus & Miley 1990). NGC 4945 is a one target in the MAGNUM survey to study feedback from AGN in Seyfert galaxies and its effect on galaxy evolution: a clear ejected cone emerges from the central area which was traced by  $[N II]$  emission to the NorthEast of the nucleus (Venturi et al. 2017).

The physical conditions in the circumnuclear region can be detected by tracing emission line ratios for  $H\alpha$ ,  $H\beta$ ,  $[N II]$ , and  $[S II]$  along a distance of  $\sim 80$  arcsec from the nucleus, with  $PA = 90^\circ$ . The ratio of the doublet emission lines of  $[S II]$  ranges from 1.0 to 2.5, and values of  $[N II]/H\alpha$  and  $[S II]/H\alpha$  ratios in the nuclear region are

1.3 and 0.94 respectively (Lípari, Tsvetanov & Macchetto 1997). This suggests that the gas has been shocked in this area, thus enhancing the ratio of forbidden lines with respect to  $H\alpha$ . Furthermore, it has filamentary extraplanar material which is seen in PAH emission (McCormick, Veilleux & Rupke 2013) (see Figure 1.12). It is clear in all regions of the galaxy and it follows the same shape of the wide cone that is suggested by Nakai (1989a) and Heckman, Armus & Miley (1990) in optical emission.

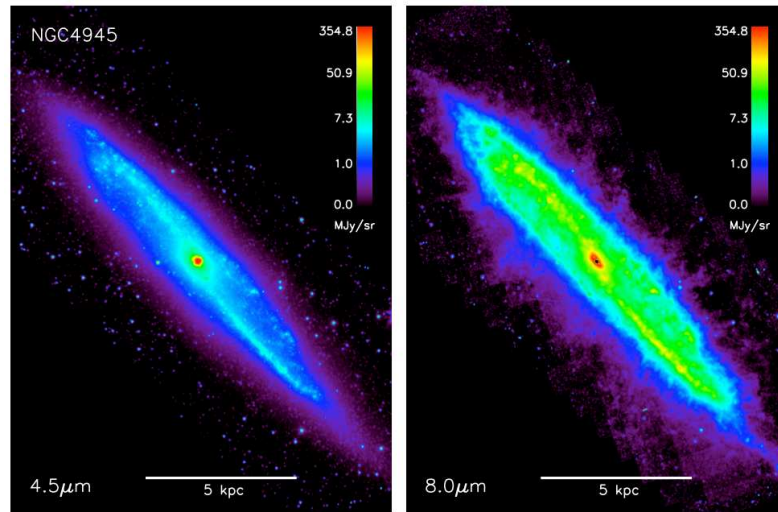


Figure 1.12: IRAC 4.5  $\mu\text{m}$  and 8.0  $\mu\text{m}$  images of NGC 4945 tracing PAH and hot dust emission. The intensity scalings are inverse hyperbolic sine in both panels. North is top and East is left (McCormick, Veilleux & Rupke 2013).

### 1.4.2 NGC 300

NGC 300 is a member of the Sculptor group at a distance of 1.9 Mpc (Gieren et al. 2005b). This group contains five prominent spiral galaxies (NGC 55, NGC 247, NGC 253, NGC 300, and NGC 7793) and about 20 dwarf galaxies (Côté et al. 1997). NGC 300 is the nearest neighbour to the Local Group (Jerjen, Freeman & Binggeli 1998).

NGC 300 is a face-on spiral galaxy (see Figure 1.13) of morphological type SB(s)d (Gieren et al. 2005a). It has low mass and is nearly bulgeless (Westmeier, Braun & Koribalski 2011). Radio observation using ATCA<sup>3</sup> (21 cm) reveals a dense inner HI disc which is parallel to the optical one and extends with a major axis of about  $1^\circ$  on the sky (Rogstad, Wright & Lockhart 1976; Wiegert & English 2014), and the rotation curve derived from those data is shown in Figure 1.14. The mass of atomic hydrogen is estimated to be  $\sim 1.5 \times 10^9 M_\odot$ , and the stellar mass in the disc is estimated to be  $\sim 1 \times 10^9 M_\odot$  (Westmeier, Braun & Koribalski 2011). The total SFR is estimated to be  $0.08\text{--}0.30 M_\odot \text{ yr}^{-1}$  by utilising various wavelength observations including: H $\alpha$  luminosity (Helou et al. 2004), X-ray luminosity (Bernard et al. 2012), far-UV (Karachentsev & Kaisina 2013), mid-IR emission (Helou et al. 2004).

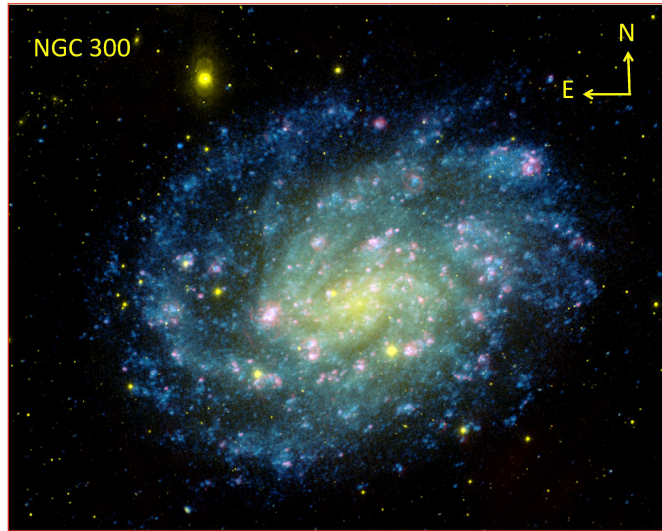


Figure 1.13: Color composite image of NGC 300 from NASA/JPL-Caltech/OCIW [http://www.galex.caltech.edu/media/glx2005-01r\\_img01.html](http://www.galex.caltech.edu/media/glx2005-01r_img01.html).

---

<sup>3</sup>The Australia Telescope Compact Array.

The diffuse ionized gas in NGC 300 was investigated by many (Marcelin, Boulesteix & Georgelin 1985; Hoopes, Walterbos & Greenwalt 1996; Hlavacek-Larrondo et al. 2011) to determine the rotation curve and systemic velocity of the galaxy. The latter used  $H\alpha$  emission based on Fabry-Pérot observations using the Marseille Telescope (36 cm) in La Silla, Chile, to map  $\sim 1'.3$  (7.3 kpc) around the centre of the galaxy. Its diffuse ionized gas extended across the entire H I disc, with prominent H II regions across the disc; the optical rotation curve was determined and is shown in Figure 1.15. Kang et al. (2016) suggested that NGC 300 could have experienced a fast growth of its disc. There is less infalling primordial gas onto the disc currently, based on a simple chemical evolution model for this galaxy.

NGC 300 has prominent H II regions and was the subject of extensive research. The first catalogue for H II regions in NGC 300 was established by Sérsic (1966), and many of the catalogued H II regions have been examined through spectrophotometry (Pagel et al. 1979; D’Odorico, Rosa & Wampler 1983; Webster & Smith 1983). The direct chemical abundances and electron temperatures were determined in NGC 300 by tracing emission lines ( $[O\ III]4365$ ,  $[S\ III]6312$ , and  $[N\ II]5755$  from H II regions (Bresolin et al. 2009b). They found that the oxygen abundance has a negative radial gradient ( $-0.077 \pm 0.006$  dex  $kpc^{-1}$ ), which is steeper than has been measured in planetary nebulae (PNe) (Stasińska et al. 2013).

Interesting eruptive sources have been discovered recently, such as SN2010da which represents the eruption of massive stars ( $10-12 M_{\odot}$ ). SN2010da shows a dusty and complex circumstellar environment, which probably plays an important role in the stellar evolution of increased activity and mass loss (Villar et al. 2016).

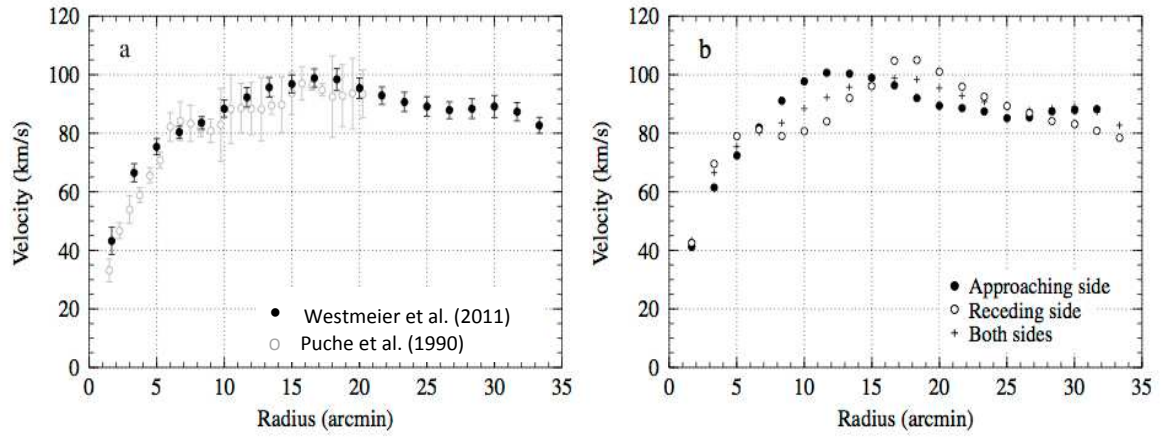


Figure 1.14: The rotation curve of NGC 300 from two different works based on ATCA and VLA observations (Muñoz-Mateos et al. 2007).

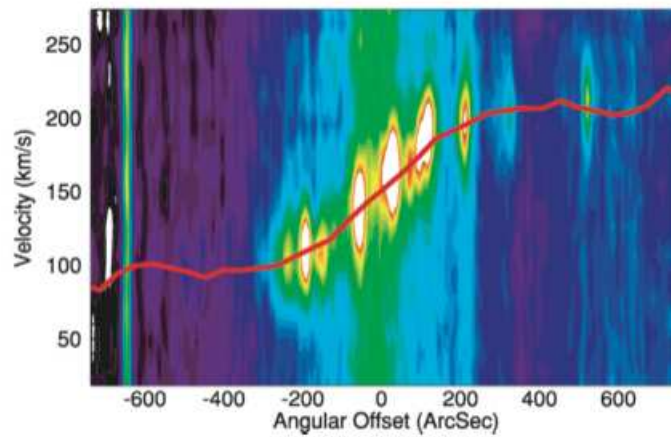


Figure 1.15: The optical rotation curve of NGC 300 based on Fabry-Pérot observation (Muñoz-Mateos et al. 2007).

## 1.5 Aims and outline

The overall aim of this thesis is to search for evidence of disc–halo interaction in spiral galaxies by tracing ionized outflows from the disc, and to study their influence on the evolution of disc galaxies by quantifying the impact of the outflows on the surrounding ISM as well as examining the physical conditions of the areas which have ejected ionized gas. This is to be achieved by utilising two main sources of ionized outflows (AGN and H II regions) in two late-type spiral galaxies: edge-on galaxy NGC 4945 and face-on NGC 300. Observations on which this project is based were taken using the two modes of the RSS (The Robert Stobie Spectrograph): Fabry-Pérot (FP) and long-slit (LS).

- Chapter 2: this chapter introduces the principles behind, and overview of, the instruments used and data reduction adopted in this thesis.
- Chapter 3: in this chapter, I chose NGC 300 as an example of a nearby face-on galaxy to study the ionized outflows by observing emission lines from 18 H II regions which are distributed across two fields ( $8'$ ) by using the two modes of the RSS (FP and LS). The goal of this chapter is to examine the physical, chemical and kinematical properties of selected areas (H II regions) in order to quantify the impact of the outflows on ambient ISM.
- Chapter 4: in this chapter, I analyse two modes of RSS observations that trace the ionized outflows from the centre of NGC 4945. This galaxy ejected material from the centre in the form of a cone that is extended to about 2 kpc away from the centre and 6 kpc along the disc. The ionized outflows from the centre of NGC 4945 were mapped to study the morphology and kinematics using different emission lines.
- Chapter 5: this chapter represents an ongoing project (long-term project). The aim of this chapter is to study the outflows from active regions such as H II regions or AGN by tracing Balmer recombination emission lines, and investigate dusty extraplanar gas blown by galactic winds. As a first stage, I analysed H $\alpha$  observations for 9 out of 36 edge-on galaxies using FP (LR) mode.
- Appendices: in these appendices I show charts of Long-slit observations, spectra of objects of interest in NGC 300, an example of input file used in CLOUDY model and Tables for the full sample of galaxies included in the optical and radio survey.

## Chapter 2

# Observations and data analysis

This section will introduce the instruments used to achieve the analysed observations in this thesis, and the analytical methods that are applied.

### 2.1 SALT

Our observations were obtained with the 10 m Southern African Large Telescope (SALT) shown in Figure 2.1. SALT is the largest single optical telescope in the world, and has a hexagonal primary mirror array comprising 91 individual hexagonal mirrors.



Figure 2.1: The Southern African Large Telescope, image taken by the author.

The primary mirror in SALT is stationary during the time of observation while the secondary optics unit is moved along the primary mirror's focal plane to track an object, this system is usually different from most of the telescopes in the world. It can provide 8 arcmin as a field of view.

There is a limitation of SALT telescope observations according to its altitude ( $47^\circ$ – $59^\circ$ ). SALT can observe an object which has Hour Angle and Declination which are inside the annular region that is shown in the Figure 2.2. The RSS (Robert Stobie Spectrograph) is a prime-focus spectrograph, which is installed on SALT, and can provide three modes including: long-slit, multi-object, and Fabry-Pérot imaging spectroscopy.

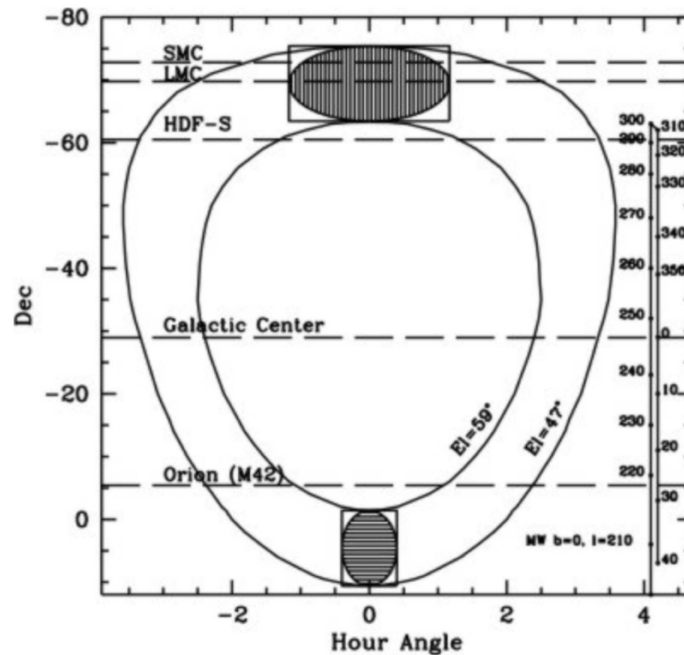


Figure 2.2: The toilet seat diagram of SALT, objects have values of Hour Angle and Declination in the annular regions that can be observed by SALT. A tracker motion range at two different declinations are shown with the hashed regions, [http://pysalt.salt.ac.za/proposal\\_calls/current/ProposalCall.html](http://pysalt.salt.ac.za/proposal_calls/current/ProposalCall.html).

## 2.2 The long-slit spectroscopy

The long-slit spectrograph is an appropriate instrument for observing extended objects like galaxies. Although its observations are in one dimension, it has the capability for uncovering the spectrum of the emission and absorption lines from the target. Hence, many parameters of the line profile can be quantified from this spectrum like systemic velocity and velocity dispersion as well as the intensity of these lines that can provide information about abundances of the elements and physical conditions in the observed areas.

The traditional long-slit spectrograph consists of five important elements (see Figure 2.3):

- The slit: The slit confines the light which enters the spectrograph. The width of the slit is set according to the type of observed object and the purpose of observation, as well as the spectral resolution that is needed.
- The collimator: collects the light from the object and converts it to parallel beams.
- Grating: It disperses the light beam to produce a spectrum.
- The camera: Its function is usually to focus and project the produced spectrum onto the detector.
- The detector: A charge-coupled device (CCD) uses to record signals (photons) which are collected by the optical system of the telescope and converted to electrons by the photoelectric effect. These electrons then pass through amplifier. A computer converts the out-put signal into a two-dimensional digital image.

The resolving power is the ability to differentiate between two successive wavelengths separated by  $\Delta\lambda$ , and it depends on the slit width and wavelength. It is determined by:

$$R = \frac{\lambda}{\Delta\lambda} \quad (2.1)$$

the resolving power can also be derived in terms of  $\Delta\lambda$  (in units of  $\text{\AA}$  or nm). <https://www.slideshare.net/TianaRuchti/micron-optics-fiber-fabryperot-tunable-filter-products>

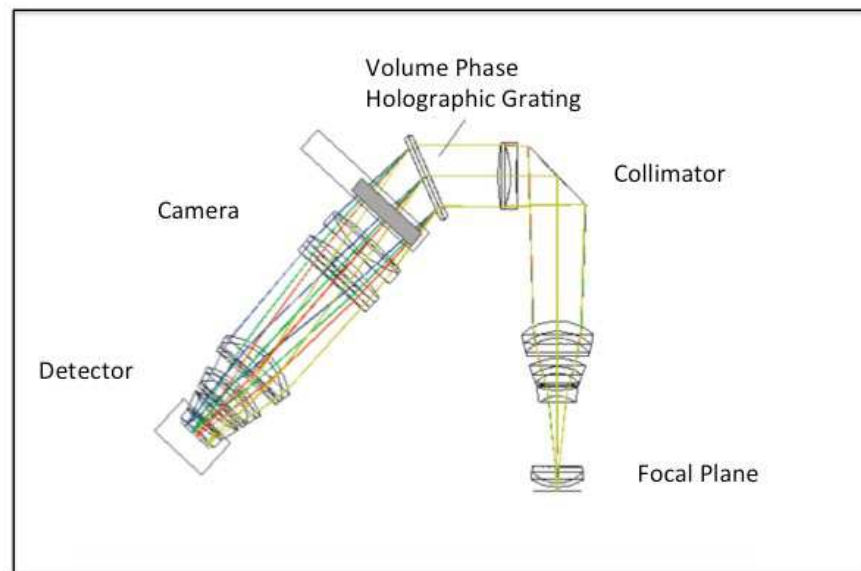


Figure 2.3: The schematic represents the important optical components of the long-slit spectroscopy mode of RSS in SALT. <https://old.salt.ac.za/telescope/instrumentation/rss/>.

### 2.2.1 Long-slit data reduction

When we acquired spectroscopic data from the SALT telescope, a few steps of data reduction were already done for these long-slit data including: bias-subtraction, dark frame subtraction and flat fielding (see Figure 2.4). But, the received data required

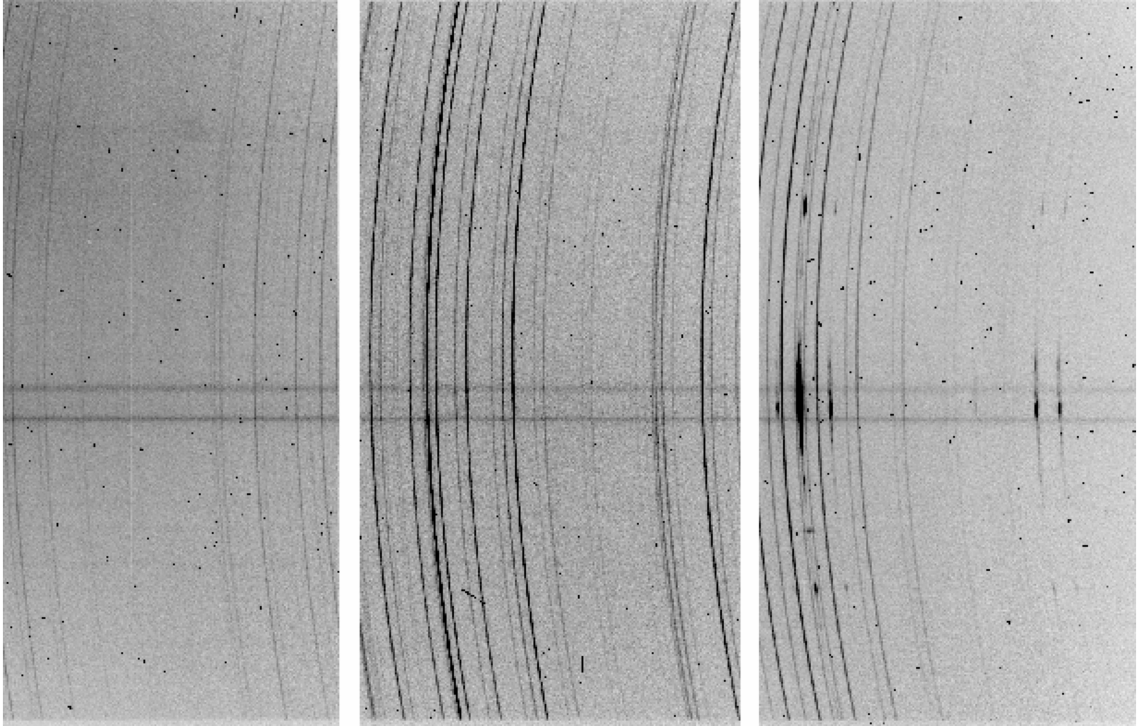


Figure 2.4: An example of received data of the long-slit from SALT. Notice the curved telluric emission lines, and the two data gaps between the three CCDs. X-axis represents observed wavelengths and the y-axis shows the position on the sky.

more important reduction processes. These extra reductions were done by using the *PYSALT SALTSPEC* package, *PYRAF*<sup>1</sup> and IRAF<sup>2</sup> (The Image Reduction and Analysis Facility). The produced raw images via SALT RSS spectroscopy have double extensions (header of the fitfile) and to reduce these data by the *IRAF* or *PYRAF* *PYSALT* package, these images are required to be converted to one extension. The

---

<sup>1</sup>Which represents a command language being based on python language that is used to run *IRAF* tasks.

<sup>2</sup>More information about IRAF can be found at <http://iraf.noao.edu>.

*SALT2IRAF* task in *SALTRED* from *PYRAF PYSALT* package was used to produce images with a single extension. The next step was to clean all frames from cosmic ray events which cause artefacts in images produced by CCD detectors. This work was done by using the *PYSALTSALTSPEC* package, by removing all bad pixels that have unusual shapes or sizes by adopting an algorithm of fluctuation of Laplacian edge detection. It is important to be sure that the process did not remove any science signal by comparing the old and the new frame. The cleaned frame is presented in Figure 2.5.

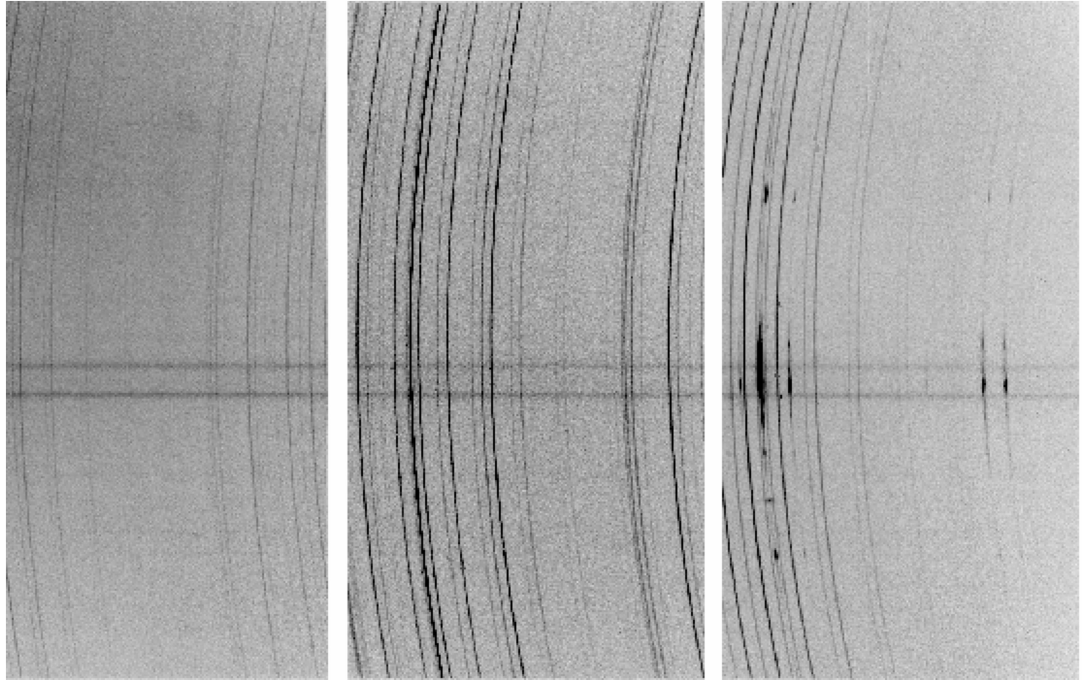


Figure 2.5: The long slit frame after filtering cosmic ray events.

The more important step of the data reduction procedure was the wavelength calibration, where the emission lines were identified by using an arc lamp spectrum, for the red part of the spectra the Ne arc was used and for the blue part the CuAr arc was used. This step was achieved by adapting different tasks in the *noao* package from *PYRAF*:

- *identify* to find dispersion functions for spectra of the arc-line calibration spectra, see Figure 2.6. We need identified spectra for the arc-scan (Figure 2.7) which was done in the same conditions for the observations (grating station, filter, articulation angle and grating rotation angle) in order to compare with the object scan. The identify arc-line calibration spectra is shown in Figure 2.6.

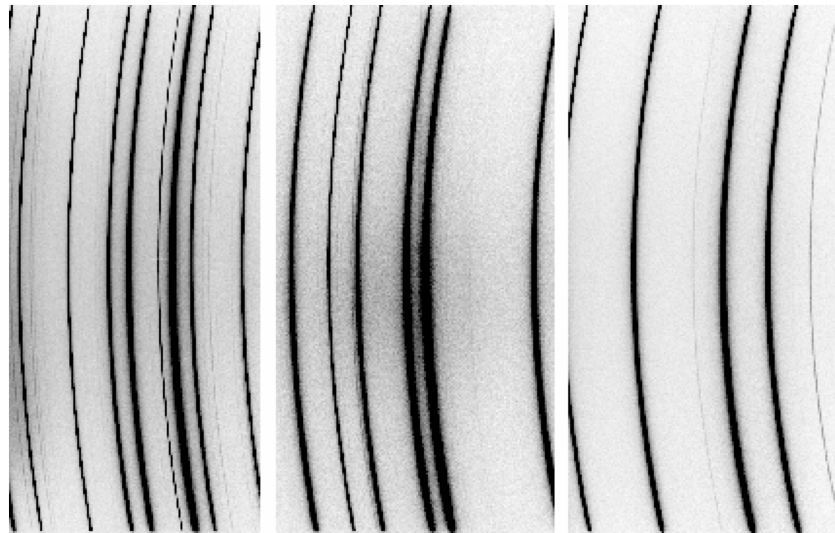


Figure 2.6: An example of arc lamp calibration that was observed after the object observation in the same setting.

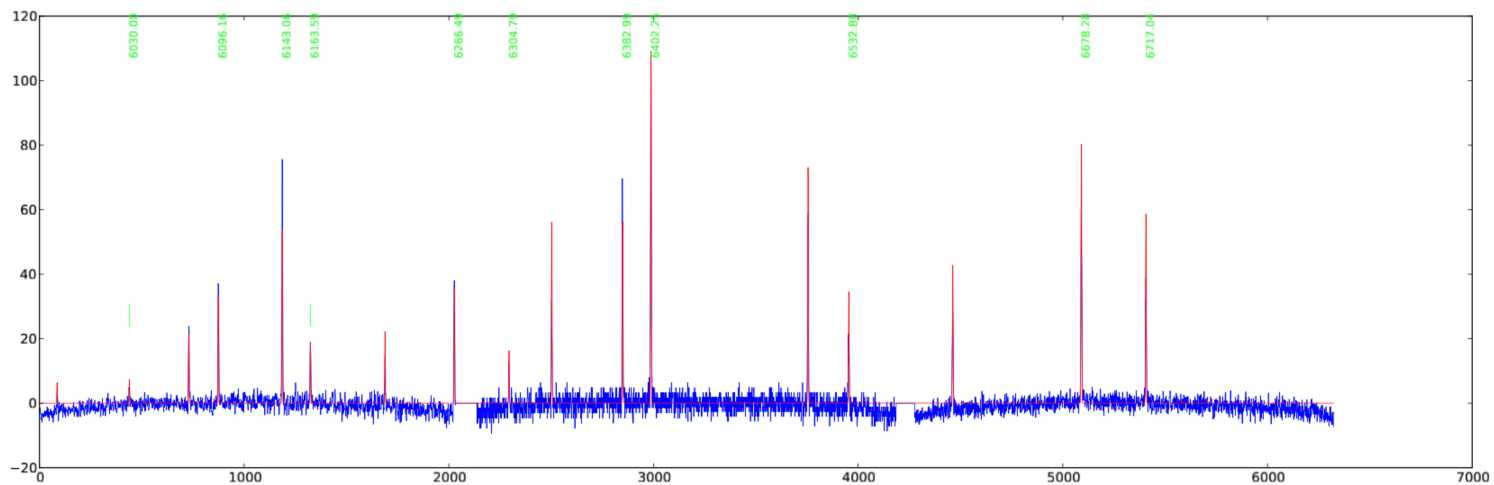


Figure 2.7: An example of arc lamp spectrum which was used to identify lines of the arc-line calibration spectra which were created by *PYSALT SALTSPEC* package.

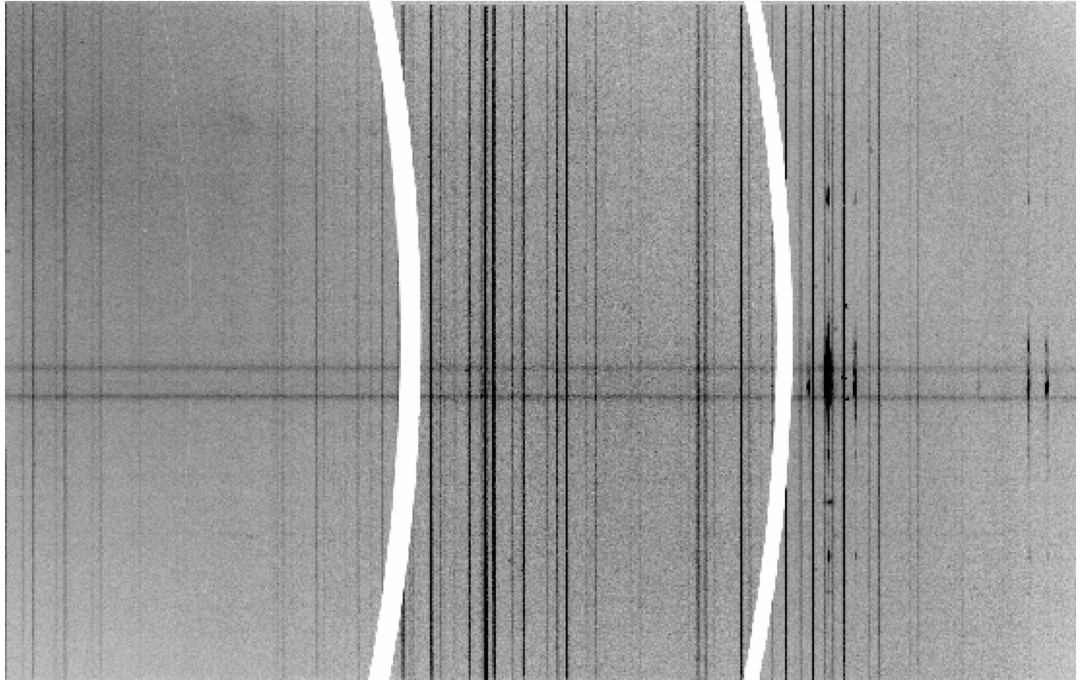


Figure 2.8: The long-slit frame after transforming the identified arc lamp frame solution. Notice the telluric emission lines are now straight, but the CCD gaps have become curved.

- *reidentfiy* to transfer the dispersion solutions from the identify spectra to the arc calibration spectra. Each arc calibration has a file which contains a list of lines and corresponding intensity in *PYSALTSALTSPEC* package. It is used to identify the coordinates, and we accepted the wavelength solution when the RMS has small value nearly 0.02.
- *fitcoords* to fit user coordinates to the image coordinates.
- *transform* to transfer the wavelength solution from the arc frame to the science frame (see Figure 2.8).

The *background* task of standard *PYRAF* offers the ability to fit the background of the sky lines across the observed area, this task is more than sufficient for extended objects such as galaxies. Figure 2.9 shows the clean frame after removed sky background. An IDL routine was used to subtract and plot the final spectra.

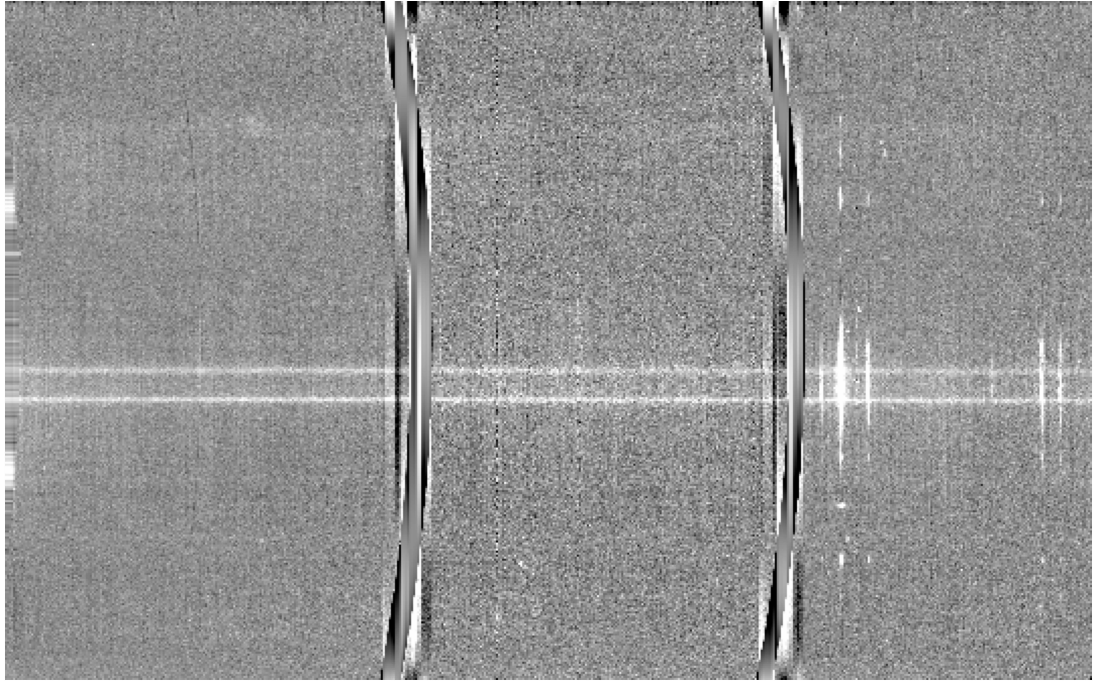


Figure 2.9: The final frame after removing sky lines.

## 2.3 Fabry-Pérot spectral imaging

FP is an observational technique that offers three dimensional information about the observed target. FP produces data in the form of data cubes. These data cubes are comprised of two spatial dimensions  $[x, y]$  and a wavelength dimension ( $\lambda$ ) (see Figure 2.10).

The FP mode of the RSS on SALT covers a wavelength range between 4300 to 8600 Å and has three main resolving power modes at 6500 Å, low (LR), medium (MR), and high (HR), their values are 800, 1500, and 8000 respectively.

Firstly, we adopted the MR mode of FP to obtain spectroscopic imaging over a different range of wavelengths for some observations but, unfortunately, the use of MR etalon in the SALT telescope was stopped in October 2015, due to technical issues related to a degradation in the coatings of the etalon.

FP technology has evolved in astronomy since its first use by Fabry himself (Buisson, Fabry & Bourget 1914) to detect the Orion nebula. Several large telescopes now use FP mode with different system such as the the Ohio State imaging FP (Pogge et al. 1995), the Goddard FP imager (Gelderman, Woodgate & Brown 1995), and the Hawaii imaging FP interferometer (Bland & Tully 1989). The FP technology has been

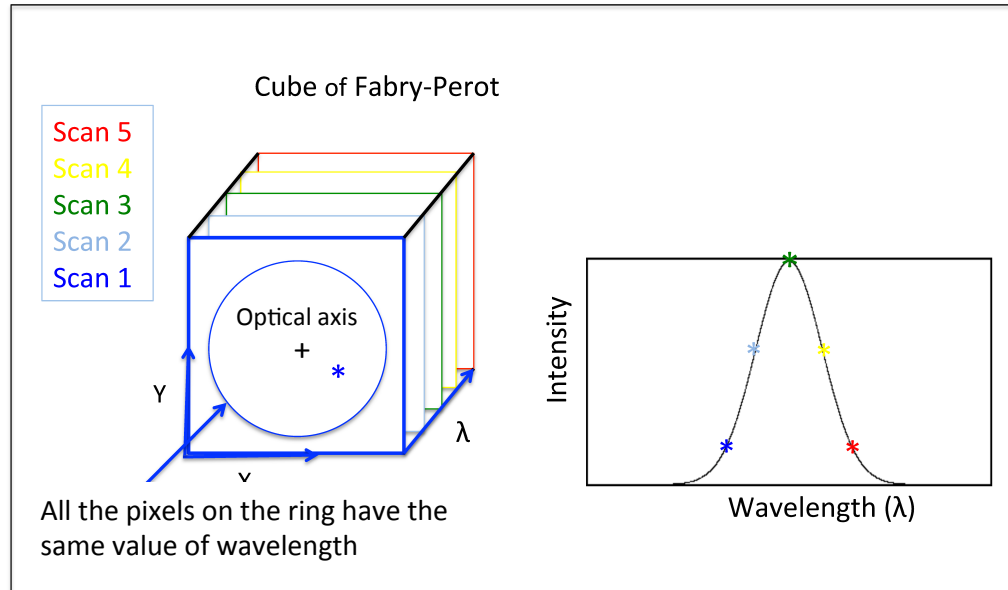


Figure 2.10: Representative diagram of a data cube of Fabry-Pérot. The data cube produces three dimensional information (two spatial, one wavelength), therefore, all pixels have the same position in the successive scans of the cube, and the emission line profile.

developed to cover the near infrared range like the UNSWRIF system (Ryder et al. 1998). The spectroscopic imaging yields a spectral cube, and can present kinematical information of the adopted fields. The important components are shown in Figure 2.11. In general, the interferometer has main components including: a collimating lens<sup>3</sup>, a Fabry-Pérot etalon, and a focusing lens.

The etalon of FP consists of two glass plates, which are designed to be parallel with each other and perpendicular to the optical axis of the etalon. The inner surfaces of the two plates are coated with partially reflective material. Air or nitrogen is used to fill the gap in between the two plates. The gap separation ( $d$ ) controls the adjusted wavelength or by changing the refractive index of the gap medium in this case the etalon represents a tunable filter (Rangwala et al. 2008). The incident light on the etalon with angle  $\theta$  will experience multiple reflections between the parallel plates, resulting in an interference pattern (constructive and destructive interference).

<sup>3</sup>The convex lens directs the observed light beam onto the first plate of the etalon. The transmitted beams with required wavelength from the second plate are parallel for each other. Hence, we need to focus these beams by using another lens before pointing them on the CDD or CDDs.

The constructive interference happens if the transmitted beams are in phase, and the destructive interference if the beams are out of phase. Both cases are determined by different parameters: the wavelength of the reflected light, the angle of the reflected light through the etalon, the gap of the etalon, and the refractive index of the material between the plates. The following relation gives the phase difference between the multiple reflected beams:

$$N\lambda = 2nd \cos \theta \quad (2.2)$$

where:

$n$  = refractive index of the material between the plates.

$d$  = gap separation.

$N$  = order of an interference.

$\theta$  = the incident angle.

$\lambda$  = wavelength of the reflected light into the gap medium.

where:

$$\lambda = \frac{\lambda_o}{n} \quad (2.3)$$

$n$  = refractive index of the gap medium.

$\lambda_o$  = wavelength of the reflected light in the vacuum.

The separation between any successive interference orders represents the free spectral range ( $FSR$ ) which informs us of a range of wavelengths that can be observed.  $FSR$  is a function of the gap separation, and is determined by considering the phase shift between a particular wavelength ( $\lambda$  with order  $N + 1$ ) and  $\lambda + FSR$  with order  $N$ , and apply equation (2.2) for  $\theta = 0$  or  $2\pi$ .

$$(N + 1)\lambda = 2nd \quad (2.4)$$

$$N(\lambda + \Delta\lambda) = 2nd \quad (2.5)$$

The maximum of two wavelengths overlaps:

$(N + 1)\lambda = N(\lambda + \Delta\lambda)$  Then:

$$\Delta\lambda = \frac{\lambda}{N} \quad (2.6)$$

From 2.2 with  $\theta = 0$  or  $2\pi$ :

$$N = \frac{2nd}{\lambda} \quad (2.7)$$

$$\Delta\lambda = \frac{\lambda^2}{2nd} \quad (2.8)$$

$$FSR = \Delta\lambda = \frac{\lambda}{N} = \frac{\lambda^2}{2nd} \quad (2.9)$$

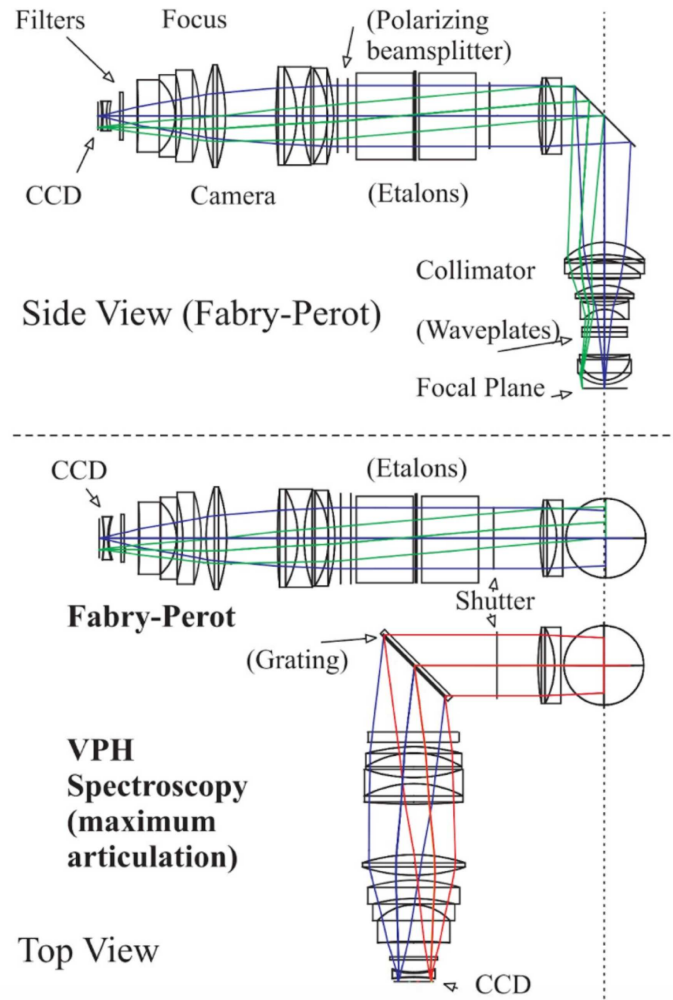


Figure 2.11: The major components of the interferometer: Collimating lens, Fabry-Pérot etalon, and focusing lens, [http://pysalt.salt.ac.za/proposal\\_calls/current/ProposalCall.html](http://pysalt.salt.ac.za/proposal_calls/current/ProposalCall.html).

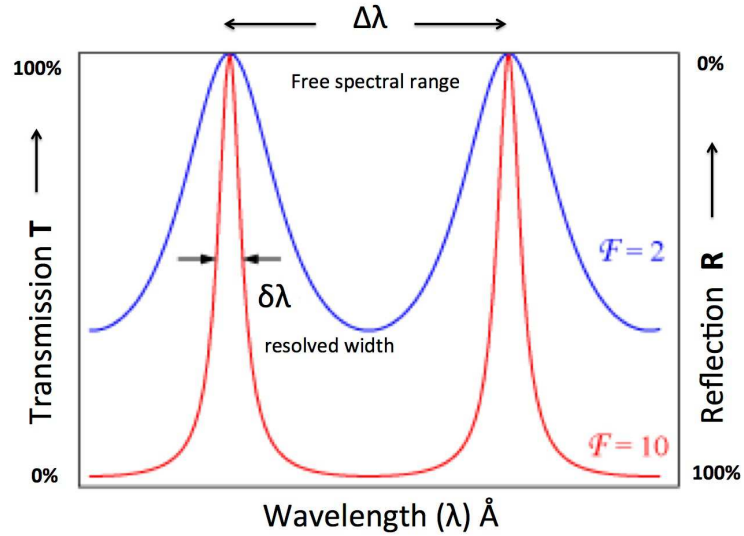


Figure 2.12: The transmission profile of Fabry-Pérot: The red line shows the FP transmission profile with high finesse ( $\mathcal{F} = 10$ ), and the blue one represents the FP transmission profile with low finesse ( $\mathcal{F} = 2$ ), adopted from <https://www.slideshare.net/TianaRuchti/micron-optics-fiber-fabryperot-tunable-filter-products>.

Another important parameter in the etalon is finesse  $\mathcal{F}$ , which is a criterion of the interference fringes width (or sharpness), which is only determined by the reflectance in an ideal etalon (no absorption or scattering  $T=1-R$ ), and named reflectivity finesse ( $\mathcal{F}_r$ ).

$R$  = reflectivity of the coating plates ( $0 \leq R < 1$ ).

$T$  = transmissivity of the coating plates ( $0 \leq T < 1$ ).

$$\mathcal{F}_r = \frac{\Delta\lambda}{\delta\lambda} \quad (2.10)$$

$\delta\lambda$  = wavelength resolution, as illustrated in Figure 2.11.

The resolving power of the FP is given by:

$$\mathcal{R} = \frac{\lambda}{\delta\lambda} = N\mathcal{F}_r \quad (2.11)$$

$$\mathcal{R} = N\mathcal{F}_r \quad (2.12)$$

Hence, the resolving power can be improved in two ways, by increasing reflectivity, or interference order ( $N \propto 2d\lambda$ ).

The non-flatness of the FP plates increases the defect finesse ( $\mathcal{F}_D$ ) and reduces the expected finesse and spectral resolution by reducing the transmitted intensity. There are three major types of defects in practical FP: Roughness and irregularities of the surface, curvature in the plates, and parallelism of the plates. Hence, to determine the effective finesse  $\mathcal{F}$ , the combination of the reflectance and defect finesse should be taken into account, according to the following equation:

$$\frac{1}{\mathcal{F}^2} = \frac{1}{\mathcal{F}_r^2} + \frac{1}{\mathcal{F}_D^2} \quad (2.13)$$

Where  $\mathcal{F}_D$  represents the combination of all types of the defects. More details about the SALT FP mode can be found in (Rangwala et al. 2008).

The value of  $\mathcal{F}_r$  at the LR in Étalon 1052 for SALT PFIS is approximately 30 at 6500 Å with reflector coating 90%  $\pm$  4 & from 4300 Å to 8600 Å, which can be determined from the following equation:

$$\mathcal{F}_r = \frac{\pi R^{\frac{1}{2}}}{1 - R} \quad (2.14)$$

and the defect finesse can be derived from the following equation:

$$\mathcal{F}_D = \frac{m}{2} \quad (2.15)$$

$m$  = the plate flatness in waves ( $\lambda/m$ ).

The defect finesse can be estimated  $\sim$  21 from the finesse in LR mode plot at the Étalon 1052 measurements on salt website for more information see [http://astronomers.salt.ac.za/wp-content/uploads/sites/71/2014/10/Etalon\\_1052\\_Report.pdf](http://astronomers.salt.ac.za/wp-content/uploads/sites/71/2014/10/Etalon_1052_Report.pdf).

### 2.3.1 Fabry-Pérot reduction

Detailed information is illustrated in the following subsection about data reduction of FP that is used in this project. The first step was to transform SALT images from a double to a single extension, and to remove cosmic rays which is done in the same way as for long-slit images. Typically, FP data reduction has some preliminary steps that are the same as those which are used to reduce CCD images.

### 2.3.2 Mask

The RSS detector is normally illuminated by the RSS FP system, while in the portion that is un-illuminated, it records only noise and scattered light in the signal. As a result, the un-illuminated region is very noisy especially after division by the flat field so, all FP scans were mask to be zero by using Mask code as add an on program in FP package that was written by Ted Williams (Mitchell et al. 2018), and this will reduce time of the cosmic ray detection routines by avoiding dealing with the noise as cosmic rays. In other words, the masking operation speeds up the processing.

### 2.3.3 Ghost

Ghost images appear in FP scans as a result of reflection and scattering between optical components of FP mode, that can reduce the quality of the observations by adding fake signals (Mitchell et al. 2015). The reflection between the CCD detector and the FP etalon is the main cause that is responsible for creating ghosts in the image. This ghost image occurs in focus and shows mirror-symmetry around the optical axis, with an amplitude of nearly 5-8%. Multiple factors determine the ghost amplitude including: the etalon transmission profile, reflection, the transmission curve of the filter, and the reflectivity and efficiency of the CCD and the source spectrum. As a result of the complex relation between these factors, the amplitude of the ghost differs throughout the image as well as the ghost strength dropping linearly with radius about a point (the ghost amplitude centre). To decide the accurate position of the ghost centre in the FP scan, the position of 20 bright stars and their ghosts were determined in the average scan for the successive scans in FP datacube (by using *imcombine* in *IRAF*). The *qphot* task in the *noao* package in *IRAF* was used to determine the photometry of these stars, in other words, the precise position and magnitude of these stars and their ghosts.

It is worth mentioning that the CCD used by SALT comprises three chips which are optimised for spectra, not for imaging, and give a probability movement of the outer CCDs relative to the central CCD2. Due to these movements the centre of the

ghost of CCD1 and CCD3 will shift from that of CCD2. To take into account these shifts, we choose stars in positions that cover the three CCDs. The ghost amplitude and ghost reflection were determined by fitting the linear relation between the flux ratio of the star and its corresponding ghost as a function to their position from the centre of the image. The ghost centre in CCD2, the ghost centre offset in CCD1 and CCD3 were determined from the position of the 20 stars and their ghost positions. The penultimate step was to create a ghost image by rotating each FP scan around the optical axis by  $180^\circ$ , then scaling it by using the main scale factor ( $M$ ):

$$M = \sum_{j=1}^N \frac{1}{N} \frac{Gf_j}{Sf_j} \quad (2.16)$$

where:

$N$  = number of FP scans in datacube.

$Gf$  = ghost flux.

$Sf$  = star flux.

The ghost image was subtracted from each corresponding FP image; this step was done by using the *imarith* task in *PYRAF*. Figure 2.13 (right panel) shows some examples of ghosts, and Figure 2.13 (left panel) shows their deghosted positions in the FP scan. We can notice this procedure eliminates the galaxy ghosts successfully where the ghosts could have more an impact on our observation, and some stellar ghosts were over or under subtracted.

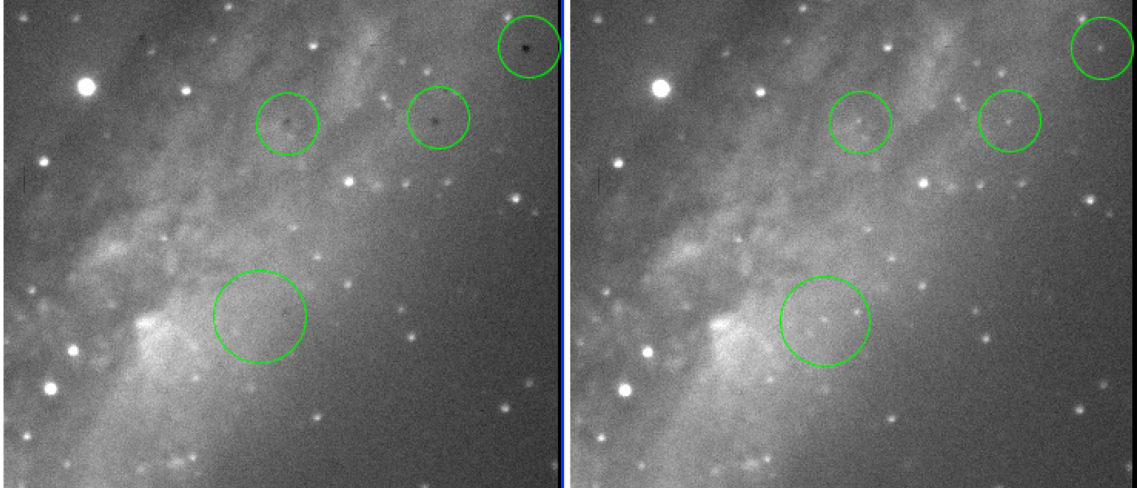


Figure 2.13: The left panel shows the deghosted frame and the right panel represents the ghost frame. The green circles show examples of the treated areas.

### 2.3.4 Flat field

The flat-field correction was done after the ghost process had been done because if it is done before, it would distort the ghost reflection amplitude pattern. This correction is important in images that are produced by CCDs due to the response variation of the CCDs from pixel to pixel. Flat-field correction is carried out by dividing each FP image by the corresponding flat-field frame. The principle of this process is that areas which are faintly illuminated in the flat-field frame become highly illuminated and the brighter areas become dimmer. These corrections are for any vignetting, uneven illumination, and dust grains effects in the FP image. This step was done by using the standard *PYRAF* package *imarith* task. The SALT optical system is highly complicated so, the accuracy of flat-field correction is approximately 5 %. We tested the standard deviation (stddev) across different frames before and after flatfielding in different position, we found the flat field process reduced the stddev.

### 2.3.5 Flux calibration and scaling

Flux calibration is required to convert the observation to values in physical units in order to compare with other physical models. The *IRAF* package *apphot* task *qphot* was used to make aperture photometry on 20 isolated stars. This technique is useful to reduce the impact of clouds and the filter transmission on the photometric variation to normalize the successive scans. In other words, this is putting all the FP scans in

Table 2.1: An example of the main parameters of the input task *qphot* used in *PYRAF* for Fabry-Pérot scans.

Parameter	Definition	Value used
cbox	The centering box width in pixels	8
annulus	The inner radius of sky annulus in pixels	8
dannulus	The width of the sky annulus in pixels	7
apertures	The list of photometry apertures	4

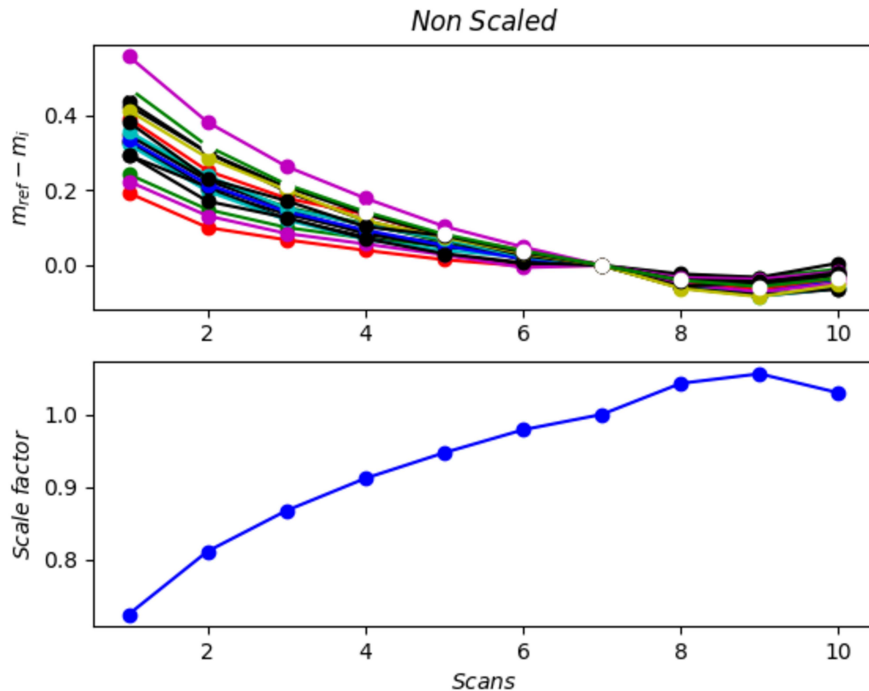


Figure 2.14: The top panel shows the normalised magnitude of the chosen stars in each FP scan, while the bottom panel displays the scale factors. Scan number 7 was chosen as reference.

similar conditions before extracting their information. The parameters of the *qphot* setting used are shown in Table 2.1 according to the intensity profile of the stars in question, which was achieved by doing the *imexam* task in standard *PYRAF*.

One scan was chosen to be the reference for the other scans; the scale factor of each scan was determined by subtracting the magnitude of its stars ( $m_i$ ) from that in the reference scan ( $m_{\text{ref}}$ ).

$$\mathcal{F}_i^j = 10^{-\frac{(m_{\text{ref}} - m_i)}{2.5}} \quad (2.17)$$

where:  $j$  = the number of the FP scans.

The next step was to find the average scaling factor of all the stars by using:

$$scale^j = \frac{1}{N} \sum_{i=1}^N \mathcal{F}_i^j \quad (2.18)$$

where  $N$  is the number of selected stars. Figure 2.14 shows the difference in the magnitudes of the chosen stars with respect to that in the reference scan, and the scaling factor as a function of successive scans of FP. All FP scans are divided by the corresponding scale factor value by using the standard *PYRAF* package *imarith* task. The reference scan was chosen by checking the FWHM of the stars in each scan and taking the scan with constant FWHM for all the stars in the scan.

### 2.3.6 Wavelength calibration

The night-sky emission has an impact on the observed spectrum of stars, galaxies, and nebulae. However, it has advantages, such as using them for wavelength calibration. In our range of observations, the sky-lines are from the Meinel rotation vibration band of OH (Osterbrock et al. 1996), the spectrum of the sky-lines that is used in our work is shown in Figure 2.15. To identify the recorded night-sky lines in every observed images, the median<sup>4</sup> of all FP images was subtracted from each single observed image<sup>5</sup>, as presented in Figure 2.16. Two sky-lines were identified in Figure 2.16.

---

<sup>4</sup>This step was done by using *epar imcombine* task in standard *PYRAF*.

<sup>5</sup>The *imarith* task in *PYRAF* was used to do this process.

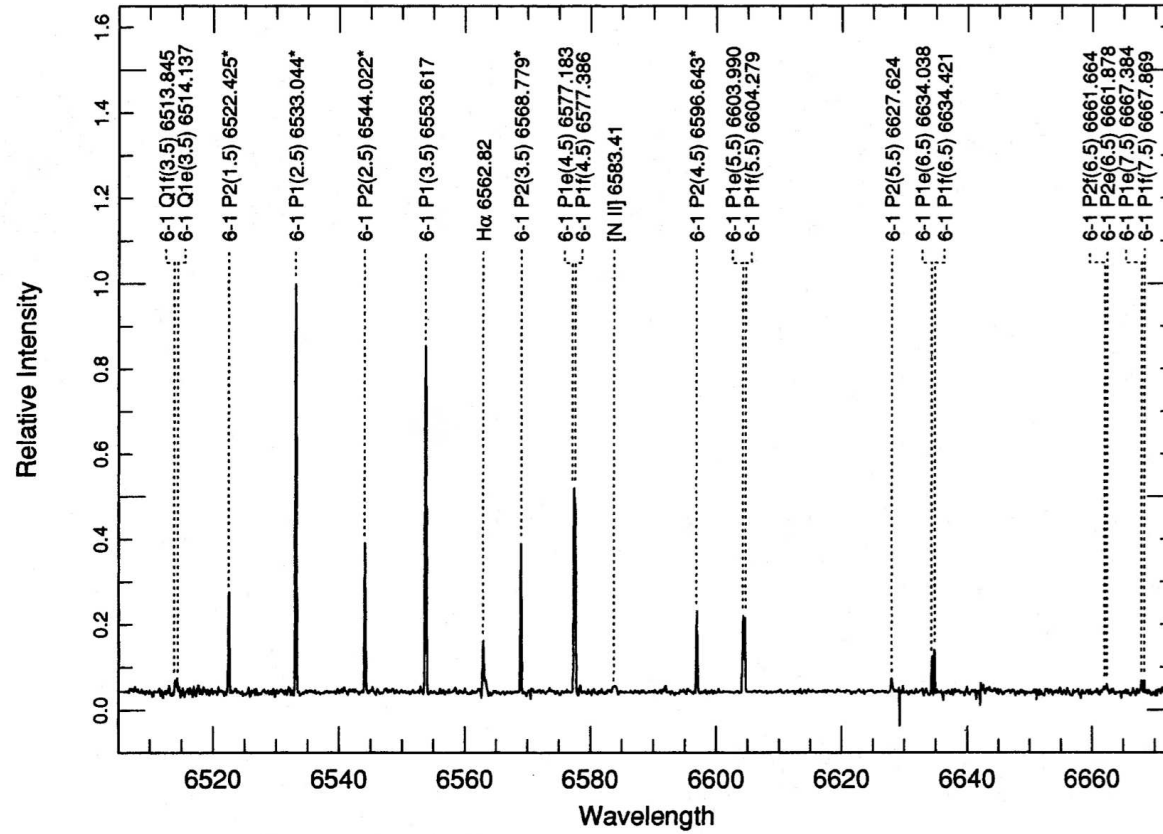


Figure 2.15: The OH sky-lines emission in the range between 6000 Å to 6680 Å (Osterbrock et al. 1996).

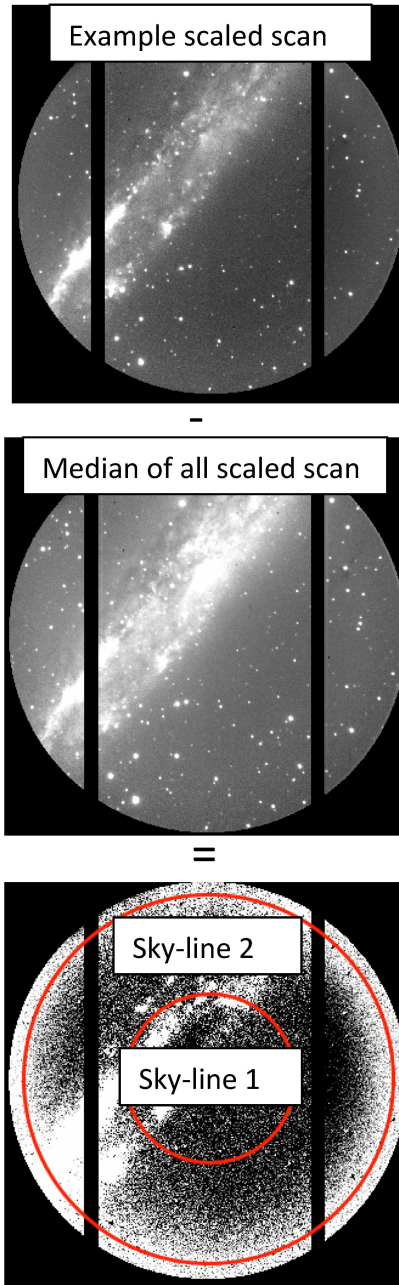


Figure 2.16: The extraction method of sky-lines.

Before starting to identify the recorded sky-lines by the extraction method (shown in the bottom panel in Figure 2.16), it is important to display the shape of the interference pattern rings which are created by illuminating the etalon with monochromatic light, as shown in Figure 2.17 (Moiseev 2002). The  $\cos\theta$  in Figure 2.17 can be described by:

$$\cos \theta = \frac{f}{\sqrt{f^2 + r^2}} = \frac{1}{\sqrt{1 + (\frac{r}{f})^2}} \quad (2.19)$$

where:

$r$  = distance from the optical axis to the ring in pixel units.

$f$  = camera optics focal length in pixel units.

The condition for constructive interference pattern can be expressed by the equation 2.2:

$$N \lambda = \frac{2 d n}{\sqrt{1 + (\frac{r}{f})^2}} \quad (2.20)$$

where:

$n$  = refractive index of the material between the plates.

$d$  = gap separation.

$N$  = order of an interference.

$\theta$  = incident angle.

$\lambda$  = wavelength of the reflected light into the gap medium.

It is clear from equation (2.20), that the ring radius is a function of both the wavelength and the gap separation between the two plates of the etalon.

Four coefficients control the properties of the etalon:  $A$ ,  $B$ ,  $E$ , and  $f$ , as follows:

$$\lambda_0(z, t) = A + Bz + Et. \quad (2.21)$$

$$\lambda_r(z, t, r) = \frac{\lambda_0(z, t)}{\sqrt{1 + (\frac{r}{f})^2}} \quad (2.22)$$

where:

$z$  = controlled parameter expressing the separation between the etalon plates.

$t$  = observation time.

$\lambda(r)$  = wavelength at a distance  $r$  (in pixels) from the optical axis in Å.

$\lambda_0$  = wavelength at the peak of the sky emission line in Å.

$f$  = focal length of the camera optics in pixels.

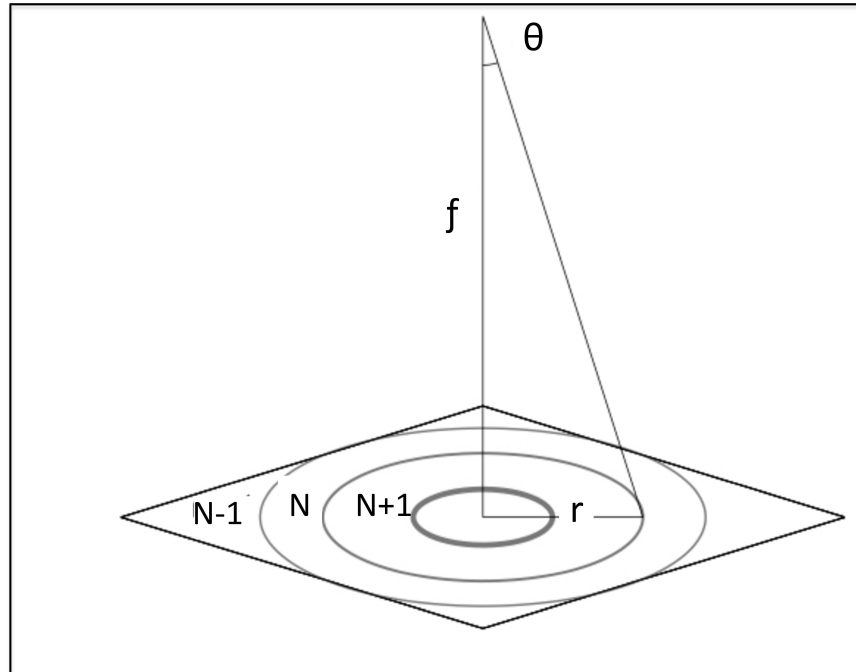


Figure 2.17: The geometry of the interference pattern produced via FP étalon from monochromatic light, shows the relation between the incident angle of the light beam, the radius of the formed rings and the focal length of the camera (Moiseev 2002).

From equation (2.21), one can see that  $\lambda_0$  is a linear function with  $z$ , and  $E$  is a coefficient that represents the stability of the instrument, and has a small fitted value  $\approx 2 \text{ \AA hr}^{-1}$  (Mitchell et al. 2015). Hence, equation 2.22 becomes less complicated:

$$\lambda_r(z, t, r) = \frac{A + Bz}{\sqrt{1 + (\frac{r}{f})^2}} \quad (2.23)$$

A sole FP scan that is illuminated by a monochromatic source with  $\lambda_r$ , will display a ring with greatest intensity at the radius  $r$  from the optical axis of the etalon. The sky-lines rings were used to calibrate FP coefficients  $A$ ,  $B$ ,  $E$ , and  $f$ , and to determine the wavelength solution with smallest root mean square residuals, shown in Figure 2.18. I will mention the specific value for each observation with results in the following chapters.

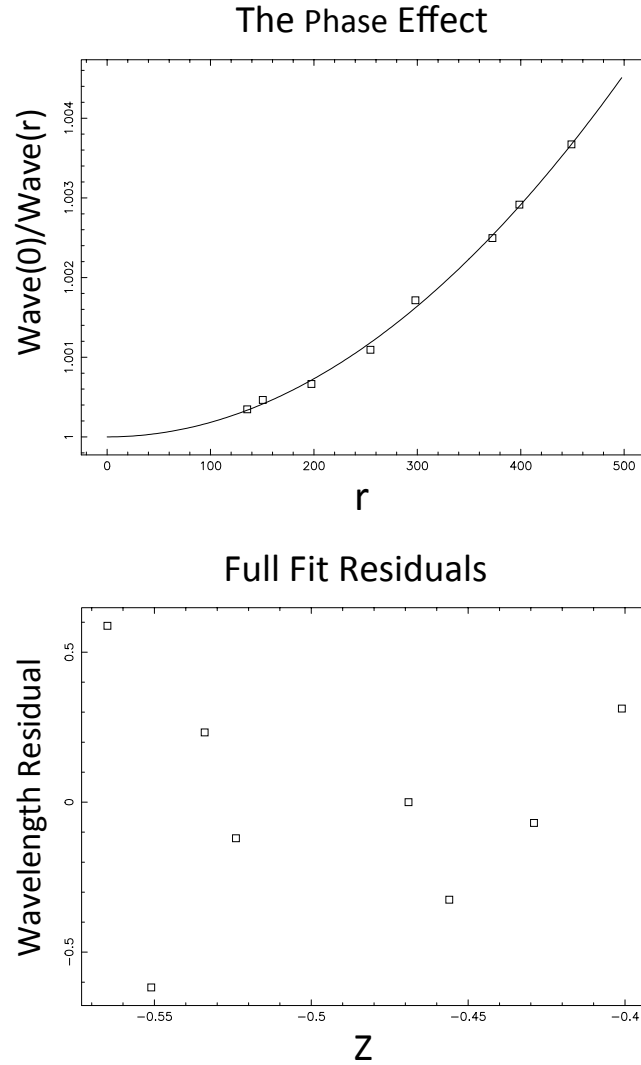


Figure 2.18: The fits of the night-sky lines wavelength as a function of  $r$  and  $z$ .

### 2.3.7 Sky-lines subtraction

The recorded sky-lines in each FP frame should be removed from the object frame (shown in Figure 2.19 top left panel). A model frame was created for these sky-lines by fitting a Lorentzian profile to these sky-lines shown in the top right panel of Figure 2.19. Then the model sky-lines frame shown in bottom left panel of Figure 2.19 was subtracted from the corresponding object frame. The bottom right panel of Figure 2.19 shows the final result of the sky-lines subtraction procedure.

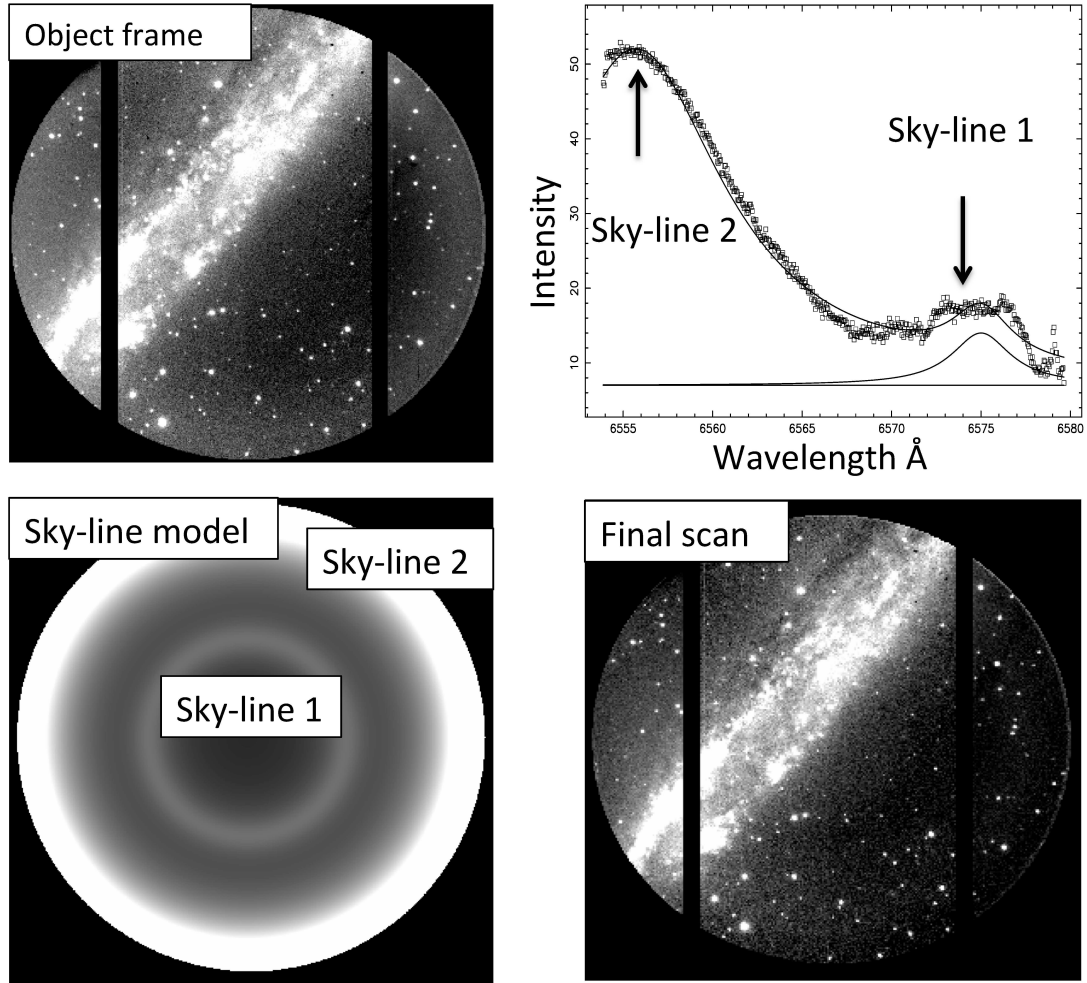


Figure 2.19: Top left: the raw FP image has the object and sky-lines. Top right: the fitted sky-lines to those recorded in the previous panel,  $6580 \text{ \AA}$  corresponds to the centre of the the FP scan. Bottom left: the model scan of the fitted sky-lines. Bottom right: the final scan after subtracting the model of sky-lines.

## 2.3.8 Kinematics map

### 2.3.8.1 Line profile

The observed profile is a convolution of instrumental and source profiles, and can be approximately described by a Voigt function (equation 2.24) which is a convolution of

a Gaussian (source) and Lorentzian (instrumental) profiles.

$$V(\lambda, \sigma, \gamma) = \int_{-\infty}^{\infty} G(\lambda, \sigma)L(\lambda, \gamma)d\lambda \quad (2.24)$$

where:

$\sigma$  and  $\gamma$  represent the two width parameters of the Voigt function: Gaussian  $\sigma$  and Lorentzian  $\gamma$ .

### 2.3.8.2 Intensity of the line emission, continuum, velocity, velocity dispersion maps

We fitted<sup>6</sup> the spectral line profile at each pixel with a Voigt function to derive: the wavelength at maximum intensity  $\lambda_p$  of the emission line and its uncertainty  $\Delta\lambda_p$ , the line strength at the peak  $I_0$  and its uncertainty<sup>7</sup>  $\Delta I_0$  (continuum intensity), the width of the Gaussian profile represents the velocity dispersion of the source. the radial velocity can be derived from the Doppler equation:

$$v = \frac{\lambda - \lambda_0}{\lambda_0}c \quad (2.25)$$

where:

$\lambda$  = wavelength of peak emission.

$\lambda_0$  = rest wavelength of the emission line, in air (because we use a ground based instrument).

In order to create reliable maps, we set a signal to noise ratio (S/N) that was determined from the ratio of  $I_0/\Delta I_0$  and excluded all values of velocities, velocities dispersion, and intensity in pixels that have values less than S/N, and we use different S/N for each cube according to the conditions, such as the intensity of the target in a specific wavelength. We will mention the specific value of S/N for each observation with results, as well as an example of emission line profile.

---

<sup>6</sup>We used ./eprofile program in FP package which is provided by Ted Williams.

<sup>7</sup>The uncertainty in this code was estimated from the line fitting procedure by using  $\chi$ -square test for the goodness of the fit.

## 2.4 CLOUDY model

CLOUDY is a simulation software intended to model the regions of emission line that fall between intergalactic medium and the Broad Line Regions of Quasars. Among the strong merits of photoionization analysis is that researcher would get many observables from the input of few parameters. CLOUDY can predict the intensities of 10 000 emission lines. These results can be achieved from only three characteristics namely, shape and intensity of the incident continuum, the gas chemical composition and finally its geometry. As a prerequisite, the shape and intensity of the incident continuum must be identified. The continuum shape may be described as a fundamental form (e.g. blackbody emission, thin bremsstrahlung emission or a power law with exponential cutoff as option), calculated from table points, or in the form of transmitted continuum based on previous predictions of CLOUDY. The continuum intensity must be identified also. This may be represented either as energy or photon flux for a specific unit surface area of cloud or as luminosity in the form of energy or photon emitted by the central object into  $4\pi$  sr. These can be specified as a flux of density or photons or as luminosity where energies are arbitrary or by providing the visual absolute or bolometric value of the source (Ferland 1996).

### 2.4.1 Chemical composition

The software can process the 30 lightest elements. It is possible to treat all the stage of the ionization process and others such as charge exchange, radiative combination and dielectronic recombination. The ionization mechanisms include photoionization from both valence and inner shells as well as excited states, collisional ionization and charge transfer.

### 2.4.2 Geometry

It is assumed that geometry is spherical but by enlarging the inner radius of the expense of the cloud thickness it can become plane parallel. The default setting is that gas has a fixed density and fills its volume completely. Other pressure laws and models can be calculated with the assumption of partial volume filling “open”.

### 2.4.3 Velocity structure

CLOUDY deals only with lines thermal broadening, assuming the absence of any type of internal velocity structure and open geometry. These settings can be manipulated in different ways. The turbulence command can be used to add microturbulence, while using the “wind” command, it is possible to calculate the large velocity gradient. In CLOUDY, the spherical nebula is divided into thin concentric shells. The thicknesses of these slices would be small enough to assume constant physical conditions within them. The thicknesses are monitored always to keep them within the required range. The shells are considered as zones and usually between 100-200 zones are counted in each optically thick model. It is a common practice to print the physical conditions of the first and last shells.

### 2.4.4 Overview

The standard notation as used by Mihalas (1978) and Osterbrock (1989) will be adopted here to define the usual quantities used by the software.

#### 2.4.4.1 Continua

Figure 2.20 is a representation of the many continua used in the calculation of the software.

- Incident continuum:  
The incident continuum is defined as the external continuum generated by the main central object which intersects the cloud’s illuminated face. Usually it is defined in the starting calculation commands. The sole source of energy of the cloud is derived from the absorption of this continuum and it is usually diminished by extinction.
- Diffuse continuum:  
The Diffuse continuum or the diffuse field is that radiation field generated by gas and grains inside the nebula such as Lyman, Balmer or the two-photon continua generated by hydrogen. Such fields are semi isotropic and may represent important sources of radiation in some cases. A major difference in the way stellar atmosphere and photoionized nebula are calculated is the way diffuse fields are treated. If the photoionization of the nebula is caused by external continuum, then this means that the diffuse fields are weaker than the incident continuum and the expected gas albedo is small. In stellar atmosphere the

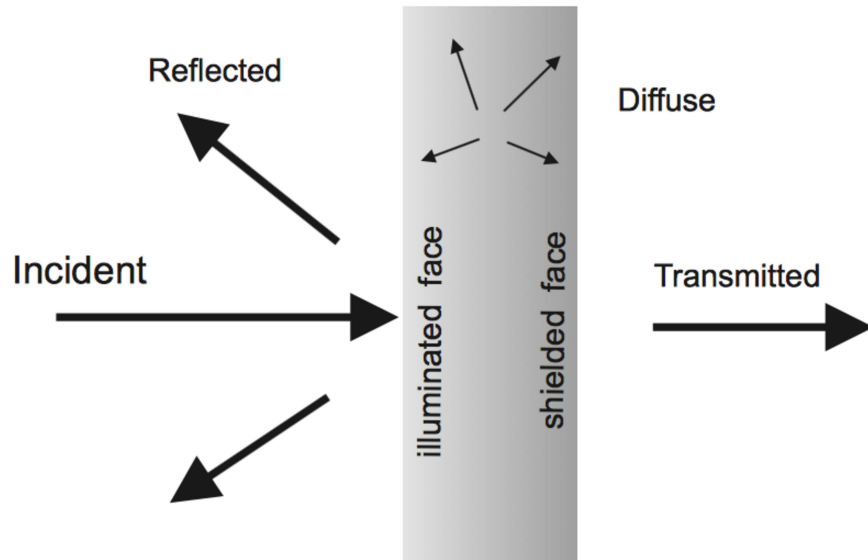


Figure 2.20: shows several of the continua that enter in the calculations of the CLOUDY model (Ferland 1996).

semi isotropic diffuse field is the main factor controlling its intensity, therefore, the diffuse fields can be dealt with through lower order approximations in a nebula and not in a stellar atmospheres.

- Transmitted continuum:  
The transmitted continuum is the total continuum emerging from the cloud's shielded face. It is composed of the incident and the transferred diffuse continuum.
- The reflected continuum:  
This is the continuum generated from the cloud's illuminated side facing the source incident continuum. This type is calculated for open geometry setting only.

Figure 2.21 represents a cross-plot of the incident and reflected continua for a case matching the Compton reflector in AGN. This is a cloud with fixed temperature ( $T=10^5$  K) with a column density of  $10^{25}$   $\text{cm}^{-2}$  and a density of  $10^{11}$   $\text{cm}^{-3}$ . The illumination source is the  $\nu^{-1}$  power law represented by dashed

line and the punch continuum command provided the reflected continuum. The Compton reflector's peak can be identified easily in the figure.

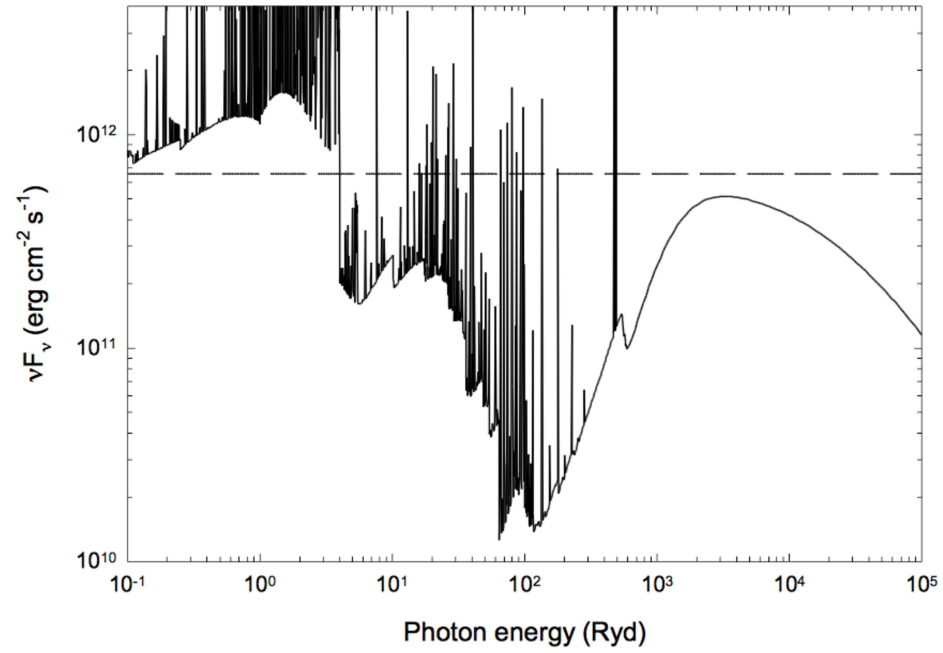


Figure 2.21: Incident (dashed) and reflected (solid) continua produced by the CLOUDY model (Ferland 1996).

### 2.4.4.2 Geometry

It is assumed that geometry is spherical but by enlarging the inner radius of the expense of the cloud thickness it can become plane parallel. It is also possible to modify the geometry to become nearly cylindrical and a simple wind can be calculated. The final summary will state whether the geometry was parallel.

- Illuminated and shielded faces of the cloud:  
The illuminated side of the cloud is the side facing the ionizing radiation source, while the opposite side is called the shielded face. The illuminated face has higher temperature and is more ionized than the other side.
- Depth and radius:  
The two possible geometries are depicted in Figure 2.22 which shows also some of the most commonly used terms. Radius is the distance from the centre of symmetry which is normally the centre of the central object. Depth is the distance between the illuminated face and a certain point within the cloud.

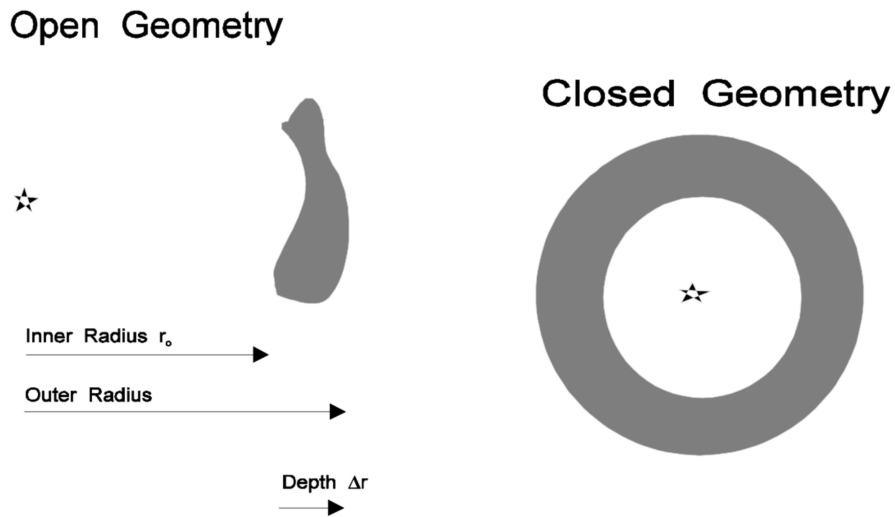


Figure 2.22: Representative diagram of the two limiting geometries (open & closed) that can be considered in the CLOUDY model (Ferland 1996).

- Covering factor:  
The covering factor is the part of  $4\pi$  sr that is covered with gas if viewed from the source of radiation. It depicted as  $\Omega/4\pi$  (Osterbrock 1989) with values more than 0 and less than 1. It represents the fraction of radiation generated

by the central object that strikes nebular gas. Luminosity values calculated from the predicted line are for a shell covering  $\Omega$  sr while the line intensities are determined per cloud's unit area. The later has a nearly linear scale with increasing covering factor. Line intensities depend weakly on it.

- Filling factor:

The filling factor indicates the presence of tiny clumps within the region of emission-line. When setting the filling factor, the hydrogen density is usually referring to the gas regions and assuming vacant regions around it. Osterbrock & Flather (1959) provided an account of the distinctive effects of a filling factor.

- Radii:

The radii as used here us depicted in Figure 2.22. The inner radius is designated as  $r_0$ , the depth as  $\Delta r$  and the current radius as  $r$ .

- Hydrogen density:

The total hydrogen density ( $\text{cm}^{-3}$ ) is used in CLOUDY model which is given by:

$$n(H) = n(H^0) + n(H^+) + n(H^-) + 2n(H_2) + 2n(H_2^+) + 3n(H_3^+) \quad (2.26)$$

- Column densities:

The hydrogen column density ( $\text{cm}^{-2}$ ) is given by:

$$N(H_{tot}) = \int [n(H^0) + n(H^+) + n(H^-) + 2n(H_2) + 2n(H_2^+) + 3n(H_3^+)] f(r) dr \quad (2.27)$$

where:

$f(r)$  = filling factor.

$n$  = volume density ( $\text{cm}^{-3}$ ).

$N$  = column density ( $\text{cm}^{-2}$ ).

- Open vs. closed geometry:

There are two limiting cases that are essential to define geometry and its impact on the calculations. These are designated as “open” and “closed” geometries. Examples of the two types are depicted in Figure 2.22. The best approximation depends to large extent on the gas covering factor. The selection impacts the calculation of the diffuse fields mainly.

Open geometry:

Open geometry is achieved when the gas covering factor is small. The total

radiation moving from the illuminated side toward the source would escape without further interaction with the gas. This might be the case in the Crab Nebula either in its broad-line region of active nuclei or the filaments. In such case,  $\text{Ly}\beta$  and higher hydrogen lines and H and the H ionizing radiation may escape from the nebula. This geometry is considered as the default for the code if the sphere command is not determined.

Closed geometry:

In this type of geometry, emission-line gas would cover  $4\pi$  sr as seen by the central star. In the case where the star is small compared to the nebula, then all those diffuse fields escaping from the illuminated face towards the star would eventually strike the nebula's other side. This geometry type is adopted in most calculations of nebulae and H II regions. It will be used upon the entry of the sphere command.

Static vs. expanding:

The “sphere” command has two options: “static” and “expanding” which describes the way in which line photons coming from either side of the shell would interact with each other. In the static option, the code will consider the shell is stationary and hence all lines interact across the nebula. In such cases, hydrogen Lyman line interaction must ensure that the case B emissivity is achieved. In an expanding nebula, if the  $\Omega/4\pi \sim 1$  then the diffuse continua would interact across that nebula. However, the shell expansion velocity prevents the diffuse line photons from doing so. In such cases, the expanding option should be selected. The second case would be the default if the sphere is selected but with no options. The open vs closed and static vs expanding options are important for the predicted emission-line spectrum at the = 10% level. This is due mainly to the different treatments of the diffuse fields and the optical depth of lines.

- Matter-bound and radiation-bound geometries:

Matter-bound geometry:

If the outer limit to the region of emission-line of the nebula is delineated by the outer edge of the ionized cloud, then it would be described as matter bounded and the cloud is thin to the incident continuum. In such cases, the volume and density of the cloud would determine the intensity of a combination line and it is not related to the luminosity of the ionizing continuum.

Radiation-bound geometry:

If the outer limit to the emission-line region of the nebula is marked by a hydrogen ionization front, then the nebula is described as radiation bounded. In this case, both warm ionized and cold neutral regions may exist together.

The cloud would be optically thick to the hydrogen ionizing portion of the continuum and so most of the incident continuum would be absorbed by it. In this model, the intensity of a recombination line is defined by the luminosity of the ionizing continuum and may have little dependence on the cloud properties.

Is a starting radius necessary?

CLOUDY should be able to delineate the surface flux of photons at the cloud's illuminated side. The incident continuum may be defined either as luminosity or as intensity. In the luminosity case, it is essential to identify an inner or starting radius and the emission lines will be considered as luminosities. In the case of intensity, there is no need to set a starting radius. The lines will be treated as intensities if the starting radius is not provided. In this second case, a default radius of  $10^{25}$  cm will be used. This should generate a nearly plane-parallel geometry.

#### 2.4.4.3 Application

Some of H II regions in the nearby galaxy NGC 300 were modelled by using photonization code CLOUDY 13.02 (Ferland et al. 2013) to simulate emission lines from these regions (see Subsection 3.3.5). The physical properties in the model were determined by using emission line ratios, and compared with the physical environment in the selected H II regions in NGC 300. As well as this, the temperature in these regions were determined by using predicted intensities of [N II]5755 which was undetected in the observations.

## Chapter 3

# Outflows from diffuse nebulae in the face-on spiral galaxy NGC 300

### 3.1 Introduction

Face-on galaxies provide a complementary view of the distribution of ionized outflows to edge-ons, by tracing their emission lines across the face of the galaxy. This makes it possible to examine the physical properties of the outflowing gas and explore their ionizing and driving sources. The ionizing fluxes of O stars are the most effective ionizing agent. Massive stars have an impact on the surrounding interstellar medium. A large amount of outflowing gas could be blown by the winds of these stars. Their strong radiation driven winds could reach the halo of the host galaxy, or even to the intergalactic medium, and that could explain the existence of heavy elements in the halo (Garnett 2002). Otherwise, H II regions have been used to trace the current chemical composition of the interstellar medium in different parts of the galaxy (Bresolin et al. 2009a; Peimbert 1975). The feedback from ionized outflows has played an important role in quenching or enhancing the star formation process in low mass galaxies (Hopkins, Quataert & Murray 2012; Cazzoli et al. 2014).

An optical study of H II regions in the face-on galaxy NGC 300 is presented in this chapter, based on new SALT observations with Fabry-Pérot and long-slit spectroscopy modes (see Figure 3.1). The spatial variation in the physical conditions along various H II regions was investigated to quantify the impact of the outflows (galactic winds) onto the ambient ISM. The H $\alpha$  and H $\beta$  Fabry-Pérot cubes were exploited to trace ionized outflowing gas from the active regions; I discovered interesting kinematics in specific areas which display splitting of the H $\alpha$  profile. These signatures could be interpreted in terms of shock excitation. Concerning the long-slit observation across these areas, different bright optical emission lines ([S II] & [N II]) originating in low and high ([O III] $\lambda\lambda$ 4959,5007) excitation regions were measured as well as Balmer lines (H $\alpha$  & H $\beta$ ), to study their profile shapes, kinematics and line ratios. The oxygen abundance  $12+\log(\text{O}/\text{H})$  was estimated for the H II regions based on the strong line methods, and I examined these abundances as a function of the distance from the centre of the galaxy.

The adopted distance of the NGC 300 galaxy is 1.88 Mpc (Gieren et al. 2005b), and the resulting angular scale  $2'$  corresponds to 1 kpc.

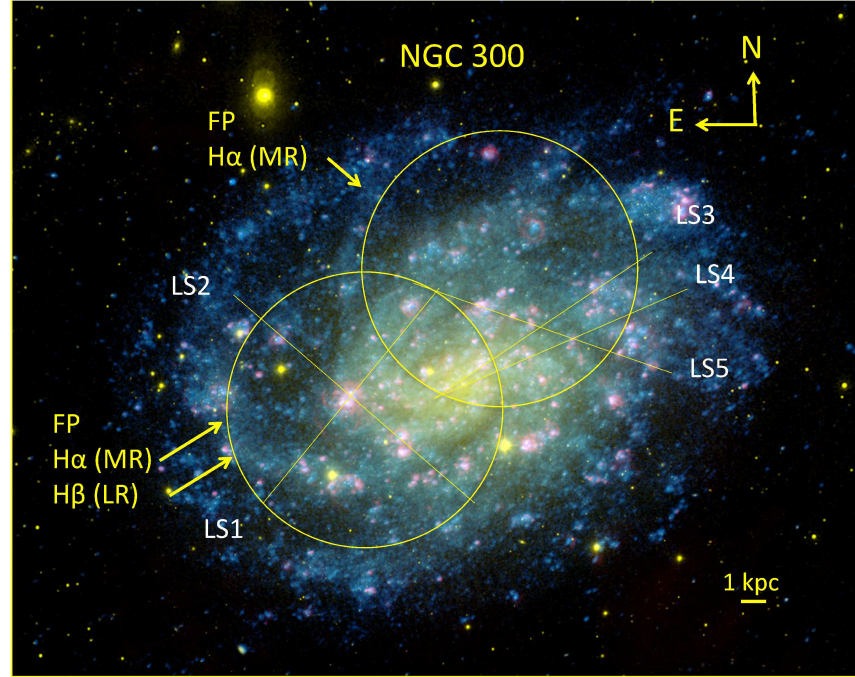


Figure 3.1: An image of NGC 300 illustrating the summary of observations used in this chapter. Two FP fields are located at (RA:  $00^h 55^m 08^s$ , Dec:  $-37^\circ 41' 50''$ ) and (RA:  $00^h 54^m 45^s$ , Dec:  $-37^\circ 37' 0''$ ) respectively. Five long-slit positions (LS1, LS2, LS3, LS4, LS5) were oriented with PA =  $44^\circ$ ,  $155^\circ$ ,  $119^\circ$ ,  $111^\circ$ ,  $68^\circ$  respectively. The base image is a combination of visible-light and ultraviolet images, the red and yellow colours represent visible light observed using the Carnegie Institution of Washington’s 100-inch telescope at Las Campanas Observatory, and the blue colour represents ultraviolet observations from NASA’s Galaxy Evolution Explorer. [https://en.wikipedia.org/wiki/NGC\\_300](https://en.wikipedia.org/wiki/NGC_300).

## 3.2 Fabry-Pérot observations

NGC 300 was observed in FP mode in two fields of view. The centres of these fields are (RA:  $00^h 55^m 08^s$ , Dec:  $-37^\circ 41' 50''$ ) and (RA:  $00^h 54^m 45^s$ , Dec:  $-37^\circ 37' 0''$ ) respectively. Tables 3.1 and 3.2 give details of the observations of  $H\alpha$  and  $H\beta$ . The medium resolution (MR;  $R \approx 1400$ ) of the imaging spectroscopic mode was chosen in the two fields to span a spectral region of  $6561\text{--}6581 \text{ \AA}$  and  $6561\text{--}6577 \text{ \AA}$  in equally spaced  $2 \text{ \AA}$  steps after taking into account the systemic velocity of NGC 300 ( $144 \text{ km s}^{-1}$ ). The integration time for the  $H\alpha$  (MR),  $H\alpha$  (LR) and  $H\beta$  (LR) observations was 120 seconds, 122 seconds and 480 seconds respectively. The chosen spectral range

covers the  $H\alpha$  profile and continuum. On the other hand, the  $H\beta$  observation was done by using low resolution (LR;  $R \approx 700$ ). A spectral range of 4851.9–4867.6 Å was chosen to sample the  $H\beta$  profile and some continuum on either side. The integration time for  $H\beta$  was increased in order to obtain sufficient signal, as the intensity of  $H\beta$  is one third of the  $H\alpha$  intensity. The reduction of FP data was discussed in detail in chapter 1.5. The  $H\alpha$  datacube was reduced using the described procedure and the produced mean square residual for the wavelength solution ( $\lambda_{rms}$ ) was 0.096 Å, which is equivalent to 4.3 km s<sup>-1</sup>, and in the second field the  $\lambda_{rms}$  was 0.112 Å (5 km s<sup>-1</sup>). Osterbrock et al. (1996) state that they did not detect any night sky-lines at wavelengths shorter than 5200 Å. Hence, sky-lines cannot be used to calibrate the wavelength in  $H\beta$  observations, and so the emission ring of Xe line measured at the time of observation was used to check the wavelength calibration A parameter.

Table 3.1: The main parameters of NGC 300 observations of  $H\alpha$  and  $H\beta$ , with Fabry-Pérot MR and LR mode respectively.

	MR	LR
Date of observation	9 <sup>th</sup> June & 1 <sup>st</sup> July 2015	30 <sup>th</sup> Aug. 2017
Telescope	SALT	SALT
Instrument	RSS	RSS
Detector	E2V CCD 44-82 chips	E2V CCD 44-82 chips
Mode	Fabry-Pérot (MR)	Fabry-Pérot (LR)
Resolving power	$\approx 1400$	$\approx 700$
Filter	PI06530	PI04820
Free spectral range ( $\text{\AA}$ )	75	8.64
Steps	11 & 9	6
Exposure time/step (seconds)	120 & 124	480
Pixel scale ( $'' \text{ pixel}^{-1}$ )	0.5068	0.5068
Seeing ( $''$ )	$\sim 2$	$\sim 2$

Table 3.2: Étalon configuration wavelengths for the FP  $H\alpha$  and  $H\beta$  observations of NGC 300.

no.	$H\alpha$ (first field)	$H\alpha$ (second field)	$H\beta$
	MR	LR	LR
1	6561	6561	4851.9
2	6563	6563	4857.5
3	6565	6565	4859.6
4	6567	6567	4863.5
5	6569	6569	4865.5
6	6571	6571	4867.6
7	6573	6573	
8	6575	6575	
9	6577	6577	
10	6579		
11	6581		

### 3.2.1 Results of Fabry-Pérot mode

To search for evidence of interaction between the outflowing gas and their surroundings, deep Fabry-Pérot observations were analysed in order to identify H II regions and determine the kinematics and excitation conditions. A spectral line profile was fitted at each pixel with a Voigt function to derive the wavelength at maximum intensity of the H $\alpha$  emission, in order to determine the radial velocity at each pixel. The H $\alpha$  profile was fitted with five parameters:  $\sigma$  (Gaussian width),  $\gamma$  (Lorentzian width),  $\lambda_c$  (the wavelength at the profile's peak),  $I$  (the line strength),  $I_0$  (continuum intensity) and the estimated uncertainty in these parameters. The same procedure was used with the H $\beta$  cube.

Figure 3.2 shows the distribution of H $\alpha$  and H $\beta$  emission in the first field. This was achieved by integrating all intensities (line + continuum) along the wavelength axis of each cube after reducing its scans. The distribution of H $\alpha$  emission in the second field is shown in Figure 3.3. The white edges in each panel (a, c) represent CCD gaps, and the white area in the bottom of (a) represents a guiding probe. 18 objects were identified in both fields with different size and morphological appearance, across a region  $\sim 8'$  in diameter for each field. As well as this, bright dots in different positions are noticed, which represent foreground stars. In the first field, to the northwest, bright emission appears in the centre (black cross) of the galaxy, which gradually decreases and extends to  $\sim 1$  kpc around the centre. Three regions were identified and labelled A, B, C in Figure 3.2, which shows the zoomed-in maps in panels (b) and (d): these will be discussed in more detail later. In the second field, high emission is obvious around the centre of the galaxy (a black cross) to the left bottom of Figure 3.3. Its intensity reduces gradually away from the centre. 12 objects are labelled in Figure 3.3, and 10 of them were re-observed by long-slit spectroscopy. Four objects (K1, K7, K11, K12) are the largest objects in the second field. Bright spots are noticed in different positions across the field, which are foreground stars.

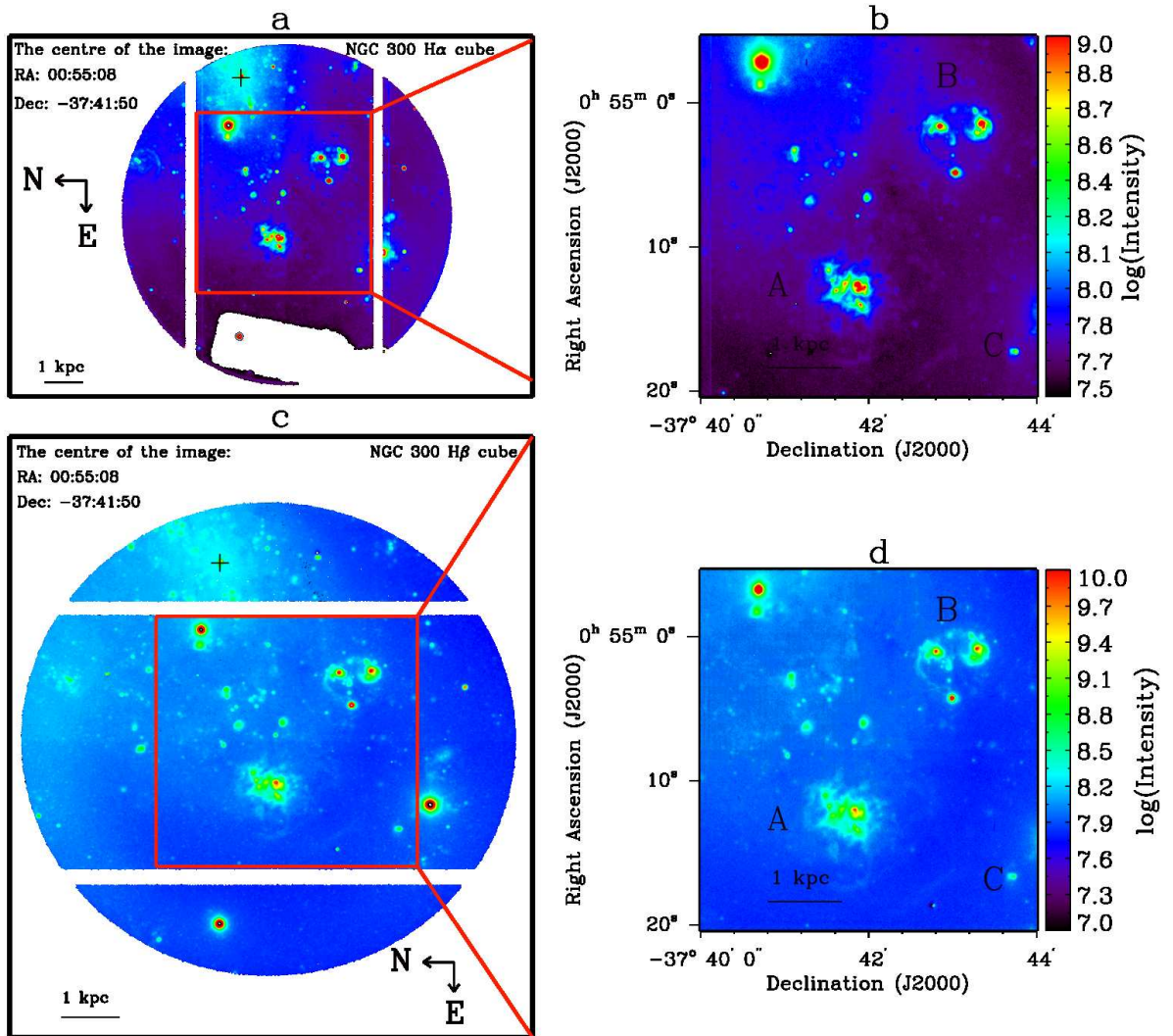


Figure 3.2: Total intensity maps of the observed field (RA:  $00^{\text{h}}:55^{\text{m}}:08^{\text{s}}$ , Dec:  $-37^{\circ}:41':50''$ ) in NGC 300 showing H $\alpha$  (upper panels) and H $\beta$  (lower panels). The intensity is in arbitrary units, and the centre of the galaxy is marked with a black cross. The bar in the left bottom corner represents 1 kpc.

Figures 3.4 and 3.5 show the maps of these parameters. For H $\alpha$  maps, a threshold was set by accepting intensities higher than 1200 (arbitrary units) and only velocities and velocity dispersions were accepted in pixels above this threshold. In this observation the signal is low compared with that in H $\beta$  because of the differences in the exposure time and resolving power between these two observations despite H $\beta$  being

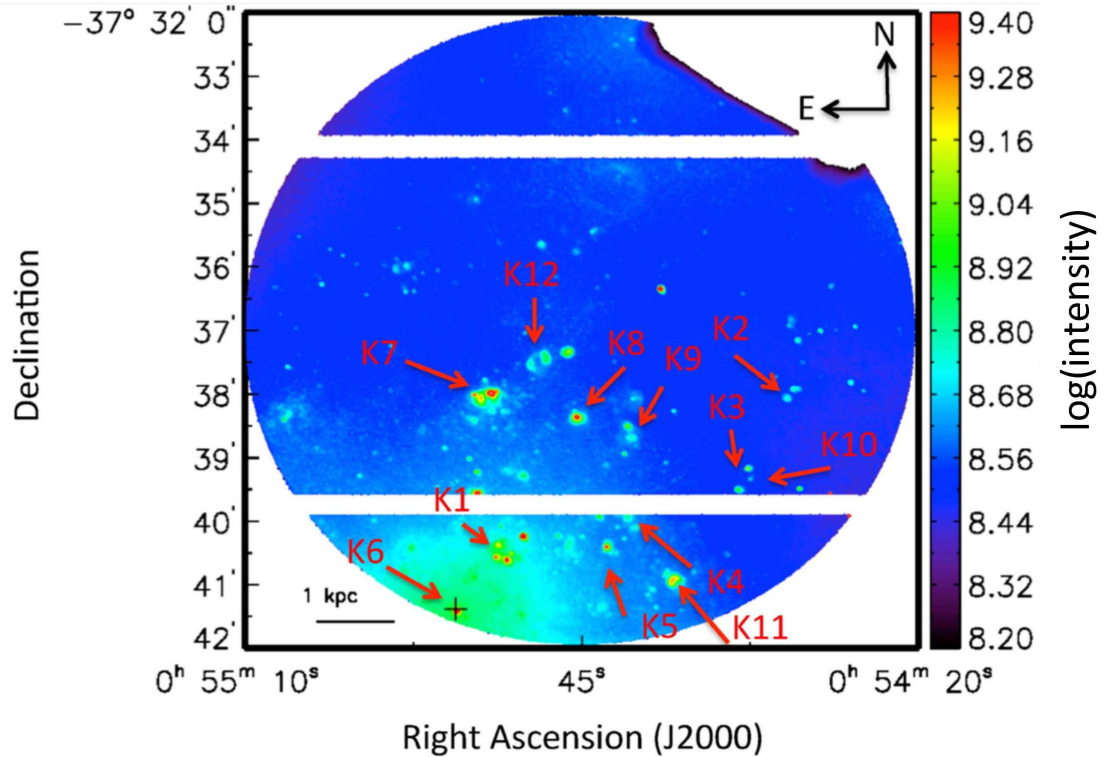


Figure 3.3: Total intensity map in the observed field (RA:  $00^h:55^m:08^s$ , Dec:  $-37^\circ:41':50''$ ) in NGC 300 showing  $H\alpha$ . The intensity is in arbitrary units, and the centre of the galaxy is marked with a black cross. The red arrows identify 14 objects in the field (K1–K14).

about three times fainter than  $H\alpha$ . The S/N threshold was fixed to 4 for the  $H\beta$  observations, and only velocities and velocity dispersions were accepted in pixels above this threshold. A large amount of continuum emission is obvious in the area near to the centre of the galaxy, which is the result of continuum emission from stars whose spectra dominate in this area. NGC 300 is a starburst galaxy, and young massive stars as well as older red-giant branch (RGB) stars are thought to be highly concentrated in this area (see panel (b) in both of Figures 3.4 and 3.5). Figure 3.6 shows  $H\alpha$  emission, continuum, velocity and velocity dispersion in the second field, and Figure 3.7 is a zoom of Figures 3.6. The noise level is high near the centre, and the S/N threshold was fixed to 5. I could not trace any continuum emission in the centre and its surrounding.

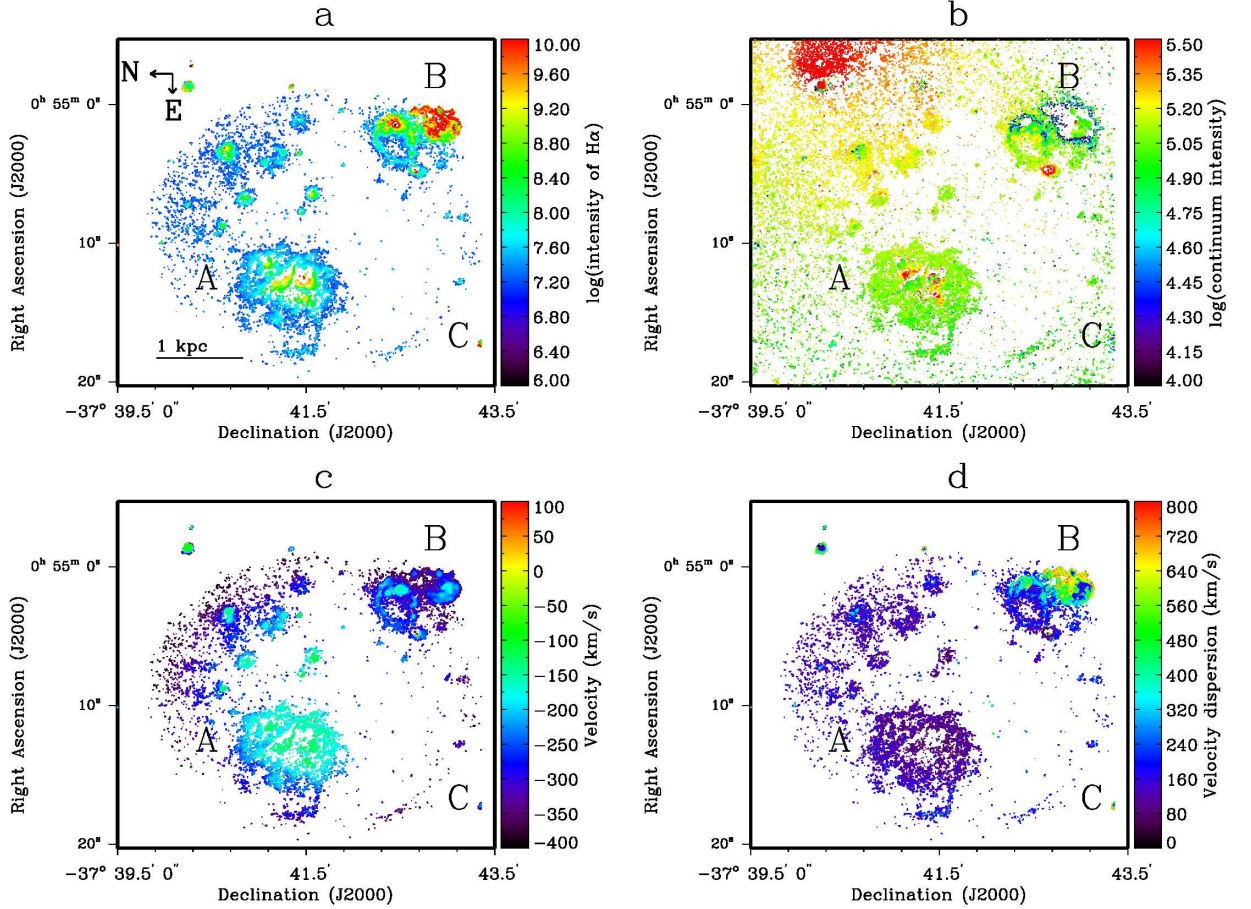


Figure 3.4: After fitting the data cube of H $\alpha$  of the first field, from top left to bottom right: (a) the maximum intensity of the H $\alpha$  profile, (b) continuum, (c) velocity and (d) velocity dispersion. The intensity is in arbitrary units.

The morphology and kinematics will be discussed in detail in 3.3.2.3 and 3.3.2. Complex H II regions A and B were zoomed-in and mapped in order to investigate, in detail, the kinematics and distribution of the ionized gas and to quantify the impact onto the surrounding interstellar matter, as shown in Figures 3.8 and 3.9.

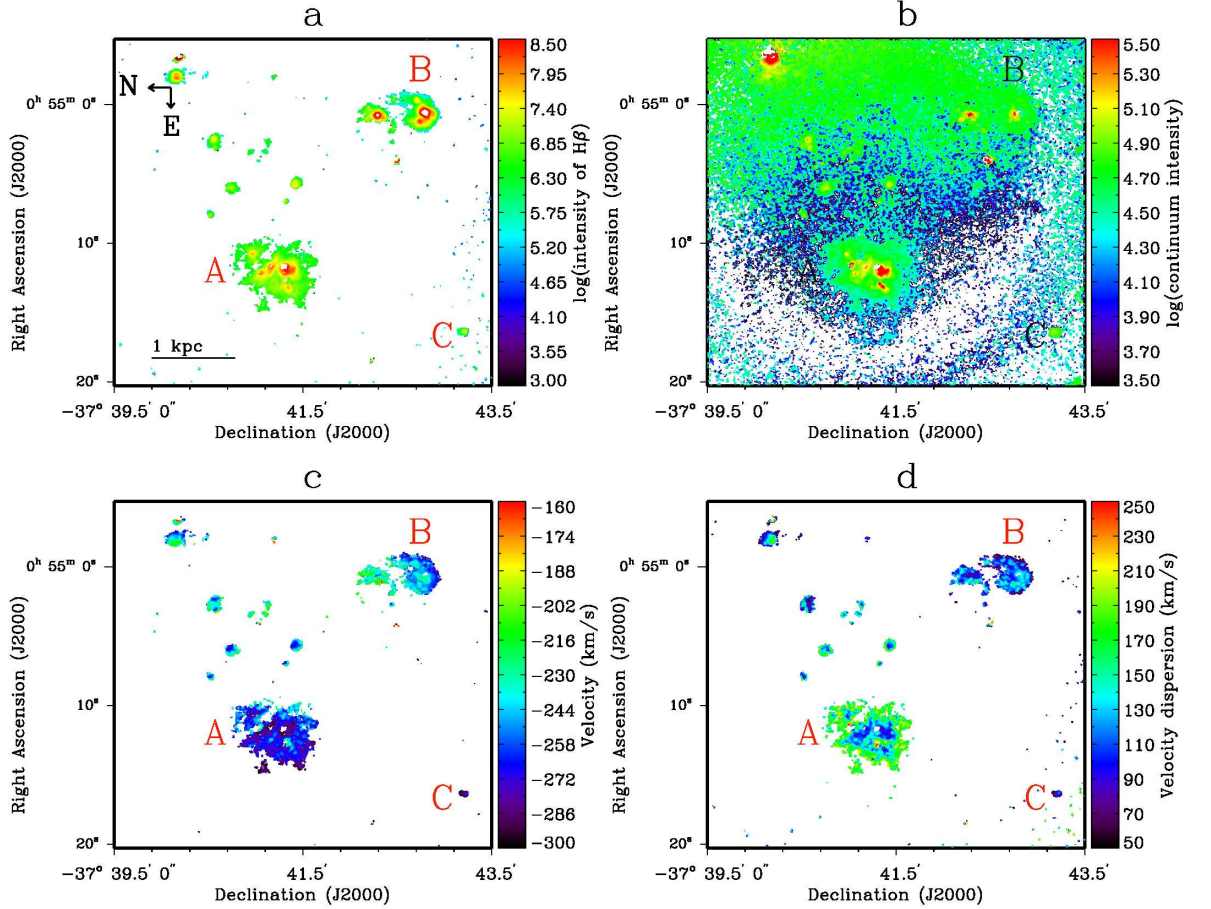


Figure 3.5: As Figure 3.4, but for H $\beta$ .

### 3.2.2 Long-slit observations

The RSS long-slit spectroscopy mode was used, with the two volume phase holographic (VPH) gratings PG3000 and PG2300 to cover all interesting lines in the two spectral ranges 4335–5016 Å and 5904–6756 Å. The slit width was 1", which offers spectral resolution of about 0.76 Å and 1 Å respectively, and a reciprocal dispersion of approximately 0.268 Å pixel<sup>-1</sup>. The spectra of Ne and CuAr comparison lamps were acquired for wavelength calibration. Five long slit settings were used in order to cross the regions of interest. Their charts are shown in Appendix A Figures A.1– A.5. All the important parameters of the long-slit observations are provided in Table 3.3. The data reduction is detailed in chapter 1.5. The produced spectra display many emission lines, which can be approximated as a Gaussian profile, therefore my IDL code was used by

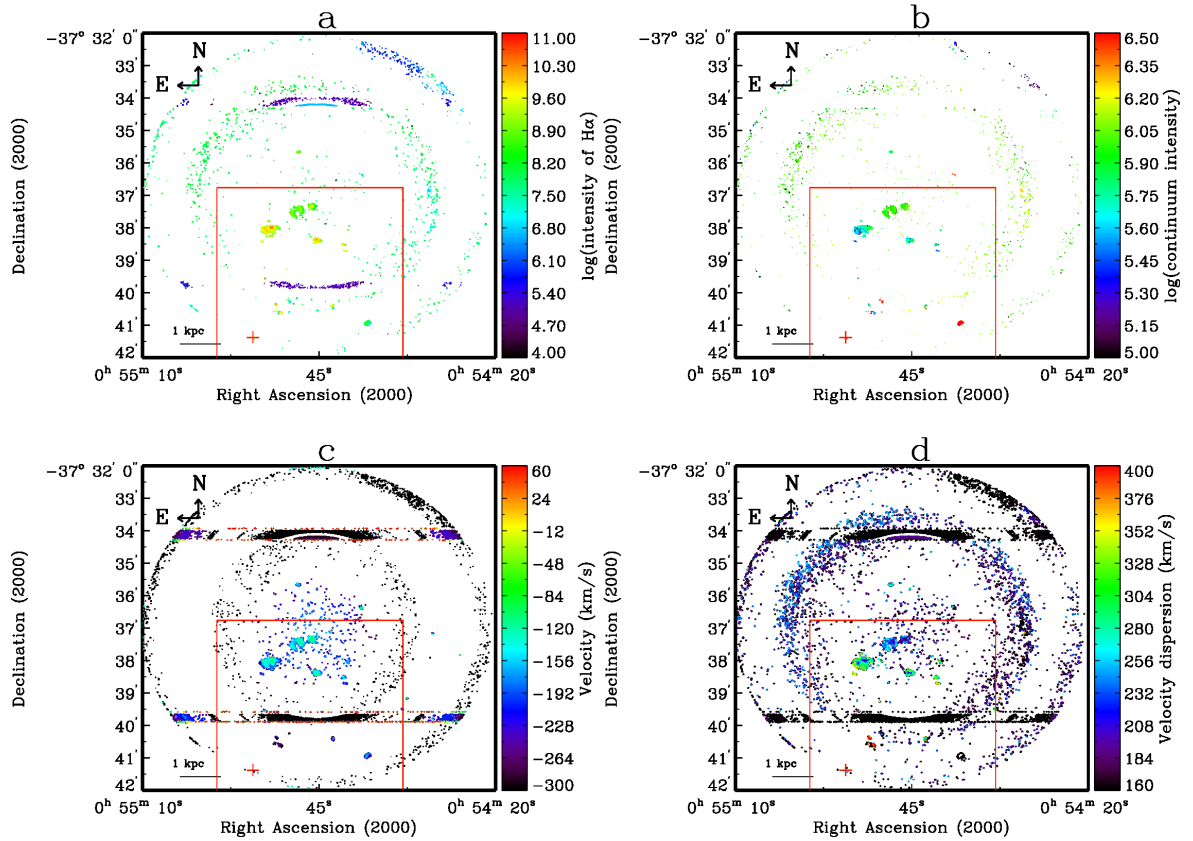


Figure 3.6: As Figure 3.4, but for the second field.

adapting the MPFITEXPR routine. The uncertainty in the maximum intensity, wavelength at the peak of the emission line profile and  $\sigma$  are estimated by determining the uncertainty in the Gaussian parameters from the MPFITEXPR routine.

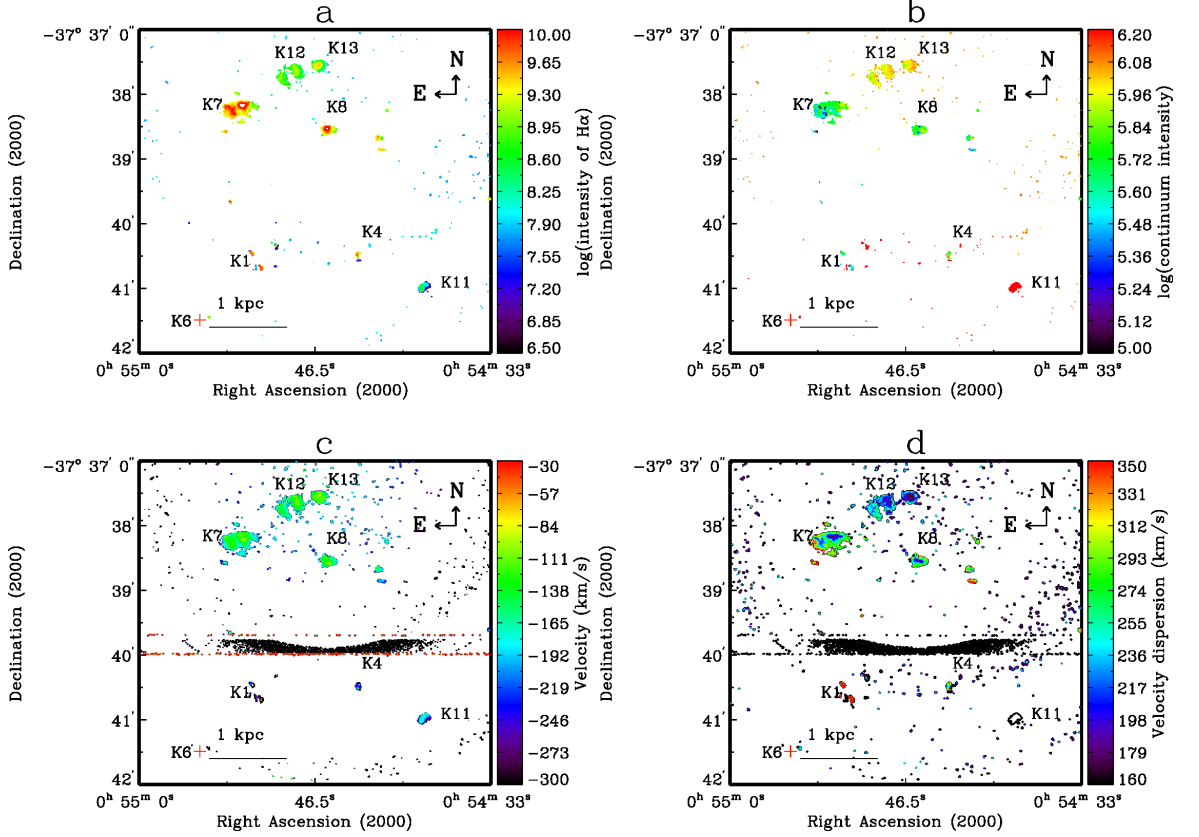


Figure 3.7: zoom into the red rectangular area in Figure 3.6.

### 3.2.3 Spectral analysis

FP observations show prominent areas with strong ionized emission in both  $H\alpha$  and  $H\beta$ . I have examined the shape of the emission line across the objects (A, B and C) (see Figures 3.4 and 3.5). I noticed that the profile shows signs of broadening and splitting (see Figure 3.15) in specific positions resulting in interesting kinematics and morphology. Two long-slit observations (LS1, LS2) were used to re-observe the two objects A and B. As well as this, prominent areas in the second field of FP were re-observed with three long-slit settings (LS3, LS4, LS5) to examine 10 objects (K1–K10), which are shown in Figure 3.3.

Figure 3.10 shows the image of the red and blue sides of the long-slit spectra with  $PA = 44^\circ$  and  $155^\circ$ . Five prominent areas can be discerned in this image: objects R (no object was found in the literature by Vizier on this position), A, B-1, B-2, and D; the spectra of each object were calculated by integrating their emission. The

Table 3.3: Summary of the spectroscopic (long-slit) observations of NGC 300.

Date of observation	23 <sup>th</sup> – 25 <sup>th</sup> Oct. 2016 & 24 <sup>th</sup> Nov. 2017
Telescope	SALT
Instrument	RSS
Detector	E2V CCD 44-82 chips
Mode	Long-slit
Grating	PG3000 & PG2300
Slit width	1''
Exposure time	300 seconds
Pixel scale	0.5068'' pixel <sup>-1</sup>
Reciprocal dispersion	0.268 Å pixel <sup>-1</sup>
Spectral resolution	0.76 Å
Slit centre of LS1 (PA = 155°)	RA (2000) = 00 <sup>h</sup> 55 <sup>m</sup> 12 <sup>s</sup> Dec (2000) = -37° 41' 20''
Slit centre of LS2 (PA = 44°)	RA (2000) = 00 <sup>h</sup> 55 <sup>m</sup> 13 <sup>s</sup> Dec (2000) = -37° 41' 36''
Slit centre of LS3 (PA = 119°)	RA (2000) = 00 <sup>h</sup> 54 <sup>m</sup> 40 <sup>s</sup> Dec (2000) = -37° 39' 15''
Slit centre of LS4 (PA = 111°)	RA (2000) = 00 <sup>h</sup> 54 <sup>m</sup> 44 <sup>s</sup> Dec (2000) = -37° 40' 22''
Slit centre of LS4 (PA = 68°)	RA (2000) = 00 <sup>h</sup> 54 <sup>m</sup> 40 <sup>s</sup> Dec (2000) = -37° 39' 17''

same procedure was followed with the spectra of the blue side which has H $\beta$  and [O III] lines. Another long-slit observation with PA = 155° crosses object A and two additional objects named E and F. In the next paragraphs, I will introduce more detail about the results of LS1 and LS2 only, and the spectra of objects from K1 to K10 were analysed using the same method.

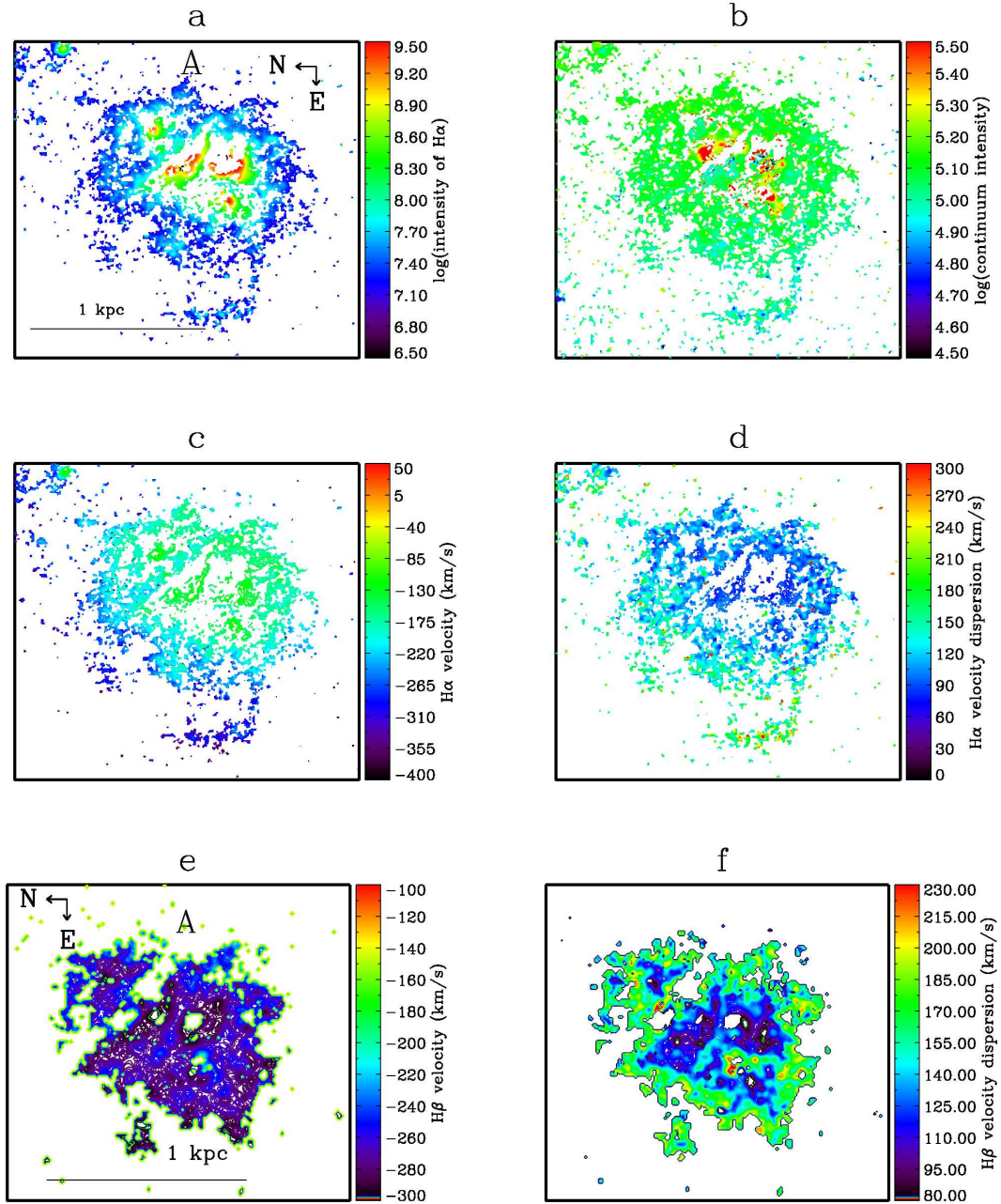


Figure 3.8: Zoomed-in maps of object A: (a) intensity of H $\alpha$ , (b) intensity of continuum emission, (c) H $\alpha$  velocity and (d) H $\alpha$  velocity dispersion; (e) and (f) show the H $\beta$  velocity and velocity dispersion respectively. The intensity is in arbitrary units. The bar to the left bottom corner in panels (a) and (e) represents 1 kpc.

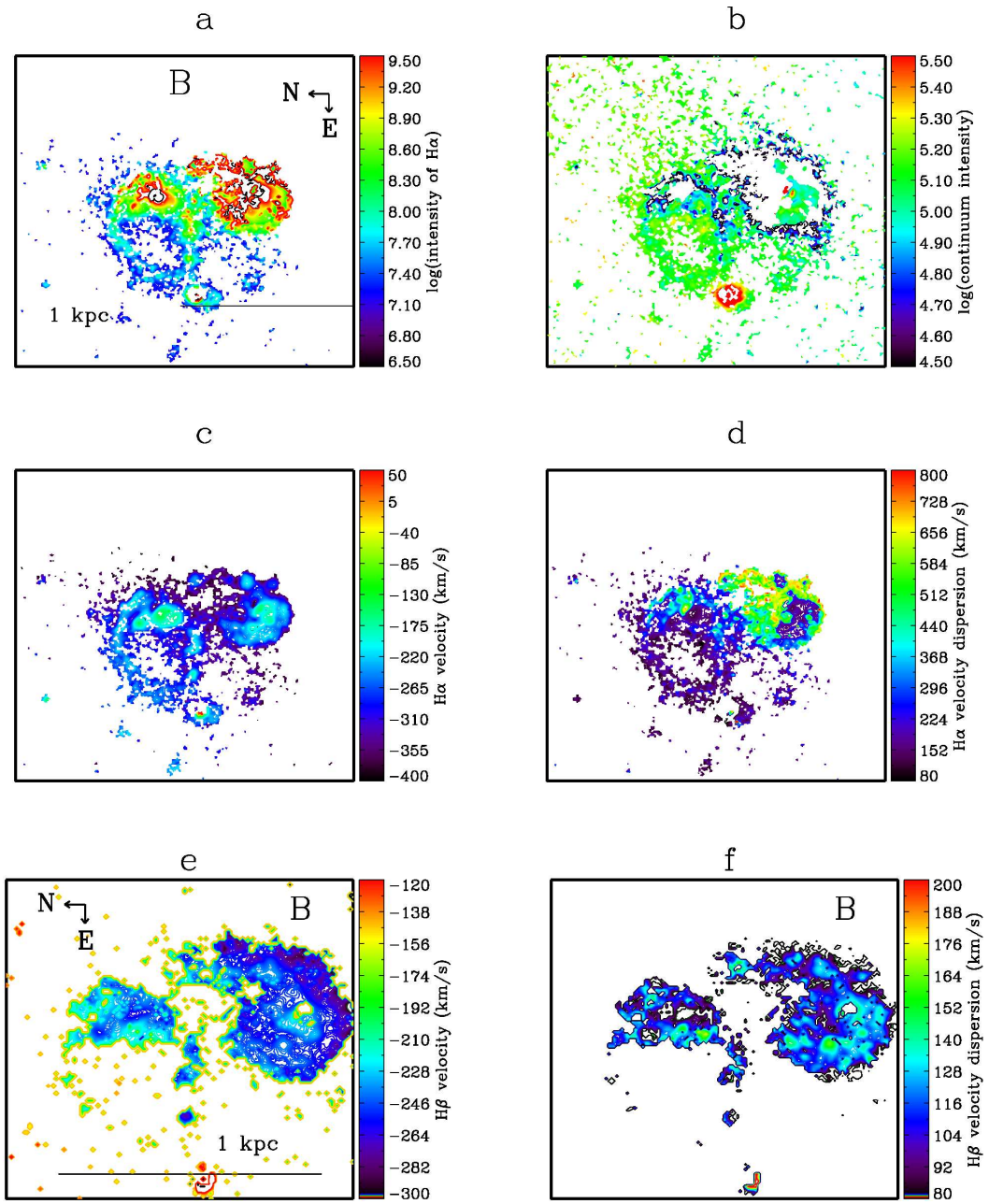


Figure 3.9: As Figure 3.8, but for object B.

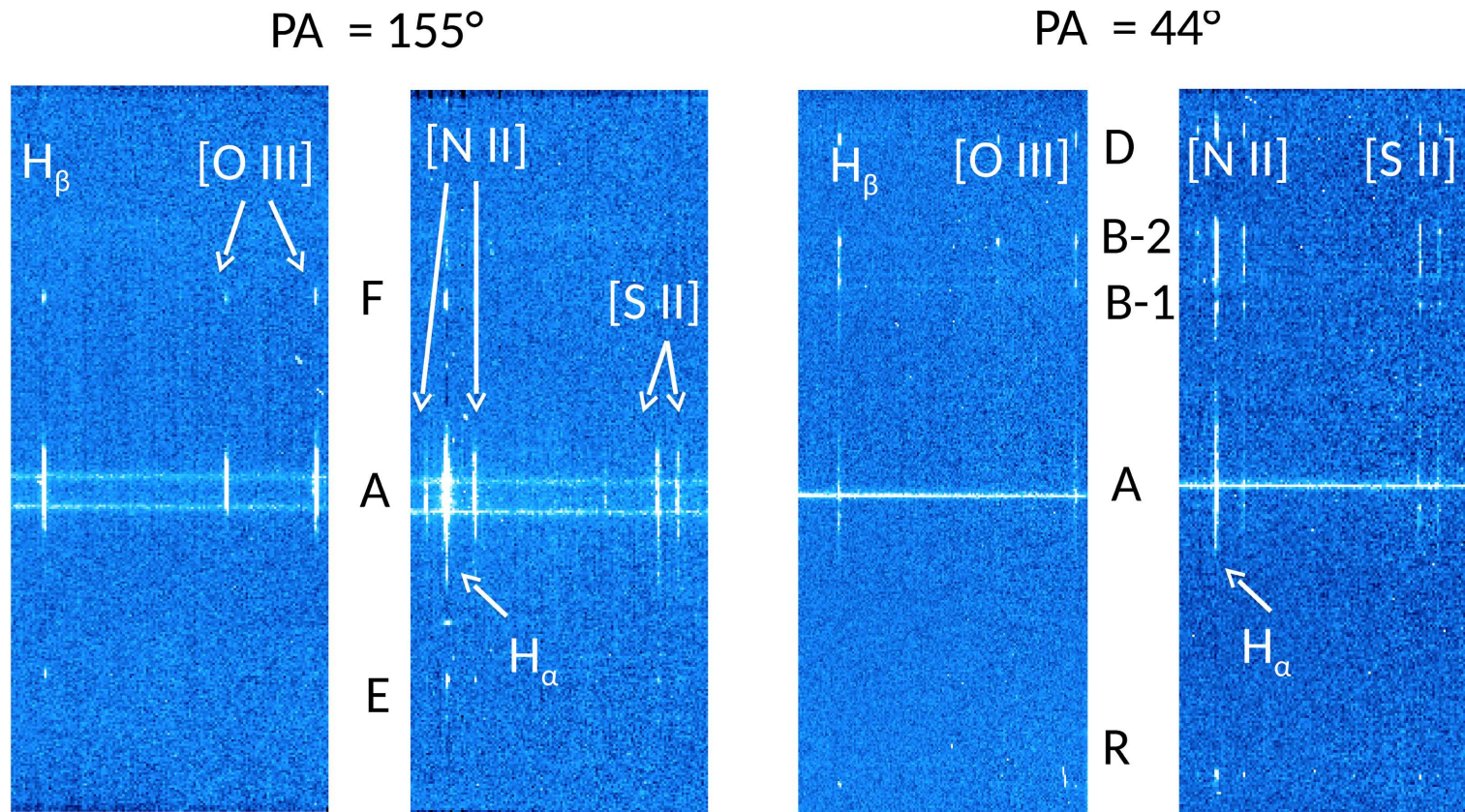


Figure 3.10: The long-slit frames of the blue and red side of the spectra at PA = 155° (left panel) and PA = 44° (right panel): the interesting objects and emission lines are marked on the frames.

The five settings of the long-slit observations cover spectra with wavelength ranges 4335–5016 Å and 5904–6756 Å. A total of eight optical emission lines were found in the final spectra including Balmer lines ( $H\alpha$  &  $H\beta$ ), low excitation lines ( $[N\ II]\lambda\lambda 6549, 6583$  &  $[S\ II]\lambda\lambda 6716, 6732$ ), and high excitation lines ( $[O\ III]\lambda\lambda 4959, 5007$ ). The Balmer recombination lines occur when the recombining electron results in the emission of photons that may escape from H II regions, cooling them. These areas contain sufficient energy from O and B stars to ionize H atoms. In addition, massive stars eject metals, some of which are produced by the nucleosynthesis in the core of these stars. Forbidden line emission of metals is commonly seen in H II regions and PNe, and represent another cooling process of nebula gas: radiative de-excitation. In addition to strong  $H\alpha$  emission concentrated in H II regions that are shown in FP observations,  $[N\ II]$  and  $[S\ II]$  emission was traced in all objects. The  $[O\ III]$  lines appear in objects which display high photoionization level. The ratio of these emission lines were examined in these objects, and I found A, F, D, R show higher ratio of  $[O\ III]/H\beta$  compared to others, and K6 shows the highest ratio of  $[S\ II]/H\alpha$ , which indicates that the ISM experienced a shock in these areas.

These emission lines were fitted with a single Gaussian function to determine the parameters describing their profiles and thus investigate the kinematic and physical properties of these objects. Figures B.1 – B.8 show the spectra of the total emission in object A (PA = 44°), A (PA = 155°), F, E, B-1, B-2, D and R respectively. The kinematics and the line ratios of the optical emission lines are listed in Tables 3.4 and 3.5. It is important to know that the emission lines in the objects of interest are very narrow, thus the velocity dispersion was not corrected for the instrumental width.

Table 3.4: Emission line parameters from the spectra of objects of interest in NGC 300.

Object	H $\alpha$		[N II]		[S II]		[O III]		H $\beta$	
	Velocity km s <sup>-1</sup>	FWHM km s <sup>-1</sup>								
R (PA=44°)	9 ± 1	72 ± 5	2 ± 8	68 ± 7	63 ± 8	106 ± 8	-25 ± 1	100 ± 1	19 ± 4	77 ± 6
A (PA=44°)	-32 ± 8	65 ± 4	-8 ± 20	86 ± 4	-57 ± 4	74 ± 4	-19 ± 2	86 ± 3	-12 ± 3	102 ± 8
B-1 (PA=44°)	-3 ± 1	71 ± 3	-11 ± 5	64 ± 7	-37 ± 1	68 ± 4	-11 ± 7	43 ± 7	3 ± 2	73 ± 1
B-2 (PA=44°)	-1 ± 1	72 ± 2	14 ± 6	62 ± 4	33 ± 5	63 ± 3	-25 ± 1	71 ± 2	-23 ± 1	74 ± 2
D (PA=44°)	16 ± 1	60 ± 3	-4 ± 1	57 ± 3	-32 ± 1	57 ± 2	5 ± 1	63 ± 4	24 ± 2	77 ± 4
A (PA=155°)	-55 ± 2	94 ± 5	-61 ± 3	83 ± 9	-54 ± 2	85 ± 2	-8 ± 1	92 ± 2	-43 ± 1	94 ± 7
F (PA=155°)	-64 ± 1	68 ± 3	-69 ± 1	61 ± 9	-79 ± 5	54 ± 5	-14 ± 3	60 ± 5	-34 ± 6	76 ± 5
E (PA=155°)	-28 ± 2	72 ± 5	-43 ± 6	62 ± 6	-31 ± 4	70 ± 4	-43 ± 4	73 ± 7	-34 ± 5	105 ± 7
K1 (PA=119°)	65 ± 4	72 ± 3	27 ± 3	67 ± 6	29 ± 4	59 ± 4	-52 ± 4	25 ± 7	67 ± 5	68 ± 7
K2 (PA=119°)	85 ± 5	68 ± 3	86 ± 3	56 ± 6	48 ± 4	89 ± 4	-33 ± 4	52 ± 7	102 ± 5	74 ± 7
K3 (PA=111°)	30 ± 3	57 ± 3	35 ± 3	65 ± 6	-2 ± 4	41 ± 4	-28 ± 4	65 ± 7	10 ± 5	69 ± 7
K4 (PA=111°)	61 ± 4	55 ± 4	68 ± 6	52 ± 6	27 ± 4	57 ± 4	-32 ± 4	34 ± 7	63 ± 5	64 ± 7
K5 (PA=111°)	74 ± 5	54 ± 4	80 ± 6	52 ± 6	39 ± 4	53 ± 4	-25 ± 4	59 ± 7	49 ± 5	55 ± 7
K6 (PA=111°)	98 ± 4	64 ± 4	104 ± 6	66 ± 6	28 ± 4	54 ± 4	-34 ± 4	34 ± 7	94 ± 5	65 ± 7
K7 (PA=68°)	52 ± 4	64 ± 4	57 ± 6	65 ± 6	15 ± 4	63 ± 4	-34 ± 4	47 ± 7	57 ± 5	64 ± 7
K8 (PA=68°)	66 ± 4	57 ± 4	70 ± 6	55 ± 6	27 ± 4	51 ± 4	-45 ± 4	42 ± 7	72 ± 5	67 ± 7
K9 (PA=68°)	66 ± 5	58 ± 4	75 ± 6	57 ± 6	33 ± 4	62 ± 4	-48 ± 4	44 ± 7	73 ± 5	65 ± 7
K10 (PA=68°)	88 ± 3	60 ± 4	90 ± 6	34 ± 6	45 ± 4	50 ± 4	-49 ± 4	8 ± 7	80 ± 5	76 ± 7

Table 3.5: Same as Table 3.4, but now emission line ratios.

Object	[S II]/H $\alpha$	[N II]/H $\alpha$	[O III]/H $\alpha$	H $\alpha$ /H $\beta$	[S II]6717/[S II]6731	log([O III]/H $\beta$ )	log([N II]/H $\alpha$ )	log([S II]/H $\alpha$ )
R (PA=155 $^\circ$ )	0.14 $\pm$ 0.08	0.12 $\pm$ 0.02	0.29 $\pm$ 0.05	4.5 $\pm$ 0.03	1.40 $\pm$ 0.03	-0.47	-0.92	-0.86
A (PA=44 $^\circ$ )	0.27 $\pm$ 0.03	0.15 $\pm$ 0.02	0.18 $\pm$ 0.08	5 $\pm$ 0.02	1.50 $\pm$ 0.01	-0.06	-0.83	-0.57
B-1 (PA=44 $^\circ$ )	0.45 $\pm$ 0.02	0.23 $\pm$ 0.03	0.07 $\pm$ 0.01	4.48 $\pm$ 0.41	1.51 $\pm$ 0.03	-0.52	-0.65	-0.34
B-2 (PA=44 $^\circ$ )	0.28 $\pm$ 0.10	0.20 $\pm$ 0.03	0.07 $\pm$ 0.01	5.43 $\pm$ 0.41	1.42 $\pm$ 0.05	-0.01	-0.71	-0.56
D (PA=44 $^\circ$ )	0.29 $\pm$ 0.10	0.23 $\pm$ 0.10	0.24 $\pm$ 0.01	6.10 $\pm$ 0.08	1.57 $\pm$ 0.11	0.15	-0.64	-0.54
A (PA=155 $^\circ$ )	0.17 $\pm$ 0.02	0.12 $\pm$ 0.03	0.30 $\pm$ 0.01	5.04 $\pm$ 0.08	1.64 $\pm$ 0.01	-0.06	-0.91	-0.78
F (PA=155 $^\circ$ )	0.19 $\pm$ 0.01	0.13 $\pm$ 0.12	0.35 $\pm$ 0.04	5.16 $\pm$ 0.76	1.52 $\pm$ 0.06	0.25	-0.88	-0.73
E (PA=155 $^\circ$ )	0.23 $\pm$ 0.05	0.14 $\pm$ 0.05	0.06 $\pm$ 0.02	6.20 $\pm$ 1.10	1.68 $\pm$ 0.02	-0.41	-0.87	-0.64
K1 (PA=119 $^\circ$ )	0.44 $\pm$ 0.07	0.29 $\pm$ 0.01	0.02 $\pm$ 0.11	6.60 $\pm$ 0.11	1.46 $\pm$ 0.11	-0.90	-0.54	-0.36
K2 (PA=119 $^\circ$ )	0.21 $\pm$ 0.12	0.06 $\pm$ 0.03	0.07 $\pm$ 0.17	10.80 $\pm$ 0.20	1.64 $\pm$ 0.10	-0.12	-1.24	-0.67
K3 (PA=111 $^\circ$ )	0.35 $\pm$ 0.12	0.34 $\pm$ 0.11	0.06 $\pm$ 0.25	4.20 $\pm$ 0.11	1.36 $\pm$ 0.24	-0.57	-0.46	-0.45
K4 (PA=111 $^\circ$ )	0.26 $\pm$ 0.08	0.23 $\pm$ 0.09	0.05 $\pm$ 0.15	4.90 $\pm$ 0.11	1.68 $\pm$ 0.10	-0.65	-0.64	-0.57
K5 (PA=111 $^\circ$ )	0.24 $\pm$ 0.07	0.21 $\pm$ 0.08	0.03 $\pm$ 0.15	11.04 $\pm$ 0.13	1.68 $\pm$ 0.10	-0.50	-0.68	-0.67
K6 (PA=111 $^\circ$ )	0.68 $\pm$ 0.10	0.15 $\pm$ 0.16	0.04 $\pm$ 0.15	8.70 $\pm$ 0.21	1.56 $\pm$ 0.14	-0.43	-0.81	-0.16
K7 (PA=68 $^\circ$ )	0.26 $\pm$ 0.07	0.18 $\pm$ 0.07	0.10 $\pm$ 0.08	8.62 $\pm$ 0.08	1.56 $\pm$ 0.12	-0.04	-0.74	-0.59
K8 (PA=68 $^\circ$ )	0.15 $\pm$ 0.07	0.15 $\pm$ 0.08	0.09 $\pm$ 0.14	13.64 $\pm$ 0.12	1.36 $\pm$ 0.14	0.08	-0.82	-0.85
K9 (PA=68 $^\circ$ )	0.17 $\pm$ 0.06	0.16 $\pm$ 0.09	0.07 $\pm$ 0.08	12.84 $\pm$ 0.08	1.85 $\pm$ 0.12	-0.02	-0.79	-0.80
K10 (PA=68 $^\circ$ )	0.42 $\pm$ 0.13	0.11 $\pm$ 0.16	0.03 $\pm$ 0.21	9.23 $\pm$ 0.23	1.31 $\pm$ 0.26	-0.54	-0.98	-0.38

## 3.3 Discussion

### 3.3.1 Archival properties of selected objects

Supporting information about our objects was collected through Vizier (Figures 3.11). Object A comprises some 25 objects, including 13 Wolf–Rayet stars (Breysacher et al. 1997; Schild et al. 2003). These stars can trace young stellar populations, and their presence often reflects low metallicity (Schild et al. 2003). Three H II regions were detected at radio frequencies with spatial resolution  $\approx 2''$  and X-ray observations with an energy range of 0.3–6.0 keV (Payne et al. 2004), and a radio supernova remnant (SNR) with  $\alpha \sim -0.4 \pm 0.3$  (Chomiuk & Wilcots 2009). Five OB associations appear in this area (Kim, Sung & Lee 2002). Object B has five H II regions (Deharveng et al. 1988; Roussel et al. 2005), and two SNR candidates in an optical imaging and long-slit spectroscopic study (Blair & Long 1997). Wolf–Rayet stars and OB associations are located in this object, too. Object C represents a known H II region (Deharveng et al. 1988). Figure 3.11 shows the different components which appear in objects A and B.

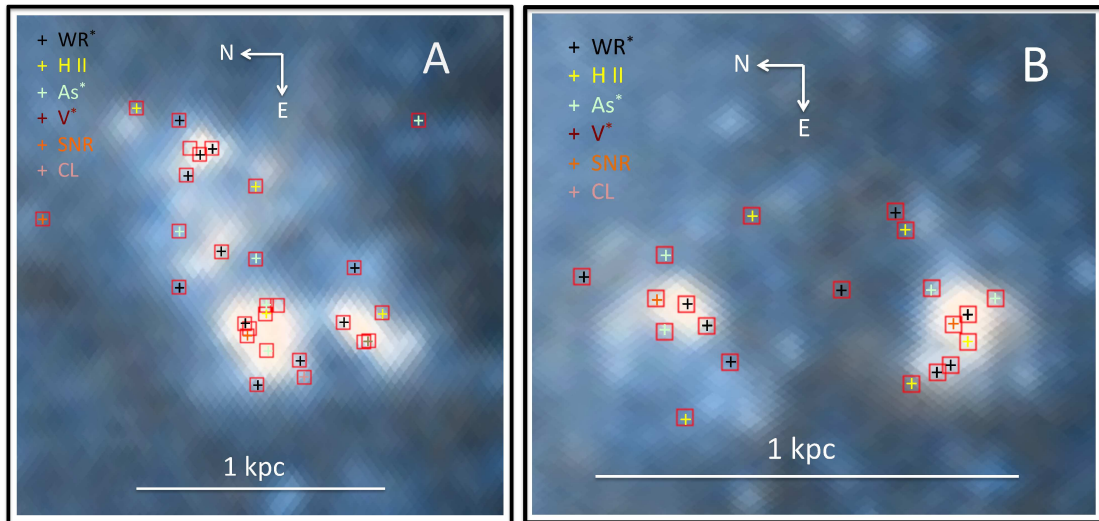


Figure 3.11: The major identified components in objects A and B which were collected through Vizier. WR\* = Wolf–Rayet star, SNR = supernova remnant, V\* = Variable star, As\* = association of stars, H II = star-formation region, CL = cluster of stars. The background image taken at optical wavelength.

### 3.3.2 Intensity maps and the kinematics of $H\alpha$ and $H\beta$

The  $H\alpha$  intensity map, which was obtained by the FP observations, and is shown in Figure 3.2, displays  $H\alpha$  emission in two prominent areas (marked A and B) as well as a few smaller areas that represent SNRs and classical H II regions, such as object C. Object A spans nearly 1 kpc across the sky, which is larger than the most active star formation regions in the local group, such as 30 Doradus in the LMC (400 pc) and NGC 604 in M33 (460 pc) (Relaño & Kennicutt 2009), and B shows two distinct areas with annular shells (loops). These prominent areas are also very obvious in  $H\beta$  emission.

It is worth focusing on Gaussian parameters to separate the continuum emission from emission lines to show the impact of these active areas on the surrounding ISM. The nucleus of NGC 300 and its vicinity are characterised by strong continuum emission, part of which is obvious in panel (c) of Figures 3.4 and 3.5, because the continuum light from old red stars dominates in these areas. From a morphological point of view, different structures can be seen in object A in  $H\alpha$  emission and continuum. These could be filaments produced by the impact of the ionized outflowing gas and could arise as a result of the stellar winds of high-mass stars in this area (see Figure 3.8 panel (a)). The  $H\beta$  map, panel (a) of Figure 3.5, also shows these structures. Likewise, object B displays clear filaments with  $H\alpha$  emission which extend to make loop structures with radii of nearly 200 pc, as shown in Figure 3.9 panel (c). These loops are less clear in  $H\beta$  emission, perhaps due to the lower spectral resolution (LR) compared with the resolution of the  $H\alpha$  observations (MR), as MR can trace fainter features of the spectra compared to LR (see Figure 3.5 panel (a)). In the following, I will examine different tracers of the ISM.

#### 3.3.2.1 A comparison of optical observation in different spectral windows

It is instructive to compare the intensity maps of  $H\alpha$  and  $H\beta$  with maps created using different spectral windows. This will uncover more knowledge about what is going on in the areas A and B, what kinds of objects are there, what is the impact or variation in the geometry of the ISM in the vicinity of the H II regions, and what are the physical conditions around them. The diffuse ionized gas is extended to about 1 kpc in objects A and B, and these H II regions supply more than one quarter of the ionized emission in the observed field from NGC 300. Hoopes, Walterbos & Greenwalt (1996) suggested that 42% of the  $H\alpha$  emission in NGC 300 originates in the diffuse ionized gas, concentrated around H II regions, and substantial emission can be noticed in the vicinity of H II regions to a distance of about 0.5 to 1 kpc. NGC 300 shows conspicuous filamentary structures of the diffuse ionized gas ( $H\alpha$ ,  $H\beta$ ) in the form of loops or shells being driven by the impact of OB associations. The loop structures

are more concentrated and visible near star formation regions (see Figure 3.4 and Figure 3.5) .

Roussel et al. (2005) investigated the A and B complexes by analysing a combination of maps that were observed with near ultraviolet ( $\text{NUV}_{eff} = 2267 \text{ \AA}$ ), far ultraviolet ( $\text{FUV}_{eff} = 1516 \text{ \AA}$ ) and optical (UBVRI,  $\text{H}\alpha$ ,  $\text{H}\beta$ ) bands. Figures 3.12 and 3.13 show six different maps for each object in that previous study and the present study. Panel (a) represents the U-band (NUV & FUV) map where bright regions represent stellar clusters or groups of clusters of massive stars. The massive stars emit copious UV radiation that can ionize the areas surrounding these stars. In comparison with (d)  $\text{H}\alpha$  and (e)  $\text{H}\beta$  maps from my FP observations, the brightest UV emission in D137a coincides with  $\text{H}\alpha$  and  $\text{H}\beta$  emission forming a “ceiling” fan shape at (RA:  $00^h 55^m 13.00^s$ , Dec:  $-37^\circ 41' 40''$ ) and extending to 200 pc around this position. While D137b shows bright UV emission the  $\text{H}\alpha$  and  $\text{H}\beta$  emission is low in the area surrounding D137b. This can be interpreted as massive stars re-shaping the ISM by forming walls on each side of these stars separated by a distance of about 90 pc. Object A shows bright emission in the  $8 \mu\text{m}$  map, broadly coinciding with the  $\text{H}\alpha$  and  $\text{H}\beta$  emission. The mid-infrared emission is mainly from PAHs, which trace star formation (Wu et al. 2005).

Panel (f) of Figure 3.12 shows radio contours overlaying the DSS2-RED image for target A. This source possibly represents a compound of supernova remnant embedded within an H II region or superimposed on an H II region. Only D137a shows a radio source, coinciding with bright optical (ceiling fan shape), UV and mid-infrared emission. It is likely that SNRs are highly sensitive to the density of the environment, as it strengthens the shocks, thus amplifying the magnetic field and heating the gas giving rise to strong radio synchrotron and X-ray emission.

The object B is shown in Figure 3.13, which presents six spectral windows (U band, mid-infrared,  $\text{H}\alpha$ ,  $\text{H}\beta$ , radio), and panels (d) and (e) show my new FP observations. D118 and D119 show the same morphological structures, in particular in the UV and  $\text{H}\beta$  maps. Both of these H II regions seem to be formed of expanding bubbles. The expanding material (shells) are clear in these maps. D118 displays radio emission, which was observed by Payne et al. (2004), and they suggested that signatures of both SNR and H II regions appear in this area. The morphological structures of H II regions in object A and B suggest that D137a and D137b might be younger than D118 and D119. Both show same morphology, and position onto the boundary of bubble structures; where the expanding gas of stellar winds sweeps up surrounding ISM in particular cold molecular gas which is comprised and then creates shells with high density, that might trigger a new star formation episode. D119 appears as a complex object spanning a larger area than D137, and it would be formed in a typical way where a dense molecular cloud collapses and triggers star formation regions. Perhaps these two objects are inclined at a different angle with respect to the observer. In real H II regions which show asymmetry structures, the impacts re-shape the surrounding

ISM according to the activity and age of the star formation regions (entrained energy and material by stellar winds). If one takes all these facts into account then one would expecte to see different shapes at different viewing angles.

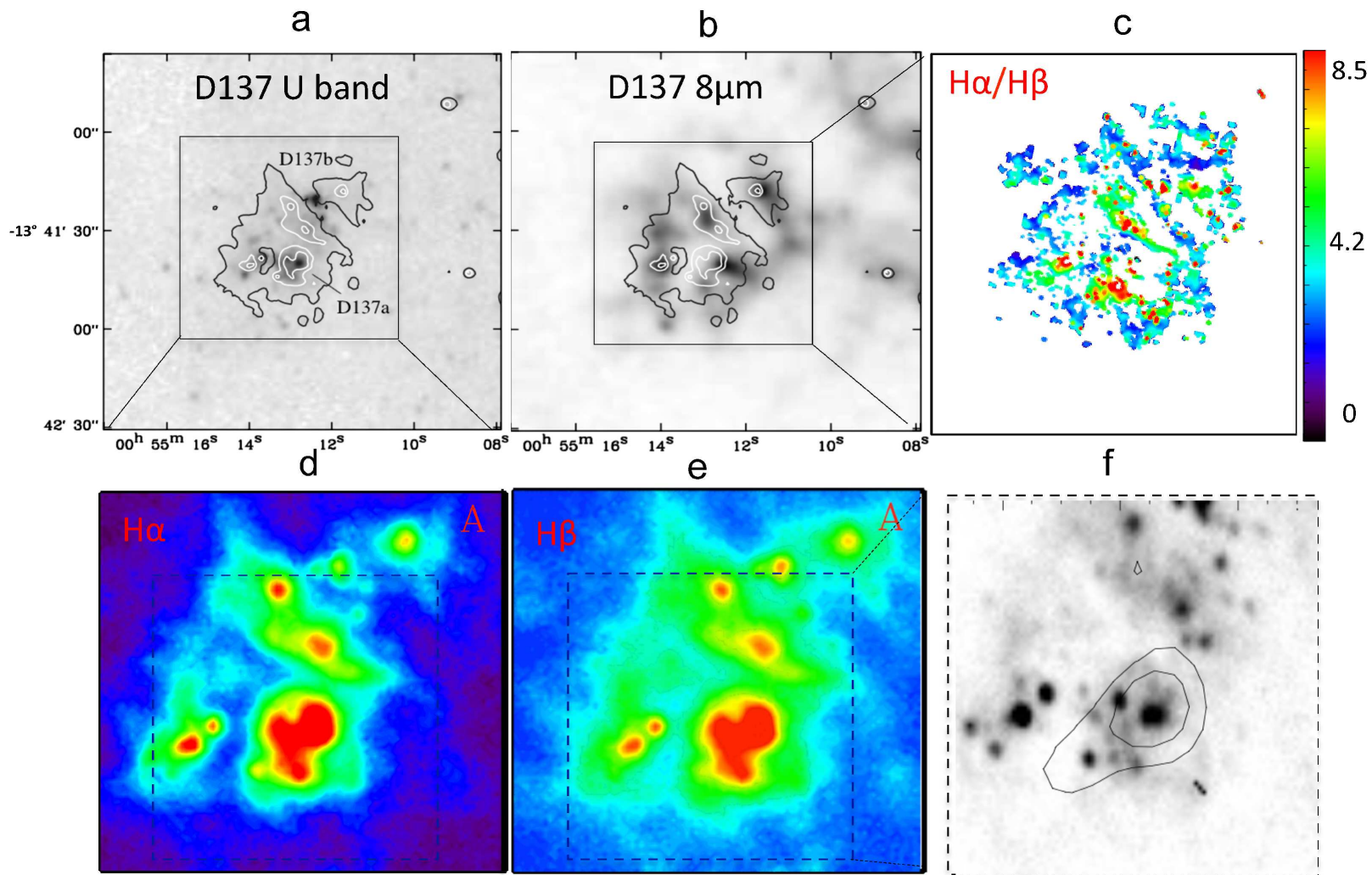


Figure 3.12: Maps of complex A: (a) U-band (near & far ultra-violet), (b) infrared emission at  $8 \mu\text{m}$ ; X-axis and Y-axis represent the RA and Dec respectively. Superposed contours onto the maps represent  $\text{H}\alpha$  emission (Roussel et al. 2005). (c) shows the ratio of  $\text{H}\alpha/\text{H}\beta$  (present study), (d) and (e) represent  $\text{H}\alpha$  and  $\text{H}\beta$  emission (present study). (f) Shows a radio image (Payne et al. 2004).

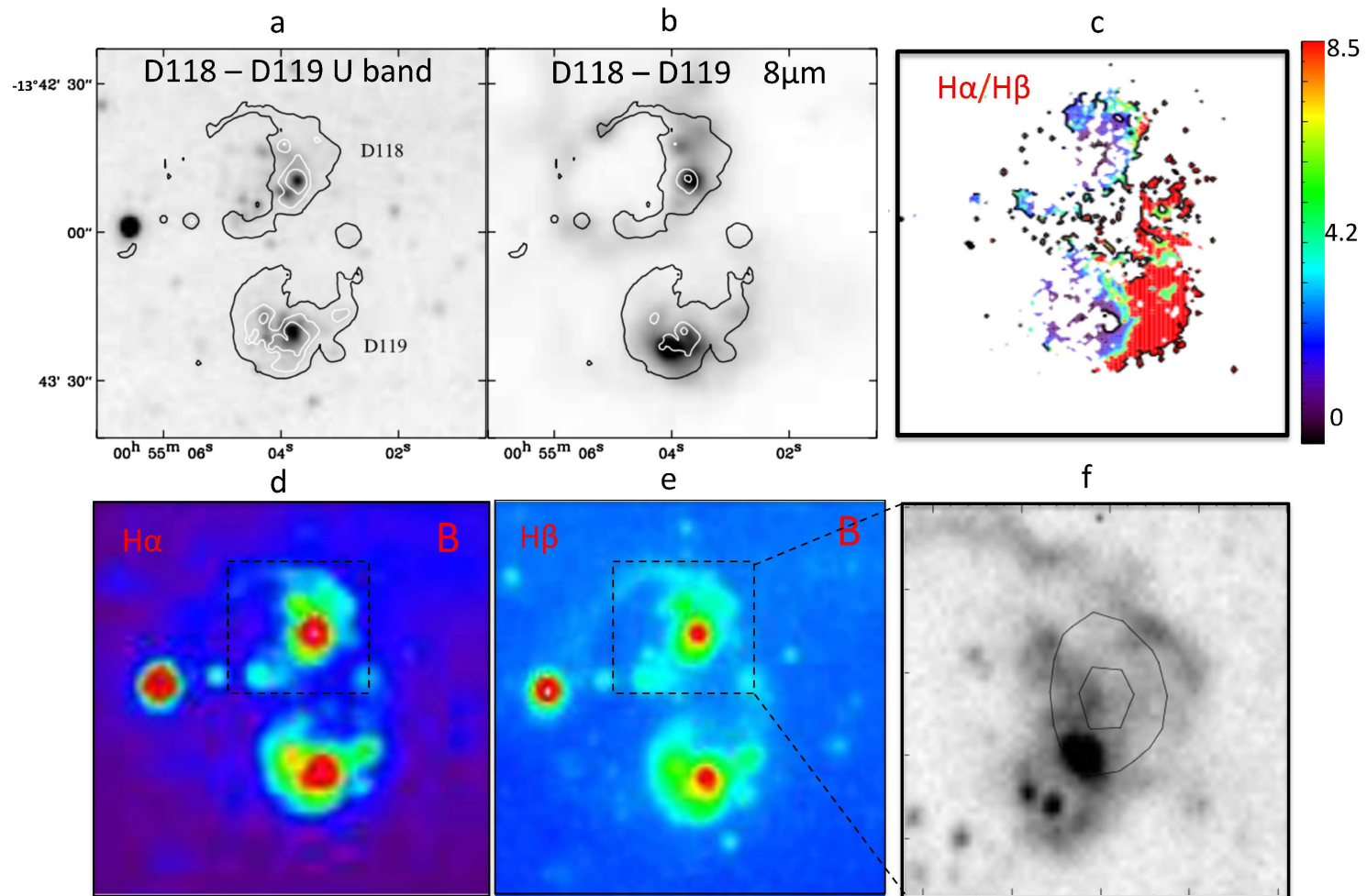


Figure 3.13: As Figure 3.12, but for object B.

### 3.3.2.2 The dust distribution

Figure 3.14 shows the line ratio map of  $H\alpha/H\beta$ , which can be used to examine the attenuation by dust. Some areas show high attenuated emission in specific regions, where a high ratio appears, and some display values very close to the theoretical ratio of  $H\alpha/H\beta$  as expected in unattenuated emission. The presence of dust in H II regions

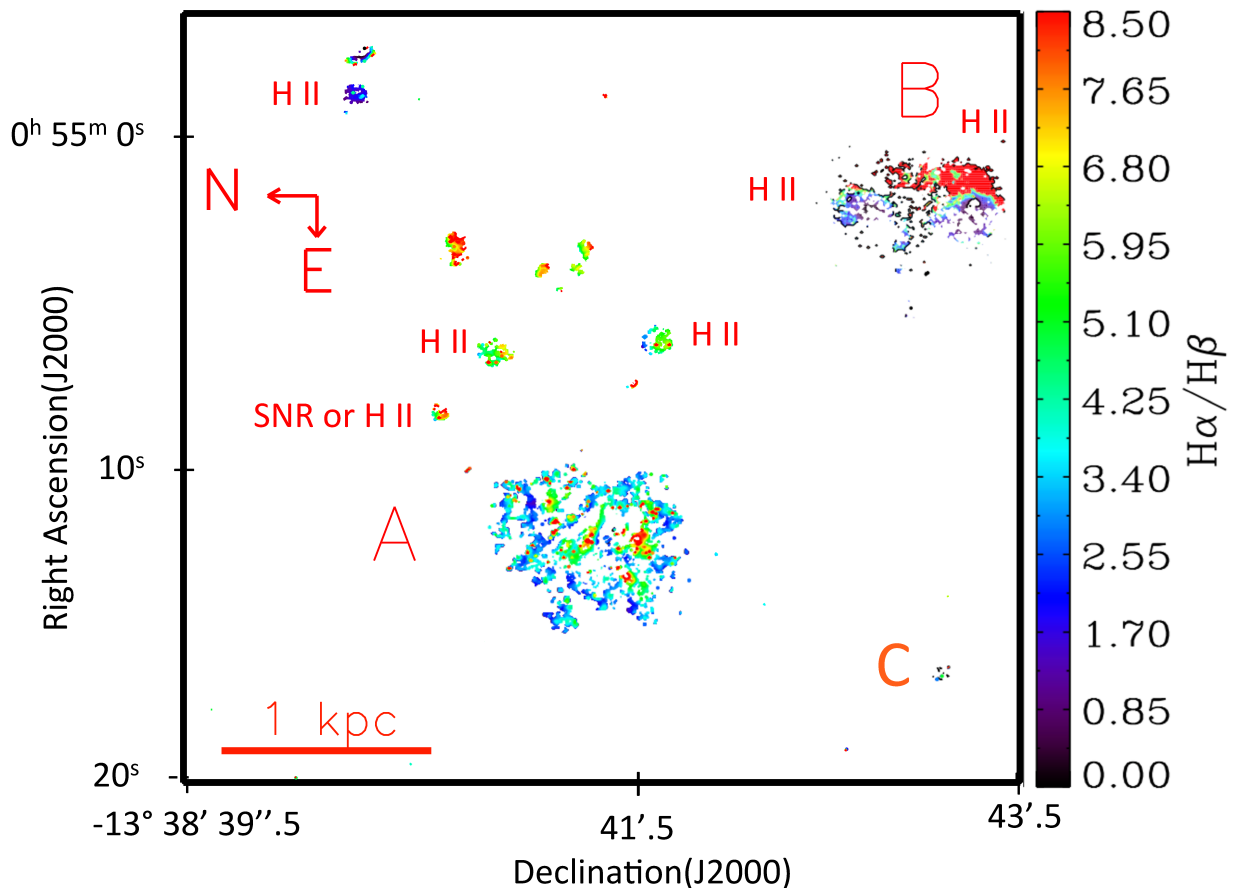


Figure 3.14: The ratio of  $H\alpha/H\beta$ . Pixels that do not have both  $H\alpha$  and  $H\beta$  emission are excluded from the map.

is common, as young massive stars are embedded in dust. The impact of the dust can reduce the detected intensity and redden the continuum. Importantly, internal reddening cause changes in the emission line profile, by attenuating certain parts that contribute to the profile more than other parts. The most common method used to correct the emission-line spectra from extinction is based on the ratio of the lower

Balmer lines ( $H\alpha$  &  $H\beta$ ); when the observed ratios are compared with those from theory, their deviations represent the effect of interstellar extinction. The ratio of  $H\alpha/H\beta$  offers an interesting trace of the dust, in front of and within the ionized gas (Osterbrock & Ferland 2006). In photoionized nebulae with a pure recombination case B ( $n_e = 10^2 \text{ cm}^{-3}$ ,  $T = 10\,000 \text{ K}$ ), the intrinsic value of  $H\alpha/H\beta$  is about 2.85 (Osterbrock and Ferland 2006). The collisional excitation of  $H\alpha$  Balmer lines should be taken into account in the case of shocks in SNRs and AGN, then the intrinsic value of the Balmer decrement ( $H\alpha/H\beta$ ) is likely to be 3.0–3.1. The lower threshold energy of  $H\alpha$  compared with that of  $H\beta$  makes it more likely to be created by collisions compared to  $H\beta$ . This explains why often an  $H\alpha/H\beta$  ratio of 3.0 is adopted—a value which is 0.15 higher than that of pure recombination only.

The method used to determine the  $H\alpha$  extinction from Balmer decrement is explained by Caplan & Deharveng (1986) and Relaño et al. (2006). Their method is based on the fact that the  $H\alpha$  and  $H\beta$  are emitted in thermodynamic equilibrium environment, and the discrepancy from the theoretical value of  $H\alpha/H\beta$  is caused by extinction of light due to the interstellar dust distribution. The  $H\alpha$  extinction produced by such environment is given by:

$$A_{H\alpha} = 5.25 \times \log \left( \frac{H\alpha/H\beta}{2.859 T_e^{-0.07}} \right) \quad (3.1)$$

Where:

$H\alpha$ ,  $H\beta$  = the observed emission of  $H\alpha$  and  $H\beta$  respectively.

$T_e$  = the electron temperature in unit  $10^4 \text{ K}$ .

2.859 = the theoretical value of  $H\alpha/H\beta$  in case B recombination ( $T = 10^4 \text{ K}$ ,  $n_e = 100 \text{ cm}^{-3}$ ).

Figure 3.14 displays the Balmer decrement ratio for different H II regions in NGC 300. In this map, pixels that do not have both  $H\alpha$  and  $H\beta$  emission are excluded from the map. The dust distribution is different over the observed areas. A few positions show areas without or having little dust, with a ratio around the theoretical value (2.85), while the dusty environments are widely apparent in the map, in particular H II regions and SNRs. High dust column densities appear in SNRs more than in H II regions. A few dusty filaments appear in object A with Balmer decrement  $\sim 6$  ( $A_{H\alpha} = 3.1$ ) and as much as  $\sim 8$  ( $A_{H\alpha} = 3.8$ ) in H II regions and SNRs. Object A spans 1 kpc on the sky, which comprises different objects such as H II regions, Wolf–Rayet stars and SNRs (see Figure 3.11 left panel).

Metals play an important role in the formation of dust grains. The latter are formed during stellar evolution and SNe, as stellar winds carry out copious amounts of metals that were produced inside the stars during the nucleosynthesis process. As well as this, the dust grains can be destroyed by SNe shocks (Lakićević et al. 2015; Temim et al. 2015). The material swept by the ejecta from stars forms a dense and cold shell

of material, which is decelerated when the SN passes through the Sedov–Taylor phase (adiabatic phase). The distribution of the dust in object A also agrees with that shown in the 8  $\mu\text{m}$  map presented by Roussel et al. (2005) (see panel (c) Figure 3.12).

Object B has two H II regions D118 and D119, which show high Balmer decrements of  $\sim 8$  ( $A_{H\alpha} = 3.8$ ) and a lower value  $\sim 3$  ( $A_{H\alpha} = 3.1$ ) on the boundary of the bubbles. D119 shows higher Balmer decrements to the East than to the West, and the position of the highest value does not coincide with the peak of 8 micron emission (see Figure 3.13), but instead shows values that are about the theoretical zero-extinction value in D119 and in other locations achieves higher values of about 4. This would result from losing some values through the data reduction process, when excluding pixels that do not have both H $\alpha$  and H $\beta$ .

### 3.3.2.3 The kinematics of H $\alpha$ and H $\beta$

Figure 3.8 panel (c) shows the kinematic map of the H $\alpha$  emission line. It was found that the velocities<sup>1</sup> of the outflows in object A are about  $-120 \text{ km s}^{-1}$  in the central area and increase to more than  $-220 \text{ km s}^{-1}$  in the outer regions. Velocity dispersions (panel d) display a similar behaviour, with a low value in the centre ( $\sim 90 \text{ km s}^{-1}$ ) and enhanced in the boundaries to about  $200 \text{ km s}^{-1}$ . Clear filaments appear with high velocity dispersion, between  $175$  to  $230 \text{ km s}^{-1}$ , in the Eastern surrounding area of object A, and filaments with lower velocity dispersion (about  $90 \text{ km s}^{-1}$ ) can be seen in the middle area of object A. The zoomed-in maps (e) and (f) in Figure 3.8 show the velocity and velocity dispersion in object A with H $\beta$  emission. The values follow the same trends as in the H $\alpha$  maps, velocities are between  $-140$  to  $-260 \text{ km s}^{-1}$ , while velocity dispersion ranges from  $110$  to  $200 \text{ km s}^{-1}$ .

In the same way, Figure 3.9, shows a zoomed in view of object B. The velocities (H $\alpha$ ) in object B are between  $-160$  to  $-180 \text{ km s}^{-1}$ . The velocity dispersion in this object has high values in some specific areas, reaching about  $270 \text{ km s}^{-1}$ . The loop has velocity dispersions  $200 \text{ km s}^{-1}$  in the boundaries and  $120 \text{ km s}^{-1}$  in the centre. The H $\beta$  kinematic maps of object B are shown in Figure 3.9 (panels e & f). The velocity measures between  $-160$  to  $-240 \text{ km s}^{-1}$ , and velocity dispersion between  $90$  to  $140 \text{ km s}^{-1}$ .

These maps present some interesting structures: the presence of large velocity dispersion is an indication of kinematic interaction between different components. In other words, it is possible that this material has possibly been shock heated in colliding outflows.

---

<sup>1</sup>after subtracting the  $V_{sys}$  ( $136 \text{ km s}^{-1}$ ) of NGC 300.

### 3.3.2.4 Signatures of shocks

The profile shape was examined in different pixels to search for any indication of splitting in these emission lines ( $H\alpha$  &  $H\beta$ ). The object B displays blended  $H\alpha$  profiles in some areas, as shown in Figure 3.15, but this does not appear in the  $H\beta$  emission. Perhaps the second component is faint in  $H\beta$  emission and cannot be measured.

As mentioned before, all the emission lines from our objects were fitted with a single Voigt function. It was noticed that the  $H\alpha$  profile displays a broader shape in various places (high velocity dispersion). These kinds of signature appear in areas where the gas experiences shocks due to the interaction among different components along the line of sight (Heckman, Armus & Miley 1990; Hoopes & Walterbos 2003). The next step was to examine the observed profile across these areas. Profiles with signs of line splitting were found in object B, and are shown in Figure 3.15. For instance, panels 1–10 could have two components with different velocities along the line of sight and different morphology of ionized gas, hence it suggests an expanding structure or outflow. The positions of the split coincide with the area of higher velocity dispersion as well as with the areas with high velocity. Notice that the split appears in both H II regions with high intensity and its surroundings with low intensity. Figure 3.16 presents a model fit with two Gaussian components to the average spectrum of 49 pixels, which are marked by the white box (see Figure 3.15). The fit suggests that there are two components, the brightest one shows lower velocity  $\sim -13 \pm 8 \text{ km s}^{-1}$  and lower FWHM ( $\sim 116 \pm 20 \text{ km s}^{-1}$ ), while the fainter one has higher blue-shifted velocity  $\sim -306 \pm 18 \text{ km s}^{-1}$  and higher FWHM ( $\sim 336 \pm 20 \text{ km s}^{-1}$ ). These two components are clear in specific areas which are marked with white box in Figure 3.16, as well as showing high velocity dispersion (see Figure 3.4 panel (d)) ranging from 400 to 640  $\text{km s}^{-1}$ , these are values from one Gaussian fitting. Surrounding areas with a sign of splitting, wide profiles were diagnosed, which show a single component that has velocity ranging between  $-160$  and  $-240 \text{ km s}^{-1}$  and velocity dispersion between 250 and 400  $\text{km s}^{-1}$ .

In object A, the one component Gaussian fitting is probably the more acceptable model for  $H\alpha$  emission, and there was no sign of splitting.

As mentioned before in this section, A and B are compound objects with H II regions and SNRs (Payne et al. 2004). The morphological structures of D118 and D119, the presence of circular shells and signatures of splitting in the emission line suggested that this material has experienced shock-heating, and the high velocity dispersion could reflect the interaction between different components along the line of sight. I will take all the previous points into account, and explore these two objects in more detail with long-slit observations in order to study the physical properties across these large objects, such as the ionization state, temperatures, abundance and electron density.

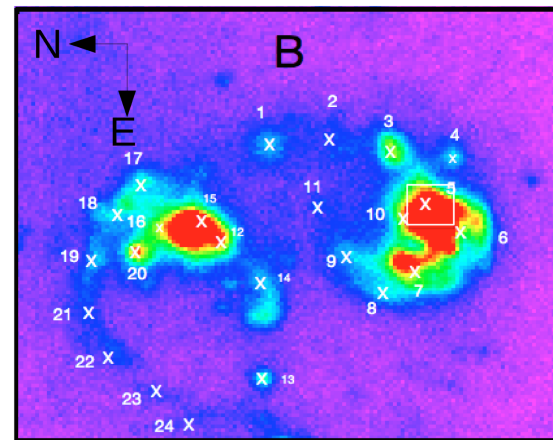
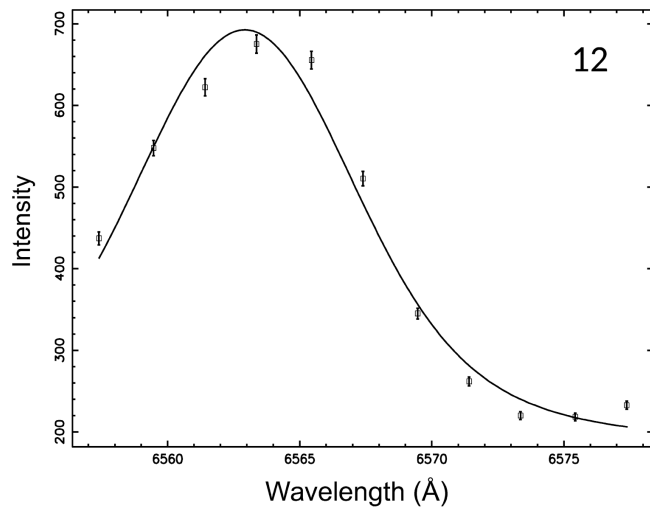
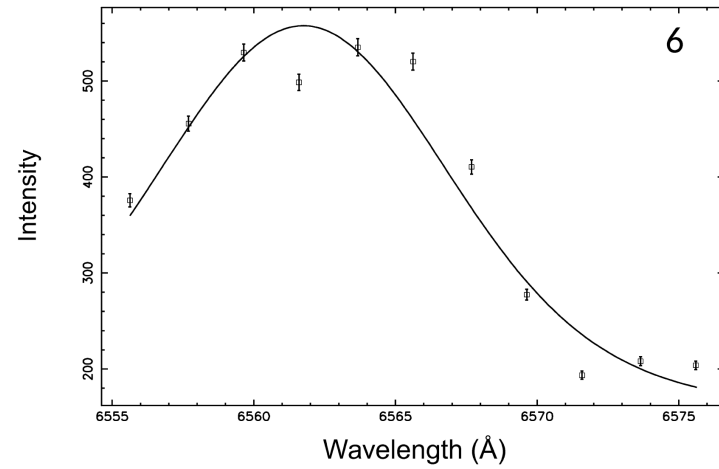
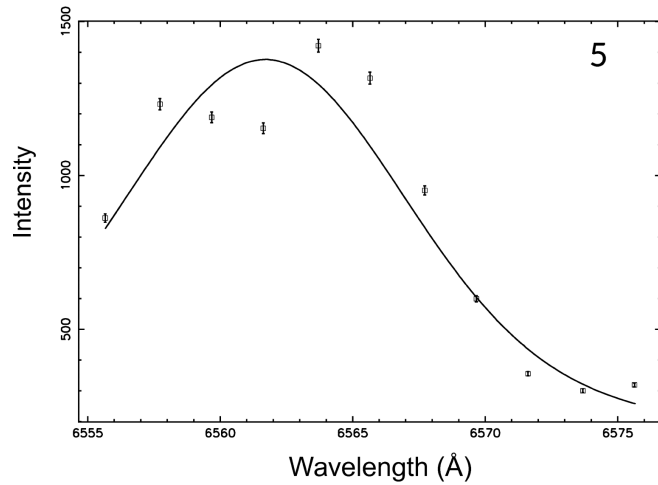


Figure 3.15: Bottom right: A map showing the total intensity in  $H\alpha$  for object B. The other panels display examples of  $H\alpha$  profiles in various regions in object B, which are marked onto the map. Notice panels (5) and (6) have signatures of splitting in the profiles. Panel (12) shows an example of a single profile. The other panels marked on the map are shown in Appendix C (Figures C.1, C.2, C.3).

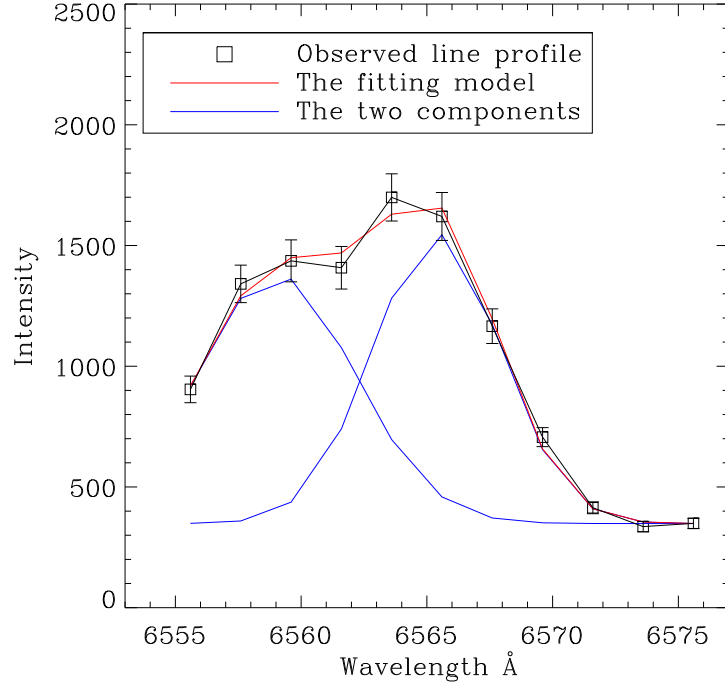


Figure 3.16: The  $H\alpha$  profile in object B with two peaks and model fit of two Gaussian components. The spectrum is an average of 49 pixels that are marked with a white box in Figure 3.15.

Table 3.6: The kinematic parameters of object B, average spectrum of 49 pixels which are marked in a white box in Figure 1.5.

$V-H\alpha^{1st}$	$-13 \text{ km s}^{-1} \pm 8$
$FWHM-H\alpha^{1st}$	$316 \text{ km s}^{-1} \pm 20$
$V-H\alpha^{2nd}$	$-306 \text{ km s}^{-1} \pm 18$
$FWHM-H\alpha^{2nd}$	$434 \text{ km s}^{-1} \pm 20$
$1^{st} = \text{first component.}$	
$2^{nd} = \text{second component.}$	

### 3.3.3 The emission line ratios and the diagnostic diagrams

In the previous sub-sections, the main physical properties were investigated for different objects in NGC 300. In the following, the environment throughout the largest object (A) is examined. The largest object (A155, A44) possesses a variety of small-scale structures. To investigate and acquire more information about what is happening in these kinds of compact regions, I will use several diagnostic diagrams, based on emission line ratios, to examine each subdivision in the interesting objects. These diagnostic diagrams can differentiate the photoionized nebulae from shock-excited objects. This method was used to study sub-structures of planetary nebulae (PNe) and to determine the excitation mechanism in PNe (Daneshkar et al. 2017; Gonçalves et al. 2004).

The ionization mechanisms in the expanding area seen in D119 (A155, A44) could be generated from collisional excitation or photoionization. It is possible to identify which mechanism presently dominates its excitation by using line ratios  $[S\ II]/H\alpha$  and  $[N\ II]/H\alpha$  in a diagnostic diagram (Sabbadin, Minello & Bianchini 1977; Camps-Fariña et al. 2017). The strength of the lines was determined by measuring the intensity at peak of the line. Figure 3.10 shows four long-slit frames on the red and blue sides of the spectra at  $PA = 44^\circ$  and  $155^\circ$ . The interesting objects are marked on these frames, and the spectra of these objects are shown in Figures B.1 – B.8.

Figure 3.17 shows the positions of the objects of interest on the diagnostic diagram. The majority of the objects fall near the boundary of the H II zone in the diagram. This suggests photoionization is currently dominant in the left-side areas, which is in contrast to the other regions (right-side) where shocks may be important, as collisional excitation rather than photoionization dominates (Camps-Fariña et al. 2016). The centre of the galaxy (K6) shows ratios of SNR, while K1, K3, K10, and B-1 display ratios between SNR and H II regions.

The analysis of the relative intensities of metal line emission to  $H\alpha$  (Table 3.5) provides the first evidence that the interstellar gas experiences shocks. These are the major sources of ionization and excitation in the ISM, and can produce high ratios of forbidden lines with respect to  $H\alpha$  (Mathewson & Clarke 1973). Object F, A155 and E have high ratios of  $[N\ II]/H\alpha$  and  $[S\ II]/H\alpha$  that are comparable to the average value of H II regions surrounding numerous massive O stars, where shock waves develop by stellar winds and leave signature of shock in the spectra of the emission lines of the shocked gas (Lagrois, Joncas & Drissen 2012). Note also B-1 shows high  $H\alpha/H\beta$  ratio (4.5) and low  $[O\ III]/H\alpha$  compared with low ionized line ratios to  $H\alpha$ . Hence, this target could undergo more than one events.

Figure 3.18 shows three different sets of diagnostic diagram. The top panel shows that approximately the entire area across object A is located in the shock-excited zones. These areas display low ratio of highly excited lines such as  $[O\ III]$  to  $H\alpha$  and high ratios of low excitations lines such as  $[S\ II]$  or  $[N\ II]$  to  $H\alpha$ . The boundary of the different zones in the diagnostic diagram were originally determined using abundances

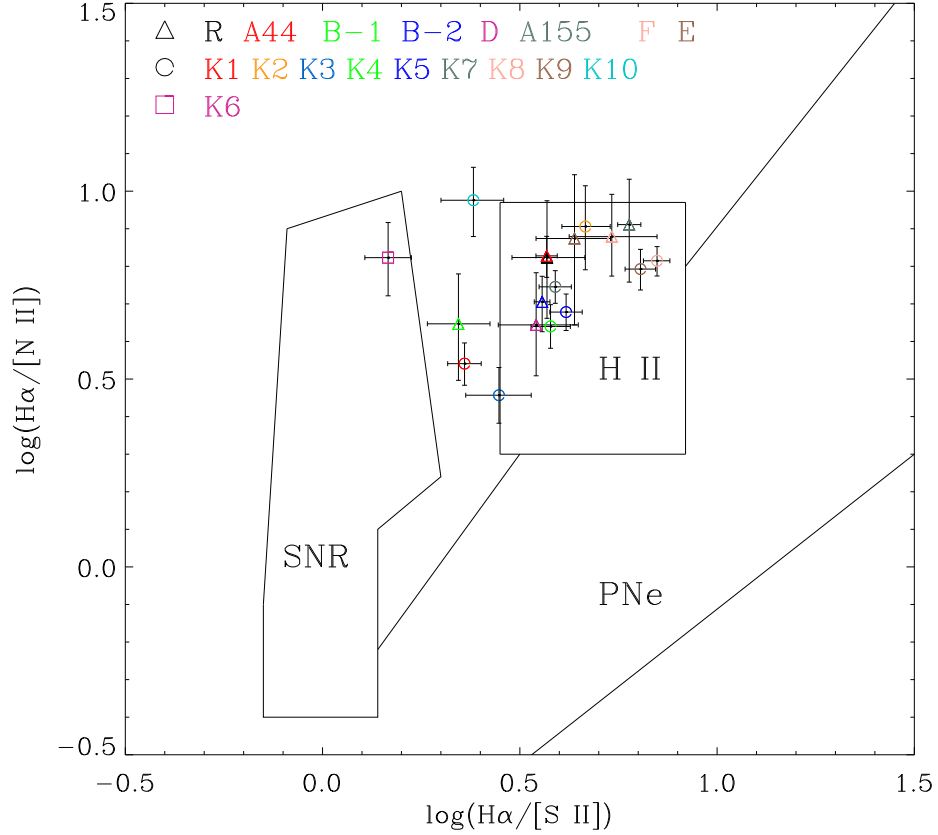


Figure 3.17: Diagnostic diagram to distinguish between H II regions, SNRs and planetary nebulae (PNe) derived from the ratios of H $\alpha$  to forbidden lines [S II] and [N II], adapted from Camps-Fariña et al. (2016).

and shock velocities for young stellar objects. The top panel of Figure 3.18 shows that 78% of the points are located in the shock regions, while 10% of the points show high ratio of high excited lines to Balmer line that agree with PNe position, and 5% have high [O III]/H $\alpha$  where the photoionization is the dominant ionizing source. The two points near to the shock boundaries (blue ones) (Phillips & Cuesta 1999; Hartigan, Raymond & Hartmann 1987) in the top panel of Figure 3.18 are the same points that are outside the H II regions in the bottom panel. These two points could be areas that are near the ionizing source of the H II regions. Their ratios of the [S II] lines are high (1.27 and 1.4), so the estimated electron densities are low ( $10\text{--}400\text{ cm}^{-3}$ ) according to Osterbrock & Ferland (2006) if the expected temperature of the nebula is 10 000 K.

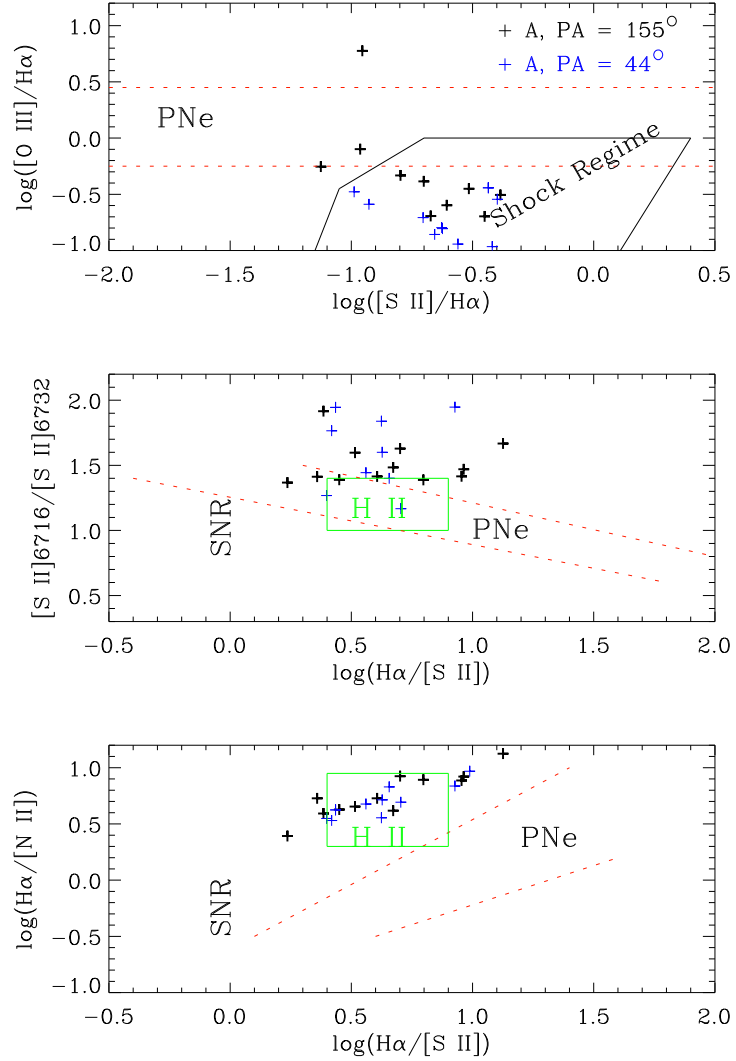


Figure 3.18: Diagnostic diagram showing the positions across object A (PA = 155°, 44°) with superimposed empirical boundaries of H II regions, PNe, and SNRs. The boundaries of the theoretical shock regime are from Phillips & Cuesta (1999); Hartigan, Raymond & Hartmann (1987). Note that the ratios used follow  $[\text{O III}] = [\text{O III}]_{4959 \text{ \AA}} + 5007 \text{ \AA}$ ,  $[\text{S II}] = [\text{S II}]_{6717 \text{ \AA}} + 6731 \text{ \AA}$ , and  $[\text{N II}] = [\text{N II}]_{6548 \text{ \AA}} + 6583 \text{ \AA}$ .

### 3.3.4 Analysis of the largest objects A44 and A155

In this section, the largest object (A44, A155) was chosen to study the trend of the line ratios and kinematics across this particularly interesting object (see Figure 3.1). Figure 3.19 shows various line ratios along the slit, which crosses object A with PA=155°. In the right panel the ratios of [N II]/H $\alpha$  and [S II]/H $\alpha$  are enhanced more in the diffuse ionized gas (DIG) than in the H II regions where H $\alpha$  emission is strong. The average value of the ratio of [S II]/H $\alpha$  in the DIG is about 0.5, and reduces gradually towards the H II region reaching 0.075 at the area between 240'' to 260''. The [N II]/H $\alpha$  ratio follows the same trend as [S II]/H $\alpha$  but with lower values. The minimum ratio in the H II region is  $\sim 0.06$ , increasing to about 0.3 in the DIG. [O III]/H $\alpha$ , on the other hand, is maximum inside the H II region.

Comparing emission lines that are close in wavelength is a more accurate method of examining the ionization level in nebulae. Such ratio will not be affected by extinction, as these lines will be in the same spectrum and can avoid any calibration issues, so using [O III]/H $\beta$  is more effective than [O III]/H $\alpha$  (see the left panel). The [O III]/H $\beta$  ratio displays an opposite trend to the previous ratios ([N II]/H $\alpha$  & [S II]/H $\alpha$ ). I notice that it reaches nearly 1.8 at area between 235'' to 245''. On the other hand, one can notice the [O III] emission disappears or becomes too weak to be detected in a few positions. The [O III] needs high energy photons ( $h\nu = 35.1$  eV) to be ionized. This is available near to the ionizing centre (OB stars), where the ionization parameter  $U^2$  is high and these kinds of high ionization states can be created, while the low- $U$  environment being away from the ionizing centre will make it difficult or impossible to ionize [O III]. Therefore, in this environment, lower ionization metals such as [S II] and [N II] become dominant, as they have lower ionization potential energy compared with the [O III] line. The H $\alpha$ /H $\beta$  has opposite trend in comparison with [O III]/H $\beta$  and shows lower values around 240'' to 250'' where H $\alpha$ /H $\beta$   $\sim 3$ . This suggests that the highly ionized region has also cleared most of the dust that affects the surrounding DIG.

The upper panel of Figure 3.20 represents the ratios of object A but with a different position angle. The ratios [S II]/H $\alpha$  and [N II]/H $\alpha$  behave in the same manner, but the [O III]/H $\beta$  shows approximately the same values in DIG and in the H II region. The H $\alpha$ /H $\beta$  ratio reaches 7 at 550'' and reduces to  $\sim 4$  on both sides of the object. It suggests that the slit position does not cross a region where O stars have caused particularly high ionization and cleared the dust.

The left-bottom panel in Figure 3.19 presents the velocity of the ionized gas, which was determined by adopting different emission lines. It is clear that the velocity of H $\beta$  has a remarkable offset from other lines, while [S II] and [N II] have nearly the

---

<sup>2</sup> $U$  represents the ratio of the density of ionizing photons to the density of the gas.

same velocity. [O III] and  $H\alpha$  show lower values from that of [S II] and [N II] by approximately  $15 \text{ km s}^{-1}$ . The left-bottom panel in Figure 3.20 shows the same but with a different long-slit position ( $PA = 44^\circ$ ), but no offset of  $H\beta$  is observed. I thus suspect that the offset seen at  $PA = 155^\circ$  is due to a calibration inaccuracy. The error bar on the [S II] velocity is high, as are some values for the [N II] velocity, because of the complicated shape of the line profile. Therefore, the estimated velocity may not be accurate for both [S II] and [N II] emission.

The mean value of all velocities (black solid line) is  $\sim -30$  to  $-35 \text{ km s}^{-1}$ . One of the plausible explanations for the velocity discrepancy between [O III], [S II], [N II] and Balmer lines is that the emission of each element needs a different environment to be created. In other words,  $O^{++}$  requires 35.1 eV (high temperature) to be ionized, while the [S II] and [N II] have lower ionizations potential energy ([S II] $\sim 23$  eV, [N II] $\sim 29$  eV). The neutral hydrogen needs photons with energies more than 13.6 eV to be ionized. Hence, each line emitted from different regions could show different kinematics. The dust ratio in these different environments could also affect the profile of the emission in different ways from one component to another one. But, the velocity difference between  $H\alpha$  and  $H\beta$  does not appear to change with  $H\alpha/H\beta$  ratio. Moreover, the Balmer profiles are highly complicated when it is compared with the [O III] line, and are commonly asymmetric, which could affect the determination of the velocity.

The right-bottom panel of Figure 3.19 shows the velocity dispersion from different emission lines. All these emission lines display the same velocity dispersion. The higher value of the mean velocity (black solid line) appears at  $255''$  to reach  $\sim 45 \text{ km s}^{-1}$ . The right-bottom panel of Figure 3.20 shows the velocity dispersion across A but with  $PA = 44^\circ$ . The mean value of velocity dispersion (black solid line) reaches  $\sim 45 \text{ km s}^{-1}$  at  $510''$ , while elsewhere it is between 30 and  $35 \text{ km s}^{-1}$ .

Interestingly, the area with low dust and high ionization around  $250''$  also presents high velocity dispersion compared with other positions. This may be the result of hotter gas, or an expanding bubble. likewise, around  $510''$  for  $PA = 44^\circ$ , the high velocity dispersion coincides with relatively strong [O III] and weak [S II] and [N II], adjacent to relatively dense gas. The [S II] doublet ratio around  $250''$  from  $PA = 155^\circ$  and  $510''$  from  $PA = 44^\circ$  shows lower values compared with elsewhere. As well as this, the velocity dispersion has a high value ( $\sigma \sim 45 \text{ \AA}$ ) around these two positions. This could be interpreted in terms of an expanding hot gas and relatively dense areas.

Previously, the velocity and velocity dispersion of A from FP observations were discussed and shown in Figure 3.8 (c, d, e & f). The velocity dispersion across A with  $PA = 44^\circ$  shows high values in the position that coincides with high ionization and high  $\sigma$ . For  $PA = 155^\circ$ , the velocity dispersion shows high velocities reaching  $210 \text{ km s}^{-1}$  in the position of suggested expanding hot gas and relatively dense areas.

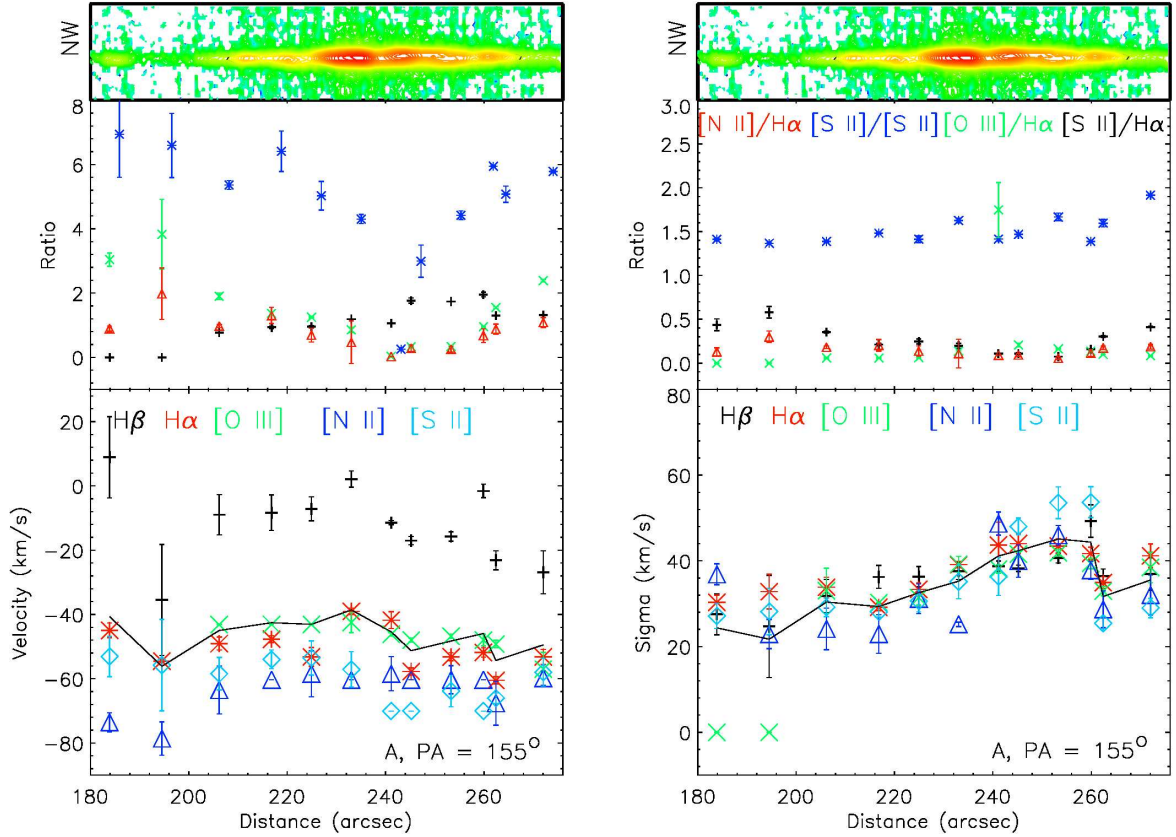


Figure 3.19: The top panels show the morphology of the H $\alpha$  emission line. Left-middle panel: ratios of H $\alpha$  (blue), [S II] $\lambda$ 6717+6731 (green), [N II] $\lambda$ 6583 (red) and [O III] $\lambda$ 5007 (black) to H $\beta$  along the slit through object A in NGC 300. Right-middle, ratios [N II]/H $\alpha$ , [S II]/[S II], [O III]/H $\alpha$  and [S II]/H $\alpha$ . The bottom panels represent velocity (left) and velocity dispersion (right), and the long-slit was oriented with PA= 155°. The solid line in the bottom panels represents the average value.

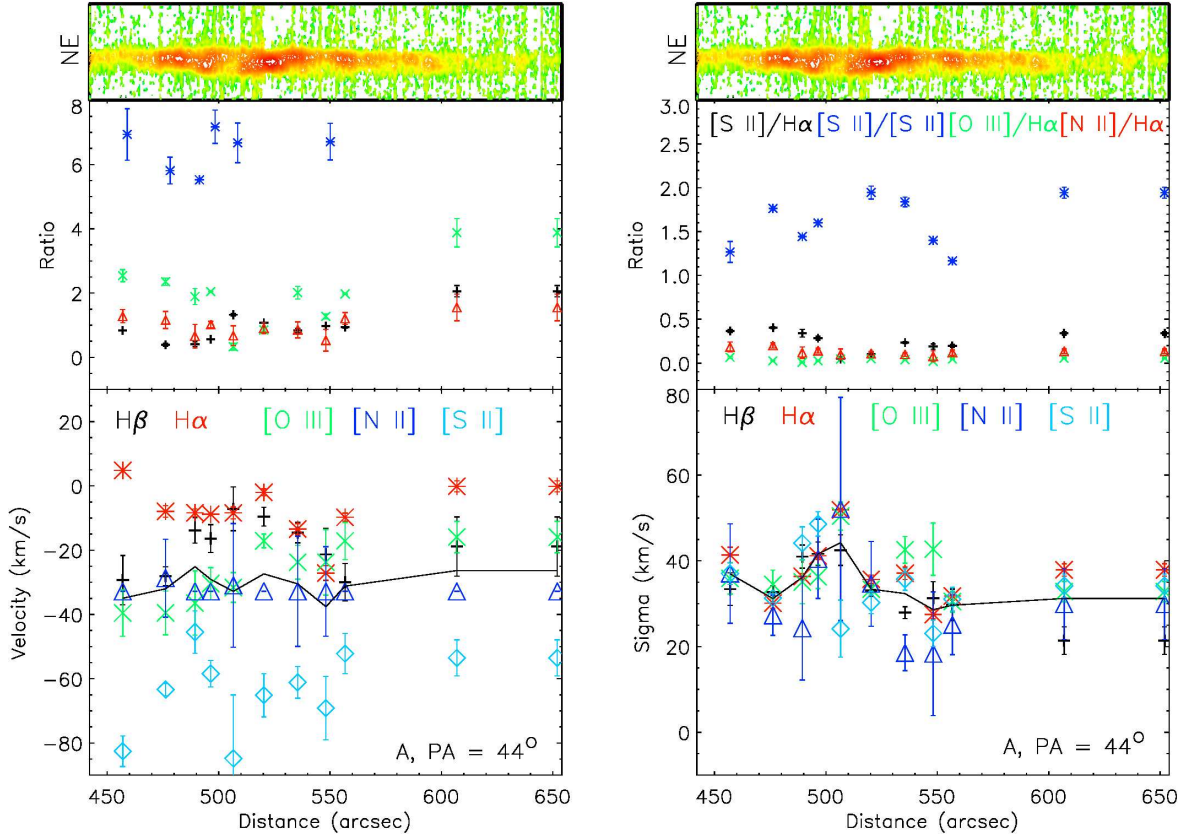


Figure 3.20: As Figure 3.19, but now the long-slit was oriented with  $PA = 44^\circ$ .

### 3.3.5 Photoionization modelling

Line ratios of the forbidden lines to the  $H\alpha$  line were examined in some local face-on galaxies, like M33, M51, and M81, by placing a slit across some H II regions. The observed features of these H II regions turned out to reflect different conditions when compared with the CLOUDY model (Sembach et al. 2000). In order to clarify the trend of the line ratios in H II regions, it is important to consider that there is no ideal H II region (a Strömgen sphere with uniform density). In other words, the filling factor would decide the fraction of ionized gas in the H II region, and this may differ for real H II regions (Osterbrock 1989).

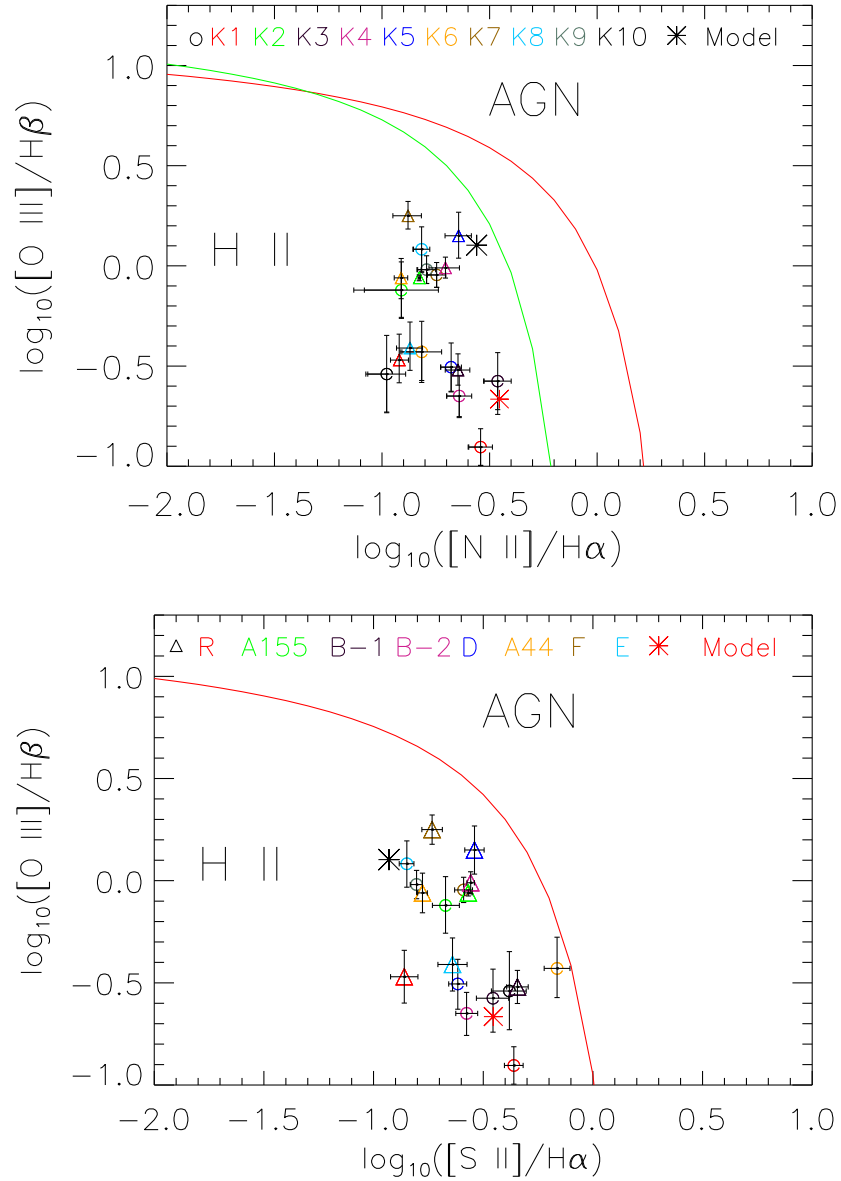


Figure 3.21: Distribution of 18 objects in diagnostic BPT diagrams compared to the predicted models (black and red asterisks). The red and green lines represent the Kewley (Kewley et al. 2001) and Kauffmann (Kauffmann et al. 2003) curves respectively. The triangle symbols represent the objects in the first FP field, and the circles represent the objects in the second FP field.

Most of the present day knowledge of H II regions is built on the comparison of models with observations. The photoionization code CLOUDY 13.02 (Ferland et al. 2013) has been applied in this study. A range of information about the nebula must be specified as input to run CLOUDY. This includes the shape and density of the continuum radiation from the ionizing source (central star) and the geometry, size, density, distance, and chemical composition of the nebula. The CLOUDY model has the ability to simulate emission lines in the nebula. Hence, different models were run to minimize the discrepancy between the observed emission line ratios and the predicted ratios from CLOUDY models. Relevant information about the CLOUDY model was introduced in section 2.4.

The best way to visualise a comparison of the line ratios of the objects is by using the diagnostic BPT diagram (Baldwin, Phillips & Terlevich 1981) (see Figure 3.21). Another important demarcation curve was introduced by Kauffmann et al. (2003) to distinguish between AGN and star-forming regions in the BPT diagram. However the area between these curves represents a combination of different ionization sources, and not one of the examined objects fall in this area. In this diagram, the 18 objects of interest can be categorized into two groups which are located to the left of the Kewley curve (Kewley et al. 2001). The diagrams in Figure 3.21 connect between two lines ratio where the wavelengths of these lines are closer to each other, therefore these ratios are insensitive to reddening. Group-1 shows high ratio of [O III]/H $\beta$  (high photoionized regions) and objects with a low ratio of [O III]/H $\beta$  (group-2) implying a less photoionized environment compared to group-1. Therefore, it would be more reliable to create two models that can cover the discrepancies in the line ratio of [O III]/H $\beta$ .

A blackbody spectrum with a temperature of 30 000 K was assumed for the ionizing stars. This can produce a luminosity  $\approx 10^{37}$  erg s $^{-1}$ . A distance of 1.8 Mpc and a filling factor of 1.0 were adopted, and a spherical geometry with an expanding shell was assumed. In other words, this option represents an expanding nebula where the shell expansion velocity prevents the diffuse line photons (which come from either side of the shell) from interacting with each other. The assumed hydrogen density was 100 cm $^{-3}$ . The elemental abundance and dust-to-gas ratio<sup>3</sup> were the same as seen in the Orion nebula (Rubin et al. 1991; Osterbrock, Tran & Veilleux 1992) (see Table 3.7). This model was found to be successful at creating some of the emission line ratios in the observed spectrum, such as [N II]6548,6583 and [S II]6716,6732, which have low ionization energy. However, the model cannot totally reproduce high ionization lines such as [O III]4959,5007.

The spectra of 35 PNe, and compact H II regions in NGC 300 display bright emission of [O III]4959,5007 compared with [N II]6548,6583 and [S II]6716,6732 in

---

<sup>3</sup>Dust-to-grain in Orion nebula  $\sim 4.15 \pm 0.01 \times 10^{-22}$  mag cm $^2$  (Chen et al. 2015)

Table 3.7: Abundance ratio in the Orion nebula (NGC 1976) and Sun.

Ratio	NGC 1976 (Osterbrock, Tran & Veilleux 1992)	Sun (Anders & Grevesse 1989)
N/O	$1.7 \times 10^{-1}$	$1.3 \times 10^{-1}$
Ne/O	$1.3 \times 10^{-1}$	$1.4 \times 10^{-1}$
Ar/O	$8.7 \times 10^{-3}$	$4.3 \times 10^{-3}$
Fe/O	$8.9 \times 10^{-3}$	$5.5 \times 10^{-2}$ (Chen et al. 2015)
Ni/O	$4.6 \times 10^{-4}$	$2.1 \times 10^{-3}$

both PNe and H II regions (Stasińska et al. 2013). Half of the objects (group-1) in this study show the same trends while the other half display a lower ratio of  $[\text{O III}]/\text{H}\beta$ . The H II complexes in question span a wide range of physical scales from few hundreds of parsecs to about 1 kpc, and display a wealth of kinematic complexity from FP and long-slit observations (on a scale of 9 pc/arcsec), meaning these areas are likely affected by leaking high-ionizing radiation from the combination of massive stars. Roughly 80% of the photons escape from the H II region according to hybrid models for H II regions by Morisset et al. (2016).

Bearing these points in mind, I need to increase the number of ionizing photons by increasing luminosity to  $\approx 10^{40}$  erg s $^{-1}$  for stars with  $T_{eff} \approx 40\,000$  K, and keep all the other parameters fixed. The model ratio of the  $[\text{O III}]$  emission lines is comparable to observed ratios. The low ionization lines  $[\text{N II}]$  have the same trend as  $[\text{O III}]$ , but  $[\text{S II}]$  lines have underestimated ratios.  $[\text{S II}]6717,6731$  forbidden lines are highly affected by electron density (Osterbrock & Ferland 2006), therefore a filling factor of 0.2 was introduced in the input CLOUDY model. This model can provide an acceptable representation of the spectrum for selected H II regions (group-1). This model is marked with a black asterisk symbol in Figure 3.21.

The second model was run with the same parameters but with lower temperatures (30 000 K) because group-2 shows lower intensity of high ionization lines: I expect lower temperatures of the ionizing stars. The model predicted  $[\text{O III}]$  lines but with low intensity, which is less than what appears in group-2. The filling factor was increased to 0.3 because the number of ionizing photons used was increased, so I suspected that the filling factor needed to be higher. The predicted ratios from the model (red asterisk symbol in Figure 3.21) show good agreement with the  $[\text{O III}]/\text{H}\beta$  and  $[\text{S II}]/\text{H}\alpha$  ratio while  $[\text{N II}]/\text{H}\alpha$  is slightly overestimated.

Intensities reproduced by the model are all relative to  $\text{H}\beta$ . The observed and reproduced intensities are shown in Table 3.8.

Figure 3.21 shows  $\log([\text{O III}]/\text{H}\beta)$  versus  $\log([\text{S II}]/\text{H}\alpha)$  and  $\log([\text{N II}]/\text{H}\alpha)$  di-

agnostic diagrams for objects of interest and the predicted models. In Figure 3.21 the model (black asterisks) is analogous to objects D, A155, A44, B-2, while object F shows a higher ratio of  $\log([\text{O III}]/\text{H}\beta)$  ( $\sim 0.16$ ) compared with others. However, it is still in the boundary of the H II regions area, and could be interpreted in terms of the effect of binary interaction in the centre of this object. Xiao, Stanway & Eldridge (2018) produced a numerical model of H II regions in spiral galaxies and compared with 254 H II regions of low redshift spiral galaxies. Two types of ionizing sources were adopted in these models: single stars and binary stars with various ages.  $[\text{N II}]$ ,  $[\text{S II}]$ ,  $[\text{O III}]$  and  $[\text{O I}]$  lines were strongly affected by binary interaction through the evolution of binary stars due to the appearance of hot Wolf–Rayet and helium stars in the later stages of evolution, when a high  $[\text{O III}]/\text{H}\beta$  ratio can be produced. Single-star models rapidly reduce ionization strength.

On the other hand, objects of group-2 could have a different environment with a low ionizing source, resulting in the lowest ratio of  $[\text{O III}]/\text{H}\beta$  compared with group-1, in particular F. In conclusion, four of these objects of group-1 (A155, A44, B-2 & D) display similar physical conditions to the black model, while the others have different conditions that can be related to the activity of the ionizing source (temperatures) and the local conditions.

The temperature of nebulae can be measured from emission lines, such as  $[\text{O III}]$  and  $[\text{N II}]$  (Osterbrock & Ferland 2006). The auroral lines  $[\text{O III}]4363$  and  $[\text{N II}]5755$  were undetected in my observations. Unfortunately,  $[\text{O III}]4363$  is weak and close to  $\text{H}\gamma 4358$ . The  $[\text{O III}]4363$  line was not reproduced in the model, so I adopted the relative intensity of  $[\text{N II}]5755/\text{H}\beta$  (0.01) from the CLOUDY model to estimate the temperature of the nebulae. From the ratio of  $[\text{S II}]6716/[\text{S II}]6732$  (see Table 3.5), the  $n_e$  can be estimated as  $1 \text{ cm}^{-3}$  in these objects. Osterbrock & Ferland (2006) introduced an equation to estimate the temperature of nebulae in the low density limit using  $[\text{N II}]$  lines, as follows:

$$\frac{I_{\lambda 6548} + I_{\lambda 6583}}{I_{\lambda 5755}} = \frac{7.35 \exp\left(\frac{2.50 \times 10^4}{T}\right)}{1 + 2.7 \times 10^{-3} \frac{n_e}{T^{1/2}}} \quad (3.2)$$

It is more accurate to use emission line ratios of the  $[\text{N II}]$  doublet relative to  $\text{H}\alpha$  to avoid any flux calibration and data reduction issues. So, I used  $[\text{N II}]6548/\text{H}\alpha$  and  $[\text{N II}]6583/\text{H}\alpha$  from my observations and used a predicted value of  $[\text{N II}]5755/\text{H}\alpha$  from the two models (Black and Red) to determine the temperatures of the objects of interest. Numerical methods were used to determine each object's temperature, and the results are shown in Table 3.8 for both models. These objects have temperatures between 6500 and 10 000 K. The error in the temperature was estimated from differences in the intensity of the  $[\text{N II}]6548$ ,  $6583$  lines between the observations and model.

The higher temperature of  $\sim 16\,200 \pm 1200$  K appears in K2, which falls within the group having a higher ratio of  $[\text{O III}]/\text{H}\beta$ . Meanwhile, a lower value appears in K3

( $\sim 7800 \pm 200$  K), which is in the group of lower  $[\text{O III}]/\text{H}\beta$  ratios. Most of the objects showing a lower photoionization environment have lower temperatures (excluding K10, R & E) while most higher photoionized objects display higher temperatures (excluding D).

Table 3.8: The estimated temperature and observed line ratios in 18 objects in NGC 300 and as predicted from the models.

Object	[O III] $\lambda$ 5007/H $\beta$	[N II] $\lambda$ 6548/H $\beta$	H $\alpha$ /H $\beta$	[N II] $\lambda$ 6584/H $\beta$	[S II] $\lambda$ 6716/H $\beta$	[S II] $\lambda$ 6732/H $\beta$	T (Black model) K	T (Red model) K
R	0.34 $\pm$ 0.01	0.32 $\pm$ 0.04	4.50 $\pm$ 0.03	0.98 $\pm$ 0.02	1.12 $\pm$ 0.10	0.64 $\pm$ 0.05	12400 $\pm$ 900	11400 $\pm$ 800
A44	0.88 $\pm$ 0.02	0.27 $\pm$ 0.08	5.00 $\pm$ 0.02	0.74 $\pm$ 0.01	0.81 $\pm$ 0.10	0.54 $\pm$ 0.01	11400 $\pm$ 700	10500 $\pm$ 600
B-1	0.30 $\pm$ 0.03	0.37 $\pm$ 0.01	4.48 $\pm$ 0.41	1.01 $\pm$ 0.03	1.21 $\pm$ 0.10	0.80 $\pm$ 0.01	9600 $\pm$ 300	8900 $\pm$ 300
B-2	0.97 $\pm$ 0.03	0.36 $\pm$ 0.01	5.43 $\pm$ 0.41	1.07 $\pm$ 0.05	0.88 $\pm$ 0.02	0.62 $\pm$ 0.02	10200 $\pm$ 500	9500 $\pm$ 400
D	1.43 $\pm$ 0.10	0.47 $\pm$ 0.01	6.10 $\pm$ 0.08	1.38 $\pm$ 0.11	1.07 $\pm$ 0.06	0.68 $\pm$ 0.04	9600 $\pm$ 400	9000 $\pm$ 300
E	0.39 $\pm$ 0.02	0.35 $\pm$ 0.01	6.20 $\pm$ 1.10	0.83 $\pm$ 0.15	0.89 $\pm$ 0.03	0.53 $\pm$ 0.01	12900 $\pm$ 1300	11800 $\pm$ 1100
A155	0.88 $\pm$ 0.03	0.17 $\pm$ 0.01	5.04 $\pm$ 0.08	0.62 $\pm$ 0.01	0.52 $\pm$ 0.01	0.32 $\pm$ 0.02	12500 $\pm$ 1300	11500 $\pm$ 1200
F	0.18 $\pm$ 0.01	1.80 $\pm$ 0.12	0.18 $\pm$ 0.04	5.16 $\pm$ 0.76	0.68 $\pm$ 0.02	0.57 $\pm$ 0.03	11700 $\pm$ 700	10800 $\pm$ 600
K1	0.12 $\pm$ 0.01	0.46 $\pm$ 0.11	6.61 $\pm$ 0.38	1.89 $\pm$ 0.03	1.71 $\pm$ 0.04	1.17 $\pm$ 0.02	9000 $\pm$ 400	8500 $\pm$ 400
K2	0.75 $\pm$ 0.02	0.89 $\pm$ 0.10	10.79 $\pm$ 0.72	1.33 $\pm$ 0.09	1.43 $\pm$ 0.15	0.86 $\pm$ 0.07	16200 $\pm$ 1200	14200 $\pm$ 1000
K3	0.26 $\pm$ 0.04	0.48 $\pm$ 0.08	4.18 $\pm$ 0.17	1.44 $\pm$ 0.01	0.85 $\pm$ 0.01	0.62 $\pm$ 0.06	8300 $\pm$ 200	7800 $\pm$ 200
K4	0.22 $\pm$ 0.01	0.33 $\pm$ 0.04	4.88 $\pm$ 0.14	1.11 $\pm$ 0.03	0.81 $\pm$ 0.02	0.48 $\pm$ 0.01	9700 $\pm$ 400	9100 $\pm$ 400
K5	0.31 $\pm$ 0.01	0.74 $\pm$ 0.06	11.04 $\pm$ 0.82	2.31 $\pm$ 0.12	1.67 $\pm$ 0.09	0.99 $\pm$ 0.04	10000 $\pm$ 500	9300 $\pm$ 400
K6	0.37 $\pm$ 0.02	1.07 $\pm$ 0.01	8.69 $\pm$ 0.95	1.32 $\pm$ 0.06	3.63 $\pm$ 0.40	2.32 $\pm$ 0.14	10000 $\pm$ 200	9300 $\pm$ 200
K7	0.90 $\pm$ 0.01	0.60 $\pm$ 0.04	8.621 $\pm$ 0.24	1.54 $\pm$ 0.02	1.35 $\pm$ 0.01	0.86 $\pm$ 0.01	10400 $\pm$ 500	9600 $\pm$ 400
K8	1.21 $\pm$ 0.02	0.76 $\pm$ 0.07	13.64 $\pm$ 1.34	2.08 $\pm$ 0.07	1.11 $\pm$ 0.04	0.82 $\pm$ 0.01	11300 $\pm$ 600	10400 $\pm$ 600
K9	0.95 $\pm$ 0.02	0.82 $\pm$ 0.16	12.84 $\pm$ 0.81	2.07 $\pm$ 0.02	1.31 $\pm$ 0.02	0.70 $\pm$ 0.02	12200 $\pm$ 2800	12000 $\pm$ 2700
K10	0.28 $\pm$ 0.01	0.41 $\pm$ 0.05	9.23 $\pm$ 1.27	0.97 $\pm$ 0.06	2.18 $\pm$ 0.15	1.66 $\pm$ 0.01	13300 $\pm$ 1000	12100 $\pm$ 900
CLOUDY model (black)	1.27	0.30	3.21	0.88	0.21	0.16		
CLOUDY model (red)	0.22	0.38	3.22	1.13	0.26	0.2		

### 3.3.6 Calculation of abundance from the ratios of emission lines

As mentioned before, the auroral lines [O III] $\lambda$ 4363 and [N II] $\lambda$ 5755 were undetected during the present work, so it was not possible to use the direct method of electron temperatures (Kewley & Ellison 2008) to determine oxygen abundance. However, the strong line methods can be used to calculate the oxygen abundance by employing two strong line diagnostics. Alloin et al. (1979) suggested this method to determine an  $O3N2$  index by the following formula:

$$O3N2 = \log \left( \frac{[\text{O III}]\lambda 5007}{\text{H}\beta} \times \frac{\text{H}\alpha}{[\text{N II}]\lambda 6583} \right) \quad (3.3)$$

There are different empirical calibrations for the diagnostic of  $O3N2$  in the literature, which involve adopting a large number of H II regions that have oxygen abundances determined by using the direct method. In this study the calibration by Marino et al. (2013) was used to determine  $O3N2$ , covering the  $O3N2$  index over the range of  $-1.1$  to  $1.7$ . The linear fitting of the calibration leads to:

$$12 + \log \left( \frac{\text{O}}{\text{H}} \right) = 8.533 - 0.214 \times O3N2 \quad (3.4)$$

The oxygen abundance can also be calculated by using the strong line diagnostic  $N2 = \log([\text{N II}]\lambda 6583/\text{H}\alpha)$  (Storchi-Bergmann, Calzetti & Kinney 1994; Denicoló, Terlevich & Terlevich 2002; Pérez-Montero & Contini 2009). The linear fitting, which is suggested by Marino et al. (2013), leads to a correlation between the  $N2$  index and oxygen abundance for  $N2$  values ranging from  $-1.6$  to  $-0.2$ , which is described by:

$$12 + \log \left( \frac{\text{O}}{\text{H}} \right) = 8.743 + 0.462 \times N2 \quad (3.5)$$

Another parameter,  $\log(\text{N}/\text{O})$  can be estimated from the calibration that was introduced by Pérez-Montero & Contini (2009):

$$\log \left( \frac{\text{N}}{\text{O}} \right) = 1.26 \times N2S2 - 0.86 \quad (3.6)$$

Where  $N2S2$  can be determined through  $\log([\text{N II}]\lambda 6583/[\text{S II}]\lambda 6716,6732)$ . The metallicities of the objects are shown in Table 3.9.

The two methods produce comparable values of  $12 + \log(\text{O}/\text{H})$ , as shown in Figure 3.22, which includes the line fit for the resulting values. The  $\chi^2$ -square test statistic  $\chi^2 = 0.011$  for the values from these two methods. However, it would be more accurate to use the second method (using  $N2$  index), which uses two lines in the same scan to avoid any observation or data reduction issues.

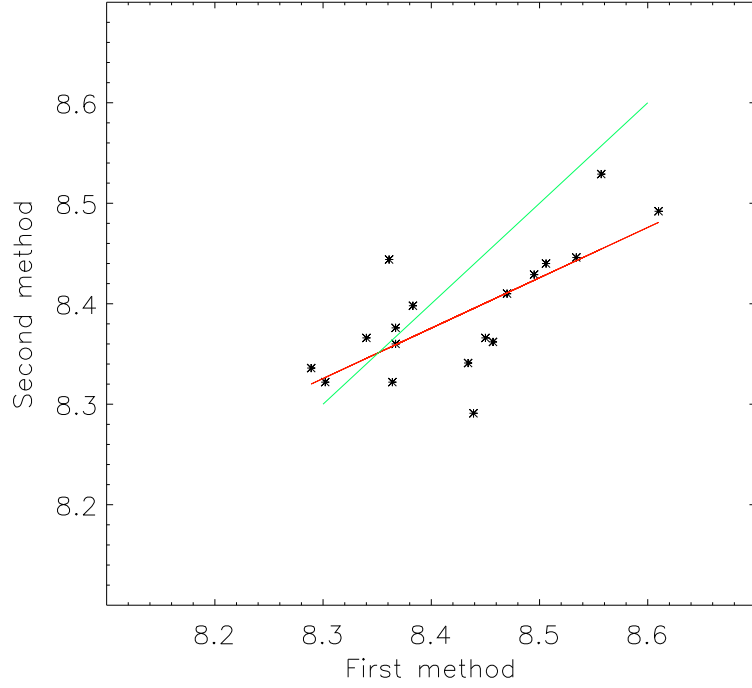


Figure 3.22: A comparison between the two methods used to determine the  $12+\log(\text{O}/\text{H})$ ; the red line is a linear fit to the results. The green line represents one-to-one correlation.

Table 3.9: The metallicities of the objects in NGC 300.

Object	O3N2	$12+\log(\text{O}/\text{H})$	N2	$12+\log(\text{O}/\text{H})$	N2S2	$\log(\text{N}/\text{O})$
A155	1.080	8.302	-0.911	8.322	-0.134	-1.028
A44	0.773	8.367	-0.827	8.360	-0.259	-1.187
B-1	0.773	8.470	-0.705	8.410	-0.148	-1.047
B-2	0.124	8.506	-0.647	8.440	-0.254	-1.180
D	0.800	8.361	-0.645	8.444	-0.102	-0.988
R	0.353	8.457	-0.823	8.362	-0.102	-1.180
F	1.135	8.289	-0.879	8.336	-0.146	-1.044
E	0.462	8.434	-0.873	8.341	-0.235	-1.156
K1	-0.362	8.610	-0.904	8.492	-0.181	-1.088
K2	0.788	8.364	-0.121	8.322	-0.238	-1.160
K3	-0.112	8.557	-0.575	8.529	-0.007	-0.868
K4	-0.008	8.534	-0.649	8.446	-0.065	-0.942
K5	0.173	8.495	-0.505	8.429	-0.062	-0.939
K6	0.385	8.450	-0.429	8.366	-0.652	-1.681
K7	0.700	8.383	-0.045	8.398	-0.156	-1.057
K8	0.898	8.340	0.083	8.366	0.033	-0.818
K9	0.773	8.367	-0.018	8.376	0.011	-0.845
K9	0.438	8.439	-0.539	8.291	-0.597	-1.613

The relation between the ratio of  $\log(\text{N}/\text{O})$  and the oxygen abundances in star forming regions has been a subject of intense observational and modelling studies (Vin-

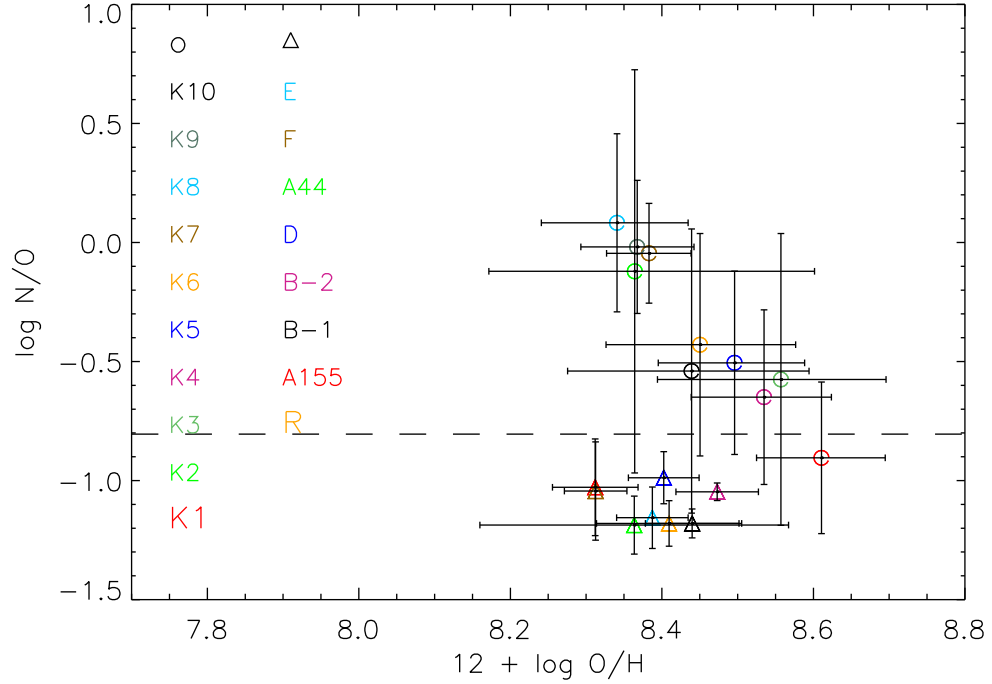


Figure 3.23: Trends of  $\log(N/O)$  with oxygen abundance. The black dashed line represents the solar values.

cenzo et al. 2016; Amorín, Pérez-Montero & Vílchez 2010; Köppen & Hensler 2005; Wolfire, Hollenbach & McKee 2010). Stars with H and He can produce nitrogen as a primary origin while nitrogen already present in stars having metals besides H and He is of secondary origin. This relation can be used to trace the origin of nitrogen in different metallicity systems. Izotov & Thuan (1999) introduced theories for production of nitrogen in three metallicity ranges (low, intermediate, high metallicities). The primary origin of nitrogen in low metallicity systems ( $12+\log(O/H) < 7.6$ ) is thought to come from massive stars only. In the intermediate metallicity ranges ( $7.6 < 12+\log(O/H) < 8.3$ ), the nitrogen is primarily produced by massive and intermediate-mass stars<sup>4</sup>. But in high metallicity ranges ( $12+\log(O/H) > 8.3$ ), the origin of the nitrogen is thought to be secondary.

I have examined the relation between the ratio of  $\log(N/O)$  and the oxygen abundance for the 18 H II regions in NGC 300. All objects of interest show values of  $12+\log(O/H)$  higher than 8.3, which fall in the high metallicity range (Izotov & Thuan 1999). The values of  $\log(N/O)$  are consistent with those determined by Stasińska

<sup>4</sup>Through hydrogen burning via the CNO cycle.

et al. (2013). For high metallicity H II regions in the Milky Way ( $12+\log(\text{O}/\text{H}) > 8.3$ ),  $\log(\text{N}/\text{O})$  rises linearly with  $\log(\text{O}/\text{H})$ , referring to that, in this metallicity system, N is primarily a secondary production (Henry & Worthey 1999). In the sample of interest in NGC 300 the trend of  $\log(\text{N}/\text{O})$  is not clear, but with increasing the sample of the study it may become clearer. However, an average of  $\log(\text{N}/\text{O})$  of the selected H II regions is about solar value, therefore I conclude that what happens in the disc of the Milky Way are also happening in the disc of NGC 300.

It can be noticed that the sample of the objects cluster in two groups with the same oxygen abundance, but with a high ratio of  $\log(\text{N}/\text{O})$  in the first group and about solar value in the second group. A few scattered objects with an intermediate value of  $\log(\text{N}/\text{O})$  also appear in the plot. A part of the first group falls in the second field of FP observation and all of the second group fall in the first field. This would suggest issues with the measurements, however only four objects from the second field show high  $\log(\text{N}/\text{O})$  while six objects show values which are comparable to the solar value. Perhaps different types of H II regions (physical properties, ages and morphological structures) were selected in the two different fields.

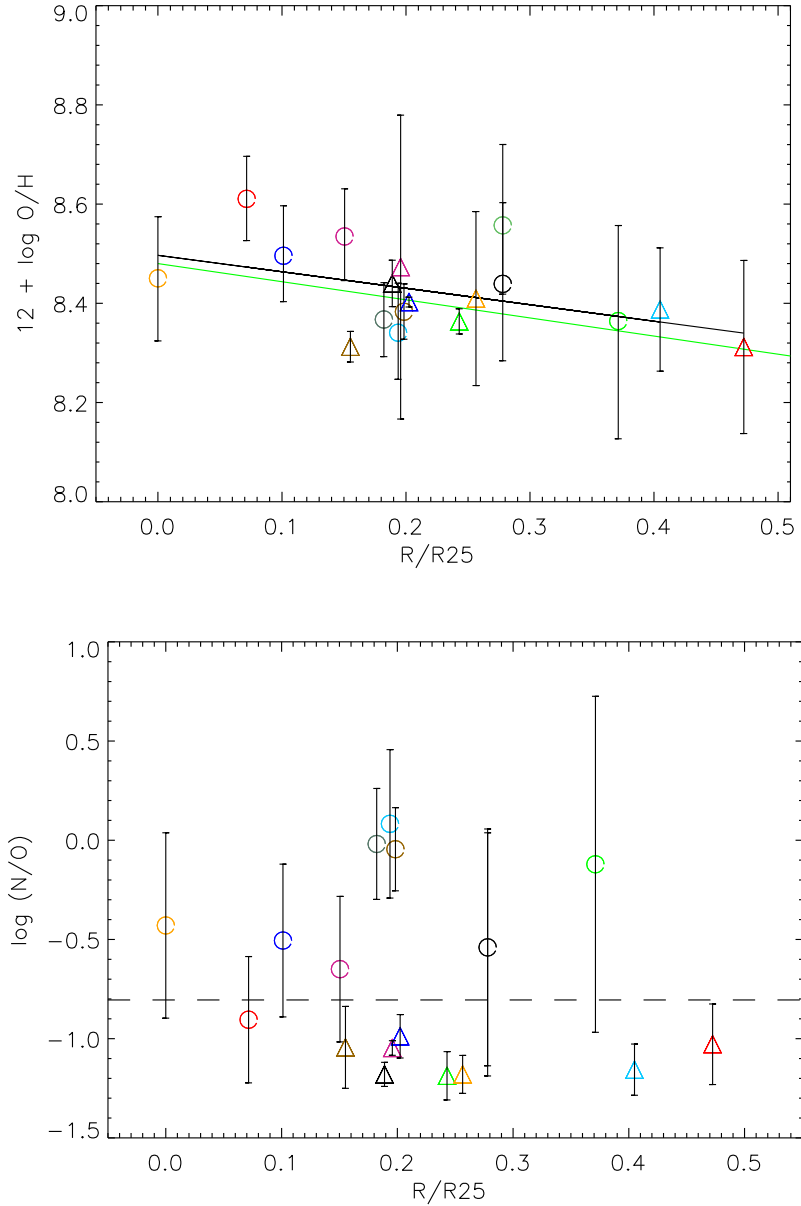


Figure 3.24: Upper panel: Observed trends of oxygen abundance as a function of the normalized galactocentric radius ( $R/R_{25}$ ). The continuous green line represents the linear fitting of the H II regions sample from Stasińska et al. (2013), and the black line shows the linear fitting of the sample of interest. Lower panel: Trends of  $\log(N/O)$  with the normalized galactocentric radius ( $R/R_{25}$ ). The black dashed line represents the solar values. The labels are as in Figure 3.23.

The first group includes K2, K7, K8, and K9, which display a high velocity

dispersion ( $\sim 350 \text{ km s}^{-1}$ ) (see Figure 3.6) compared to the second group (E, F, A44, D, B-2, B-1, A155, R) (see Figure 3.4) which displays a velocity dispersion less than  $120 \text{ km s}^{-1}$ , excluding D which has high velocity dispersion  $\sim 600 \text{ km s}^{-1}$ . The two groups show similar ratios of  $[\text{O III}]/\text{H}\beta$ , 0.3–0.9 (excluding K8 and D  $\sim 1.3$ ), while the mean value of  $[\text{N II}]/\text{H}\alpha$  (0.14) appears to be not very different compared to the second group (0.17). This could indicate that the high N abundance is somehow related to the local impact of the outflows (winds). The first group is thought to either be experiencing outflow (winds) from massive stars ( $M > 8M_{\odot}$ ) such as Wolf–Rayet stars with overabundances of nitrogen, or the group is embedded with supernova remnants or PNe, as PNe show higher N/O than H II regions, as seen in a number of galaxies: Milky Way (Henry, Kwitter & Bates 2000), Magellanic Clouds (Leisy & Dennefeld 2006), M33 (Bresolin et al. 2010).

The trend that  $\log(\text{N/O})$  displays with respect to metallicity is not clear. K2, K7, K8, B-1, B-2 and D show higher ratios compared to the others, and they show strong ionized outflows in FP observation (see Figure 3.4) with high velocity dispersion. Therefore, I expect the enhanced ratio could be a result of local chemical pollution, which is due to the impact of stellar winds from massive stars, in particular Wolf–Rayet stars. The latter are very common in these areas (see Figure 3.11).

Bresolin et al. (2009b) did not find the value of  $\log(\text{N/O})$  to be more than the solar value in a sample of 28 H II regions covering a radius of  $\sim R_{25}$  in NGC 300. Stasińska et al. (2013) analyzed 35 objects (H II regions and PNe in NGC 300): in H II regions  $\log(\text{N/O})$  is no more than  $-0.3$ , while in PNe it can reach 0.5.

The most noticeable heavy element that was observed in the optical window is oxygen. Therefore, it is used to approximate the total metallicity. The oxygen abundance ratio was used as a function of the fractional galactocentric distance  $R/R_{25}$ <sup>5</sup> (Vila-Costas & Edmunds 1992a) after correcting for the inclination effect. The upper panel of Figure 3.24 shows the metallicity (oxygen abundances) as a function of the fractional galactocentric distance for my sample.

The oxygen abundances ( $12+\log(\text{O/H})$ ) of the 18 H II regions in NGC 300 are in good agreement with those of giant H II regions in the samples studied by Stasińska et al. (2013). Values of the oxygen abundances in the examined H II regions are in the range of 8.3–8.6 across distances of  $(0.2-0.5)R_{25}$  with a mean value of  $8.41 \pm 0.08$ . Three of the H II regions (K1, K3 & K4) show oxygen abundances above the fitted line<sup>6</sup> of Stasińska et al. (2013), 14 of them (A155, A44, B-1, B-2, R, F, E, K2, K4, K5, K6, K7, K8, K9, K10) successfully follow the fit, and D is below the line. The standard deviation of the differences between the values of  $12+\log(\text{O/H})$  in my sample

---

<sup>5</sup>The isophotal radius is the radius of the galaxy at which the surface brightness falls to 25 B–mag  $\text{arcsec}^{-2}$  ( $R_{25}$  of NGC 300  $\sim 5.4$  (Westmeier, Braun & Koribalski 2011)).

<sup>6</sup>The fitted line is represented by this equation:  $y = A + B \times (R/R_{25})$ ,  $A = 8.480 \pm 0.034$  and  $B = -0.361 \pm 0.049$ .

of H II regions and the fitted line is 0.075. The black solid line in the upper panel of Figure 3.23 represents the linear fitting ( $A= 8.496$ ,  $B= -0.332$ ) from the 18 objects of interest, which shows a negative gradient, and is consistent with the green fit from Stasińska et al. (2013). In the fitting process, I take into account the error on the abundance ratio, and discard the uncertainties in the radial distance.

The radial distribution of nitrogen abundance as a function of the normalized galactocentric radius is shown in Figure 3.24. There is no clear trend for the behaviour of  $\log(N/O)$  with respect to the radius; a negative trend has been seen in NGC 300 with different H II regions (Bresolin et al. 2009b; Stasińska et al. 2013).

Star forming regions in dwarf galaxies show an anti-correlation between the metallicity and the star formation rate. This anti-correlation is thought to appear in star formation regions that are fuelled by external low metallicity gas, or which, through stellar winds and SNe, transport most of the heavy elements out of the regions (Sánchez Almeida et al. 2018). The star formation rate in H II regions can be expressed in terms of the intensity of  $H\alpha$  emission, and the index N2 ( $\log([N II]/H\alpha)$ ) can reflect the metallicity of these regions. Figure 3.25 shows the correlation between the index N2 and the normalized  $H\alpha$  intensity (the normalized values were determined by dividing the values of  $H\alpha$  intensity by the maximum value of  $H\alpha$  intensity). Figure 3.25 does not show a clear anti-correlation, though there is a hint of a trend in the same sense as the model (linear fit)<sup>7</sup>. Three areas (R, E & K2) show a high deviation from the model. They show lower metallicity compared to the others, although they fall in the expected range of  $H\alpha$  intensity. The estimated mean value coincides with the value measured at  $0.4 \times R_{25}$  (8.41) in a spectrophotometric study of 28 H II regions up to  $R_{25}$  (Bresolin et al. 2009b). Six of these H II regions are included in this study (K2, K4, K7, K8, K9 & K10). The H II regions in the sample of the study are in the high metallicity regime ( $12+\log(O/H) > 8.3$ ), and their values range from 8.30–8.61, which is comparable to the oxygen abundance near the Sun of  $12 + \log(O/H) = 8.54 \pm 0.02$  (Oliveira et al. 2005). The negative gradient is common in spiral galaxies, such as M33, M101, and M51 (Vila-Costas & Edmunds 1992b; Searle 1971; Shields 1974) and is qualitatively comparable to the one in the Milky Way (Shaver et al. 1983; Afflerbach, Churchwell & Werner 1997). The gradient of the oxygen abundance inferred in this study is  $-0.033 \pm 0.015$  dex  $kpc^{-1}$ . M31 is the largest nearby spiral galaxy showing negative trends (slope =  $-0.023 \pm 0.002$  dex  $kpc^{-1}$ ), which is shallower than that of NGC 300, and has a range in metallicity of 8.71–8.91 (Zurita & Bresolin 2012). Meanwhile the Milky Way oxygen abundance gradient is  $-0.06 \pm 0.01$  and  $12+\log(O/H) = 8.67 \pm 0.04$ .

---

<sup>7</sup>The fitted line is represented by this equation:  $y = A + B \times \log_{10}(\text{normalized } H\alpha \text{ intensity})$ .

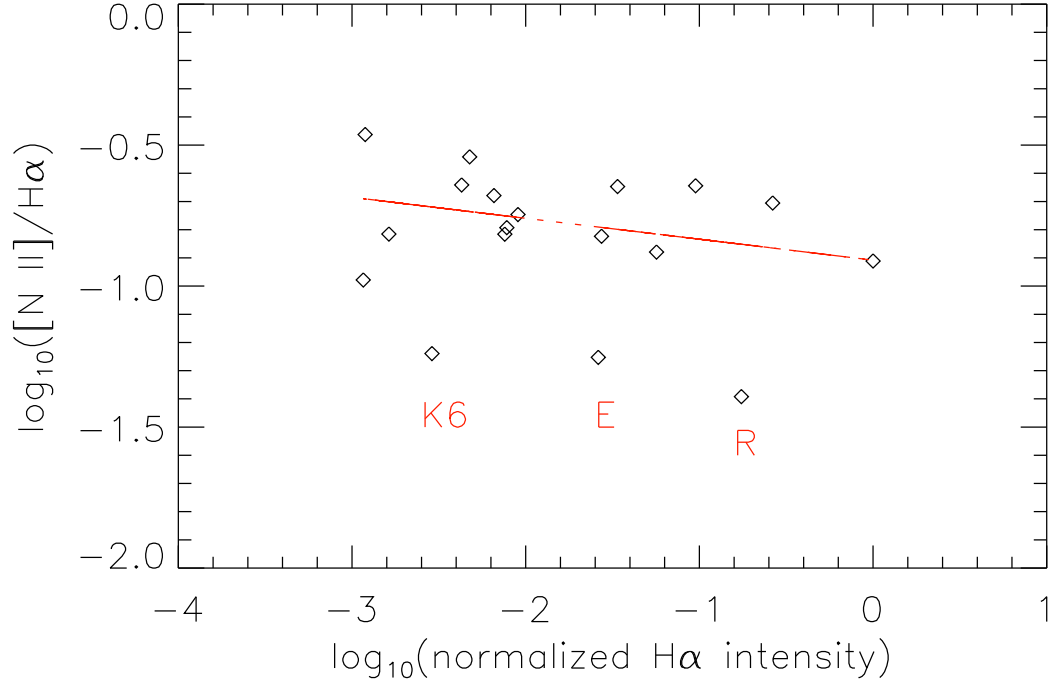


Figure 3.25: The relation between the intensity of H $\alpha$  and the index N2 ( $\log([N II]/H\alpha)$ ). The red line represents the fitted model.

### 3.3.7 The centre of NGC 300

The observed spectrum of NGC 300 centre is shown in Figure 3.26, and the observed emission lines are marked. Only 8 lines were found in the spectra. There is no split in the emission lines of the centre. It shows oxygen abundance higher than solar value, and shows  $\sim$  the mean value of the oxygen abundance of the 18 H II regions. In the BPT diagram Figure 3.21, K6 positions area with low  $[O III]/H\beta$  (see upper panel of Figure 3.21 which suggests a low photonization area, but shows a higher ratio of  $[S II]/H\alpha$  compared to other objects of interest. It would suggest that shocks in this area play more important role to enhance forbidden to recombination emission.

## 3.4 Conclusions

An analysis of 18 H II regions in terms of line ratios and abundances, as well as kinematics of the ionized outflowing gas has been presented, based on optical Fabry-Pérot and

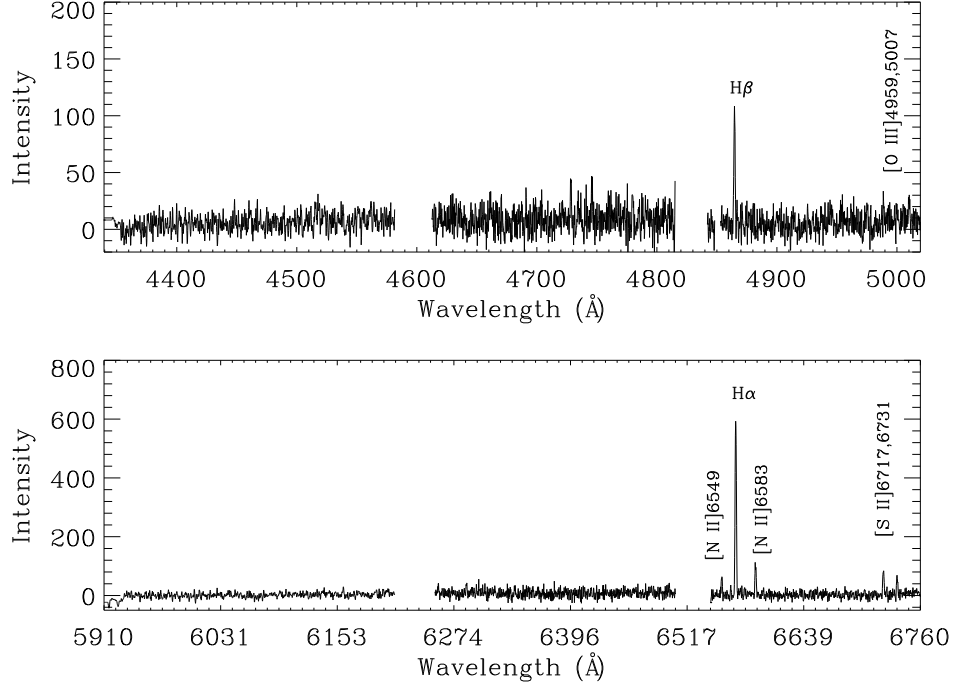


Figure 3.26: The upper panel displays the blue side and the bottom one shows the red side of the spectra of the centre of NGC 300. The observed lines are marked. The spectra was extracted from LS3.

long-slit observations with the instrument RSS@SALT. The aim of this chapter was to study the disc–halo interaction by quantifying the impact of the ionized outflows in face-on galaxies on the surrounding ISM.

Morphological and kinematical maps of two fields of view across NGC 300 were constructed with  $H\alpha$  and  $H\beta$  observations, to trace ionized outflows from some selected H II regions. The average velocity of the ionized outflowing gas from these areas was estimated to be  $\sim -200 \text{ km s}^{-1}$ , and the velocity dispersion shows a wide range of values (100–700  $\text{km s}^{-1}$ ). The high values of velocity dispersion are evidence of the presence of shock-heated collisions between the outflows and surrounding ISM. In some positions across object B, a double-peaked profile is traced, revealing two components with different velocities:  $-13 \text{ km s}^{-1}$  and  $306 \text{ km s}^{-1}$  with high velocity dispersion ( $\sim \text{km s}^{-1}$ ). Different filaments and shells, which relate to H II regions, are clear in  $H\alpha$  and  $H\beta$  emission.

The current chemical abundances across the observed fields, in particular in the selected H II regions, have been determined. They show a readily negative gradient w.r.t. the centre.

The physical properties across the selected H II regions were examined and showed in diagnostic PBT diagram. The photoionization model (CLOUDY) was used to estimate regions in order to compare their physical properties with the selected regions from the observations. Each model explains half of the sample of H II regions. The Temperature of these H II regions was estimated by using [N II] emission lines from observation and models, and show values between 7800 and 1600 K.

From the previous results, I can conclude that the impact of the ionized outflowing gas onto the surroundings plays an important role in the evolution of spiral galaxies in different ways: re-shaping the surrounding ISM by forming knots, filaments and shells that introduce a mechanism by which gas is recycled between the disc and halo in galaxies showing high SFR. These outflows change the metallicity of the ambient ISM by providing heavy elements. The ionized outflows compress and shock the ambient ISM, which may trigger new SF events or may quench current SF.

## Chapter 4

# The kinematics of the gas surrounding the active nucleus of NGC 4945

### 4.1 Introduction

Galactic winds (GWs) driven by an amalgamation of stellar winds from massive stars in the starburst and/or AGN have been suggested as an operating mechanism in the formation and evolution of galaxies. Galactic winds may enrich the surrounding ISM with metals, as well as re-shape the gas and dust distribution in the host galaxy. Edge-on galaxies are ideal objects to investigate the outflowing gas (GWs) from the nucleus of the galaxy. NGC 4945, a nearby spiral galaxy, shows an ejected cone from the nucleus which displays both the properties of starbursts and weak AGN. The partially obscured nucleus and its surroundings make NGC 4945 a more challenging object to investigate, particularly its outflows in the optical range. Furthermore, few studies have been carried out in the optical range to study the physical conditions and kinematics of the emerged material from the starburst and/or AGN to the North-West of this galaxy. Therefore, this ionized cone needs additional optical observations to uncover more physical, morphological, and kinematic properties. In this study, the GWs from the central area of NGC 4945 were observed by using Fabry-Pérot (LR) and the long-slit spectroscopy modes to quantify the mass of the ionized outflows and construct kinematic maps, as well as to investigate the impact of the GWs in re-shaping the surrounding ISM. Figure 4.1 shows the summary of the observations that were analyzed in this chapter.

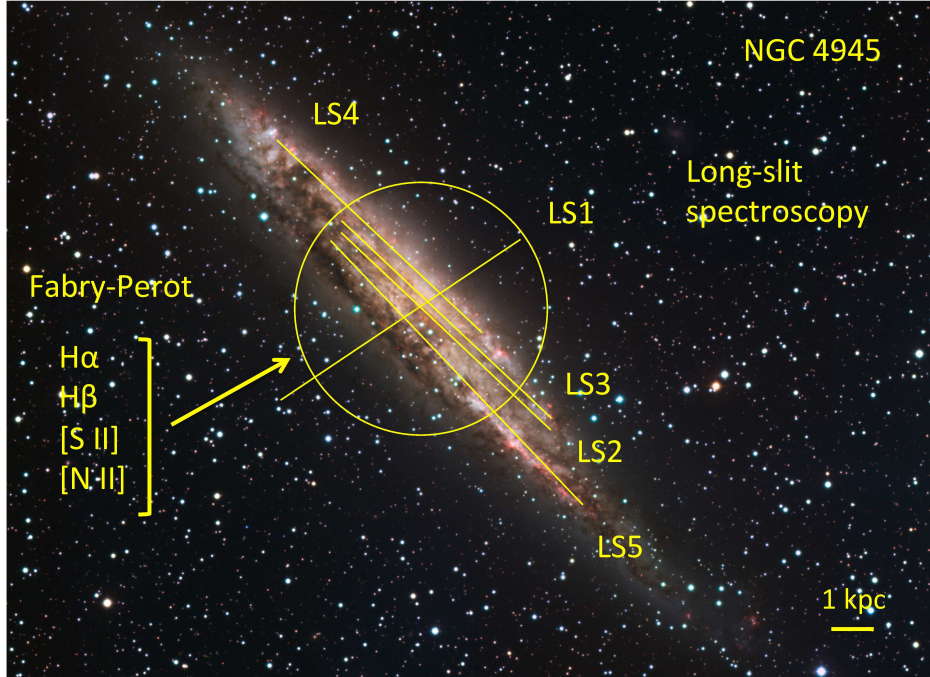


Figure 4.1: An image of NGC 4945 illustrating the summary of observations used in this chapter. The FP field is located at (RA:  $13^h 27^m 30^s.0$ , Dec:  $-49^\circ 28' 4''.5$ ). Four long-slit positions are labelled LS1, LS2, LS3 and LS4. The base image is a combination of images taken in five bands (B, V, R,  $H\alpha$  and [S II]) with the 2.2-metre MPG/ESO telescope at La Silla. <http://www.eso.org/public/images/eso0931a/>.

## 4.2 Observations

The RSS (Robert Stobie Spectrograph) Fabry-Pérot single etalon was used to detect different emission lines. On the night of 10<sup>th</sup> January 2018, the  $H\alpha$  was measured from the area around the nucleus of NGC 4945. The field was located at RA:  $13^h 05^m 27^s.30$  and Dec:  $-49^\circ 28' 4''.5$  and covered  $8'$ . The low-resolution ( $R \sim 700$ ) of the imaging spectroscopic mode was chosen to cover a spectral region of  $6548\text{--}6600 \text{ \AA}$  in equally spaced  $4 \text{ \AA}$  steps. This range was chosen after the speed of NGC 4945 ( $563.7 \text{ km s}^{-1}$ ) was taken into account, with an integration time of 169 seconds for each step. The total time of the observations including integration, readout, and acquisition time was 3723 seconds. The CCD detector provided an image scale of  $0''.5068 \text{ pixel}^{-1}$  after a binning by 4.

The data reduction of the FP instrument was discussed in detail in Chapter 1.5. The H $\alpha$  datacube was reduced using the previous procedure and the produced mean square residual for the wavelength solution ( $\lambda_{rms}$ ) was 0.329 Å, which is equivalent to 15 km s<sup>-1</sup>. The [S II] forbidden emission line from the centre was observed on 15<sup>th</sup> April 2016, for the same field of view. A low resolution of R~700 was used. We chose a spectral range of 6720–6753 Å after taking into account the velocity of the object. Twelve steps were used to cover the adopted range, and the exposure time of each step was 90.2 seconds. The total observation took 3365 seconds including the exposure of two cycles, readout, and acquisition time. Unfortunately, [S II] observations were done in bad weather and the flux calibration and scaling process was not sufficient to produce clear features of the [S II] profiles. In other words, it was impossible to avoid the negative impact of the cloudy weather. Therefore, this part of the observation has been re-proposed again to SALT, but in the period of observation for NGC 4945 the use of FP (LR) was stopped due to technical issues. Hence, these observations will not reveal any kinematical information, or give a line ratio map but will be limited to morphological information.

The red line of [N II]6583 was observed on 23<sup>rd</sup> February 2017 from the nucleus of NGC 4945, with low resolution (R~700). The centre of the field was located at RA = 13<sup>h</sup> 05<sup>m</sup> 27<sup>s</sup>.30 and Dec = -49° 28' 04".0. The covered range was 6584–6620 Å, in equally spaced 4 Å steps. The exposure time for each step was 90 seconds. The total observation time was 1612 seconds including one cycle, readout, and acquisition time. The H $\beta$  emission was observed from the central area and surroundings with low resolution (R~700). The covered range was 4857–4886 Å with six steps, each one with exposure time 95.2 seconds, and the total observation time was 1238 seconds. The H $\beta$  observation did not reveal any kinematics because of the limited exposure time, which did not provide sufficient signal. Therefore, only the distribution of H $\beta$  will be discussed in this chapter. The observation details are summarized in Tables 4.1 & 4.2.

Table 4.1: The main parameters of NGC 4945 observations with Fabry-Pérot mode (LR).

The emission line	H $\alpha$		[S II]		[N II]		H $\beta$
Date of observation	10 <sup>th</sup>	January 2018	15 <sup>th</sup>	April 2016	6 <sup>th</sup>	June 2016	24 <sup>th</sup> February 2017
Telescope	SALT		SALT		SALT		SALT
Instrument	RSS		RSS		RSS		RSS
Detector	E2V CCD 44-82 chips		E2V CCD 44-82 chips		E2V CCD 44-82 chips		E2V CCD 44-82 chips
Mode	Fabry-Pérot		Fabry-Pérot		Fabry-Pérot		Fabry-Pérot
Étalon separation	0.6 nm		0.6 nm		0.6 nm		0.6 nm
Resolving power	700		700		700		700
Free spectral range Å	8.64		8.64		8.64		8.64
Range Å	6548–6600		6720–6753		6540–6588		4857–4886
Filter	PI06530		PI06765		PI06645		PI04820
Steps	14		12		10		6
Exposure time seconds/step	169		90.2		90		95.2
Pixel scale	0'' 5068		0'' 5068		0'' 5068		0'' 5068
Seeing	~2''		~2''		~2''		~2''

Table 4.2: Étalon configuration wavelengths for the Fabry-Pérot H $\alpha$ , H $\beta$ , [N II], and [S II] observations of NGC 4945.

no.	H $\alpha$	H $\beta$	[N II]	[S II]
	LR	LR	LR	LR
1	6548	4857	6584	6720
2	6552	4866	6588	6723
3	6556	4870	6592	6726
4	6560	4872	6596	6729
5	6564	4876	6600	6732
6	6568	4886	6604	6735
7	6572		6608	6738
8	6576		6612	6741
9	6580		6616	6744
10	6584		6620	6747
11	6588			6750
12	6592			6753
13	6596			
14	6600			

### 4.3 Flux calibration for Fabry-Pérot observations

The normalization step of the FP data reduction was done by using stellar photometry for one standard image (scan). Vizier and Aladin were used to identify a few stars, as calibrators, which have accurate BVRI photometry. The aperture photometry of these selected stars was determined from the standard image to find the net counts (NC). In the adopted FP image, the calibrator star is LTT2415.

From Hamuy et al. (1994) and Hamuy et al. (1992), the spectrophotometric standard stars have colours similar to that of the chosen stars. The next step is to calculate the spectral flux density ( $f_\nu$ ) from:

$$M_{AB} = -2 \log f_\nu - 48.59 \quad (4.1)$$

$M_{AB}$  = the monochromatic AB magnitude in units of  $\text{erg s}^{-1} \text{Hz}^{-1} \text{cm}^{-2}$ .  
It can be expressed in terms of flux per unit wavelength  $f_\lambda$ .

$$f_{\lambda} = f_{\nu} \frac{c}{\lambda^2} \quad (4.2)$$

and then using the R magnitude difference to calculate  $f_{\lambda}$  for the chosen star in the FP image.

The FP line profile was approximated as a Lorentzian, and its FWHM was calculated from the calibration arc image. The equivalent width of the Lorentzian profile was determined by the following equation:

$$eqw = \pi \frac{FWHM}{2} \quad (4.3)$$

To find the total equivalent width ( $eqw_{tot}$ ) of the passbands of the FP which passed through the filter it was needed to take into account the transmission of each passband ( $t_i$ ) and the transmission of the passband at the FP wavelength ( $t_o$ ), as follows:

$$n_{eff} = \frac{\sum t_i}{t_o} \quad (4.4)$$

So the  $eqw_{tot}$  is given by:

$$eqw_{tot} = n_{eff} \times eqw \quad (4.5)$$

Then the total flux of the star can be calculated by:

$$f_{tot} = eqw_{tot} \times f_{\lambda} \quad (4.6)$$

Finally, the flux calibration of the FP image can be determined by multiplying the FP image by  $f_{\lambda}$  and dividing by NC.

## 4.4 Results of Fabry-Pérot observations

The distribution of the total intensity (continuum plus  $H\alpha$  emission) around the nucleus of NGC 4945 ( $8'$ ), is presented in Figure 4.2. The total intensity was obtained by integrating all intensities along the wavelength axis of the cube. Bright emission is seen near to the nucleus, in the form of a cone structure. A few filaments and other sub-structures related to the cone are also noticed. In order to examine the morphology of these structures, the integrated intensity map was zoomed in and shown in panel (b) of Figure 4.2. The same procedure was done for the  $[N II]$  cube and shown in panel (d) of Figure 4.2. The integrated intensity of  $[S II]$  and  $H\beta$  emission were mapped too, and are shown in Figure 4.3; the central area was zoomed in and shown in panels (c) and (d) for the  $[S II]$  and  $H\beta$  lines respectively. Prominent spots with high intensity spread across the field of view represent foreground stars. The white stripes in panels (a, b) in Figures 4.2 and 4.3 represent CCD gaps, and the white area represents a guiding probe. The white patch near the middle in Figure 4.2 (c) appears after sky lines subtraction was done as part of the data reduction process. I expect that the sky line fit is overestimated in this area, resulting in the subtraction of some real emission of the galaxy.

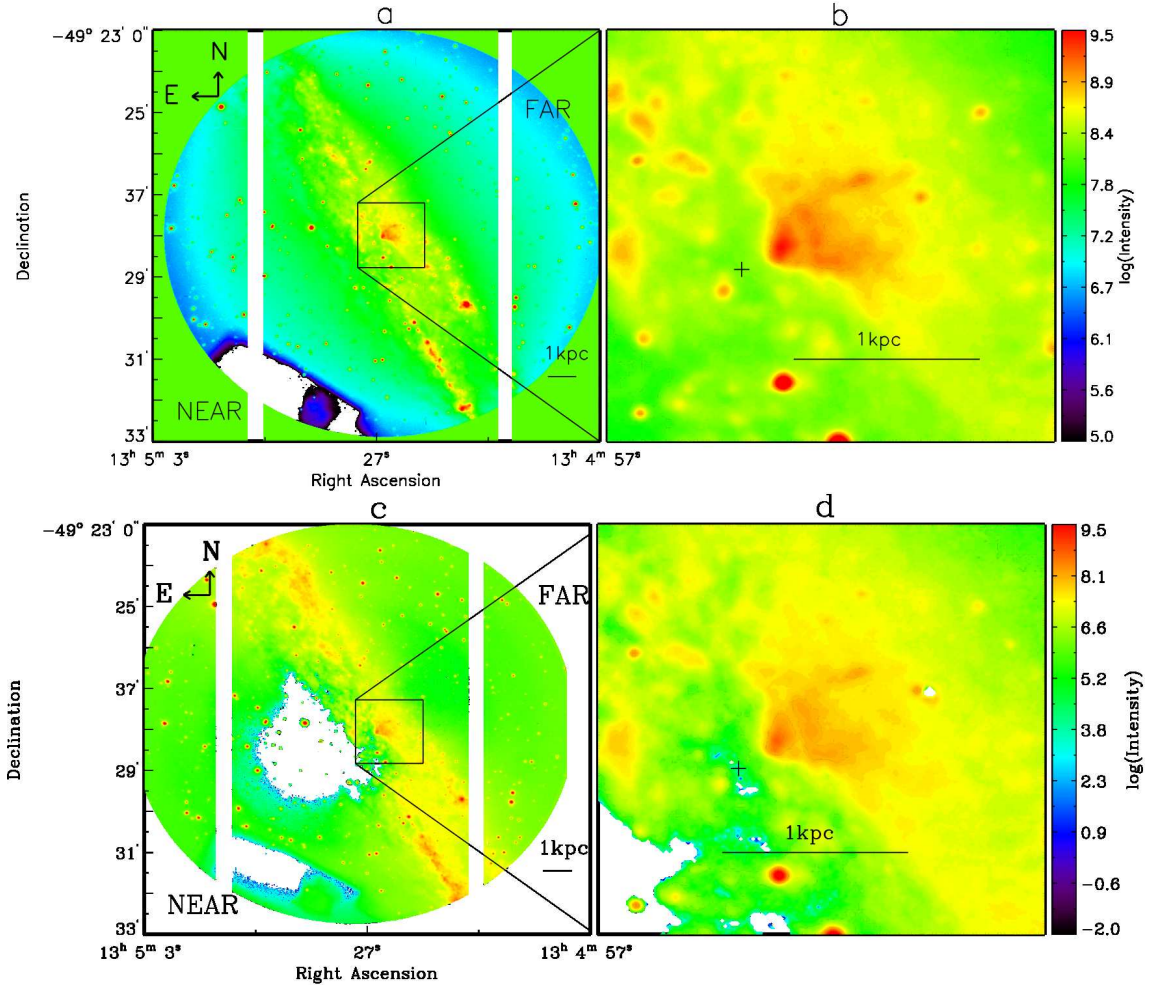


Figure 4.2: Total intensity maps of the observed field (RA:  $13^{\text{h}} 05^{\text{m}} 27^{\text{s}}30$  and Dec:  $-49^{\circ} 28' 04''.5$ ) in NGC 4945, showing H $\alpha$  (upper panels). Lower panels show the intensity maps of [N II]6583. The centre of the galaxy is marked with a black cross symbol in panels (b) and (d), and the intensity is in arbitrary units. The North and East of the galaxy are marked to the top left corner in (a) and (c), and the black bar represents 1 kpc.

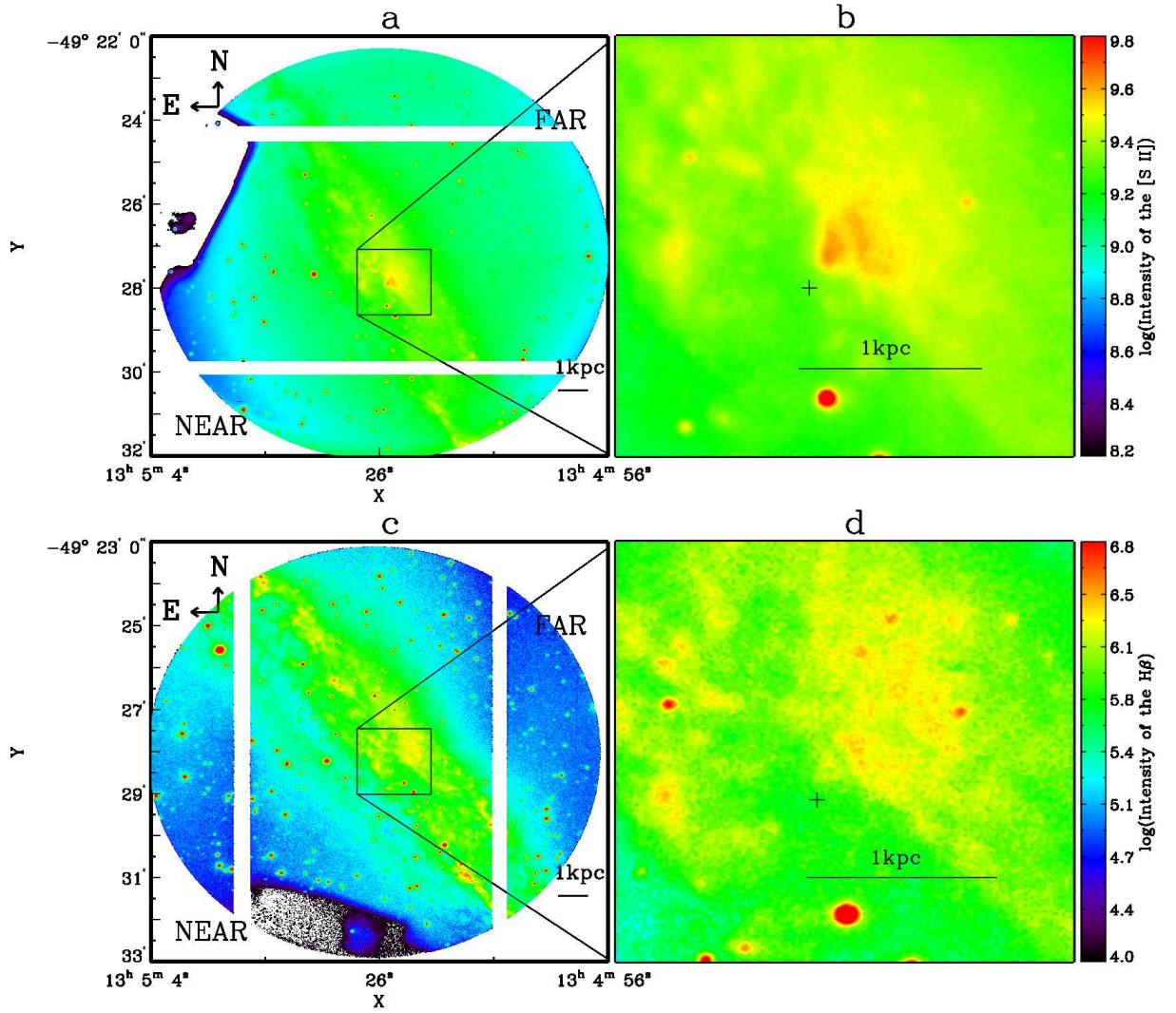


Figure 4.3: Total intensity maps of the observed field (RA:  $13^{\text{h}} 05^{\text{m}} 27^{\text{s}}.3$  and Dec:  $-49^{\circ} 28' 04''.0$ ) in NGC 4945, showing [S II] (upper panels). Lower panels show the intensity maps of  $\text{H}\beta$ . The centre of the galaxy is marked with a black cross symbol in panels (b) and (d), the intensity is in arbitrary units, and the black bar represents 1 kpc.

The spectral line profile ( $\text{H}\alpha$ ) was fitted at each pixel with a Voigt function to derive the wavelength at maximum intensity of the emission line, in order to determine the radial velocity, FWHM, maximum intensity and continuum intensity at each pixel. These parameters were mapped in Figure 4.4. The [N II] cube was analyzed in the same way, and shown in Figure 4.5.

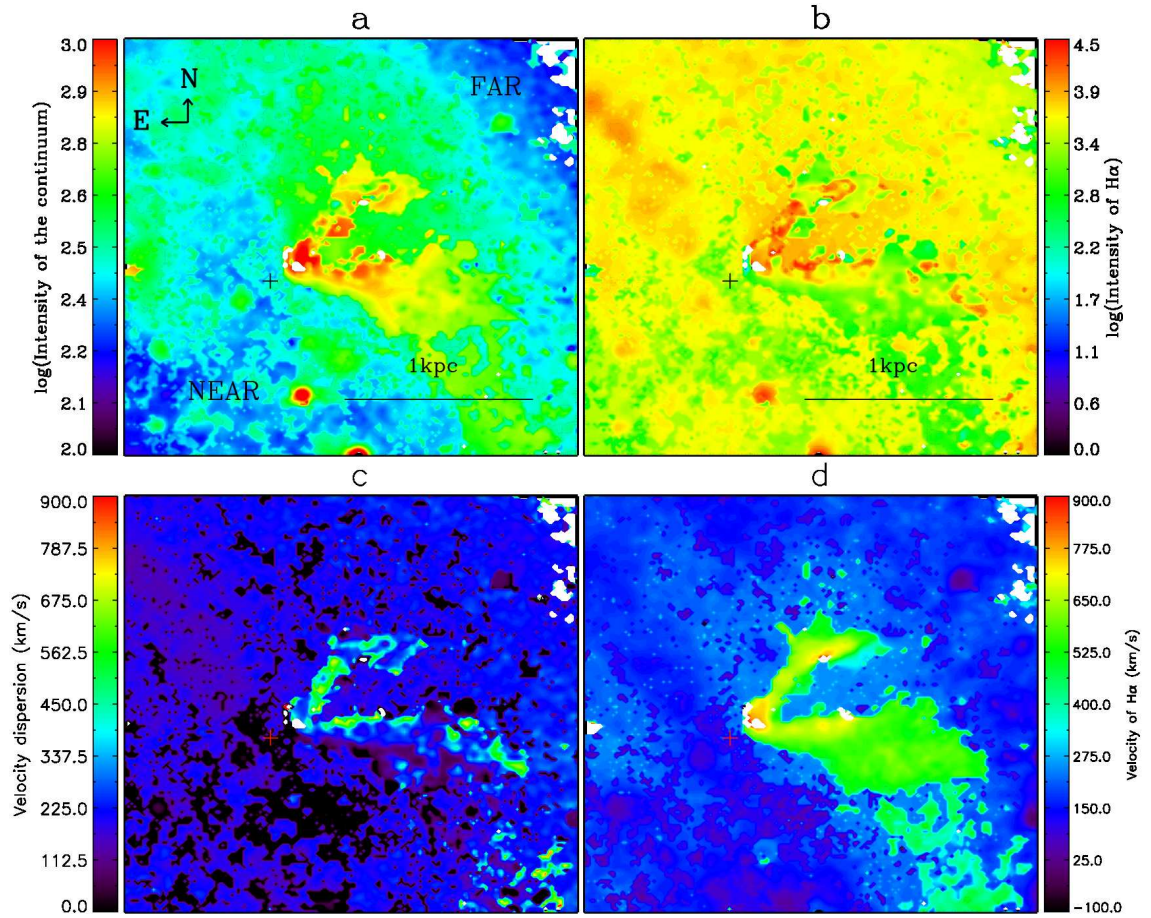


Figure 4.4: After fitting the data cube of  $H\alpha$ , from top left to bottom right: (a) the continuum, (b) maximum intensity of the  $H\alpha$  profile, (c) velocity dispersion and (d) velocity in the centre of NGC 4945 and its surroundings. The cross represents the centre of the galaxy in all panels, and the N and E represent the North and East. The accepted values of the fitting parameters have intensities with a  $S/N > 5$ .

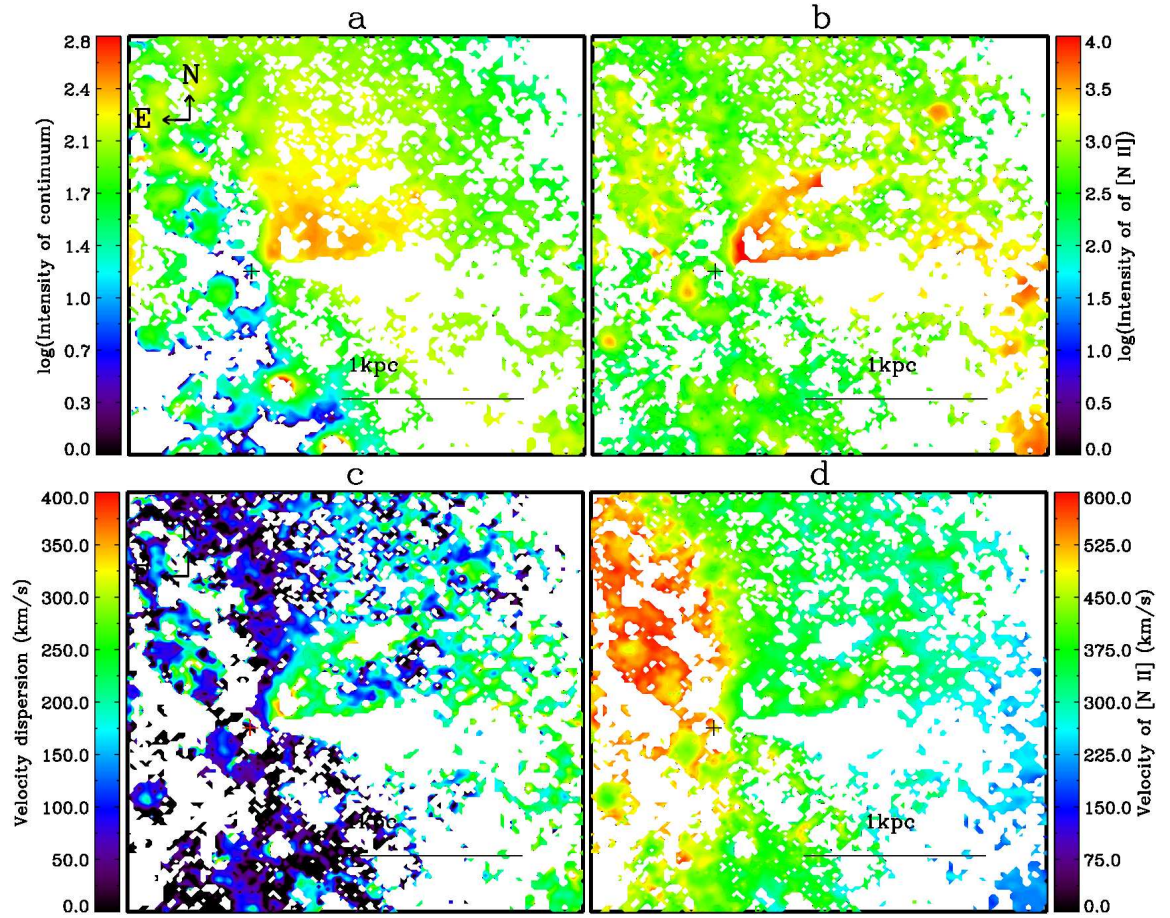


Figure 4.5: After fitting [N II]6583, from top left to bottom right: (a) the continuum, (b) maximum intensity of the H $\alpha$  profile, (c) velocity dispersion and (d) velocity in the centre of NGC 4945 and its surroundings. The cross represents the centre of the galaxy in all panels, and the N and E represent the North and East. The accepted values of the fitting parameters have intensities with a S/N is  $> 8$ .

### 4.4.1 Ionized gas distribution in the nucleus

Figures 4.2 and 4.3 show a clear cone at a distance of  $\sim 200$  pc to the North-East (NE) of the centre of NGC 4945. Two prominent areas appear with high intensity, one in the head of the cone with a nearly triangular shape, the second almost like an arch ( $\sim 400$  pc). Two clear filaments are extended from the end of the arch to the North-West (NW) by 400–500 pc in  $H\alpha$  and [N II], and  $\sim 200$  pc in [S II], while it is not clear in  $H\beta$ . A few filaments with lower intensities are visible with different shapes and lengths. The more prominent one is extended to more than 2 kpc along the disc, and it is clear in all four of the maps. The cone in the  $H\beta$  map is faint. Two areas in the cone have no  $H\beta$  emission: one is located in the area between the triangle-shape and the arch, and the other one in the middle of the cone. To the E area from the centre of NGC 4945 there is some bright matter in the form of filaments, which appears in  $H\alpha$ , [N II], [S II] and  $H\beta$ . This could represent areas from the second part (far-side) of the bi-conal structure. The light from this bright matter could be less affected by the dust than in other parts of the cone, or may represent H II regions that were created in the interface layer between ejected material and the surrounding ISM. Therefore, the bright matter in the suggested far-side of the cone needs more examination to understand its nature and origin. In order to do this, the area was re-observed with long-slit mode, to extract the physical properties (see subsection 4.7.3).

#### 4.4.1.1 $H\alpha$ emission

Panel (b) of Figure 4.2 shows the nuclear region of NGC 4945 that is highly obscured in optical emission ( $H\alpha$ ). A prominent dust lane is clear to the SE of the nucleus, and crossing it, but there is some radially extended  $H\alpha$ -emitting material to the NW of the nucleus. This material forms a one-side conical shape that is in a perpendicular direction to the stellar disc, and with an opening angle of  $\sim 130^\circ$  between both its edges to the NE and SW of the nucleus. It can be deduced that: (1) The outflowing gas extends to about 1.4 kpc away from the midplane and extends to about 4 kpc along the disc. (2) The intensity of the cone reduces radially away from the centre, with complex micro structures in the form of filaments and knots of bright matter which are clearly ruptured and extended in different directions.

The logarithmic intensity of the continuum emission in the area of interest is shown in panel (a) of Figure 4.4. Two prominent filaments share the same base and make a V shape with an opening angle of about  $80^\circ$  between both filaments. Therefore, these filaments presumably emerged from the same area and have the same origin. Also, in panel (b) these filaments are clear in  $H\alpha$  emission. Interestingly, the interior of the V-shaped structure is faint in continuum but bright in  $H\alpha$  emission, whereas, the opposite is true of the regions immediately exterior to the V-shaped structure. The

V-shaped filament also displays some interesting kinematics as shown in panels (c) and (d). The velocity dispersion is maximum along the V-shaped filament, where it reaches about  $680 \text{ km s}^{-1}$ , i.e.  $\sim 200\text{--}600 \text{ km s}^{-1}$  redshifted w.r.t. the disc motion near the nucleus. The velocities of the gas in these filaments have higher values ( $\sim 780 \text{ km s}^{-1}$ ) in the same area with higher intensity and velocity dispersion. The velocity across the V-shape filament ranges between  $400\text{--}780 \pm 15 \text{ km s}^{-1}$ .

The shape of the emission profile was examined in different positions across the area of interest, and it was found that the profile does not show clear signatures of splitting in these filaments (V-shape), but it becomes wider.

#### 4.4.1.2 [N II] emission

The fitting parameters of the [N II] profile were mapped and are shown in Figure 4.5. The cone is also clear in [N II] emission (see panel (b) of Figure 4.5), and it shows the familiar V-shaped filaments. This time, the interior seems brighter in continuum emission and relatively faint in [N II] emission. The V-shape has high velocity dispersion  $\sim 340 \pm 15 \text{ km s}^{-1}$ . The mean velocity of the V-shape filaments is  $\sim 400 \text{ km s}^{-1}$ , about  $100 \text{ km s}^{-1}$  redshifted w.r.t. the disc motion near the nucleus. The highest velocity ( $\geq 600 \text{ km s}^{-1}$ ) appears in the NE side of the cone, where the high intensity of  $\text{H}\alpha$  and [N II] are noticed. This area does not show high  $\text{H}\alpha$  velocity, as shown in panel (d) of Figure 4.4.

#### 4.4.1.3 The Ratio of [N II]/ $\text{H}\alpha$

In order to understand the variation in the line ratio of [N II]/ $\text{H}\alpha$  across the FP field, one part of the diagnostic diagram (BPT) was used and is shown in Figure 4.6. In this map, pixels that do not have both  $\text{H}\alpha$  and [N II] emission are excluded from the map. The values of [N II]/ $\text{H}\alpha$  are enhanced along the V-shape, and have the highest value in the base of the V-shape ( $\sim 0.3$ ). At a distance of  $1200 \text{ pc}$  from the midplane to the NW of the centre, the ratio shows a range of values ( $-0.25$  to  $0.03$ ) along the extended filament. According to the BPT diagram, a ratio of more than  $0.2$  normally appears in areas having higher ionizing source than H II regions, such as AGN. So the base of the cone (red area) is thought to be ionized by a hard ionizing source (AGN), and the V-shape is likely to be ionized by shocks or photo-excitation from a lower ionizing source (H II regions).

The V-shape also shows a high velocity dispersion in  $\text{H}\alpha$  and [N II] emission (see panel (c) of Figures 4.4 and 4.5). The velocity dispersion of  $\text{H}\alpha$  reaches  $600 \text{ km s}^{-1}$  along this shape while it is  $\sim 300 \text{ km s}^{-1}$  in the [N II] tracer. It may be that the radiation is emitted from spatially distinct regions of the nebula. Perhaps the

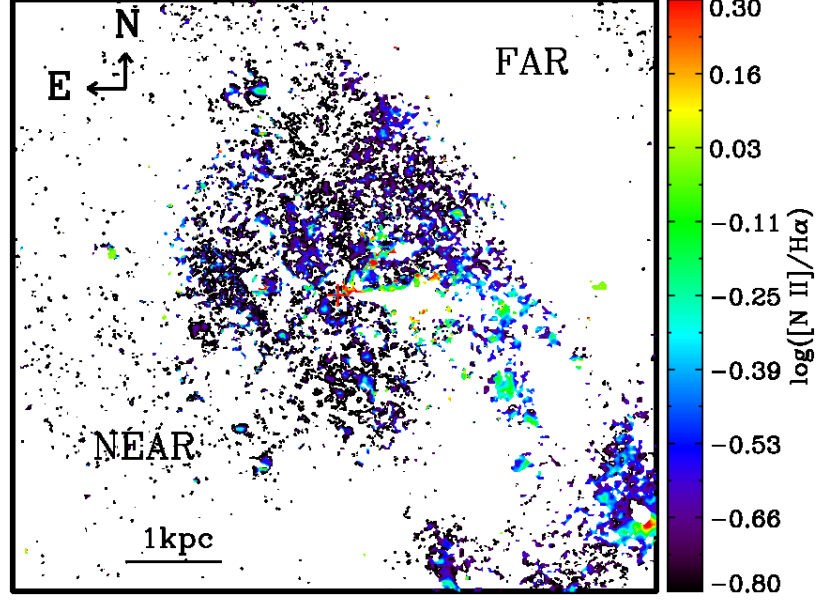


Figure 4.6: The ratio of  $[\text{N II}]/\text{H}\alpha$ . Pixels that do not have both  $[\text{N II}]$  and  $\text{H}\alpha$  emission are excluded from the map. The centre of the galaxy is marked with a red cross symbol.

large velocity dispersion of  $\text{H}\alpha$  is due to a large range of projected outflow velocities compared to  $[\text{N II}]$ , or maybe the turbulence in the V-shaped structure which was traced by  $\text{H}\alpha$  is larger than that which was traced by  $[\text{N II}]$ . The inner part of the V-shaped structure shows a low ratio of  $\sim -0.3$ , which may be reflecting the physical conditions of the cone, which appears in some areas and disappears in the white patches that are due to the loss of signal from pixels having high noise, which is excluded from the presented map. I expect the V-shaped structure is filled with ionized gas and it is more observable through the rim than in the front and back of the cone.

#### 4.4.1.4 The estimated mass of the ionized energetic outflows

The mass of the ionized outflow can be estimated from the following equation (Bae et al. 2017; Nesvadba et al. 2006):

$$M_{\text{gas}} = \frac{L_{\text{H}\alpha}}{h\nu_{\text{H}\alpha} \alpha_{\text{H}\alpha}^{\text{eff}}} m_p n_e^{-1} = (9.73 \times 10^8 M_{\odot}) \times L_{\text{H}\alpha,43} \times n_{e,100}^{-1} \quad (4.7)$$

where:

$L_{\text{H}\alpha,43}$  = luminosity of  $\text{H}\alpha$  in units of  $10^{43} \text{ erg s}^{-1}$ .

$h$  = Plank constant in units of  $\text{m}^2 \text{kg s}^{-1}$ .

$\nu_{H\alpha}$  =  $H\alpha$  frequency in units of Hz.

$m_p$  = proton mass.

$n_{e,100}$  = mean value of the electron density in units of  $100 \text{ cm}^{-3}$ .

$\alpha_{H\alpha}^{\text{eff}}$  = recombination coefficient of hydrogen in units of  $\text{cm}^{-3} \text{s}^{-1}$ .

Case B conditions with a temperature of  $10^4 \text{ K}$  (Osterbrock & Ferland 2006) were assumed to calculate the mean value of  $n_e \sim 150 \pm 20 \text{ cm}^{-3}$  (from long-slit observation) which is in agreement with earlier studies (Lípari, Tsvetanov & Macchetto 1997; Moorwood & Oliva 1994). The cone extends to  $\sim 1.4 \text{ kpc}$ . The estimated mass of the ionized gas for the visible side of the cone is  $2.5 \times 10^5 M_\odot$ . The kinetic energy of the ionized outflowing gas ( $E_{\text{out}}$ ) represents the bulk energy ( $E_{\text{bulk}}$ ) and the turbulence energy ( $E_{\text{turb}}$ ), and can be determined from

$$E_{\text{out}} = E_{\text{bulk}} + E_{\text{turb}} = \frac{1}{2} M_{\text{gas}} (v_{\text{gas}}^2 + \sigma_{\text{gas}}^2) \quad (4.8)$$

where:

$v$  = velocity of the gas in units of  $\text{km s}^{-1}$ .

$\sigma$  = velocity dispersion of the gas in units of  $\text{km s}^{-1}$ .

If I assume the velocity of the ionized outflows ( $v$ ) is equal to  $v_{\text{gas}}$  ( $650 \text{ km s}^{-1}$ ), then the rate of the outflow of mass ( $\dot{M}_{\text{out}}$ ) of a conical geometry<sup>1</sup> can be given by (Maiolino et al. 2012)

$$\dot{M}_{\text{out}} = 3 \times v \frac{M_{\text{gas}}}{R_{\text{out}}} = \frac{M_{\text{gas}}}{\tau_{\text{dyn}}} \quad (4.9)$$

where:

$\tau_{\text{dyn}}$  = dynamical timescale.

$R_{\text{out}}$  = radius of the biconical outflows.

The energy injection rate and the momentum flux can be determined by, respectively:

$$\dot{E}_{\text{out}} = \frac{1}{2} \dot{M}_{\text{out}} v^2 \quad (4.10)$$

$$\dot{P}_{\text{out}} = \dot{M}_{\text{out}} v \quad (4.11)$$

The integrated  $\dot{M}_{\text{out}}$  is  $\sim 0.34 M_\odot \text{ yr}^{-1}$  which is consistent with the estimated mass outflows rate ( $0.1\text{--}10$ )  $M_\odot \text{ year}^{-1}$  in nearby Seyferts with black hole mass  $\sim 10^5\text{--}10^7 M_\odot$  that are derived from optical observations (Veilleux, Cecil & Bland-Hawthorn 2005). The kinematic energy of the ionized outflows  $E_{\text{out}}$  in the AGN of NGC 4945 is  $\sim 1.8 \times 10^{54} \text{ erg}$ . This value is comparable to that in starburst-driven winds. The

---

<sup>1</sup>which is uniformly filled with outflowing gas.

Table 4.3: The physical properties of the outflows from the centre of NGC 4945.

$L_{H\alpha}$	$M_{gass}$	$E_{out}$	$\dot{M}_{out}$	$\dot{E}_{out}$	$\dot{P}_{out}$
$L_{\odot}$	$M_{\odot}$	erg	$M_{\odot} \text{ yr}^{-1}$	erg $\text{s}^{-1}$	dyne
$1 \times 10^6$	$2.5 \times 10^5$	$1.8 \times 10^{54}$	0.34	$4.3 \times 10^{40}$	$7.1 \times 10^{32}$

dynamical time taken for the ionized outflows to reach 1.4 kpc with  $v$  ( $650 \text{ km s}^{-1}$ ) is  $\sim 7.3 \times 10^5 \text{ yr}$ , which was determined by using the second part of Equation 4.9. The kinematic outflow rate (energy injection rate) and momentum flux in this dynamical timescale are  $\sim 4.3 \times 10^{40} \text{ erg s}^{-1}$  and  $7.1 \times 10^{32} \text{ dyne}$  respectively. The integrated physical properties of the ionized outflow of NGC 4945 are summarised in Table 4.3.

## 4.5 Long-slit observation and reduction

The RSS long-slit spectroscopy mode was used in this study; more information about the long-slit properties was introduced in the previous chapter. Four different long-slit positions are used to study the cone's structure which emerges from the centre of the edge-on galaxy NGC 4945. The maximum dispersion error in the four long-slit positions is  $\sim 0.028 \text{ \AA pixel}^{-1}$ , which would result in a velocity error of  $3 \text{ km s}^{-1}$  for the  $H\alpha$  line. This was included as an instrumental error in the velocity calculations.

One long-slit position crossed the cone structures in a perpendicular direction to the disc through the nucleus (hereafter LS1) as shown in Figure 4.7, and two positions crossed the cone structures parallel to the disc, with two different offsets:  $0'23$  (hereafter LS2) and  $0'4$  (hereafter LS3) respectively (see Figure 4.8). The observations were done in October 2016. Another long-slit setting (LS4) was done on 18<sup>th</sup> Jan. 2017 to cross the cone to the NW of the centre, as shown in Figure 4.1. Charts of these four long-slit observations are shown in appendix A in Figures A.6 to A.9.

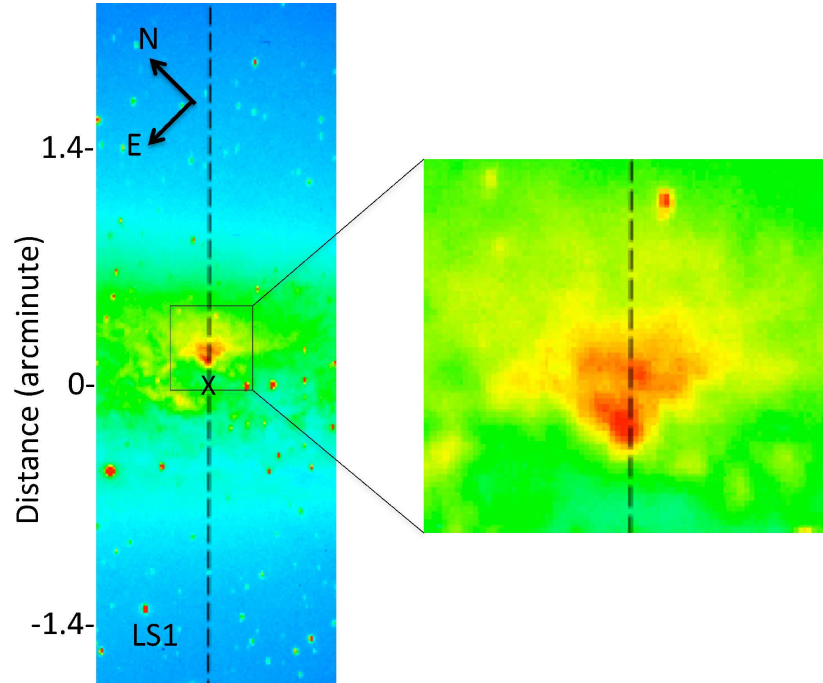


Figure 4.7: Two images of NGC 4945: (left panel) the long-slit position (LS1) in a perpendicular direction to the disc through the nucleus, and (right panel) zoom into the black rectangular area ( $0.53' \times 0.5'$ ). The black cross symbol represents the centre of the galaxy.

All important parameters of the observations are shown in Table 4.4. The data reduction was described in detail in chapter 1.5.

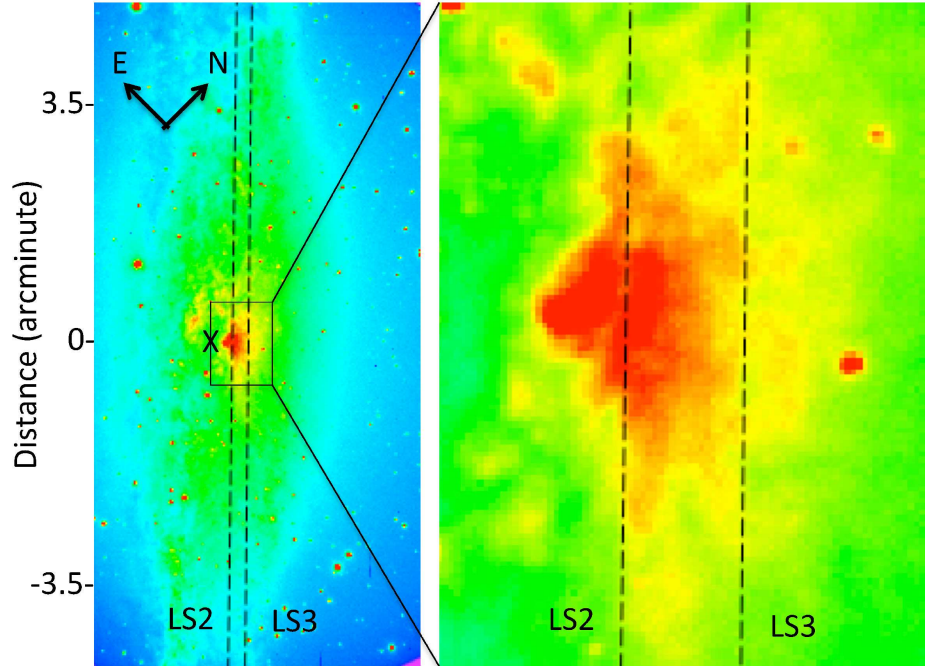


Figure 4.8: Two images of NGC 4945: (left panel) two different long-slit positions crossed the cone structures parallel to the disc, with two different offsets:  $0'23$  (LS2) and  $0'4$  (LS3) respectively, and (right panel) zoom into the black rectangular area. The black cross symbol represents the centre of the galaxy.

## 4.6 Results and data analysis

The observed spectra show several permitted and forbidden emission lines, such as Balmer lines ( $H\alpha$  &  $H\beta$ ), low excitation lines ( $[N II]\lambda\lambda 6549, 6583$  &  $[S II]\lambda\lambda 6716, 6732$ ), and high excitation lines ( $[O III]\lambda\lambda 4959, 5007$ ). The emission line characteristics (maximum intensities, FWHMs, central wavelengths) were determined by fitting a Gaussian function. These lines were fitted by one or two Gaussian functions according to the shape of their profiles.

### 4.6.1 The kinematics and physical properties along the cone

A kinematic map of the  $[N II]6549, 6583$  and  $H\alpha$  emission was created by mapping the positions of the slit relative to the central galaxy position and the heliocentric velocity (see left panel of Figure 4.9). This map covers  $2'8$  in the perpendicular direction to the

Table 4.4: Summary of the spectroscopic (long-slit) observations of NGC 4945.

Dates of observation	23 <sup>th</sup> –25 <sup>th</sup> Oct. 2016 & 18 <sup>th</sup> Jan. 2017
Telescope	SALT
Instrument	RSS
Detector	E2V CCD 44-82 chips
Mode	Long-slit
Grating	PG3000 & PG2300
Slit width	1''
Spectral resolution	0.76 & 1 Å
Exposure time	300 seconds
Pixel scale	0''5068
Reciprocal dispersion	0.268 Å pixel <sup>-1</sup>
Slit centre of LS1 (PA = -45°)	RA (2000) = 13 <sup>h</sup> 05 <sup>m</sup> 17 <sup>s</sup> Dec (2000) = -49° 28' 4''4
Slit centre of LS2 (PA = 45°)	RA (2000) = 13 <sup>h</sup> 05 <sup>m</sup> 26 <sup>s</sup> Dec (2000) = -49° 27' 40''
Slit centre of LS3 (PA = 45°)	RA (2000) = 13 <sup>h</sup> 05 <sup>m</sup> 26 <sup>s</sup> Dec (2000) = -49° 27' 54''
Slit centre of LS4 (PA = 49°)	RA (2000) = 13 <sup>h</sup> 05 <sup>m</sup> 34 <sup>s</sup> Dec (2000) = -49° 25' 59''

disc and crosses the centre of the galaxy. In the left panel of Figure 4.7, the position of the slit (LS1) is shown. The long-slit crosses different morphological structures along the cone. The kinematic maps for [S II] and H $\beta$  lines were constructed for the same area and presented in the middle and right panels of Figure 4.9 respectively. The crossed structures are clear in H $\alpha$  and [N II]6583 emission, and there are 7 areas showing extreme kinematics. The most prominent one is at 0'.1, and clear split components lie at 0'.33 to the NW of the nucleus. Another three separate areas in the same direction w.r.t. the nucleus are seen at 0'.5, 0'.63 and 0'.74 respectively. To the SE, two distinguishable areas lie at -0'.1 and -0'.4, which show clear emission in H $\beta$ .

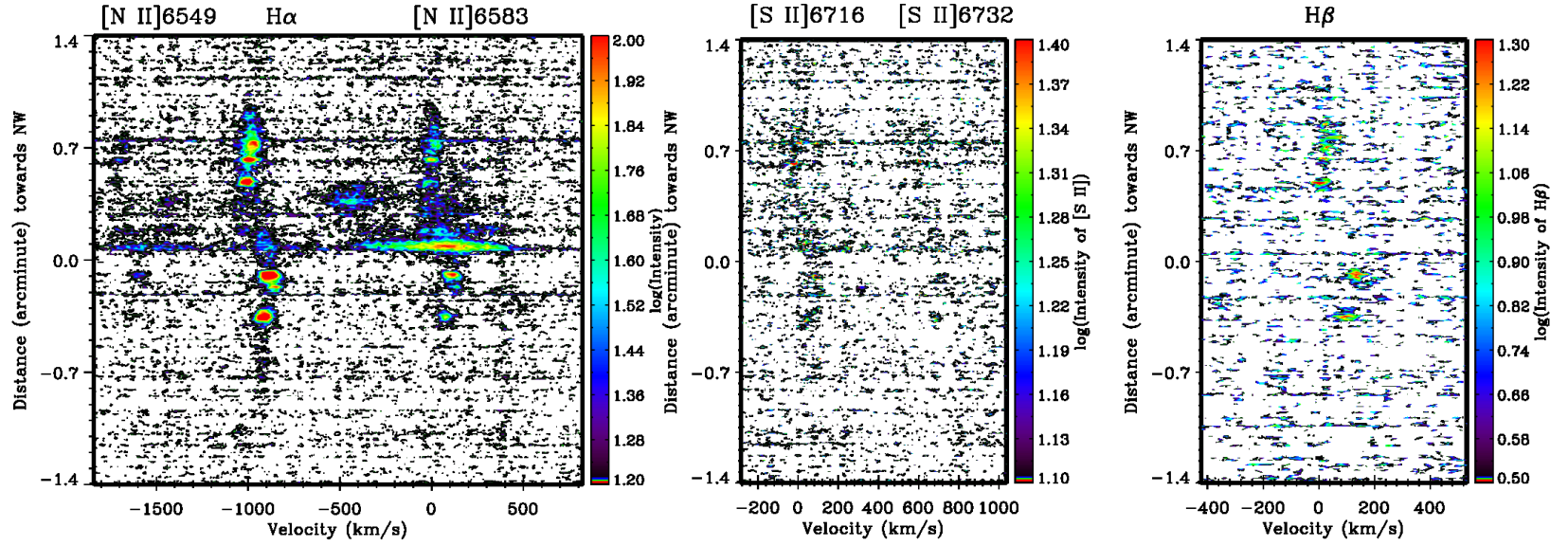


Figure 4.9: The spatial and kinematic maps of the [N II] doublet and H $\alpha$  (left panel), [S II] doublet (middle panel), and H $\beta$  (right panel) along the slit (LS1). The wavelength axis is transformed into heliocentric Doppler velocity for the [N II]6583 line, [S II]6716 and H $\beta$  lines respectively. The long-slit was oriented with PA =  $-45^\circ$  (perpendicular to the disc of NGC 4945).

Across the long-slit (LS1), one of the most striking results is that there are no high ionization lines such as [O III], but perhaps they are too faint to be observed. The [O III] $\lambda\lambda$ 4959,5007 lines are common in H II regions or AGN spectra, where the emitted photons from massive stars, or active nuclei can provide the required energy (35.1 eV) to ionize oxygen atoms to O<sup>2+</sup>.

The nucleus of NGC 4945 does not show any emission in H $\alpha$ , [N II], H $\beta$  and [S II], but in areas just above or below that along the slit, strong emission is observed in various separated regions. In the FP observations, (see Figures 4.2 and 4.3) I showed that there is no point source in the maps from H $\alpha$ , [N II], H $\beta$  and [S II] that corresponds to the position of the nucleus. NGC 4945 has a heavily obscured Seyfert nucleus in the optical range and below 10 keV (Iwasawa et al. 1993). It has a powerful radio continuum source which emits 2 Jy at 6 GHz (Whiteoak & Wilson 1990). The overall structures of the ionized gas in the nucleus and its surroundings are clumpy, having various free–free optical depths (6-23) (Lenc & Tingay 2009b). The 2–3 GHz images taken with VLBI<sup>2</sup> show a radio source with a one-sided jet-like structure near the position of the AGN. The counter-jet would be free–free absorbed, as has been detected in gaseous discs in some Seyfert galaxies (Gallimore et al. 1999).

To the NW of the centre at  $\sim 0'.1$  (see Figure 4.9 left panel) lies the most spectacular feature, which is bright in [N II], and positioned near to the base of the cone. It shows a broadened profile with bulk motion ranging between  $-500$  and  $500$  km s<sup>-1</sup>. It can be fitted as two components, as will be discussed later on. The splitting becomes clearer at a distance of  $0'.3 - 0'.4$  to the NW, and the blueshifted feature ( $\sim 300$  km s<sup>-1</sup>) is dominated by [N II] emission. [S II] $\lambda\lambda$ 6716,6732 and H $\beta$  show broad underlying emission, but the high noise level precludes reliable fitting at this position on LS1.

This observed side of the cone was investigated by Heckman, Armus & Miley (1990) by using medium resolution long-slit spectroscopy with two different positions. They found a split in the [N II] and H $\alpha$ , and the obtained velocity blueshifted component had velocity  $-250$  km s<sup>-1</sup> while the velocity of the redshifted component was  $\sim 50$  km s<sup>-1</sup>. Each component had a FWHM of  $200-400$  km s<sup>-1</sup>. As well as this, L ipari, Tsvetanov & Macchetto (1997) identified a split in the [N II] and [S II] lines by using long-slit spectroscopy with a resolution  $\sim 4$   , and found the velocity of blueshifted component to be  $\sim -200$  km s<sup>-1</sup> with a FWHM  $\sim 700$  km s<sup>-1</sup>, while the H $\alpha$  did not show any sign of splitting. These discrepancies could be understood in terms of the different resolution, slit positions and orientations. Structures with similar properties to those in the right panel of Figure 4.9 have been found by Moorwood et al. (1996) with long-slit observations. They suggested a broad (FWHM  $\sim 600$  km s<sup>-1</sup>) and complex dynamics at about  $0'.1$  ( $\approx 240$  pc)<sup>3</sup> to the NW of the centre.

---

<sup>2</sup>Very long baseline interferometry

<sup>3</sup>The used angular scale was ( $1'' = 19$  pc.)

The asymmetry in profile shape in Figure 4.11 could be an indication of galactic winds (GWs). The presence of the clear split in [N II] and H $\alpha$  at 0'33 from the centre can be interpreted in terms of GWs, according to the outflow scenario along the surface of the bicone-structure that emerges from the nucleus of disc galaxies by Tomisaka & Ikeuchi (1988). The front surface of the cone (near cone to the observer) produces a strong, blueshifted component, and the back side produces a component around the systemic velocity (or redshifted, depending on the inclination). This is consistent with the FWHM of the blueshifted component being larger than that of the other components, due to a change in the range of projected velocities.

Five H II regions are identified along LS1, three to the NW and two to the SE of the nucleus. I would suggest that they are located within the spiral arms of the disc, the H $\alpha$  line in these H II regions show FWHM  $\sim 70 \text{ km s}^{-1}$  and the average velocity in the H II regions in the NW and SE is  $\sim 60 \text{ km s}^{-1}$  and  $\sim -25 \text{ km s}^{-1}$  respectively. A velocity asymmetry is seen between the two groups of H II regions, and the difference between the two is  $\sim 90 \text{ km s}^{-1}$  due to the (projected) rotation of the disc.

There is no H $\beta$  emission in the area spanning about 350 pc to the NW (between 0'0 to 0'5) of the centre. However, there are a few bright areas with H $\beta$ , as shown in the right panel of Figure 4.9. These areas lie along the minor axis of the galaxy which has outflows with H $\alpha$ , [N II] and [S II] emission. The radii of these areas are  $\geq 140 \text{ pc}$ , meaning they are giant H II regions (Heckman, Armus & Miley 1990). The H $\beta$  profile shows no split signatures after being examined using the SPLIT task in IRAF, where there is measurable emission along the slit. H II regions to the SE show broader H $\beta$  profiles (in particular the outer on  $\sim 130 \text{ km s}^{-1}$ ) than are located in the NW. This suggests that the broadening in H $\beta$  profile may result from interaction with another bulk motion. Surprisingly, this does not occur with H $\alpha$  profiles in these H II regions.

The interesting part of the slit was subdivided into 11 parts with each part covering one specific feature. The spectrum of each subdivision was calculated by averaging the spectra of all the pixels in these regions. The resulting spectra are displayed in Figure 4.10.

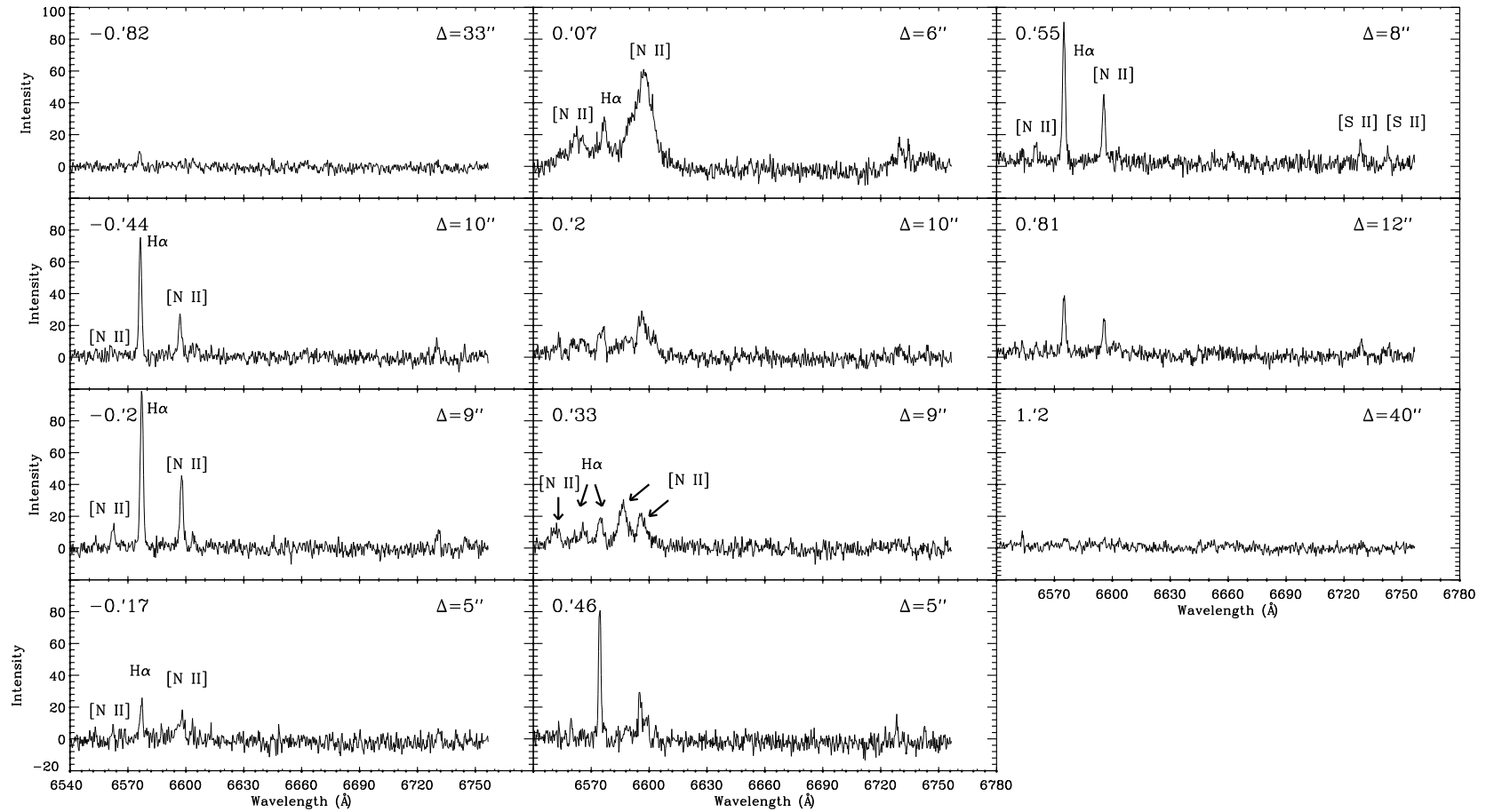


Figure 4.10: Red part (6540–6760 Å) spectra in subsequent subdivisions along the interesting part of LS1. The labels in the top left corners represent the central position of the structures, and the labels in the top right corners are the spatial width of the structures.

The highest intensity in  $H\alpha$  and  $[\text{N II}]$  is at  $-0'.2$ . The broadening and blue asymmetry are obvious in  $H\alpha$  and both lines of  $[\text{N II}]$  at a distance of  $0'.07$  from the centre, and the splitting becomes clearer in these lines at the position of  $0.33'$ . At  $0.46'$ , the splitting is seen in  $[\text{N II}]6583$ , but is not obvious in other lines.

In order to investigate these two regions at  $0'.07$  and  $0'.33$ , the spectra of these two particular regions were Gaussian fitted to study the shape and parameters of these lines in detail (see Figure 4.11). The left and middle panels in Figure 4.11 show the fitting of the  $[\text{N II}]$ ,  $H\alpha$  and  $[\text{S II}]$  lines at the distance of  $0'.07$ , and the right panel shows only the fitting of  $H\alpha$  and  $[\text{N II}]$  lines at the distance of  $0'.33$  because there is no  $[\text{S II}]$  emission at  $0'.33$ . The line ratios, velocities, and FWHMs of these lines are listed in Table 4.5. A noticeable difference between the velocities and FWHMs of the  $[\text{N II}]^1$ ,  $H\alpha^1$  and  $[\text{S II}]^1$  would be interpreted in terms of a strong and broad component of  $[\text{N II}]$  that appears in this region, which represents the bipolar wind that is more obvious in  $[\text{N II}]$  than other lines according to the double-component super wind model for NGC 7714 (Taniguchi et al. 1988).

The  $[\text{N II}]6583$  line shows a wide wing at the red-end of the spectra. The Gaussian fit did not identify the red-side of the profile. This wing may be the result from the wind's interaction with the existing gas. Another component could contribute to form the observed profile. Consequently, the real centroid velocity will be shifted from the value that was determined from the fit.

The two fitted components of  $[\text{N II}]$  and  $H\alpha$  show high ratios of  $[\text{N II}]/H\alpha$ , suggesting that the gas is shock-heated in this part of the cone. At position  $0'.07$ , ratios of the two fitted components show different physical properties. The first component displays  $\log([\text{N II}]/H\alpha) \sim 0.22$  and  $\log([\text{S II}]/H\alpha) \sim -0.18$ , which is consistent with conditions in H II regions. Meanwhile, the second component shows high value in both  $\log([\text{N II}]/H\alpha)$  and  $\log([\text{S II}]/H\alpha) \sim 0.4$  and  $0.03$  respectively, which appears in the areas with a high ionization power, such as AGN.

At  $0'.33$  to the NW, the first component (blueshifted) shows a higher ratio of  $\log([\text{N II}]/H\alpha) \sim 0.4$  than that in the second component ( $\sim -1.3$ ). Also, the gas in this area is suggested to be shock-heated resulting from the impact of an AGN, which may be the ionizing source for this component. The second component could be ionized by a softer source, such as in H II regions.

The first component at the latter position shows a high ratio observed along LS1, and the second component at  $0'.07$  shows a comparable value. It seems that they are either created from different clouds and are not related to each other, or the dust plays different roles at these two positions.  $H\beta$  emission is clear at this position ( $0'.33$ ) while at  $0'.07$  there is no  $H\beta$  emission that can be measured. Therefore, the dust may have affected the faint component. In other words, it could be suggested that the impact of the outflows differs locally according to the type of ionizing source and the presence of the dust.

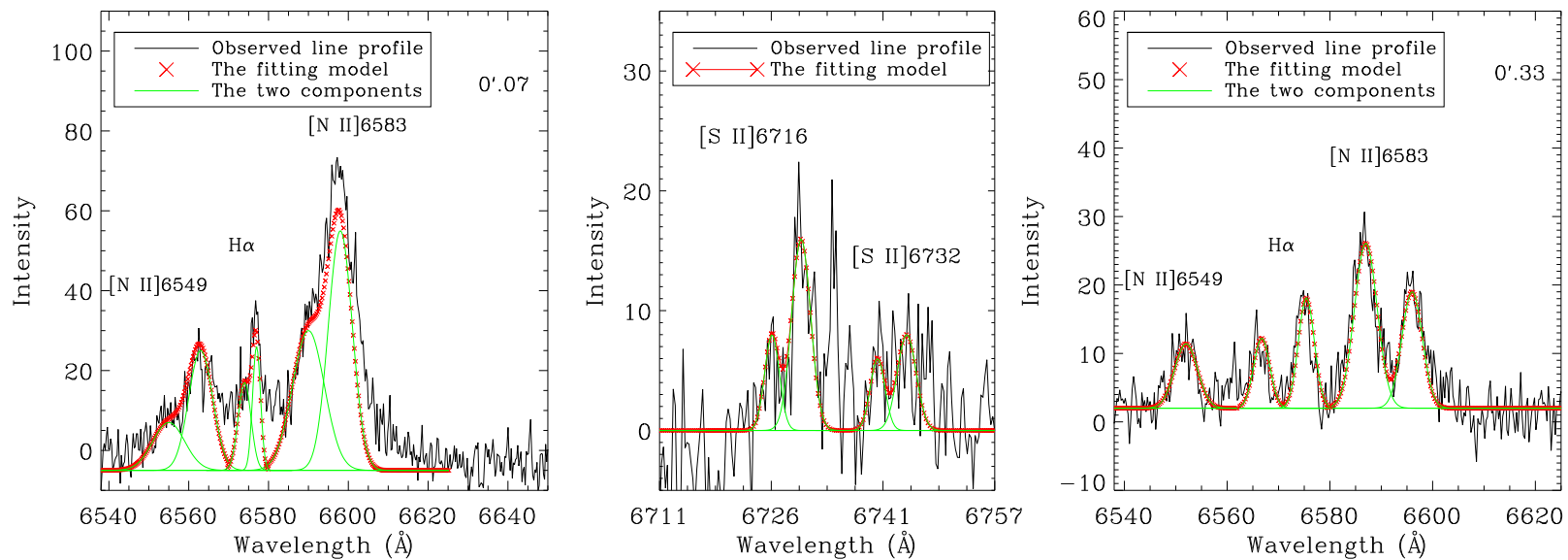


Figure 4.11: Left and middle panels show optical emission lines at a distance of 0'.07 to the NW from the centre of NGC 4945. The right panel displays H $\alpha$  and [N II] at a distance of 0'.33. The resolution is 0.75 Å and the long-slit (LS1) was oriented with PA =  $-45^\circ$  (perpendicular to the disc of NGC 4945).

Table 4.5: Emission line ratios, velocities and FWHMs at a distance of 0'07 and 0'33 from the centre of NGC 4945. Note that the [N II] line used is the red one (6583 Å).

Lines	Position 0'07		Position 0'33	
	v (km s <sup>-1</sup> )	FWHM (km s <sup>-1</sup> )	v (km s <sup>-1</sup> )	FWHM (km s <sup>-1</sup> )
[N II] <sup>1</sup>	-219 ± 14	429 ± 14	-356 ± 14	240 ± 14
[N II] <sup>2</sup>	-83 ± 14	322 ± 14	56 ± 14	215 ± 14
Hα <sup>1</sup>	-13 ± 13	172 ± 13	-375 ± 13	176 ± 13
Hα <sup>2</sup>	125 ± 13	107 ± 13	16 ± 13	168 ± 13
[S II] <sup>1</sup>	-160 ± 11	105 ± 14		
[S II] <sup>2</sup>	18 ± 11	137 ± 14		
	ratio		ratio	
[N II] <sup>1</sup> /Hα <sup>1</sup>	1.66 ± 0.20		2.46 ± 0.26	
[N II] <sup>2</sup> /Hα <sup>2</sup>	2.50 ± 0.21		1.05 ± 0.10	
[N II] <sup>1</sup> /[S II] <sup>1</sup>	2.50 ± 0.30		< 0.40	
[N II] <sup>2</sup> /[S II] <sup>2</sup>	2.30 ± 0.21			
[S II] <sup>1</sup> /Hα <sup>1</sup>	0.66 ± 0.16		< 0.25	
[S II] <sup>2</sup> /Hα <sup>2</sup>	1.09 ± 0.27			

1 = first component.

2 = second component.

The second interesting region is at  $0'.33$  to the NW of the nucleus. The spectra of this object (see Figure 4.11 right panel) show [N II] and  $H\alpha$  lines, while [S II] and  $H\beta$  are unmeasurable in this area, as shocks become weaker. The blueshifted components in both lines ([N II],  $H\alpha$ ) show nearly the same high velocity ( $-356 \pm 14 \text{ km s}^{-1}$ ,  $-375 \pm 13 \text{ km s}^{-1}$ ), and the FWHM in [N II] ( $240 \text{ km s}^{-1}$ ) is comparable to that of  $H\alpha$  ( $176 \text{ km s}^{-1}$ ). Hence, the shocks/AGN have become unimportant in the downwinds part of the outflow.

## 4.6.2 The kinematics and physical properties across the cone

### LS2

Figure 4.8 shows the position of LS2 ( $PA = 45^\circ$ ). Along the slit, different emission lines were measured and kinematic maps were created for these lines: [N II] doublet and  $H\alpha$  are shown in Figure 4.12 panel (a), [S II] lines in (b), and the ratio map of [S II] $\lambda 6716$ /[S II] $\lambda 6732$  in (c). The ratios of [N II]/ $H\alpha$  and [N II]/[S II] are displayed in panels (e) and (f) respectively. After testing various positions along the slit to examine emission line profiles, three different areas were chosen to study in detail. The extracted spectra from the marked areas (centre (red rectangle), area-1 and area-2) in (a) are plotted in Figure 4.13. The emission lines in the central area and its immediate surrounding (red rectangle) (78 pixels,  $40''$ ) are extracted and mapped (see (d) panel of Figure 4.12). The [N II] $\lambda 6583$  comprises different components which make the [N II] profile blue-asymmetric in shape, and so the profile was fit using two Gaussian components as shown in the upper panels of Figure 4.13.

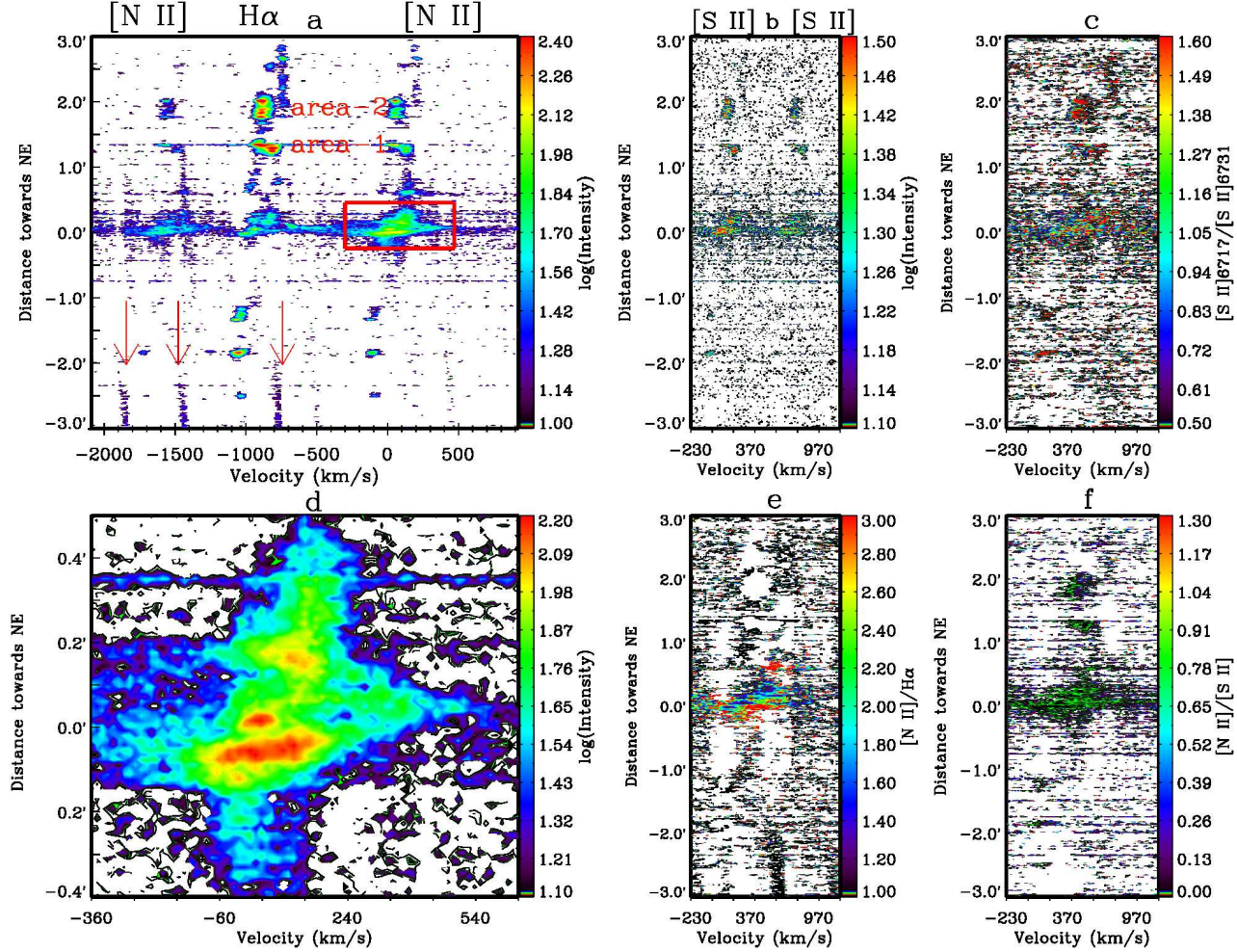


Figure 4.12: Panel (a): spatial and kinematic map of [N II] and H $\alpha$  lines along the slit position (LS2). The wavelength axis was transformed into heliocentric Doppler velocity for the [N II]6583 line. (b) [S II] lines. (c) Ratio map of [S II]6716/[S II]6732. (d) Zoom into the red rectangular area in (a). (e) and (f) show the ratios of [N II]/H $\alpha$  and [N II]/[S II] respectively. The slit (LS2) was oriented with PA = 45 $^\circ$  and shifted 0'.23 from the centre of the galaxy (parallel to the disc of NGC 4945). The North and East directions are as right panel of Figure 4.8.

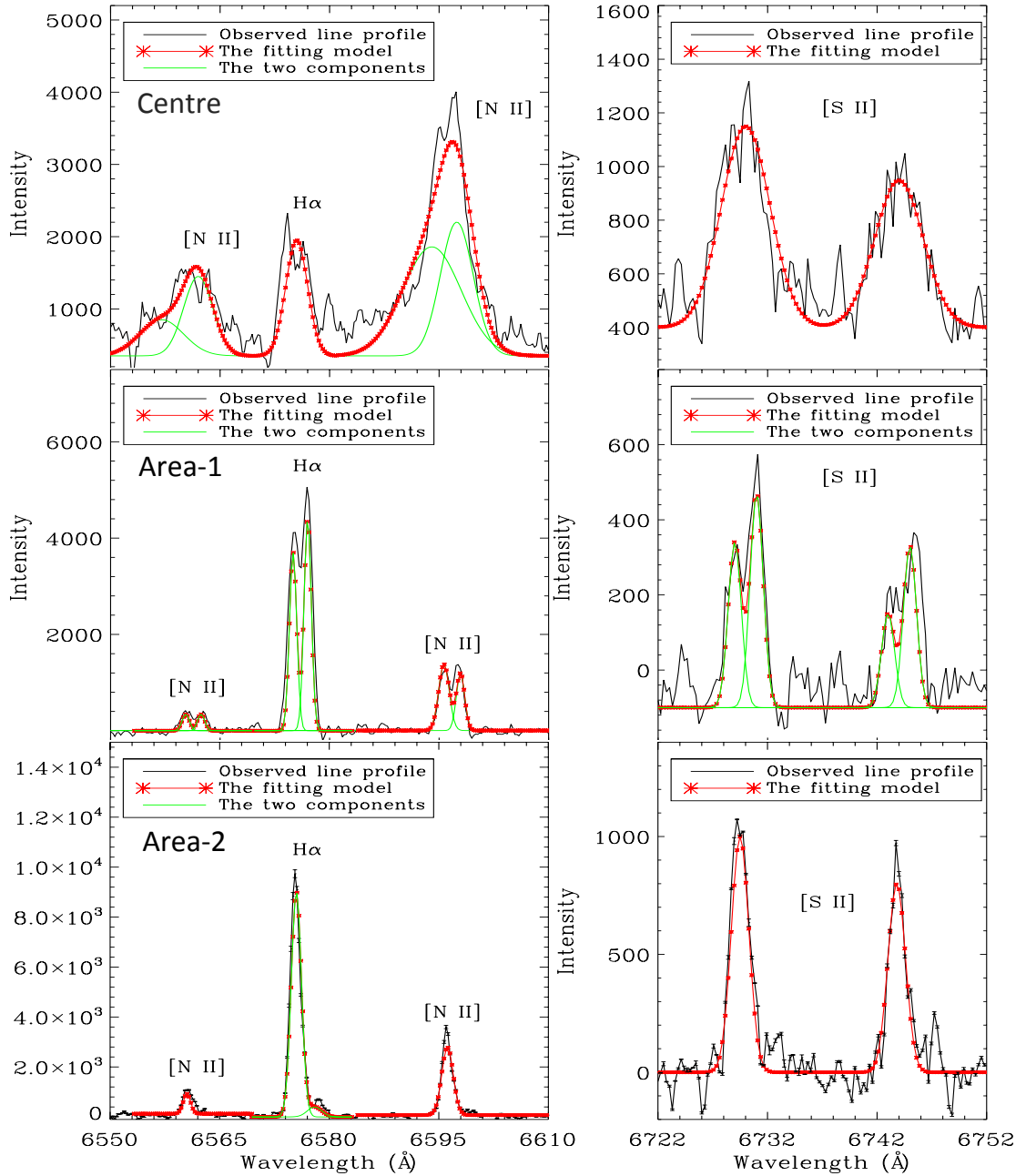


Figure 4.13: Left: spectrum of [N II], H $\alpha$  and fitted profiles; Right: spectrum of [S II] lines and fitted profile for three areas: Centre ( $\Delta = 23''$ ), area-1 ( $\Delta = 15''$ ) and area-2 ( $\Delta = 28''$ ), which are labelled in Figure 4.12. The long-slit (LS2) was oriented with PA =  $45^\circ$ , with a shift of  $0.23$  towards NW.

Table 4.6: Emission line ratios, velocities and FWHMs of three objects (red rectangle centre, area-1, area-2) along LS2 in NGC 4945.

Lines	Centre		Area-1		Area-2	
	$v$ (km s <sup>-1</sup> )	FWHM (km s <sup>-1</sup> )	$v$ (km s <sup>-1</sup> )	FWHM (km s <sup>-1</sup> )	$v$ (km s <sup>-1</sup> )	FWHM (km s <sup>-1</sup> )
[N II] <sup>1</sup>	-37 ± 1	429 ± 2	39 ± 6	80 ± 4	63 ± 5	84 ± 10
[N II] <sup>2</sup>	119 ± 7	240 ± 8	142 ± 1	62 ± 6	98 ± 4	204 ± 10
H $\alpha$ <sup>1</sup>	56 ± 1	162 ± 2	33 ± 1	54 ± 4	-56 ± 2	75 ± 4
H $\alpha$ <sup>2</sup>			125 ± 1	54 ± 4	-170 ± 1	107 ± 4
[S II] <sup>1</sup>	42 ± 2	233 ± 4	-2 ± 3	63 ± 4	-20 ± 3	84 ± 3
[S II] <sup>2</sup>			87 ± 3	63 ± 4	192 ± 7	74 ± 5
	ratio		ratio		ratio	
	[N II] <sup>1</sup> /H $\alpha$ = 0.94 ± 0.16		[N II] <sup>1</sup> /H $\alpha$ <sup>1</sup> = 0.37 ± 0.05		[N II]/H $\alpha$ <sup>1</sup> = 0.30 ± 0.04	
	[N II] <sup>2</sup> /H $\alpha$ = 1.16 ± 0.23		[N II] <sup>2</sup> /H $\alpha$ <sup>2</sup> = 0.32 ± 0.23		[N II]/H $\alpha$ <sup>2</sup> = 0.82 ± 0.10	
	[N II] <sup>1</sup> /[S II] = 1.16 ± 0.11		[N II] <sup>1</sup> /[S II] <sup>1</sup> = 2.00 ± 0.12		[N II]/[S II] = 1.5 ± 0.02	
	[N II] <sup>2</sup> /[S II] = 1.43 ± 0.03		[N II] <sup>2</sup> /[S II] <sup>2</sup> = 1.20 ± 0.21			
			[S II] <sup>1</sup> /H $\alpha$ <sup>1</sup> = 0.19 ± 0.05		[S II]/H $\alpha$ <sup>1</sup> = 0.20 ± 0.03	
	[S II] /H $\alpha$ = 0.81 ± 0.03		[S II] <sup>2</sup> /H $\alpha$ <sup>2</sup> = 0.23 ± 0.08		[S II]/H $\alpha$ <sup>2</sup> = 0.50 ± 0.03	

1 = first component.  
2 = second component.

At the centre of LS2, to the North of the nucleus, a prominent area showing a wide range of velocities  $\pm 550 \text{ km s}^{-1}$  is seen, as shown in panel (a) of Figure 4.12 (red rectangle), and in more detail in panel (d). The spectra of this area are shown in Figure 4.13. There is no  $\text{H}\beta$  and  $[\text{O III}]$  emission in the blue spectrum along LS2. I fitted the  $[\text{N II}]$  lines, which display a blue asymmetry, using two components. The broader and fainter one has  $-37 \pm 2 \text{ km s}^{-1}$  and  $\text{FWHM} \sim 430 \pm 2 \text{ km s}^{-1}$  (highest observed FWHM) while the strong component shows velocity  $\sim 120 \pm 7 \text{ km s}^{-1}$  and  $\text{FWHM} \sim 240 \pm 8 \text{ km s}^{-1}$ . These values may have been slightly exaggerated as the profile clearly has a blue wing which is not accurately fit with a Gaussian. The  $\text{H}\alpha$  was fitted with one Gaussian, and the determined velocity  $\sim 60 \text{ km s}^{-1}$  and  $\text{FWHM} \sim 160 \text{ km s}^{-1}$ . However, the profile does look split. The forbidden  $[\text{S II}]$  emission profile is chaotic and does not have a clear asymmetry, and therefore a single Gaussian fit is most appropriate. The determined velocity from  $[\text{S II}]$  is  $42 \pm 2 \text{ km s}^{-1}$  and the FWHMs are  $233 \pm 4 \text{ km s}^{-1}$ . However, this centroid and width suggests, we may have measured the blend of two components. This area (panel (d) of Figure 4.12) falls on the more prominent part of the cone, where we expect the impact of the AGN and starburst activity occur, this can be confirmed by tracing the different component that appears in this area and the asymmetry profile of the emission lines, which show a complicated kinematics with different intensities to the red and to the blue of the profiles. This area does not show any  $\text{H}\beta$  emission, as well as all the areas that position along LS2 do not show  $\text{H}\beta$  emission.

Area-1 and area-2 represent  $\text{H II}$  regions in the disc of NGC 4945 which are a little redshifted while another two  $\text{H II}$  regions are positioned at  $1'4$  and  $1'9$  to the SW of the centre and are also a little redshifted, and the velocity asymmetry between the two sides of the disc is  $\sim 100 \text{ km s}^{-1}$ , reflecting the (projected) galaxy rotation. There is an obvious splitting in the emission lines in area-1, and both components of the emission lines have approximately identical intensities. In area-2, two components are noticed in three emission lines ( $[\text{N II}]$ ,  $\text{H}\alpha$ , and  $[\text{S II}]$ ), which have considerably different intensities. Low ratios of  $[\text{N II}]/\text{H}\alpha$  and  $[\text{S II}]/\text{H}\alpha$  appear in the two regions, which reflects the physical properties of  $\text{H II}$  regions as was expected.

If one steps through the panels of Figure 4.13 from top to bottom, clear progression in the shape of the emission profiles is noticeable, as well as in their intensities. In the area near the vertex (upper panels), broad, double lines are obvious in both  $[\text{N II}]$  lines, and a broad, single line in both  $\text{H}\alpha$  and  $[\text{S II}]$ . Only the upper panel shows high  $[\text{N II}]6583$  intensity compared with  $\text{H}\alpha$ . This area displays ratios of  $[\text{N II}]^2/\text{H}\alpha^2$  ( $1.16 \pm 0.23$ ) and  $[\text{S II}]/\text{H}\alpha^2$  ( $0.81 \pm 0.03$ )<sup>4</sup> that suggests shocked gas dominates this region near the nucleus as a result of interaction with outflowing gas. In the lower panels, there is asymmetry in the red-base of the profile which would be a second component

---

<sup>4</sup> $[\text{S II}]$  doublet does not show a clear split, so this value is for one Gaussian fitting.

with low intensity. Only the  $[\text{S II}]/\text{H}\alpha$  ratio is enhanced in this area to a value of 0.5 a level about the lower limit of shocked gas.

### LS3

Figure 4.8 shows the position of LS3 ( $\text{PA} = 45^\circ$ , and offset is  $0'.4$  ( $\sim 470$  pc) to the NW of the centre of NGC 4945). The same procedure as before was carried out with LS3 data, and the results were transformed in terms of kinematic and spatial maps for the emission lines. Figure 4.14 shows the kinematic maps of  $[\text{N II}]$  and  $\text{H}\alpha$  in panel (a) and  $[\text{S II}]$  in (b). The ratio of  $[\text{S II}]$  lines,  $[\text{N II}]/\text{H}\alpha$  and  $[\text{S II}]/[\text{N II}]$  were constructed in panels (c), (e) and (f) respectively. Panel (d) displays the zoomed-in kinematic map for the  $[\text{N II}]$  (the red-rectangular area in (a)). Different regions are marked which show strong emission. The red and blue parts of the spectra for these interesting areas (area-3, area-4 and area-5) are shown in Figures 4.15. The velocities and FWHMs of these lines are listed in Table 4.7.

The ratio map of  $[\text{S II}]6716/[\text{S II}]6732$  in panel (c) shows extreme values at the edges (red on the left and blue on the right). It is suggested that the two  $[\text{S II}]$  lines were not perfectly aligned in velocity before calculating their ratio. Therefore, the values in between represent the true values.

The three chosen areas (area-3, area-4 and area-5) present the high photoionization emission line  $[\text{O III}]$ , which was not observed in any other position along LS1 and LS2. Emission lines in area-3 and area-4 display about the same velocities and FWHMs. On the other hand, area-5 shows a higher (blueshifted) velocity to that which appeared in the previous areas, and comparable FWHMs. Only in panel (d) I detect velocities between  $-600$  and  $200$   $\text{km s}^{-1}$ . Meanwhile, area-3, area-4 and area-5 have no indication of splitting, as is clear in Figure 4.15. Area-3 and area-4 show nearly the same velocities ( $\sim 35$   $\text{km s}^{-1}$  and  $\text{FWHM} \sim 70$   $\text{km s}^{-1}$ ) for  $\text{H}\alpha$ ,  $[\text{N II}]$  and  $\text{H}\alpha$ , and double the value of velocity for  $[\text{S II}]$  with the same value of FWHM. Area-5 has a higher velocity more than  $100$   $\text{km s}^{-1}$  and  $\text{FWHM} \sim 84$   $\text{km s}^{-1}$ .

Panel (d) in Figure 4.12 focuses on the area of interest (red rectangle) shown in panel (a). Extreme morphological structures are seen in  $[\text{N II}]$  emission, and a blueshifted component ( $\sim -400$   $\text{km s}^{-1}$ ) is clear to the top of the map, as well as a faint, redshifted component ( $\sim +400$   $\text{km s}^{-1}$ ) in the right-centre of the map. Furthermore, this component shows high ratios of  $[\text{N II}]/\text{H}\alpha$  ( $\sim 2$ ), as shown in panel (e). These ratios give an indication of fast outflows from the centre of NGC 4945, possibly further accelerated w.r.t. positions closer to the nucleus (cf. LS1 and LS2). Area-5 shows higher values of  $\text{H}\alpha/\text{H}\beta$  (13.6),  $[\text{S II}]/\text{H}\alpha$  (0.34),  $[\text{N II}]/\text{H}\alpha$  and  $[\text{O III}]/\text{H}\beta$  (0.53) than area-3. Hence, area-5 could represent a massive star-forming region.

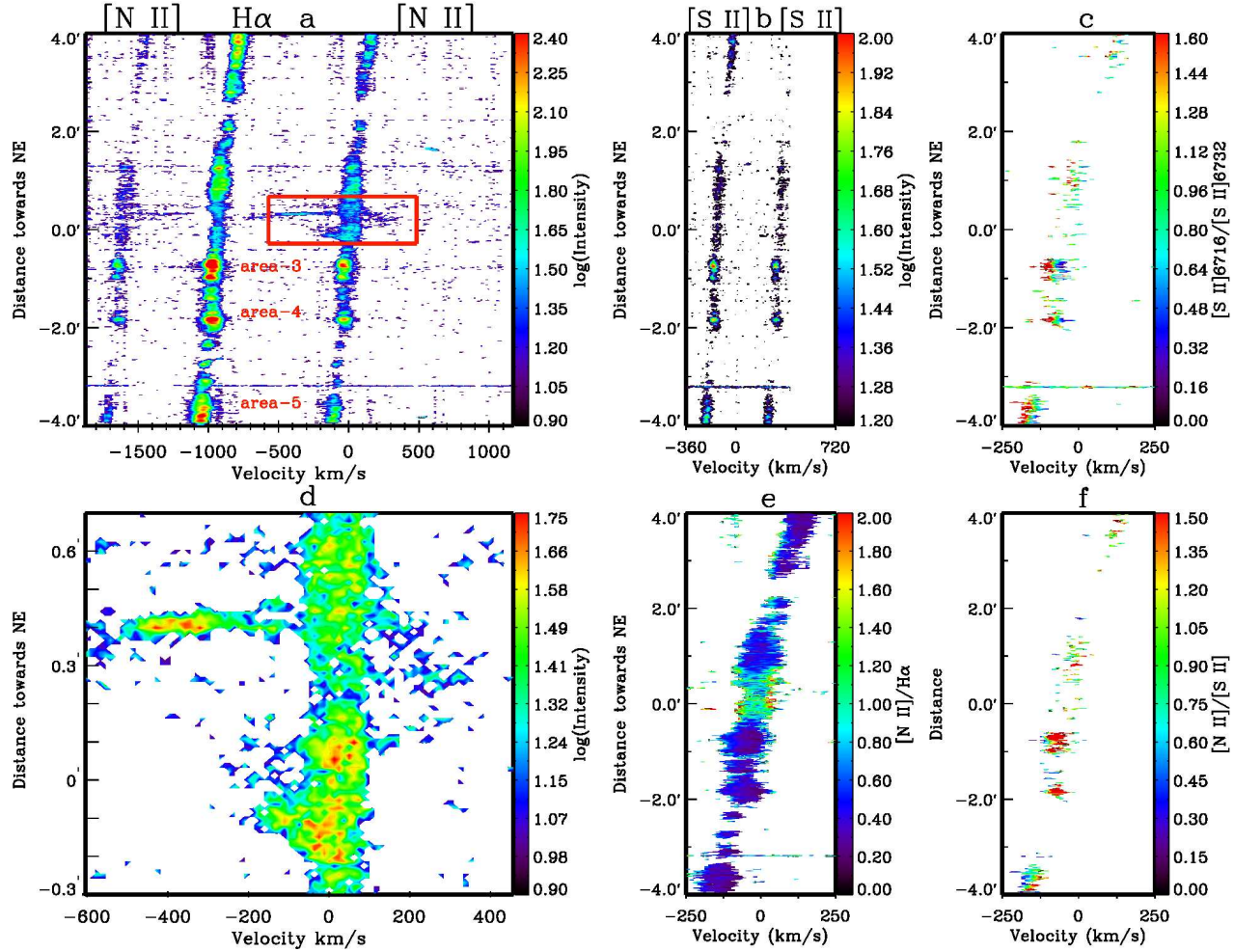


Figure 4.14: Panel (a): the spatial and kinematic maps of  $[\text{N II}]$  and  $\text{H}\alpha$  lines along the slit position (LS3). The wavelength axis is transformed into heliocentric Doppler velocity for the  $[\text{N II}]6583$  line; (b) presents  $[\text{S II}]$  lines; (c) ratio map of  $[\text{S II}]6716/[\text{S II}]6732$ ; (d) zoom into the red rectangular area in (a). (e) and (f) ratio of  $[\text{N II}]/\text{H}\alpha$  and  $[\text{N II}]/[\text{S II}]$  respectively. The long-slit (LS3) was oriented with  $\text{PA} = 45^\circ$  and shifted  $0.4''$  from the centre of the galaxy (parallel to the disc of NGC 4945). The North and East directions are as right panel of Figure 4.8.

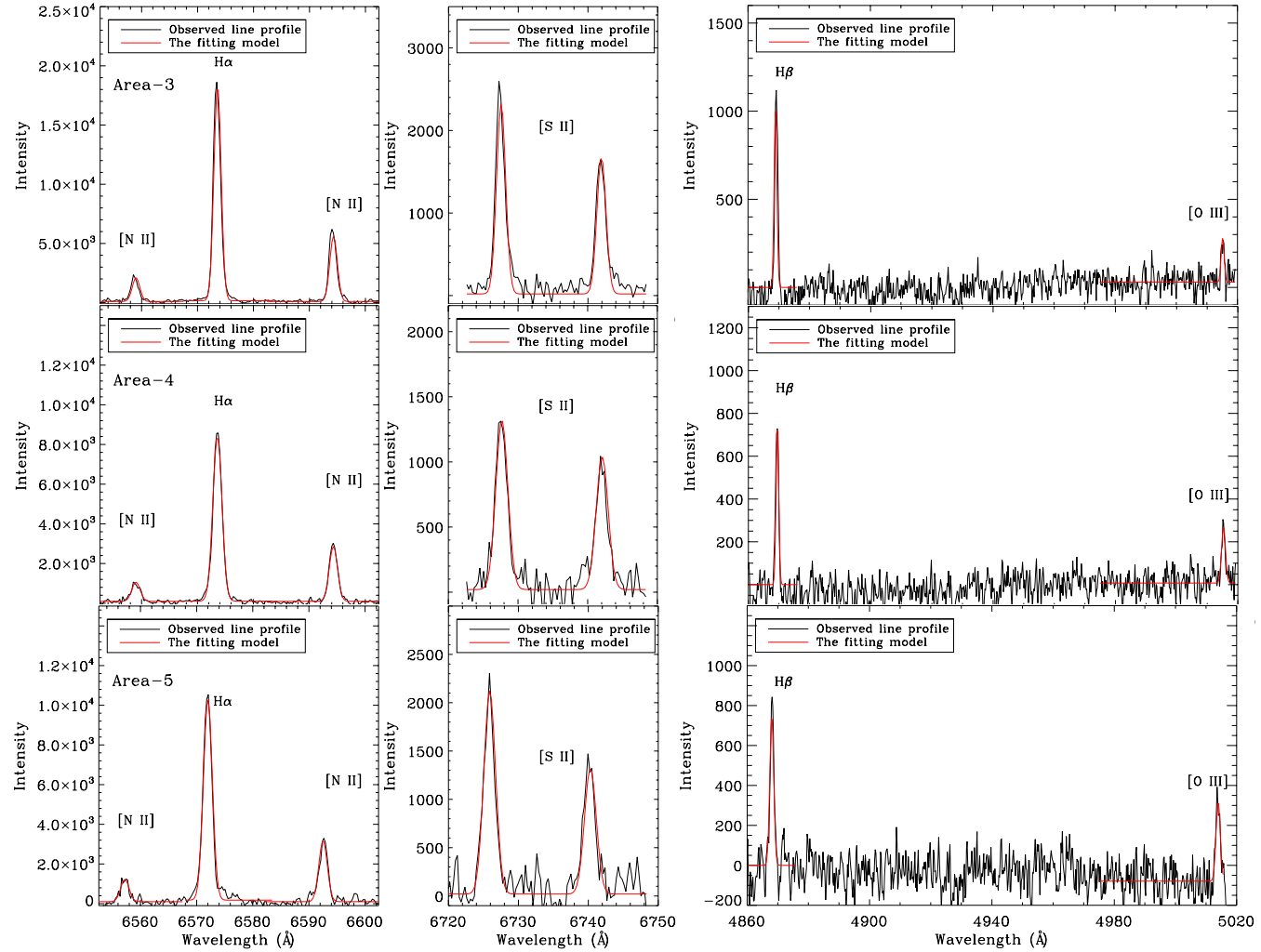


Figure 4.15: Left: spectrum of [N II], H $\alpha$  and fitted profiles; middle: spectrum of [S II] lines and fitted profiles; Right: spectrum of H $\beta$  and [O III] lines and fitted profiles; for three areas (area-3 ( $\Delta = 24''$ ), area-4 ( $\Delta = 24''$ ) and area-5 ( $\Delta = 32''$ )), which are labelled in Figure 4.14. The long-slit (LS3) was oriented with PA =  $45^\circ$ , with a shift of  $0.4$  towards NW.

Table 4.7: Emission line ratios, velocities and FWHMs for three objects (area-3, area-4 and area-5) along LS3 in NGC 4945.

Lines	area-3		area-4		area-5	
	v (km s <sup>-1</sup> )	FWHM (km s <sup>-1</sup> )	v (km s <sup>-1</sup> )	FWHM (km s <sup>-1</sup> )	v (km s <sup>-1</sup> )	FWHM (km s <sup>-1</sup> )
[N II]	-36 ± 3	73 ± 2	36 ± 3	80 ± 6	-117 ± 5	81 ± 6
H $\alpha$	-33 ± 3	70 ± 2	-33 ± 3	88 ± 4	-103 ± 4	86 ± 4
[S II]	-67 ± 4	66 ± 2	-61 ± 4	91 ± 2	-141 ± 4	84 ± 3
	ratio		ratio		ratio	
[N II]/H $\alpha$	0.11 ± 0.10		0.33 ± 0.06		0.30 ± 0.10	
[N II]/[S II]	1.39 ± 0.10		1.19 ± 0.02		1.10 ± 0.20	
[S II]/H $\alpha$	0.22 ± 0.01		0.28 ± 0.02		0.34 ± 0.03	
[O II]/H $\beta$	0.25 ± 0.10		0.35 ± 0.06		0.53 ± 0.03	
[S II]6716/[S II]6732	1.39 ± 0.14		1.27 ± 0.01		1.67 ± 0.02	
H $\alpha$ /H $\beta$	10.00 ± 1.80		11.38 ± 2.20		13.60 ± 1.92	

## 4.7 Discussion

In general, substantially ionized matter appears in various areas along the three slit positions. This material could be a shock-heated shell, after it has been swept out by an expanding hot bubble (Tomisaka & Ikeuchi 1988). As mentioned earlier, this extended material is the result of the collective effects of the stellar winds and supernovae (Chevalier & Clegg 1985). It is important to look for observational indications of superwinds across the observed area. Heckman, Armus & Miley (1990) summarized important evidence for the existence of GWs in three aspects: morphological, kinematical and physical. My discussion will be based on these three aspects.

### 4.7.1 Morphological and kinematical evidence

Figure 4.16 shows three different areas (panels (a), (b) & (d)) along the vertex of the cone at different distances from the centre. The area around the vertex at 270 pc from the centre of NGC 4945 (panel (d)) shows interesting kinematics and morphology. The [N II] emission peaks in three areas, although the upper and the lower one are equivalent to each other around the vertex. There are filaments that connect between two of these regions and extend away from the centre of the galaxy. The three bright regions may have been one object that was ruptured by winds. The connected filaments could be what remains from the interaction process.

The corresponding region on the vertex at 470 pc is less intense compared with the panel (d) and the region reveals blueshifted emission (brown arrow) with centroid velocity  $\sim -350 \text{ km s}^{-1}$  ( $\Delta v = -50$  to  $-650 \text{ km s}^{-1}$ ), and low intensity redshifted components appear (red arrows) with velocity  $\sim 300 \text{ km s}^{-1}$  ( $\Delta v = 70-390 \text{ km s}^{-1}$ ). There is noticeable, faint, diffuse emission to the bottom left of the map where a broadened area with blue-asymmetry appears with velocities between  $-350$  to  $-100 \text{ km s}^{-1}$ .

By comparing the distribution of the bright matter along LS2 and LS3 (see Figures 4.12 and 4.14) on both sides of the vertex, I conclude that nearly identical features were formed in the two halves of the cone within  $0'.4$  from the centre. However, differences in intensity between these structures and their counterparts would be related to the orientation of the cone with respect to the line of sight. In other words, a longer line of sight through the cone, includes more matter.

Panels (e) and (f) represent the cone structure of  $\text{H}\alpha$  and [N II] $\lambda 6583$  respectively. (see Figures 4.4 and 4.5). The appearance of emission in the area between filaments of the V-shaped structure is that of a split in their spectrum (see Figures 4.10 panels at  $0'.2$  and  $0'.33$ ). If one takes into account all the previous points, it can be concluded that the bright material represents a part of the wall of the ejected cone (front/back

side), where the GWs (AGN wind) interact with the ambient ISM.

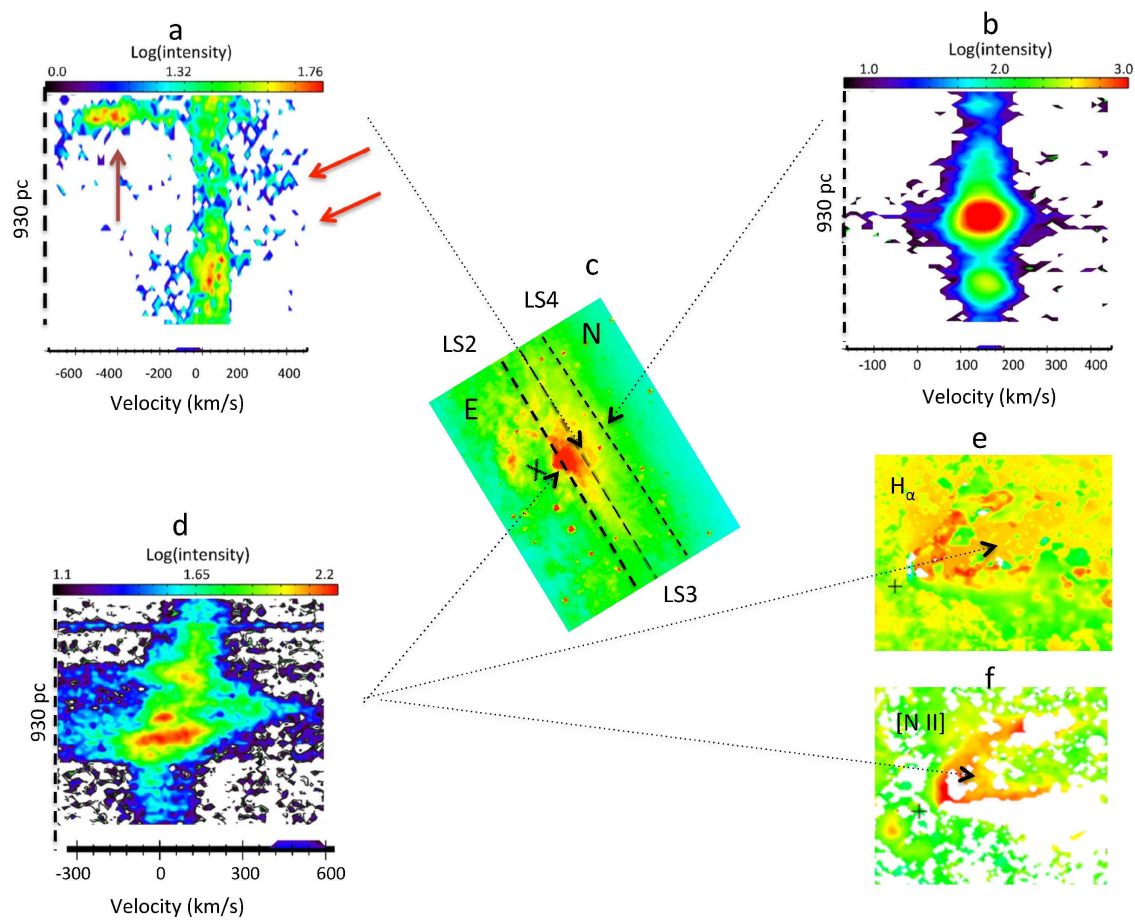


Figure 4.16: Three kinematic maps of  $[\text{N II}]\lambda 6583$  from successive regions along the vertex of the cone: (a) at 470 pc, (b) at 940 pc and (d) at 270 pc from the centre of NGC 4945. These three areas are from three different long-slit setting (LS3, LS4, LS2) respectively. Panel (c) shows the position of the three long-slit positions. (e) and (f) show intensity maps of the ejected cone by  $\text{H}\alpha$  and  $[\text{N II}]\lambda 6583$  respectively. The black cross symbol in (c) represents the centre of the galaxy.

## 4.7.2 Physical evidence

The [N II]/H $\alpha$  ratio varies widely among nine areas of interest that cover different positions on the cone, and ranges between 0.1 and 2.5. To interpret the variations in the ratio of [N II]/H $\alpha$  and [S II]/H $\alpha$ , the BPT diagrams will be used. Kewley et al. (2001) introduced a photoionization model by taking into consideration the effect of the stellar population and nitrogen enrichment, and determined a theoretical maximum limit for starburst models on the diagnostic BPT diagram. Kauffmann et al. (2003) suggested another curve to distinguish between objects that show low [N II]/H $\alpha$  ratio such as H II regions, based on observational data. Dopita & Sutherland (1995) introduced a shock model, that can reproduce a high ratio of [N II]/H $\alpha$   $\sim$  1.55 in solar abundance interstellar gas with magnetic parameter  $(B/n^2) \sim \mu\text{G cm}^{3/2}$  and shock velocity of 500 km s $^{-1}$ . The [N II]/H $\alpha$  ratios determined for the interesting objects are shown in the BPT diagram Figure 4.17. As mentioned before, only three objects show the [O III]5007 line in their spectra (area-1, area-2 and area-3), so the other objects are placed at  $\log([O III]/H\beta) = 0$  and shown with high error bars on the [O III]/H $\beta$  ratios.

The [N II]/H $\alpha$  ratio shows high values near the vertex of the cone in all components of the [N II] line, while [N II]/H $\alpha$  dramatically reduces in areas away from the vertex or away from the midplane to reach  $\leq 0.33$ .

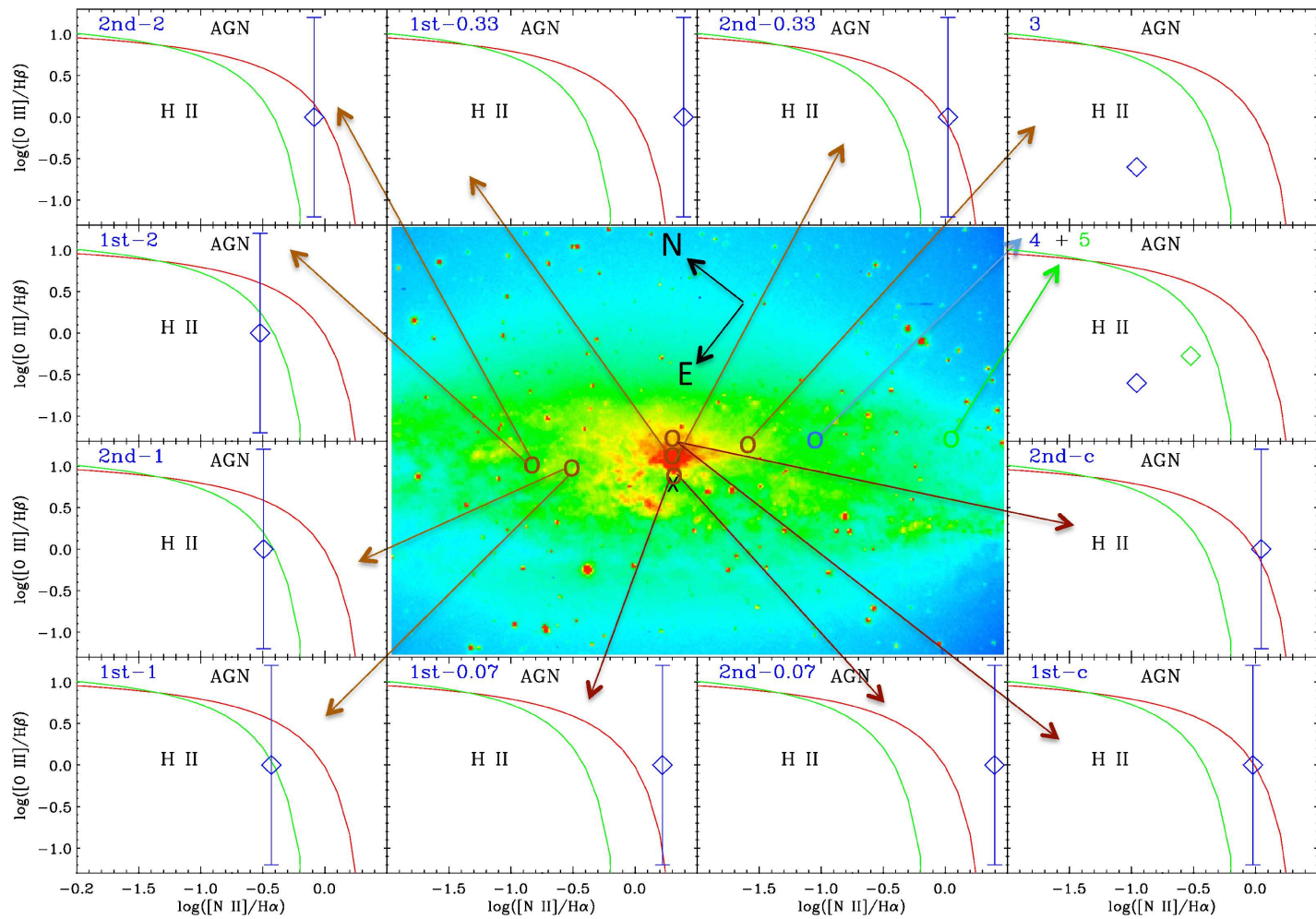


Figure 4.17: Distribution of nine objects covering different positions on the cone in the diagnostic BPT diagrams. The red line represents the Kewley curve which is used to distinguish between starburst regions and AGN (Kewley et al. 2001), and the green one represents the Kauffmann curve to separate between objects that have ionizing source power between AGN and starburst, such as weak AGN, post-AGB, or shocks by planetary nebulae (Kauffmann et al. 2003).

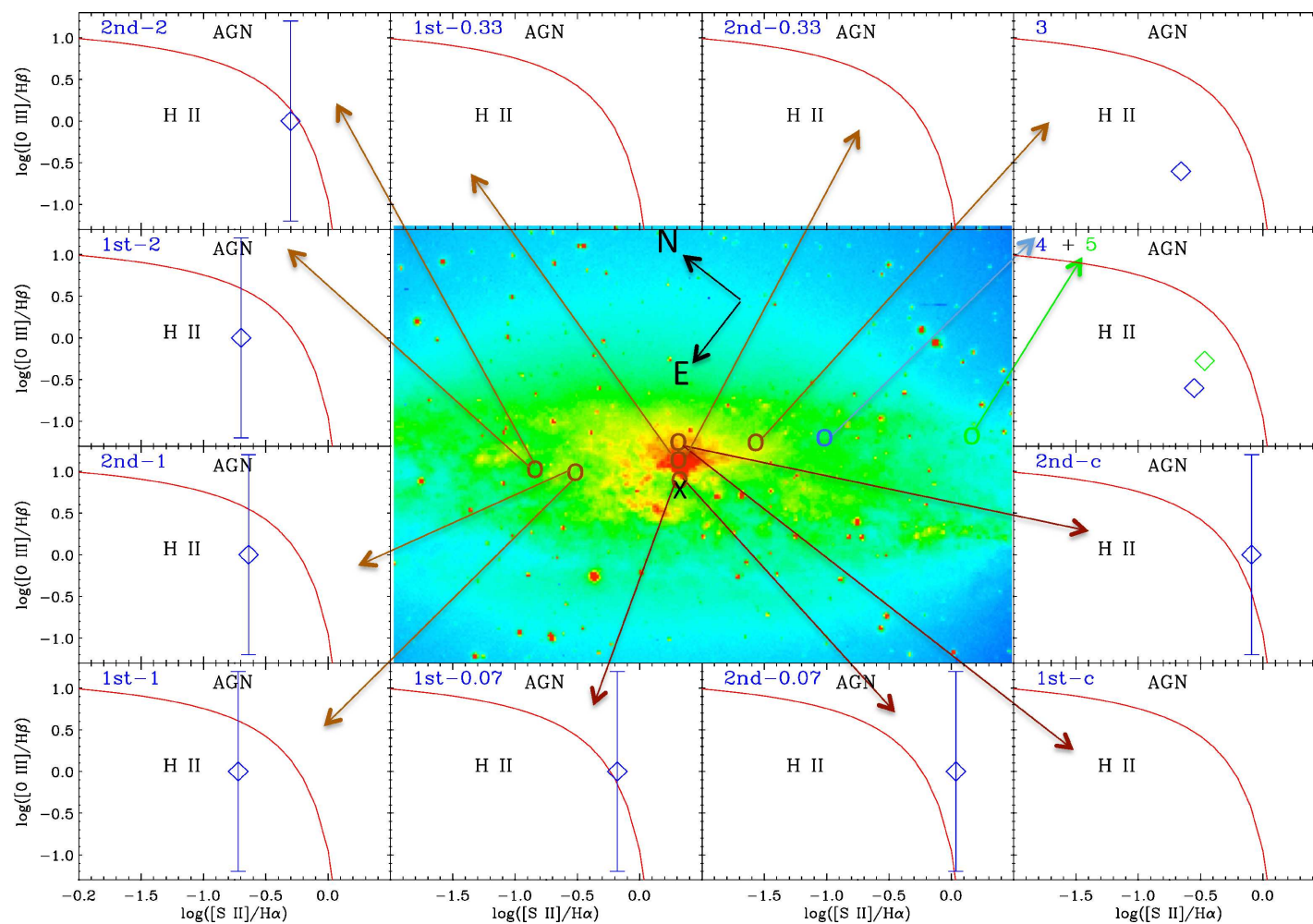


Figure 4.18: As Figure 4.17, but for  $[\text{S II}]/\text{H}\alpha$ .

The splitting was identified at  $0'.07$  from the centre to the NW, and the  $H\alpha$  and  $[N II]$  were fitted as two components. The ratio of  $[N II]/H\alpha$  for each component is  $1.36 \pm 0.20$  and  $1.13 \pm 0.21$  respectively. Hence, the physical conditions in this area suggest that the gas has experienced shock-heating. As mentioned previously,  $[S II]$  lines were fitted with one Gaussian component, the intensity of which was used to estimate the ratio of  $[S II]/H\alpha$  for the two components of  $H\alpha$  ( $0.741 \pm 0.16$ ,  $1.04 \pm 0.27$ ). These values are consistent with the typical ratios derived for Seyfert-2 nuclei and low ionization nuclear emission line regions (LINERs) (Veilleux & Osterbrock 1987). In the second region (at  $0'.33 \sim 760$  pc to the NW from the centre), the ratio of  $[N II]/H\alpha$  for both components is also consistent with what was determined in Seyfert-2 nuclei and LINERs. The line ratio of  $[N II]/H\alpha$  in the red rectangular area (see Figure 4.12) shows values which similar to in Seyfert-2 nuclei and LINERs, and displays a high value near the centre of the cone. Higher values ( $\sim 3$ ) are shown in the filamentary structures, which gradually reduce to 0.9 moving away from the vertex. Figure 4.18 shows the second part of the diagnostic BPT diagrams by comparing with the ratio of  $[S II]/H\alpha$ . Second components show ratios of  $[S II]/H\alpha$  that position them at the AGN boundary; this is consistent with the ratio of  $[N II]/H\alpha$  (see Figure 4.17). It can be concluded that the areas that show extreme kinematics and line ratios that are consistent with what is typical of an AGN environment.

The electron density was estimated in different parts of the cone. The electron density is high ( $\sim 2000 \text{ cm}^{-3}$ ) in areas with a high ratio of  $[N II]/H\alpha$ . Meanwhile, areas with lower  $[N II]/H\alpha$  have an electron density of  $10\text{--}100 \text{ cm}^{-3}$ . Area-1 has  $n_e \sim 1200 \text{ cm}^{-3}$  in the outer parts, while the central part displays low electron density  $n_e \sim (1\text{--}10) \text{ cm}^{-3}$ . Area-2 has  $n_e \sim 1000 \text{ cm}^{-3}$ . The average  $n_e$  in the red rectangular area is  $\sim 800 \text{ cm}^{-3}$  and is comparable to the value that was determined by Moorwood et al. (1996) in the same position. Note that the  $n_e$  in specific positions (boundaries) has  $n_e \geq 1200 \text{ cm}^{-3}$  while the inner positions have low  $n_e$  ( $100 \text{ cm}^{-3}$ ). These differences may be related to the impact of the outflows onto the surrounding ISM. In other words, the effect of collisional de-excitation plays an important role in this environment, as the relative excitation rate depends only on the ratio of collision strengths, and this is highly sensitive to the density (relative population of the two levels having almost the same excitation level and emitted from different energy levels).

### 4.7.3 Signatures of the second part of the bi-cone

$H\alpha$ ,  $[N II]6583$  and  $[S II]$  emission maps (see Figures 4.2 and 4.3) show bright regions to the E of the nucleus of NGC 4945, at  $\sim 470$  pc. As mentioned before, NGC 4945 shows a dusty environment in the central part and in the area to the SE of the centre. Therefore the material ejected from the active centre of the galaxy towards the SE is obscured by the approaching part of the disc which is in the line of sight is partially

obscured (second part of the bi-cone). The observed outflows are in front of the receding part of the disc, extending away from the midplane. Therefore, I expect the bright emission in areas to the E of the centre represents extended outflows from the centre.

To investigate these bright areas, new spectroscopic observations using LS were analysed. The emission lines  $[\text{N II}]\lambda 6583$  and  $\text{H}\alpha$  were mapped and are shown in Figure 4.19. Panel a shows the LS5 position and b represents a zoom into the black rectangular area. S1, S2, S3 and S4 represent different positions on the bright regions. The  $\text{H}\alpha$  line shows a second redshifted component which is obvious in all four positions. Likewise,  $[\text{N II}]$  shows a redshifted component in the four regions, which is clearer in S2 for both  $[\text{N II}]$  and  $\text{H}\alpha$ . These components would represent winds from the galaxy. To explore the properties of these areas, I use the BPT diagram to determine the ratio of forbidden line emission to the recombination line emission. Two parts of the BPT diagram are shown in Figure 4.19 panel d, S2 displays a ratio that is comparable to the ratio at the positions  $0'.07$  and  $0'.33$ , which is on the observed part of the cone. S2 shows high ratio of  $\log([\text{N II}]/\text{H}\alpha)$  and  $\log([\text{S II}]/\text{H}\alpha)$  that falls in the area of AGN. S1 falls in the area between soft ionizing sources and higher ionizing sources (AGN, shocks, ionization by post-AGB stars and planetary nebulae). S3 and S4 show values close to the Kauffmann curve (Kauffmann et al. 2003). Thus the emission line ratios of the examined regions suggest that the gas in this areas is undergoing a shock-heated as a result of the outflows from the active centre of NGC 4945 (AGN and starburst). According to the previous discussion, the expected shape of the ionized outflows from the centre of NGC 4845 shows a bi-conal structure, as shown in Figure 4.20.

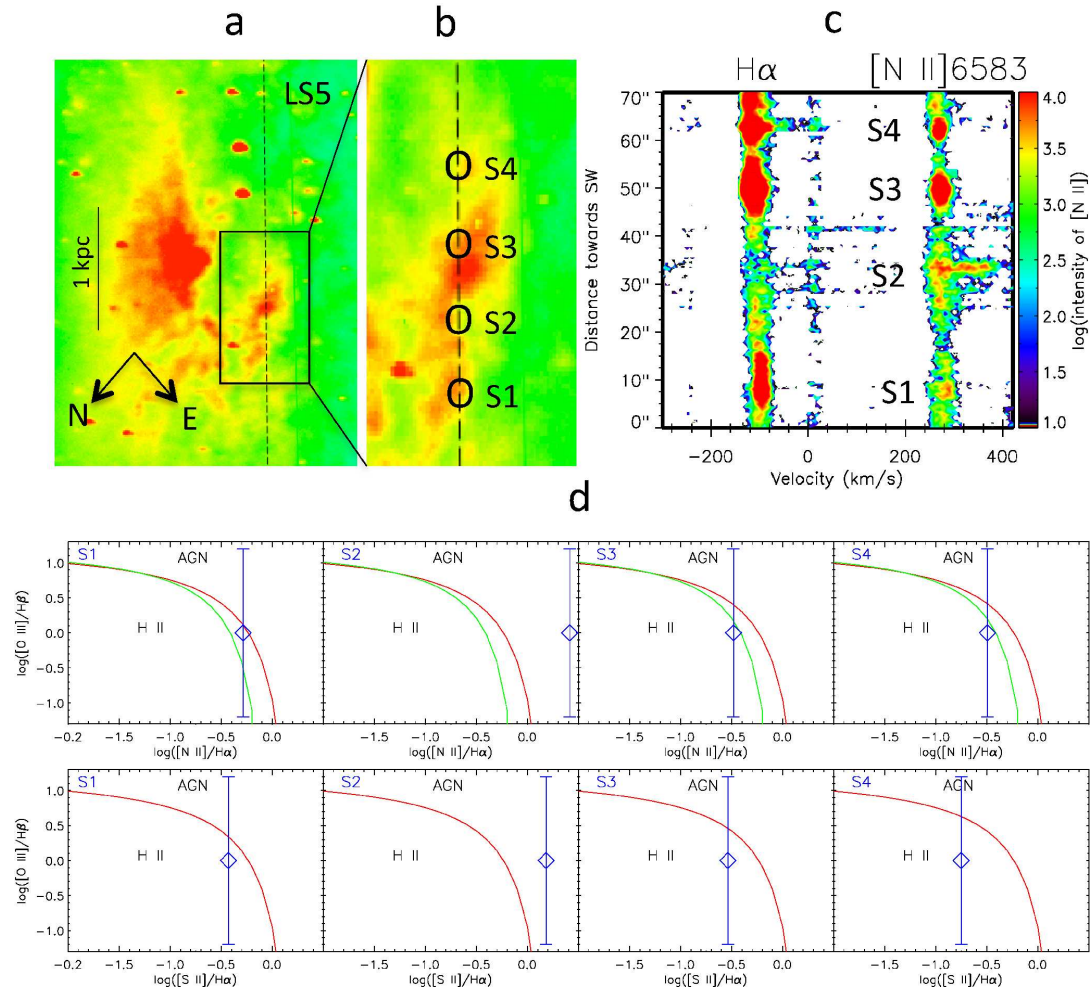


Figure 4.19: Panel a shows the position of LS5, and b zooms into the black rectangular area. Panel c represents the spatial and kinematic maps of  $[\text{N II}]\lambda 6583$  and  $\text{H}\alpha$ . The wavelength axis is transformed into heliocentric Doppler velocity for the  $[\text{N II}]\lambda 6583$  line. Panel d shows the distribution of four areas (S1, S2, S3 and S4) covering different positions on the second part of the bi-cone in the diagnostic BPT diagrams. The red line represents the Kewley curve (Kewley et al. 2001), and the green one represents the Kauffmann curve (Kauffmann et al. 2003).

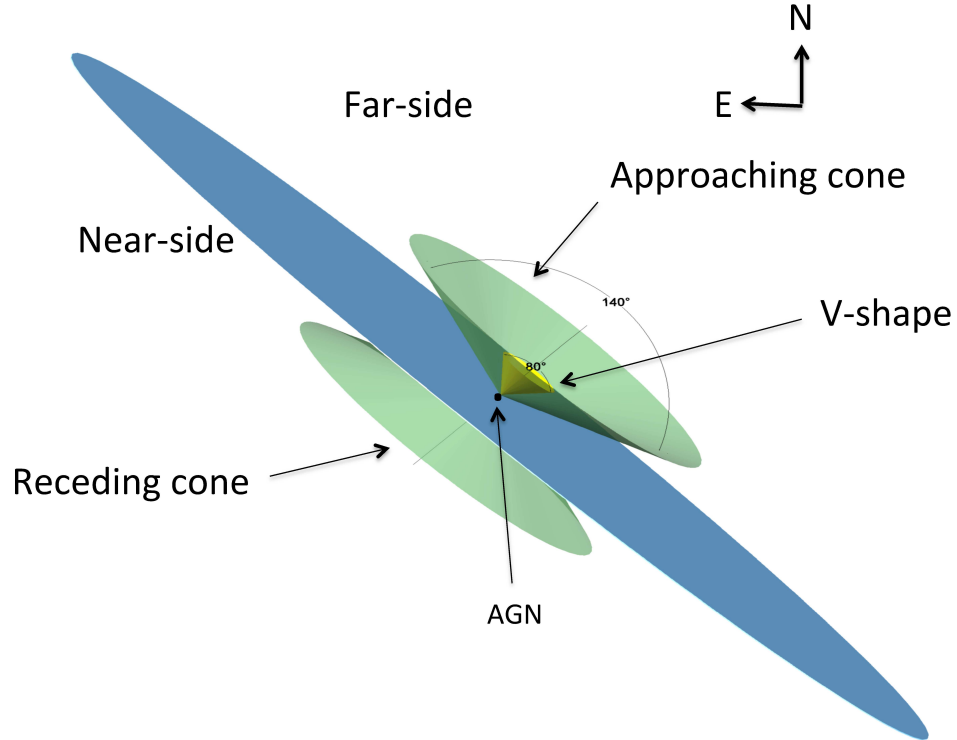


Figure 4.20: A simple model of NGC 4945 showing the emerging cone from the centre of the galaxy with inclination  $80^\circ$  w.r.t. the line of sight, and opening angle =  $140^\circ$ . The V-shaped structure which is suggested to be filled with gas, is shown with a yellow cone having opening angle =  $80^\circ$ . The unobserved part of the bi-cone is shown in the model, which has the same dimensions and structures of the observed part.

## 4.8 Conclusions

I have presented a spectroscopic study (spectral resolution  $0.75, 1 \text{ \AA}$ ) using long-slit observations with the instrument RSS@SALT. The aim of this chapter was to investigate the physical properties and kinematics of the ejected optical cone from the nuclear region in the edge-on NGC 4945 galaxy, to quantitatively examine its origin. The observing setup of the long-slit allows us to examine different positions along the optical cone. The spectra of the emission lines show interesting signatures of GWs including: a split in different emission profiles in different position on the cone; outflows with high velocity and FWHMs reaching to  $-350 \text{ km s}^{-1}$  and  $400 \text{ km s}^{-1}$  respectively. The

ejected cone shows physical properties of various environments. The outflows in the central area originate from AGN and starburst sources. The line ratios across the cone show environments of both AGN and starburst.

# Chapter 5

## The disc–halo interaction in edge-on galaxies

### 5.1 Introduction

In this chapter I will introduce a long-term project that needs more observations to complete; 9 nearby (redshift ( $z$ )  $< 0.02$ ) galaxies will be introduced, from a survey comprising a sample of 36 Southern edge-on disc galaxies<sup>1</sup>. This sample was selected by Stanchev, Nedialkov & Georgiev (2004), to calibrate the Tully–Fisher relation. This is a relation between the (distance-independent) rotational velocity and the (distance-independent) *absolute* magnitude of spiral (i.e. rotationally-supported as opposed to pressure-supported) galaxies. Stanchev et al. used the width of the 21-cm H I line profile to determine the rotational velocity, but this would be dependent on the inclination of the rotating disc of the galaxy. To minimise the uncertainties arising from the inclination effect, and to maximise the observed line width, they chose a sample of galaxies that are viewed (nearly) edge on. The main objective of our survey is to study outflows from H II regions or AGN by tracing Balmer recombination emission lines, as well as to study dusty extraplanar gas blown by galactic winds.

Edge-on galaxies offer an excellent opportunity to separate the disc, ionized extraplanar and halo components. The attenuation by interstellar dust can be mapped for both disc and extraplanar regions by using the Balmer decrement ratio ( $H\alpha/H\beta$ ). The selected galaxies cover a wide range of morphological types, from S0 through Sa to Sd. The variety of morphological types will offer a good opportunity to examine the above diagnostics as a function of morphological type. The same sample was observed by me and the supervisor with the Parkes radio telescope<sup>2</sup> to trace the hydrogen radio recombination lines emission near 8 GHz. The radio recombination lines arise from transitions between energy levels with large value of  $n$ . In this study the traced recombination lines are H91 $\alpha$ , H92 $\alpha$  and H93 $\alpha$ . The number represents the lower energy level of the transition and the Greek letter,  $\alpha$ , represents  $\Delta n = 1$ . Both surveys will offer complementary information that will enable us to estimate the total ionized gas mass within spiral edge-on galaxies. It will also be possible to introduce necessary corrections for optical emission lines to derive star formation rates in high redshift galaxies,

---

<sup>1</sup>See Appendix Table E.1 for the full sample.

<sup>2</sup>The radio observations were carried out from 7–13 Oct. 2016 for 72 hours.

and thus determine the history of cosmic star formation and study the evolution of spiral galaxies along the Hubble sequence.

Table 5.1: Basic information about the nine edge-on galaxies from the sample, observed in the first stage of the survey, the position angle (PA) is measured from the North.

Name	Morphological type	Radial velocity km s <sup>-1</sup>	Distance Mpc	Inclination degrees	PA degrees	Absolute magnitude mag
NGC 4672	Sa	3289	39.9	75	-85.9	-22.03
ESO 202-G35	Sc	1601	23.5	80	85.2	-20.79
ESO 575-G61	Sc	1588	27.0		-116.8	-18.40
ESO 505-G03	Sc	1497	15.9		-112.3	-19.10
ESO 506-G02	Sb	5729	78.8		-110.4	-22.40
ESO 321-G10	Sb	2988	30.7		-93.7	-21.72
ESO 33-G22	Sc	4346	50.5		85.7	-20.40
ESO 311-G12	Sa	1128	5.3		93.7	-20.18
IC 1963	Sab	1638	27.0		189.7	-19.52

## 5.2 Observation and data reduction

The observations were made with the RSS (Robert Stobie Spectrograph) Fabry-Pérot single etalon with low-resolution (LR;  $R \sim 700$ ). These galaxies are nearby and extend  $1' - 4'$  along their major axes, so one FP field of view perfectly covers each of them. The systemic velocity was taken into account to determine the wavelength steps required to cover the Doppler-shifted profile in each galaxy. The goal of this chapter is to study the distribution of the ionized emission as a function of height above/below the midplane, so the Doppler-shifted peak would not need to be traced. Therefore, four wavelength steps ( $scan - 2$ ,  $scan - 3$ ,  $scan - 4$  and  $scan - 5$ ) were chosen spanning the emission profile, and in order to subtract continuum emission that originates from the background galaxy and stars within the galaxy or foreground stars, two scans ( $scan - 1$ ,  $scan - 6$ ) were taken in the continuum range on the blue and red side of the profile as shown in Figure 5.1. Details of the observations are summarized in Tables 5.2 and 5.3. The data reduction for the FP instrument was discussed in detail in chapter 1.5.

Because the continuum scans are not at the same distance on either side as they were chosen to avoid spectral features, we found the best way to determine the continuum emission was by interpolating the continuum in the right wavelength by using the following formula:

$$scan_c = scan - \left( \frac{\lambda - \lambda_1}{\lambda_6 - \lambda_1} \right) \times (scan_6 - scan_1) \quad (5.1)$$

where:

$scan_c$  = subtracted continuum scan.

$\lambda$  = wavelength of each scan.

The direction of the rotation in these galaxies can be determined by comparing the observed intensity through the continuum-subtracted  $scan - 2$  (tracing blue-shifted emission (B)) and that from the continuum-subtracted  $scan - 5$  (tracing red-shifted emission (R)). Figure 5.5 shows the ratio of B/R in the sample of the galaxies. The side of the nucleus showing a high ratio of B/R will represent the approaching side of the galaxy while a lower ratio will appear in the receding part of the galaxy.

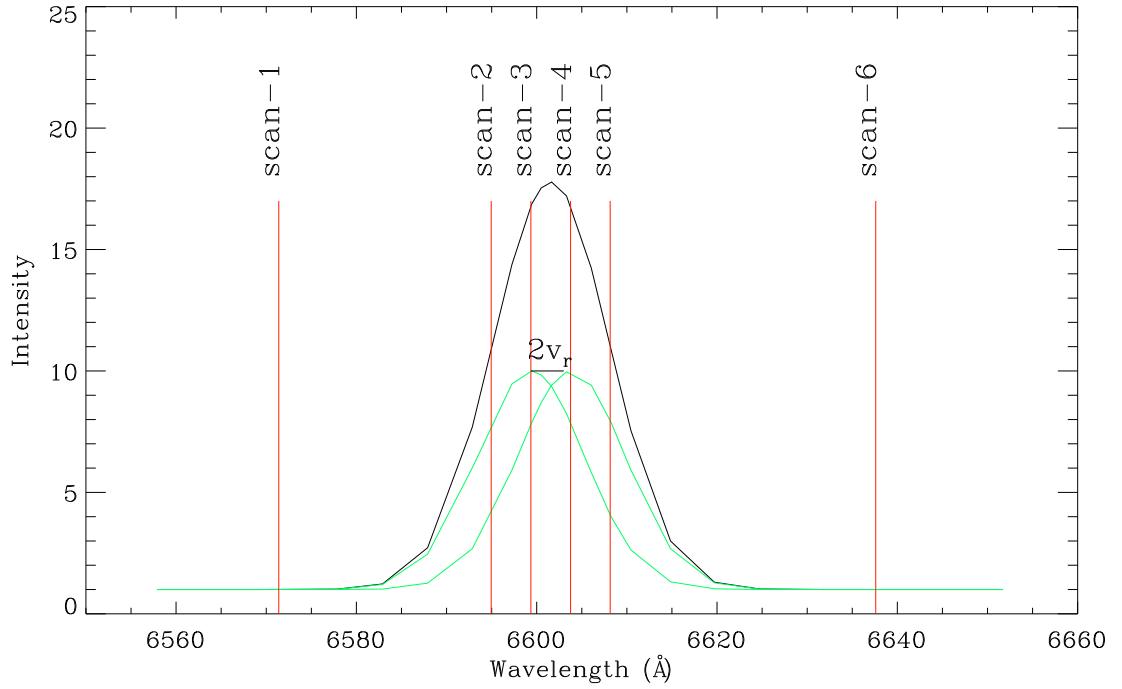


Figure 5.1: A schematic diagram showing the positions (wavelengths) of the scans of FP covering the emission profile and continuum in ESO 575-G61. *Scans* – 2 to –5 span the emission line and *scan* – 1 and *scan* – 6 are used to determine the continuum.

Table 5.2: The main parameters of the H $\alpha$  observations, using the Fabry-Pérot LR mode.

Galaxy	Date of observation
NGC 4672	25 <sup>th</sup> February 2017
ESO 202–G35	26 <sup>th</sup> February 2017
ESO 575–G61	25 <sup>th</sup> February 2017
ESO 505–G03	25 <sup>th</sup> February 2017
ESO 506–G02	25 <sup>th</sup> February 2017
ESO 321–G10	25 <sup>th</sup> February 2017
ESO 33–G22	9 <sup>th</sup> January 2018
ESO 311–G12	9 <sup>th</sup> January 2018
IC 1963	8 <sup>th</sup> January 2018
Telescope	SALT
Instrument	RSS
Detector	E2V CCD 44-82 chips
Mode	Fabry-Pérot
Étalon separation	0.6 nm
Resolving power	700
Free spectral range (Å)	8.64
Filter	PI06645
Steps	6
Exposure time (seconds/step)	100.2
Pixel scale	0''.5068
Seeing	~2''

Table 5.3: Étalon configuration wavelength for the Fabry-Pérot H $\alpha$  observations of the sample of galaxies with LR.

Galaxy	NGC 4672	ESO 202-G35	ESO 575-G61	ESO 505-G03	ESO 506-G02	ESO 321-G10	ESO 33-G22	ESO 311-G12	IC 1963
No. of scan	Wavelength (Å)								
1	6606.85	6576.10	6571.39	6573.80	6621.70	6603.00	6610.87	6630.02	6570.62
2	6630.40	6599.65	6594.95	6597.35	6645.25	6626.00	6653.67	6653.58	6594.18
3	6634.80	6604.05	6599.35	6601.75	6649.65	6631.00	6657.98	6657.89	6598.78
4	6639.20	6608.45	6603.75	6606.15	6654.05	6635.65	6662.29	6662.49	6603.10
5	6643.60	6612.85	6608.15	6610.54	6658.45	6640.05	6666.90	6666.78	6607.40
6	6673.05	6642.30	6637.60	6640.00	6687.90	6669.50	6696.20	6696.11	6637.00

## 5.3 Results

Maps of  $H\alpha$  intensity for nine nearby edge-on galaxies in the sample were constructed and are shown in Figures 5.2 to 5.4. The  $H\alpha$  intensity was determined by integrating the four scans which cover the emission line profile, after subtracting continuum emission from each scan.

All the disc galaxies in the sample show signs of an ionized extraplanar (IEP) layer that extends away from the midplane. The IEP layer takes different forms, such as outflows from star formation regions, filament structures, or extended emission from the central area, as shown in the left panels of Figures 5.2 to 5.4; more discussion will be provided later on.

The continuum emission from stars within each galaxy or in the foreground was mapped and is shown in the middle panels of Figures 5.2 to 5.4. The continuum emission is remarkably intense in the disc, in particular in the central and surrounding regions, and reduces gradually away from the midplane. The ratio of  $H\alpha$  to continuum ( $H\alpha/C$ ) was constructed and is shown in the right panels of Figures 5.2 to 5.4. There is very little information in the literature about these galaxies. Therefore, in the next subsections, the morphology of each galaxy will be discussed in detail.

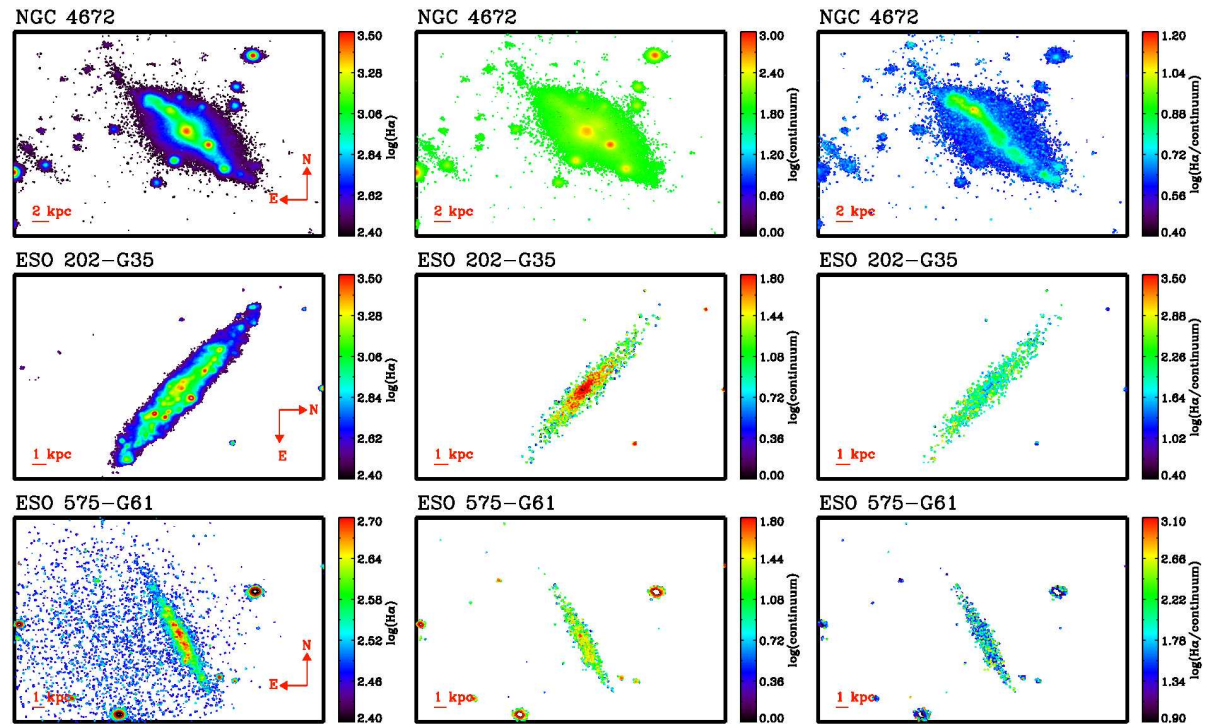


Figure 5.2: Maps show the H $\alpha$  emission (left panels), continuum (middle panels), H $\alpha$ /Continuum (right panels) in NGC 4672, ESO 202-35 and ESO 575-G61.

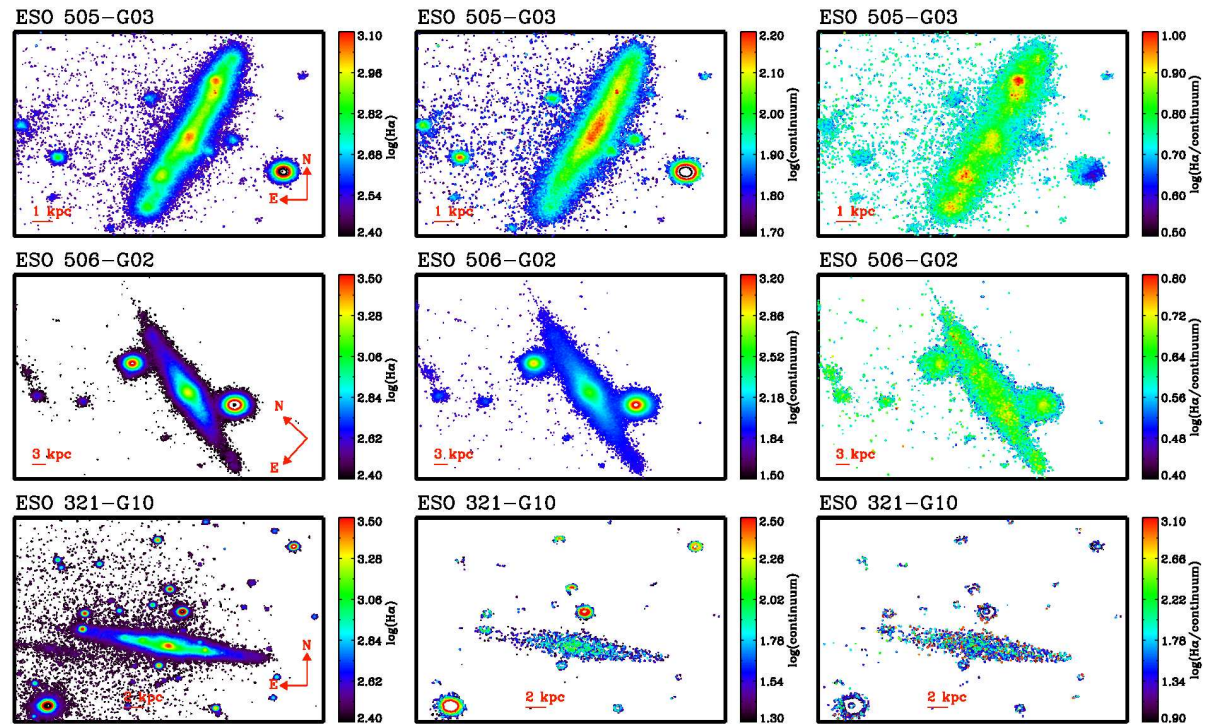


Figure 5.3: as Figure 5.2, but now ESO 505-G03, ESO 506-G02 and ESO 321-G10.

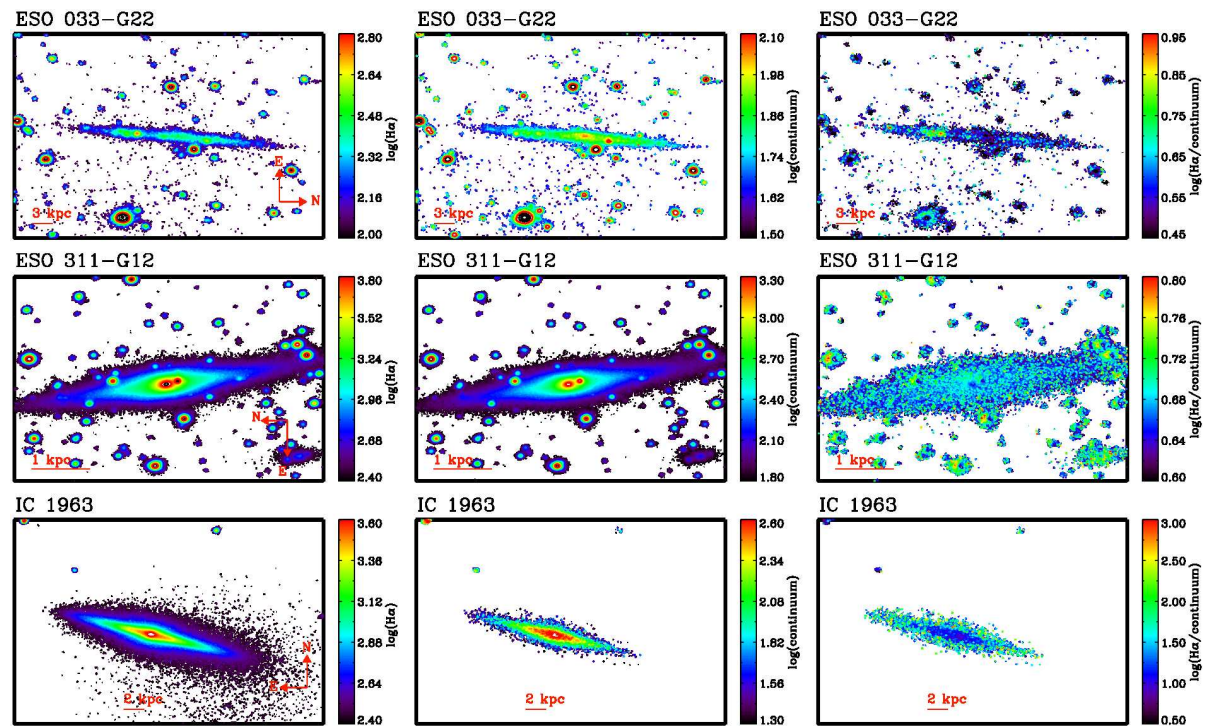


Figure 5.4: as Figure 5.2, but now ESO 033-G22, ESO 311-G12 and IC 1963.

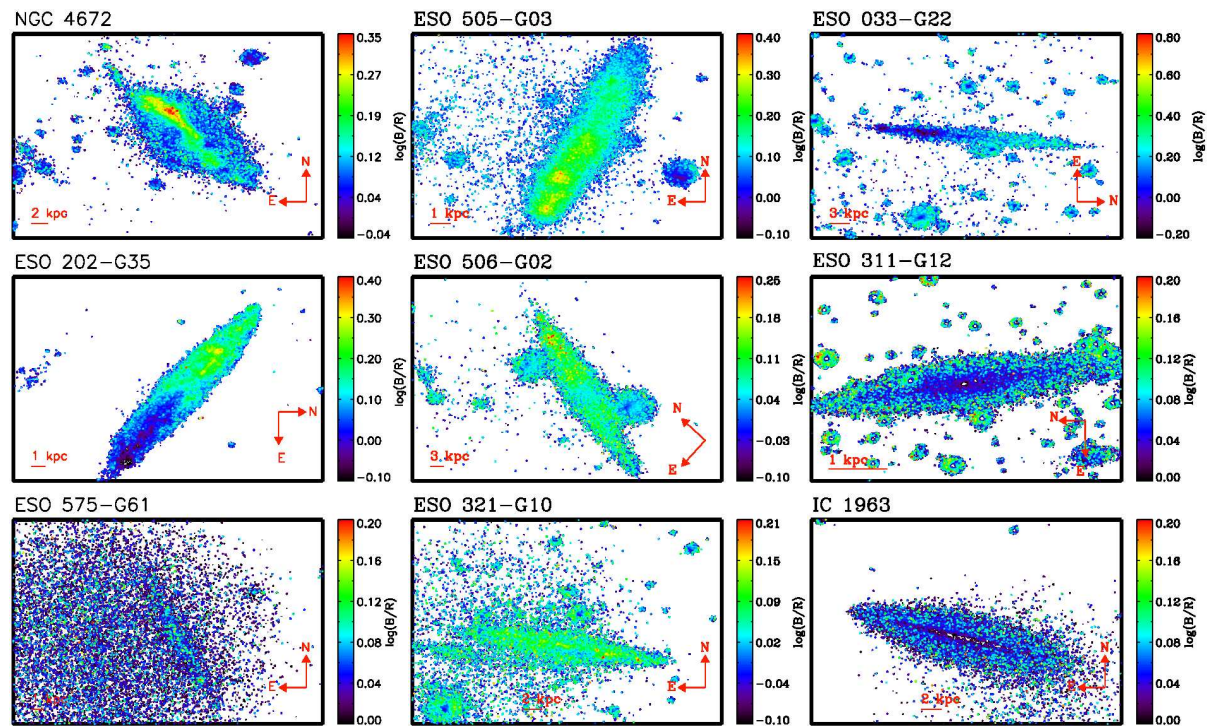


Figure 5.5: Maps show the ratio of the tracing blue-shifted emission to red-shifted emission in the sample of galaxies.

### 5.3.1 Morphological structures of the ionized emission

In order to emphasize some worthy details of the extraplanar diffuse ionized gas, a comparison with other observations was done, where these observations were accessible from the literature.

#### 5.3.1.1 NGC 4672

The early-type spiral galaxy NGC 4672 (see Figure 5.2) shows a distinguished bulge and asymmetric H $\alpha$  emission across the midplane. The ionized gas extends to more than 1.4 kpc (corrected for inclination,  $i = 75^\circ$ ) away from the midplane and form a clear disc along the midplane and this does not happen with the continuum emission. The H $\alpha$  emission shows high values in the centre of the galaxy and in an area to the NE of the centre which represents a giant H II region in the spiral arm of the galaxy, while the bright area to the SE of the centre could be cluster stars but not H II regions<sup>3</sup>. The ratio of H $\alpha$ /C is high along the bright ionized spiral arm and low in the rest of the disc. The bright area that was mentioned before displays a higher H $\alpha$ /C while the second one shows a ratio that is comparable to that elsewhere in the disc.

NGC 4672 shows a distinguished bulge which sticks out perpendicularly from the plane of the disc (Sarzi et al. 2000), however it was not obvious in H $\alpha$  (Figure 5.2). It shows a complicated dust pattern which crosses the bulge near its centre (Bertola & Corsini 2000), and the stellar velocity field of NGC 4672 includes a central zero-velocity plateau along the major axis of the galaxy. Meanwhile the velocity has a steep gradient along the minor axis. In other words, the inner regions of the bulge are rotating perpendicularly to the disc (Sarzi et al. 2000). The NE side of the galaxy represents the approaching side, as the B/R is more intense to the E of the nucleus (see Figure 5.5).

#### 5.3.1.2 ESO 202-G35

Considerably pronounced is the distribution of strong H II regions and knots which are seen all over the disc (see Figure 5.2 middle panels). The ionized gas is extended over  $\sim 1$  kpc from the midplane, while the faint IEP extends to about 2 kpc above and below the midplane, as this galaxy has inclination angle  $\sim 80^\circ$ . The continuum dominates in the inner disc while there is no H $\alpha$  emission in the centre of the galaxy. Hence, this galaxy does not show any nuclear activity.

---

<sup>3</sup>I did not find supporting information about this area through using Vizier.

ESO 202-G35 exhibits a warped disc in the optical, but it does not show any signatures of a warp in the near-infrared (Guijarro et al. 2010).

Some of the nearby edge-on galaxies show IEP resulting from bright star formation regions as nodes and filaments which represent a disc–halo interaction layer. Such as, in NGC 55, the IEP extends between 1.1 kpc and 2.2 kpc (Rueff et al. 2013) and in NGC 4013 extends to  $\sim 860$  pc (Rueff et al. 2013). The extended ionized gas in ESO 202-G35 would be the result of high star formation in the disc of this galaxy.

### 5.3.1.3 ESO 575-G61

This galaxy (Figure 5.2 bottom panels) shows IEP that is extended to more than 1.6 kpc above and below the midplane (the inclination angle of this galaxy is not determined but looks to be high). In the area that is near to the midplane a prominent structure with bright  $H\alpha$  emission is seen, which turns and splits from the original disc to reach  $\sim 700$  pc. On the other side of the galaxy there are less intense areas which represent H II regions. and less extended towards the opposite side of the disc (see Figure 5.2 bottom panels).

The continuum emission from the stellar disc, emitted by stars, is less extended compared to  $H\alpha$  emission. The former has a higher value in the central area of the midplane and reduces gradually. The ratio of  $H\alpha/C$  of this galaxy shows highly ionized gas in specific areas which reveal distinct regions where star formation takes place. Overall, star formation appears to be concentrated in the inner disc, but without a central enhancement. The approaching side of the galaxy is not clear in the B/R map (see the bottom left panel of Figure 5.5).

### 5.3.1.4 ESO 505-G03

Vertically extended ionized gas is shown in this edge-on galaxy (see Figure 5.3 upper panels), which appears to be boxy in shape and extends to  $\sim 1$  kpc away from the midplane. The  $H\alpha$  forms a distinguished ionized disc whose intensity declines away from the midplane. The emission peaks in a few areas, including the centre of the galaxy and H II complexes along the disc. The continuum is highly concentrated in the central area and reduces gradually outward from the centre in the four directions (N, E, S and W). The  $H\alpha/C$  is low in the central area which probably shows a tentative sign of nuclear activity, while the  $H\alpha/C$  in H II regions is high. Figure 5.5 (middle left panel) shows the B/R ratio in this galaxy; the SE side of the galaxy represents the approaching side of the galaxy.

### 5.3.1.5 ESO 506-G02

This galaxy shows high  $H\alpha$  emission in different regions (see Figure 5.3 middle panels); two to the NE from the centre and the centre itself shows high  $H\alpha$  emission, as well as this in the opposite side of the disc another bright area appears. The centre is dominated by the continuum and shows an asymmetrical distribution which is more extended to the NE than to the SW side of the bulge. The ratio of  $H\alpha$  emission to the continuum is shown in Figure 5.3 too. The highest emission is concentrated in areas with a high star formation rate (the centre and H II regions). The two bright objects to the N and S of the disc represent foreground stars. The  $H\alpha/C$  is high in specific areas which maybe represent H II regions in the disc, and the centre has a lower ratio. The map of B/R does not help to determine the approaching part of the galaxy.

### 5.3.1.6 ESO 321-G10

This galaxy has a bright nucleus with thin IEP up to 700 pc, as well as a few ionized patches on either side of the disc. The extended, ionized gas is obvious around bright H II regions and does not show a continuous distribution along the disc. ESO 321-G10 may be undergoing low star forming activity, because the extraplanar emission occurs only in a few locations where the star-formation is locally high. The continuum emission appears more extended than  $H\alpha$  emission in the centre (see Figure 5.3). The  $H\alpha/C$  is not clear in this galaxy (see Figure 5.3 bottom right panel). The approaching side of the galaxy is not clear in the B/R map (see middle bottom panel of Figure 5.5).

### 5.3.1.7 ESO 033-G22

ESO 33-G22 displays clumpy ionized emission (see Figure 5.4 upper panels). It is remarkably asymmetric w.r.t. the central bulge, extending to  $\sim 1.2$  kpc to the South of the nucleus. Meanwhile, to the N side it reduces to a few hundreds of pc. The bulge itself is not conspicuous in  $H\alpha$  but prominent in stellar light. The ratio of  $H\alpha$  emission to the stellar light is high to the SW where H II complexes appear, and there is no sign of nuclear activity in this galaxy. The approaching side of the galaxy is obvious in the B/R map (see upper right panel of Figure 5.5).

### 5.3.1.8 ESO 311-G12

ESO 311-G12 shows smooth, extended ionized emission that is symmetrical and extends to above and below the midplane (Figure 5.4). The  $H\alpha$  emission appears to trace the

stellar continuum light. It is not clear which is the approaching side of the galaxy in the B/R map, I suggest that results from low rotation of the galaxy (see middle right panel of Figure 5.5). It appears to show a two-component structure: a mid-plane with a low value of  $\log(B/R)$  and an extended layer with a high value of  $\log(B/R)$ , which could represent a sign of extraplanar emission ( $H\alpha$  emission) which does not follow the rotating pattern of the disc.

### 5.3.1.9 IC 1963

The  $H\alpha$  emission shows magnificent morphology which has a smooth density distribution that decreases away from the midplane. The areas above and below the centre of the galaxy shows high  $H\alpha$  emission compared to the areas to the N and S of the centre. The continuum map (middle panel of Figure 5.4) shows higher values in the central area with two peaks and declines to the N, S, E, and W. The ratio of  $H\alpha/C$  shows low values in the central part of the disc and higher values in the boundaries of the disc. Perhaps the ionized gas enhances away from the central area because there are more H II regions in the outer parts of the disc. The approaching part of the galaxy is not clear in the bottom right panel in Figure 5.5, that may be due to the low rotation of the galaxy. This galaxy shows two components (midplane and extended layer). The latter one would be an extended IEP, as  $H\alpha$  emission is more vertically extended than the continuum. As well as this, the map of  $\log(B/R)$  has a high value in the second component which suggests high emission that is not affected by the rotating disc.

## 5.4 Discussion

All galaxies in this study show clear signatures of ongoing disc–halo interaction by displaying an obvious ionized, gaseous layer which is extended above the outer disc, akin to the Reynolds layer in the Milky Way (Reynolds 1990). Typically, this layer appears as a result of internal or external processes, such as AGN, starburst, high SFR. In this sample of spirals, the disc–halo interactions are most likely caused by internal processes. There are no clear signs of companions for these galaxies to act as sources of accretion or merging material, or other processes. In general, these galaxies show different morphologies in the extraplanar material, from clumpy to smooth intensity distributions.

A large fraction of nearby edge-ons display thick extraplanar material composed of gas and dust with sub-to several kiloparsecs thickness, which can represent transition layers that separate the thin disc from the hot halo (Bizyaev et al. 2017). Observations of individual spiral galaxies (such as NGC 3628, NGC 4522 and NGC 4013) show

strong indication for recycling matter between the disc and halo. The edge-on galaxies: ESO 311-G12 and IC 1963 show extraplanar H II regions at a projected distance range from 900 pc to 3 kpc from the midplane. The low-metallicity gas in these H II regions compared to the gas close to the midplane indicates that they would have formed in the disc, or may have come from the disc material through recent fountain-driven processes (Howk et al. 2018; Stein et al. 2017). The presence of the ionized extraplanar layer is usually due to strong SF activity in the galaxy discs (Rand 1996; Rossa et al. 2008; Arribas et al. 2014), or a high activity in the centre of the galaxy such as starburst or AGN, which is usually regarded as another source of outflows such as bi-cone or bubble structures (Heckman, Armus & Miley 1990). Different theoretical scenarios were suggested to explain the method in which the gas transports from the disc into the halo, such as chimneys (Norman & Ikeuchi 1989), galactic fountains (Shapiro & Field 1976), or superwinds (Heckman, Armus & Miley 1990). Jo et al. (2018) found a correlation between the scale height of the IEP emission and dusty extraplanar layer normalized to the galaxy size and SFR.

Only 40% of an H $\alpha$  imaging survey of 74 nearby edge-on galaxies shows that the extraplanar diffuse emission is extended to a mean distance of 1–2 kpc above and below the midplane, and isolated filaments can be detected at  $|z| < 6$  kpc in a few galaxies (Rossa & Dettmar 2003). This confirms the idea that the star formation activity in the underlying disc plays an important role in creating the diffuse extraplanar emission. Disc–halo interaction is not a general phenomenon in all normal spiral galaxies, as the presence of diffuse extraplanar gas is correlated with the activity of the star formation in the disc, as galaxies with low SF activity would not show any outflows. As well as this, not all later-type galaxies (Sa–Sb) show strong evidence of disc–halo interaction, such as IC 4351 (Rossa & Dettmar 2000). Emission lines such as H $\alpha$ , H $\beta$ , [O II], [O III], [N II], and [S II] have been traced to about 4 kpc above and below the midplane by analysing the stacked spectra of 49 later-type spiral galaxies (MaNGA IFU survey), and 9 of these galaxies show extended extraplanar gas to about 9 kpc from the midplane (Jones et al. 2017). It is suggested that the properties of the extraplanar medium are determined by different parameters including star formation activity, stellar mass, and the bulge-to-disc ratio.

Because of the limited information in the literature about the sample of galaxies in this study, as well as incomplete observations of this survey, it would be more useful to compare observed galaxies with galaxies showing comparable morphological type and morphological structures when it is possible.

ESO 0321-G10 shows similar morphological structure to IC 1963 (Sc). The latter has extended ionized gas to 0.5–0.6 kpc on average from a few bright H II regions, which is similar to what is traced in ESO 321-G10. IC 1963 has a low star formation activity rate ( $0.05 M_{\odot} \text{ yr}^{-1}$ ). Therefore, the thin extraplanar layer in ESO 321-G10 would be related to low SF activity in the underlying disc.

ESO 505-G03 shows similar morphological structure to that traced in NGC 4672

(Sbc), which displays several of the same separated emission complexes in the disc as ESO 505-G03. These complexes are grouped mainly into three regions including the centre of the galaxy and two regions within the disc, and some smaller and fainter regions also appear along the disc (Rossa & Dettmar 2003). As mentioned before ESO 505-G03 shows extended filaments, which could be interpreted as chimneys according to the chimney theoretical model (Norman & Ikeuchi 1989).

The extraplanar gas is seen as a rotating component, when the outflowing material is suggested to entrain part of the rotating material of the disc. The rotation velocity of the IEP layer shows a vertical gradient (e.g. NGC 5775: Rand 2000). Consequently, it is expected that there would be a complex gas circulation in this layer. The rotation of the gas in the sample of galaxies was mapped by tracing the ratio of the blue-shifted emission to the red-shifted emission, and it shows that the gas in the IEP also follows the rotation model of the disc. Two galaxies in the sample (ESO 311-G12 and IC 1963) deviate from the rotation of the disc, which presents two components. The extended component shows high emission in both sides (approaching and receding) of the galaxy.

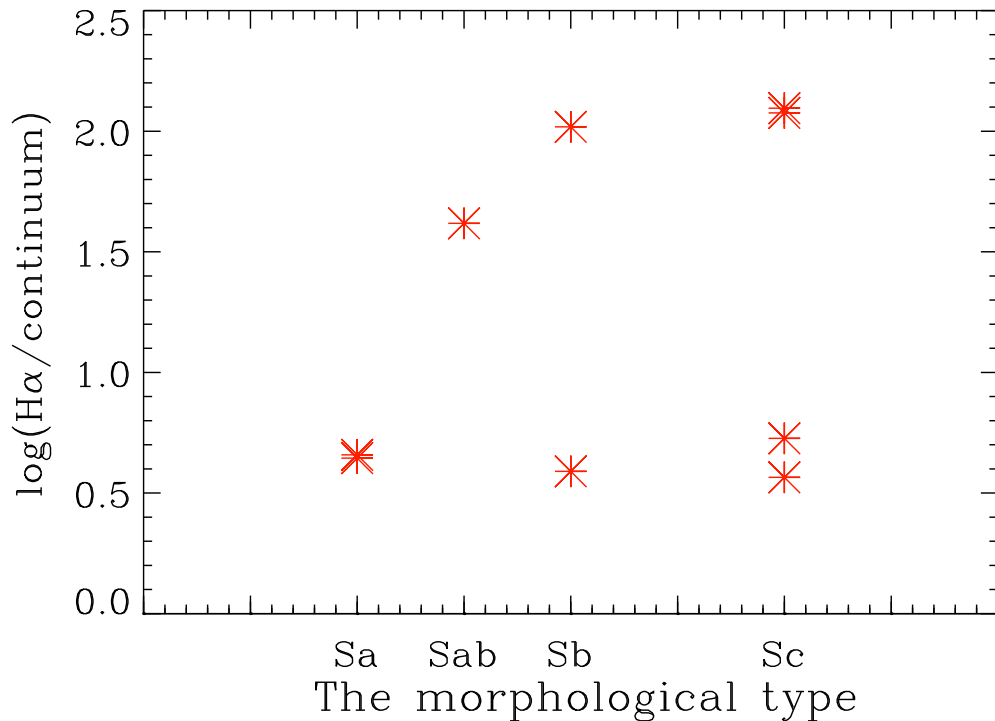


Figure 5.6: shows the correlation between the average of  $\text{H}\alpha/\text{C}$  against the morphological type in the sample of galaxies.

The continuum emission is more focussed in the centre of the galaxies and along the disc. It has a smooth density distribution in all of the edge-ons in the sample (see Figures 5.2 to 5.4), in contrast to the strong filamentary morphologies of the ionized emission of  $H\alpha$  (see Figures 5.2 to 5.4). This is expected for emission coming from stellar populations of a range of ages.

The intensity ratio of the emission of  $H\alpha$  to the continuum ( $H\alpha/C$ ) was mapped in a logarithmic scale in order to cover small values that would be difficult to show using a linear scale, and this is shown in Figures 5.2 to 5.4. The filament structures that appear with high  $H\alpha$  emission show a lower ratio of  $H\alpha/C$ , and this could reflect the activity of the star formation in these galaxies. The average value of  $H\alpha/C$  was determined in each galaxy and plotted against morphological type (see Figure 5.6). There is no clear trend in  $H\alpha/C$  w.r.t. the morphological type but we expect that with an increasing sample size, the trend will become clearer.

## Chapter 6

### Conclusion and future work

In this thesis I focussed on ionized outflows from two different types of sources in specific nearby galaxies (face-on NGC 300 and edge-on NGC 4945), as well as searching for IEP in a sample of edge-on galaxies. The first source is H II regions in NGC 300 and the other is the active centre (AGN and starburst) of NGC 4945. Observing ionized outflows is an effective method of tracing the evolution of spiral galaxies by quantifying the impact of the outflows on the ambient ISM. In other words, tracing the role of the internal energetic (active) processes, which are occurring in the disc of the galaxy, on the evolution of disc galaxies in terms of morphological structures, kinematics of the gas and physical properties in these active areas and their surroundings.

#### 6.1 Outflows from H II regions in NGC 300

The following paragraphs summarise the main results from the analysis of 18 objects (H II regions) that show clear ionized outflows, different morphology and physical properties:

- I have presented intensity and velocity-resolved maps of a few H II regions in NGC 300 in order to study the kinematics of the outflowing gas from these areas, as an important source of H $\alpha$  and H $\beta$  emission. From these maps I estimated that the average velocity of the ionized outflowing gas  $\approx -200$  km s $^{-1}$ , with a wide range of velocity dispersions. In object B, the velocity dispersion displays high values and in some areas reaches 700 km s $^{-1}$ . The morphological structure of B as a bubble in shape is more evidence for the presence of shock-heated collisions with outflows. Some positions have profiles with double peaks that could be caused by interaction between different components along the line of sight. This appears in different positions on B, in particular, in the areas showing high velocity dispersions. The double-peaked model reveals two components with velocities  $\sim -13$  km s $^{-1}$  and  $-306$  km s $^{-1}$ . These components still show a high velocity dispersions  $> 310$  km s $^{-1}$  compared with elsewhere. H $\alpha$  maps of NGC 300 show irregular patches containing a large amount of ionized emission, and the distribution of the ionized gas shows many filaments and shells that relate to the H II regions. These structures are clear near giant

objects (A & B) and reflect the morphological impact of the outflows from H II regions by re-shaping the surrounding ISM. Furthermore, the areas with strong outflows show dusty and clumpy environments. Both the wind-blown cavities and clumpy structure will have implications for the escape fraction of hydrogen-ionizing photons.

If one compares A (D137) and B (D118-D119) as complex H II regions, one can see some differences. For example, one can see different morphological structures, outflows and dust, as well as some differences in the values of the velocity and velocity dispersion due to the local physical circumstances surrounding these objects. Object B could be in the later stages of star forming regions, from both morphological and kinematic points of view; clear loops are surrounding this object (expanding hot gas), as well as signatures of shock-heated areas indicated by the high values of the velocity dispersion in this object.

- The present-day chemical abundances across a few H II regions with long-slit observations have been examined, which show a negative gradient with respect to the radius as it is observed in nearby spiral galaxies. The radial distribution of  $\log(\text{N/O})$  is compatible with a negative trend with respect to the radius. Because the distribution of the matter in spiral galaxies tends to be in the form of an exponential disc, and the activity of star formation is sensitive to local density, more metals produced in the denser locations might explain the negative gradient of the metallicity.

Outflows were clearly traced in H II regions covering a wide range of sizes, ages, morphological structures and different positions with respect to the centre of the galaxy. Outflows from H II regions and SNe are regarded as a supply of metals and energy to the environment. In this study, the impact of the outflows can be noticed from different abundances for some H II regions located at the same distance from the centre. For example, K10, K9, K7, E, B-2 are located at  $R_{25} \sim 0.2$  and show range of abundances (8.3–8.5). This can be interpreted in terms of the local impact according to the properties of the outflows that would be affected by the type of the central stars, the form of the H II region (if it is a pure H II region or a compact one) and how many events (SNe) have occurred to produce the observed outflows.

- The emission line ratios of these interesting regions were examined in order to investigate their physical properties and identify their position in the diagnostic diagram. The CLOUDY model was used to reproduce a model of H II regions in order to compare their properties with that seen in the observations. The models' positions in the diagnostic diagram explain more than half of the sample of H II regions. The temperatures of these objects were determined by

using nitrogen line ratios, and ranged between 7800 and 13 300 K. The distribution of the objects span an area having  $\log([\text{S II}]/\text{H}\alpha)$  between  $-0.1$  and  $-1$  and  $\log([\text{N II}]/\text{H}\alpha)$  is between  $-0.4$  and  $-0.9$ . Hence, they have different physical properties as a result of different responses to the influence of the outflows (stellar winds). It can be concluded that outflows from H II regions have locally different impacts on the surroundings, and the differences could be related to their ionizing source, velocity, energy, mass and temperature. So, there is no comprehensive model that can explain the observed regions. I would suggest that these regions should be studied as groups according to their conditions, in order to explain what is going on in these areas.

From the previous points, I can suggest that the evolution of spiral galaxies is affected by the impact of the ionized outflows onto the surrounding ISM in different aspects. Morphologically, they are affected by re-shaping the surrounding ISM by creating knots, filaments and shells that represent a mechanism in which the gas can transport from the disc to the halo only in galaxies with high SFR. Chemically, these outflows change the metallicity of the ambient ISM by supplying heavy elements. Kinematically, they compress and shock the surrounding ISM, which may trigger new star formation events or may quench current star formation.

## 6.2 Outflows from the centre of NGC 4945

The ejected material from the centre of NGC 4945 is more prominent in continuum emission, which forms a cone structure with an opening angle  $\sim 140^\circ$  (the head of the cone coincides with the centre of the galaxy). Interestingly, the V-shaped structure is clear and spread more towards the outer region compared to the  $\text{H}\alpha$  emission. This could represent scattered starlight on the rim of the V-shape, as the projection effect plays an important role to see the inclined cone. The V-shape could emerge near to the obscured centre of the galaxy, as a result of the impact of both AGN and starburst activity. This shape would be more collimated at the beginning near to the centre and then spread outward from the centre. Unfortunately, because of the high extinction in this area E of the centre, the inner portion of the cone is not visible. The two edges of the V-shape are asymmetric; the Southern edge shows different filaments that extend to the S, W and N from the tip of the edge. I can not confirm this with  $[\text{N II}]$  observation because of the high noise in this area. However, the two edges are more symmetrical with  $\text{H}\alpha$  emission and there is  $\text{H}\alpha$  in the area between them. Consequently, I suggest that the V-shaped structure is filled with ionized gas, as this also appears with  $[\text{N II}]$  emission. I found areas at  $0'.07$  and  $0'.33$  from the centre which show physical properties of shock-heated gas, and clear asymmetry in their emission profiles.

The V-shaped structure seems to be narrower in [N II] than  $H\alpha$  emission. The continuum emission shows strong continuum in the outer areas to the E (Figure 4.5 a) while this does not happen in [N II] (see Figure 4.4 a).

To the SE of the nucleus, some patches are prominent with [N II] emission and show the same velocity as the emerged cone. As well as this, its ratios of [S II]/ $H\alpha$  and [N II]/ $H\alpha$  indicate signs of shock-heated gas by a hard ionizing source (AGN). Hence, this could be the second part of the bi-cone structure that falls in an area with less obscuration. Therefore, the expected shape of the ejected material from the centre of NGC 4945 forms a bi-conal structure, as shown in Figure 4.20.

### 6.3 The distribution of ionized gas in edge-on disc galaxies

H $\alpha$  maps of 9 edge-on galaxies show that the distribution of the ionized gas in edge-on galaxies are not identical, but show different forms such as outflows from H II regions, extended material from the centre of the galaxy or a smooth distribution along the disc. However, the continuum emission from stars in the disc is concentrated in the midplane and the centre of the galaxy. The ratio of the ionized gas to the continuum show different values among these galaxies, so I can not suggest any correlation between this ratio and the morphological type. To estimate this correlation, I need to expand the sample of study and it would be more accurate if I could correct for dust extinction. This will be possible with upcoming observations. Two galaxies show signs of ionized extraplanar gas (ESO 311-G12 and IC 1963) that extend away from the midplane.

### 6.4 General conclusion

The main topic of this work is to uncover the contribution of the energetic events that take place in the disc of the galaxy and their role in the evolution of disc galaxies. Analysis of the spectra of two different energetic events in two nearby galaxies with different inclinations, reveal a clearer view about the morphology, kinematics, and physical conditions of the ionized gas.

The analysis of optical spectroscopy and FP imaging of H II regions and the ejected cone from an active nucleus show that the ionized outflows have enhanced ratios of the forbidden lines to the recombination lines, in particular [S II]/H $\alpha$  and [N II]/H $\alpha$ . This trend indicates that the gas has been shock-heated by hot expanding gas. In addition, the ejected material from energetic events contribute to the enhancement of the metallicity of the galaxy by providing metals. I found different areas that show splitting or broadened profiles that indicate the presence of extreme kinematics resulting from interaction between different components. I noticed this in the spectra of large H II regions (object B in NGC 300) and in the ejected cone in NGC 4945, in particular at the rim of the cone. As well as this, the ejected material forms different morphological structures, such as extended filaments, loops, bi-cone, bubble, etc.

It is important now to highlight the role of outflows which result from different events. For soft ionizing source (H II regions) it seems that their impact is local. In some cases, such as objects A and B, I expect that the influence of outflows span a wide area because they are created from different events (multiple supernovae and stellar winds), maybe successive SF episodes which are accompanied with multiple SNe. This would be more complicated and would be an asymmetry and wide distribution of the

ionized gas.

NGC 4945 shows a vertically and horizontally extended hot gaseous outflows w.r.t. the disc. This represents a mechanism of recycling gas within the environment of the host galaxy. The total mass of the ejected ionized gas by the active centre of NGC 4945 is  $\sim 2.5 \times 10^5 M_{\odot}$  from one side of the galaxy and the rate of the outflows  $\sim 0.34 M_{\odot} \text{ yr}^{-1}$ . Therefore the centre needs  $7 \times 10^5 \text{ yr}$  to produce the traced gas. If I assume the outflows are symmetrical on both sides of the galaxy, as shown in the model of NGC 4945 (see Figure 4.20), then the galaxy in this time supplies  $5 \times 10^5 M_{\odot}$  gas for this bi-cone. In the same time the galaxy needs to sustain a required amount of gas for SF events. I suggest that the ejected cone would follow the role of the bubble structure in each side of the cone (approaching and receding) and break to create a fountain in which the hot gas will cool and condense and then fall back onto the disc under gravity. In other words, the shocked ISM by outflows could induce cooling of the hot halo, which then precipitates back onto the disc. The expected escape velocity of the gas in the interesting area is  $\sim 7 \text{ km s}^{-1}$  for a mass  $\sim 10^9 M_{\odot}$ , and is less than the outflow velocity, as the outflow velocity is  $\sim 600 \text{ km s}^{-1}$ . As the gas moves outward, more of the galaxy's mass starts contributing to pulling it back; the escape velocity for the galaxy as a whole is within a few hundred  $\text{km s}^{-1}$ , so is of similar order of the observed outflow speed.

It can be concluded that the impact of ionized outflows is confined by two important factors: the ionizing sources which create the energetic events and the physical properties of the surrounding ISM. The first factor will decide the mass and energy of the ionized ejected material and the second factor will control the distribution of the outflows. In other words, the density of the ambient ISM will determine the extent and direction of the ejected material. This is obvious in the centre of NGC 4945, the ejected material forms a bi-conal structure which represents a mechanism by which the gas is exchanged between the disc and halo. Meanwhile, the impact of the outflows from H II regions is generally confined by the disc of the galaxy, but in giant H II regions it could play different roles and extend their effect to reach the halo. It would be useful to confirm this idea by observing H II regions in edge-on galaxies because face-on galaxies show what happens in the base of the fountain and edge-on galaxies show the vertical distribution of the outflows.

The galaxies (NGC 300 & NGC 4945) studied in chapters 3 and 4 are typical of  $0.15 L_*$  and  $0.6 L_*$  late-type galaxies, so are arguably reasonably representative of galaxy populations that dominate the luminosity density of the local Universe. I have found that these galaxies have the following evidence for feedback processes: re-shaping the surrounding ISM by creating filaments and shells and bi-conal structure that is extended more than 1 kpc away from the midplane, changing the kinematics of the gas that surround the active areas (H II regions and AGN), and changing the chemical properties of the ambient gas. The question is then how common these processes are in the galaxy population in the local Universe. My results in chapter 5 are an early

attempt to determine this, and my observed subset of 9 is a random sparse sample of the full sample. This full sample had been selected for calibration of the Tully–Fisher relation to determine galaxy distances. This implies that the following types of galaxies would be missing from this sample low surface brightness (LSB) galaxies, irregulars, ellipticals. The absolute magnitudes of 6 galaxies in chapter 5 show comparable values to that of NGC 300 and NGC 4945 while the other observed 3 galaxies show lower luminosity. Hence, the prior 6 galaxies would contribute to the local luminosity. The fraction of galaxies in chapter 5 with morphological evidence for outflows is high (67%), implying such processes are common. This could be compared to the fraction of local galaxies that have starbursts, based on the outliers to the Kennicutt–Schmidt relation and the stellar mass versus star formation rate relation (Silk & Mamon 2012; Wuyts et al. 2011). Also the fraction of present-day galaxies that have active nuclei is low (Osterbrock 2006). Therefore the feedback processes in chapters 3 and 4 are uncommon which is not to say that they are unimportant. Their transient nature could mean most galaxies do experience phases of activity, and these could leave lasting effects on the galaxy. Nevertheless there are very good reasons for believing that feedback created a strong coupling between stellar mass assembly and supermassive black hole growth at least at higher redshifts (Merritt & Ferrarese 2001). Indeed there is evidence for more violent outflows in higher redshift galaxies (George et al. 2014; Bayliss et al. 2014) during an epoch in which ultraluminous star formation was more common (Floc’h & Cosmos Collaboration 2011; Gruppioni et al. 2013). However these processes cannot be examined in detail, except in some rare cases of strong gravitational lensing (Tamura et al. 2015; George et al. 2014). Therefore the study of local galaxy feedback processes in this thesis is one of the very few ways of unpicking the physical processes that happened in the (cosmic noon) of peak activity of cosmic star formation and feedback.

## 6.5 Future work

What would be important to focus on, and address next? The next step in my research will be to complete the gaps in my main project about NGC 4945 and then focus on the optical survey.

### 6.5.1 Upcoming observations for the cone structure in NGC 4945

With the upcoming observation of the [S II] doublet and  $H\beta$  for the central area of NGC 4945 by using the FP mode, I will construct an electron density map for the

cone structure in the central part of the galaxy. This will complete the observations needed to study the emerging cone by BPT diagnostic diagrams, such as a map of  $[\text{S II}]/\text{H}\alpha$  and  $[\text{N II}]/[\text{S II}]$ . The Balmer decrement ( $\text{H}\alpha/\text{H}\beta$ ) map can determine the dust distribution, and this can be used to correct the  $\text{H}\alpha$  emission to determine the total ionized emission from the centre of the galaxy without the effect of the extinction. These maps can confirm the long-slit results, and reveal a complete view of the ejected material from the centre.  $\text{H}\alpha$  and  $\text{H}\beta$  images are also being obtained at the New Technology Telescope at ESO, La Silla, in July, to aid in constructing the reddening map.

### 6.5.2 Upcoming observations for the optical and radio survey

With upcoming observations, I will have a larger sample having different morphological types which will offer a more effective way of comparing the morphology of the extra-planar layer in different galaxies. As well as this, a larger sample will span different morphological structures of IEP layers.

Future planned observations in  $\text{H}\beta$  will be useful to study the dust distribution in these galaxies and search for dusty IEP layers. As well as this, these observations of galaxies covering a wide range of morphological types can provide a clearer idea about the appearance of the dusty IEP in a variety of morphological types. Problems of dust obscuration are avoided by tracing recombination lines. Hence, the total ionized mass and its kinematic extent can be estimated more accurately than using  $\text{H}\alpha$  and  $\text{H}\beta$  observations.

Finally, analyses of the radio observations will provide complementary information to the optical survey that will allow us to determine the total ionized gas mass within these galaxies and thus estimate an important correction to optical emission lines for integrating star formation rates in redshift galaxies. All these studies will help us to understand the evolution of spiral galaxies along the Hubble sequence.

# A Charts

The charts of the observed targets in Chapters 3 and 4 are shown in this appendix.

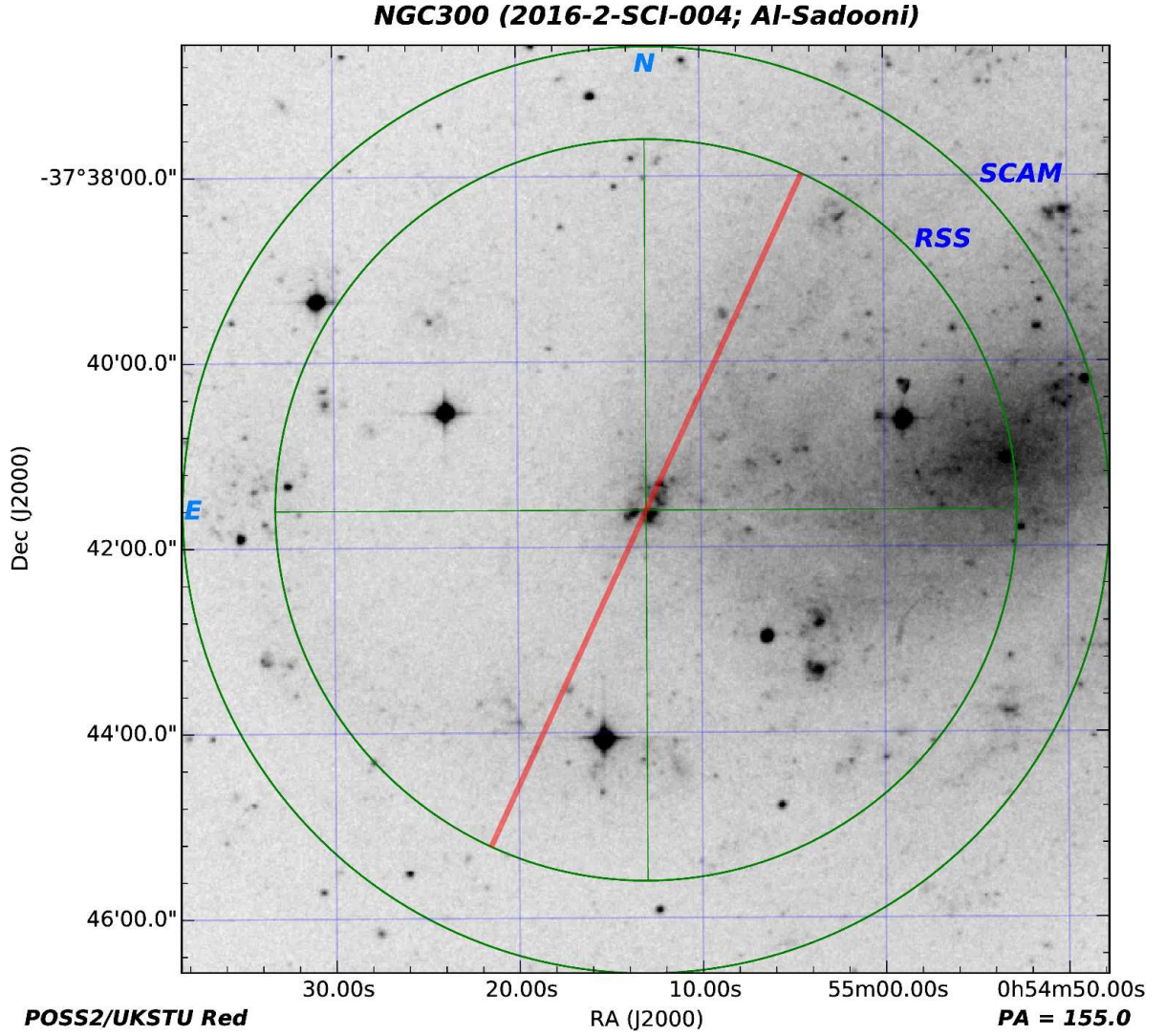


Figure A.1: A chart showing the long-slit position on NGC 300 oriented with  $PA = 155^\circ$  and with the centre of the slit (LS1 in Figure 3.1) at (RA:  $00^h 55^m 12^s$ , Dec:  $-37^\circ 41' 20''$ ).

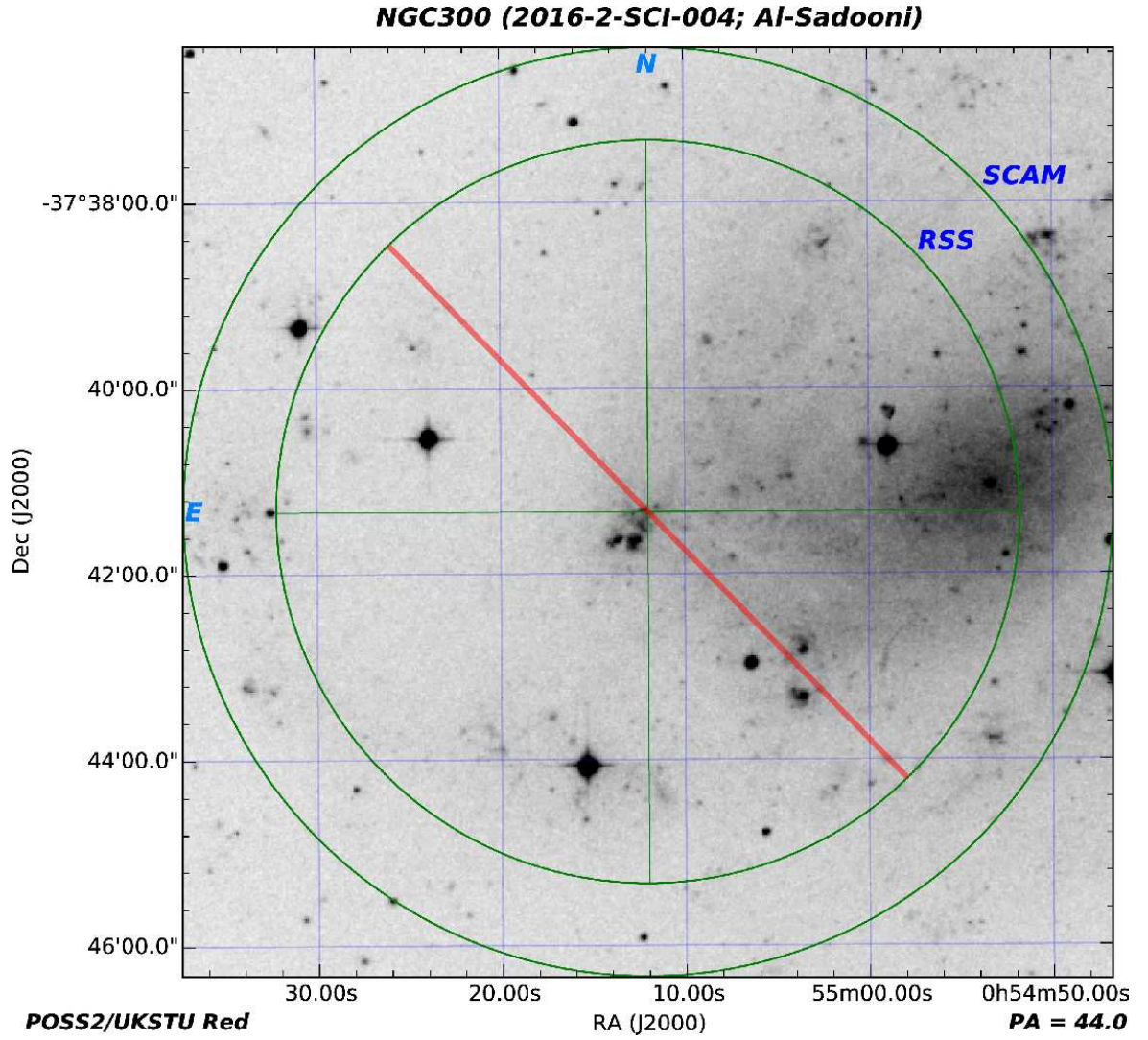


Figure A.2: As Figure A.1, but for  $PA = 44^\circ$  and the centre of the slit (LS2 in Figure 3.1) at (RA:  $00^h 55^m 13^s$ , Dec:  $-37^\circ 41' 36''$ ).

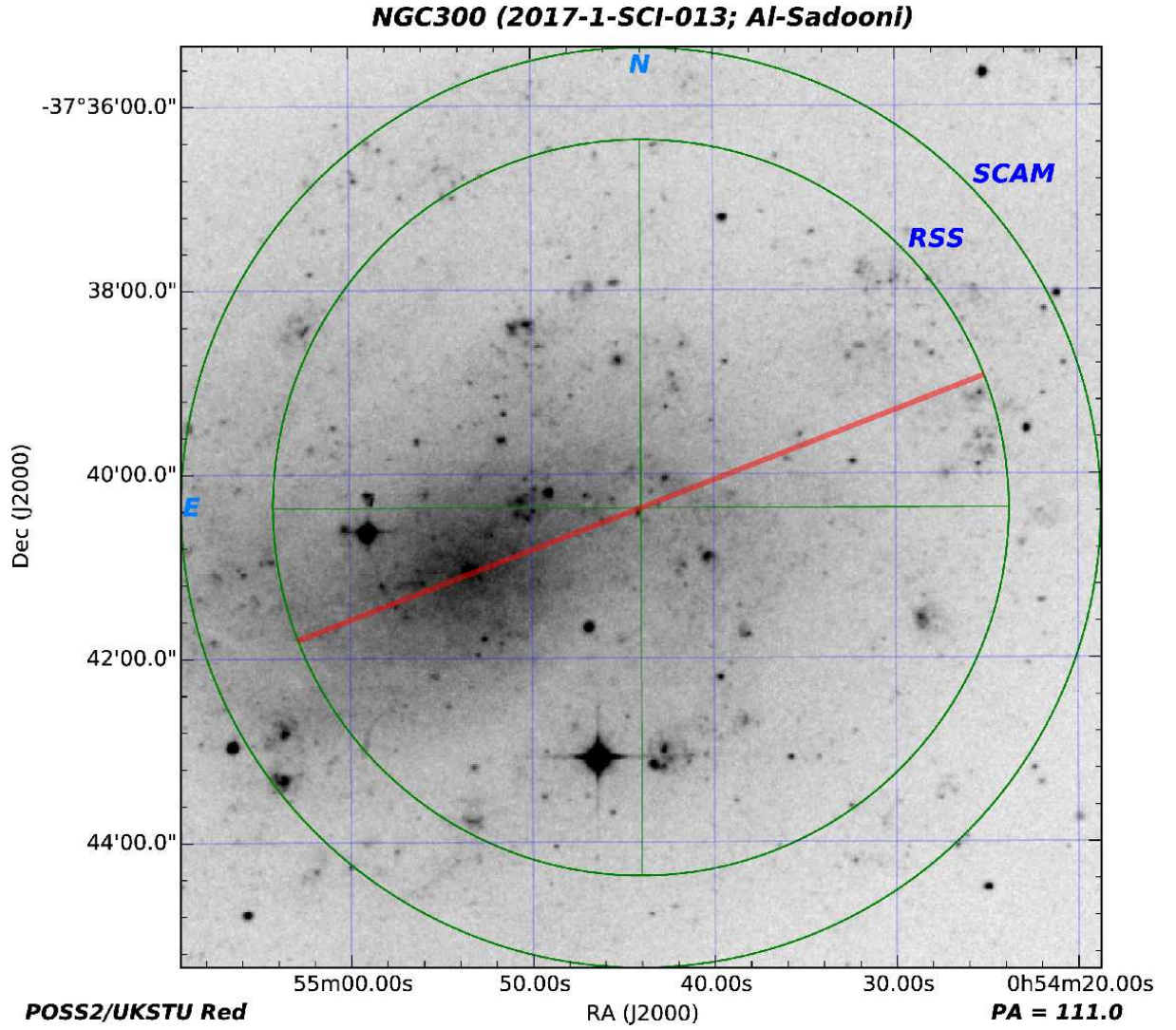


Figure A.3: As Figure A.1, but for  $PA = 111^\circ$  and the centre of the slit (LS3 in Figure 3.1) at (RA:  $00^h 54^m 44^s$ , Dec:  $-37^\circ 40' 22''$ ).

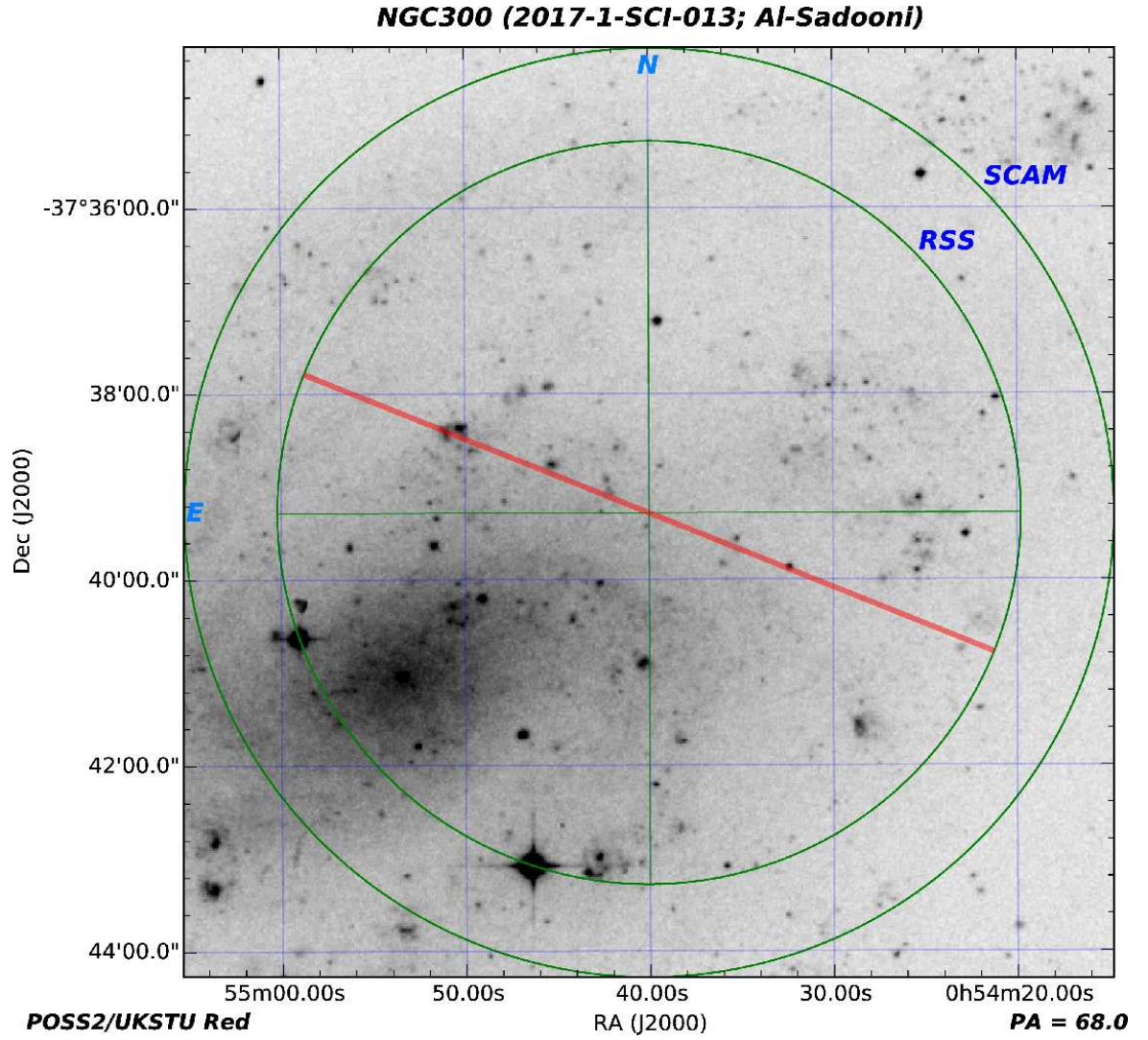


Figure A.4: As Figure A.1, but for  $PA = 68^\circ$  and the centre of the slit (LS4 in Figure 3.1) at (RA:  $00^h 54^m 40^s$ , Dec:  $-37^\circ 39' 17''$ ).

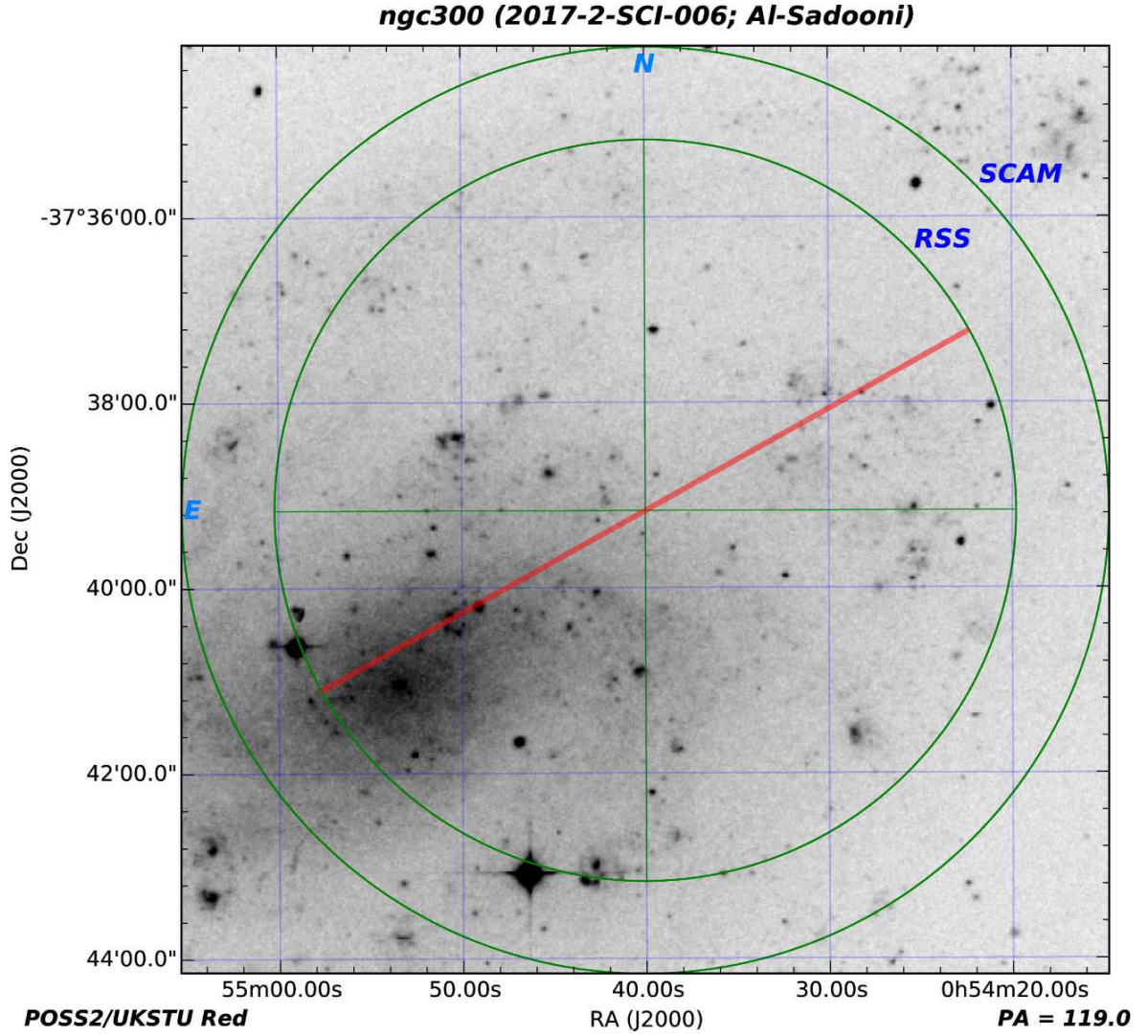


Figure A.5: As Figure A.1, but for  $PA = 119^\circ$  and the centre of the slit (LS5 in Figure 3.1) at (RA:  $00^h 54^m 40^s$ , Dec:  $-37^\circ 39' 15''$ ).

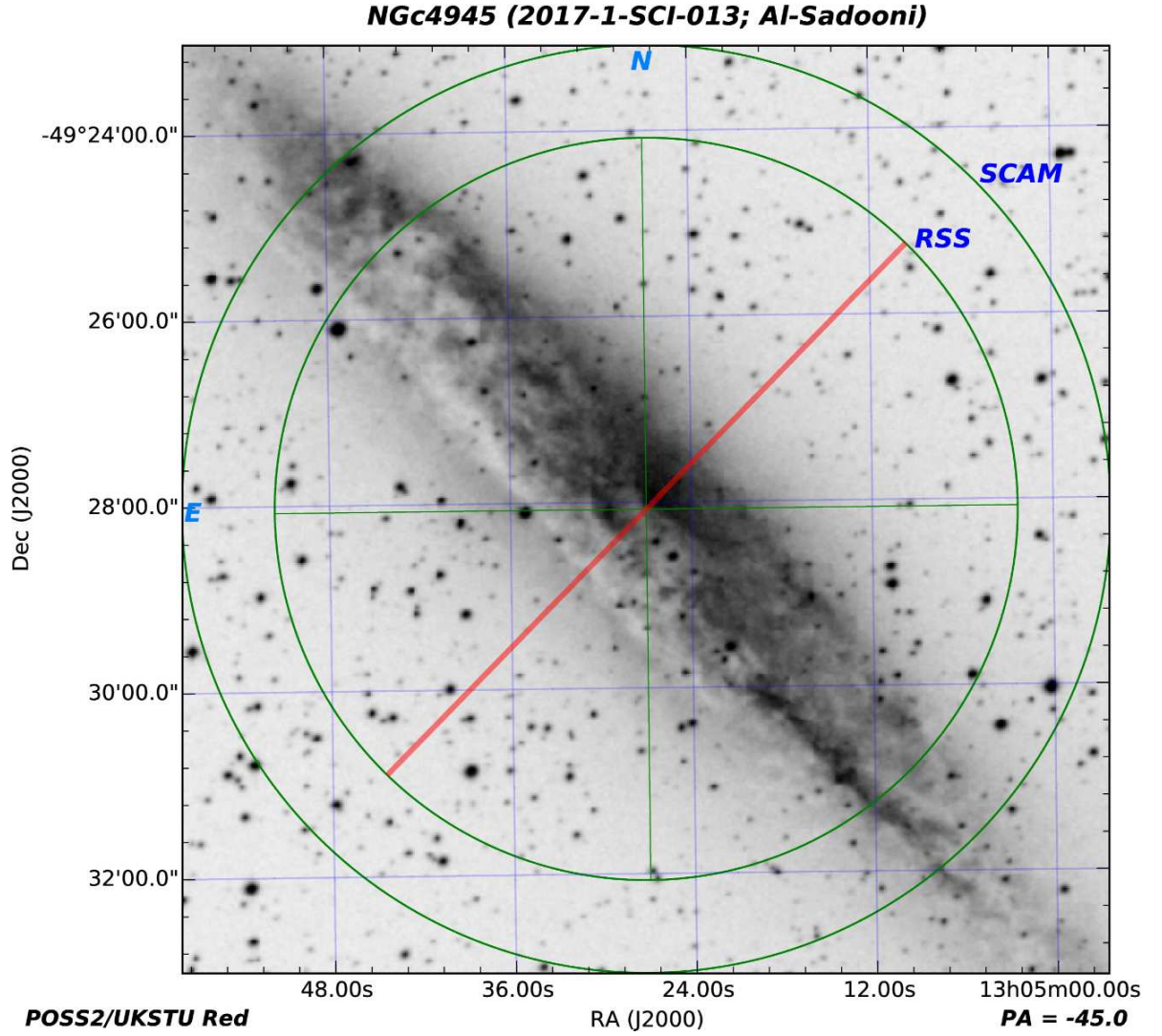


Figure A.6: A chart showing the long-slit position on NGC 4945 oriented with  $PA = -45^\circ$  and with the centre of the slit (LS1 in Figure 4.1) at (RA:  $13^h 5^m 17^s$ , Dec:  $-49^\circ 28' 4''.4$ ).

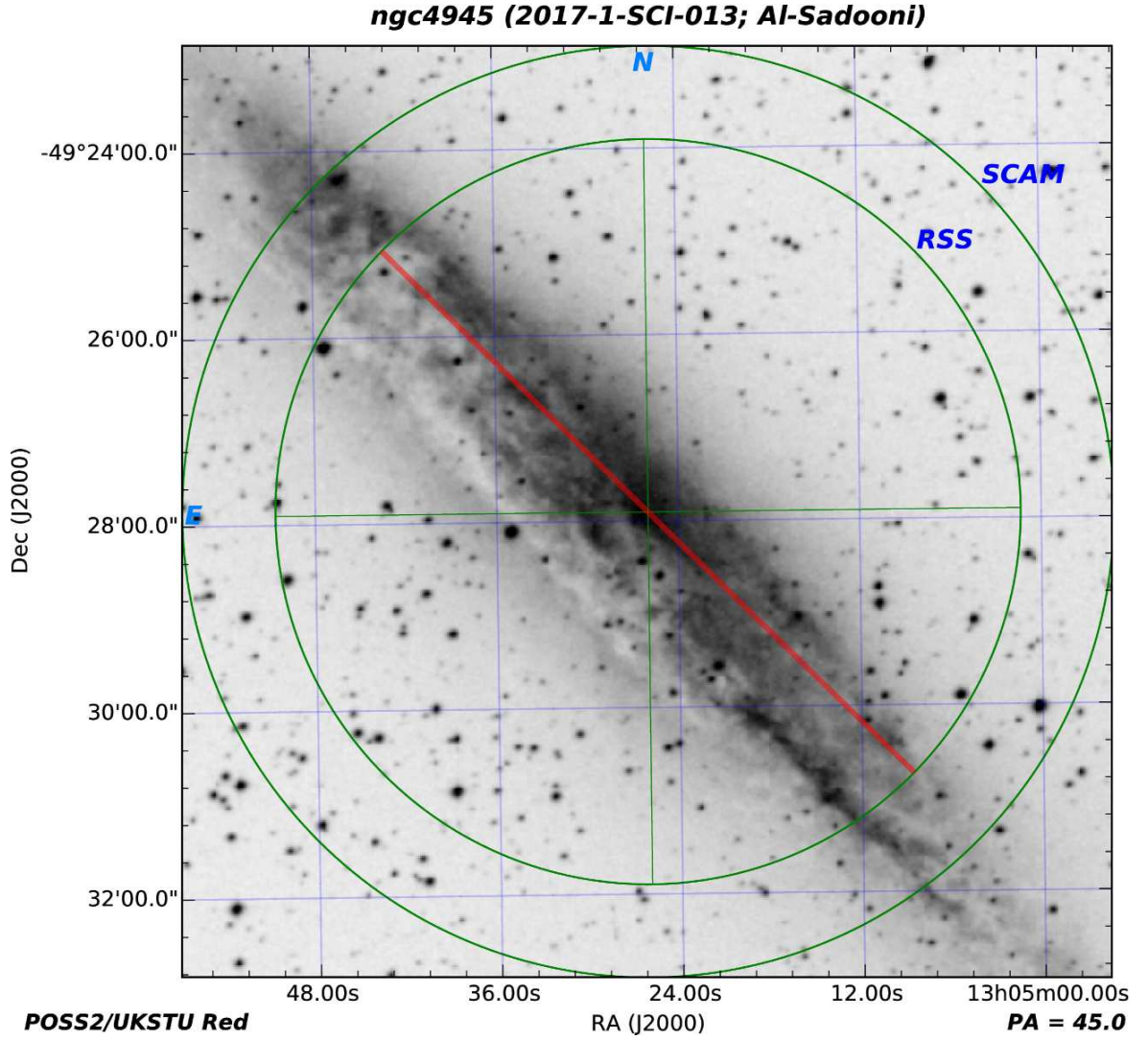


Figure A.7: As Figure A.6, but for  $PA = 45^\circ$  and the centre of the slit (LS2 in Figure 4.1) at (RA:  $13^h 5^m 26^s$ , Dec:  $-49^\circ 27' 40''.4$ ).

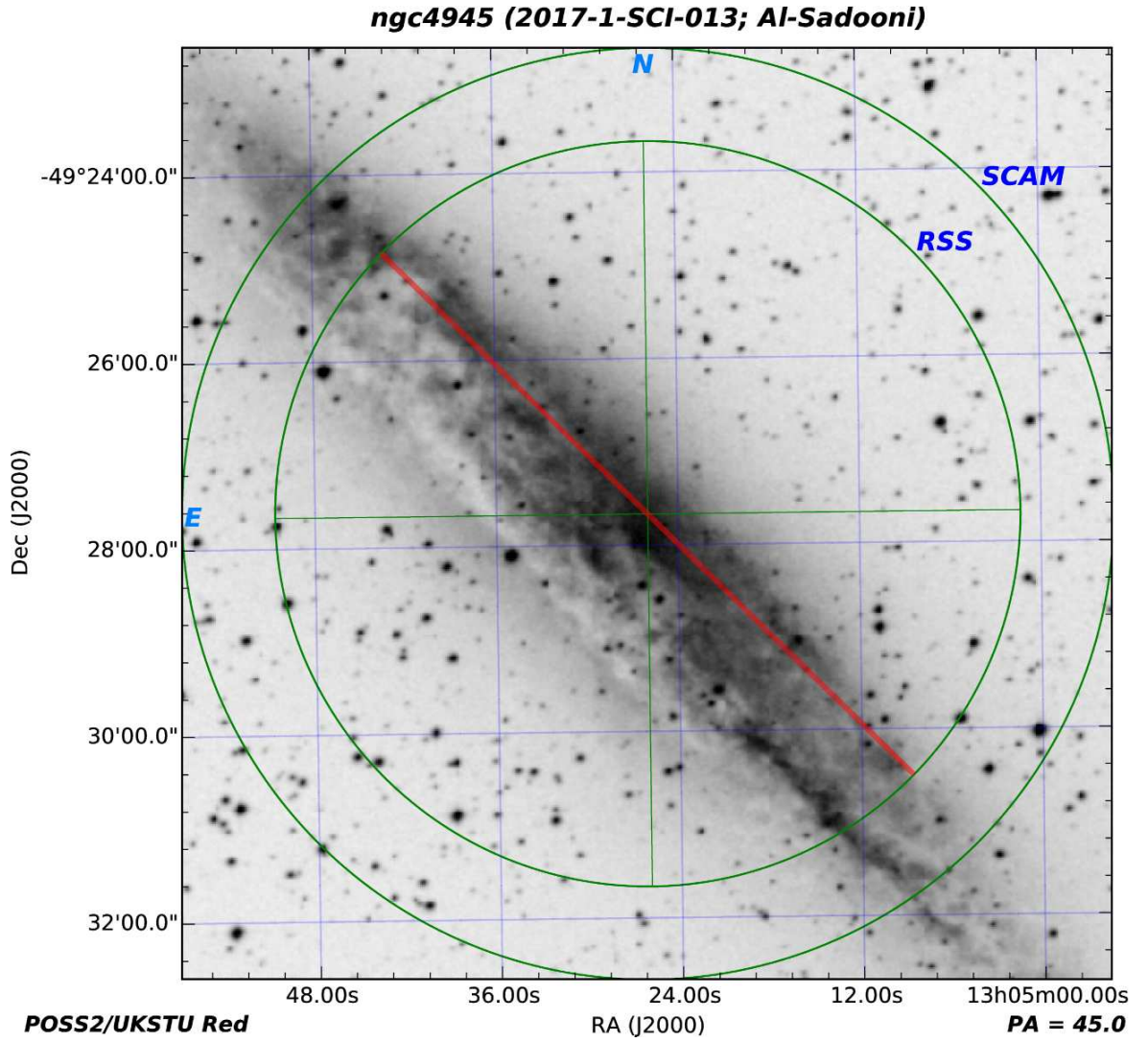


Figure A.8: As Figure A.6, but for  $PA = 45^\circ$  and with the centre of the slit (LS3 in Figure 4.1) at (RA:  $13^h 5^m 26^s$ , Dec:  $-49^\circ 27' 54''.4$ ).

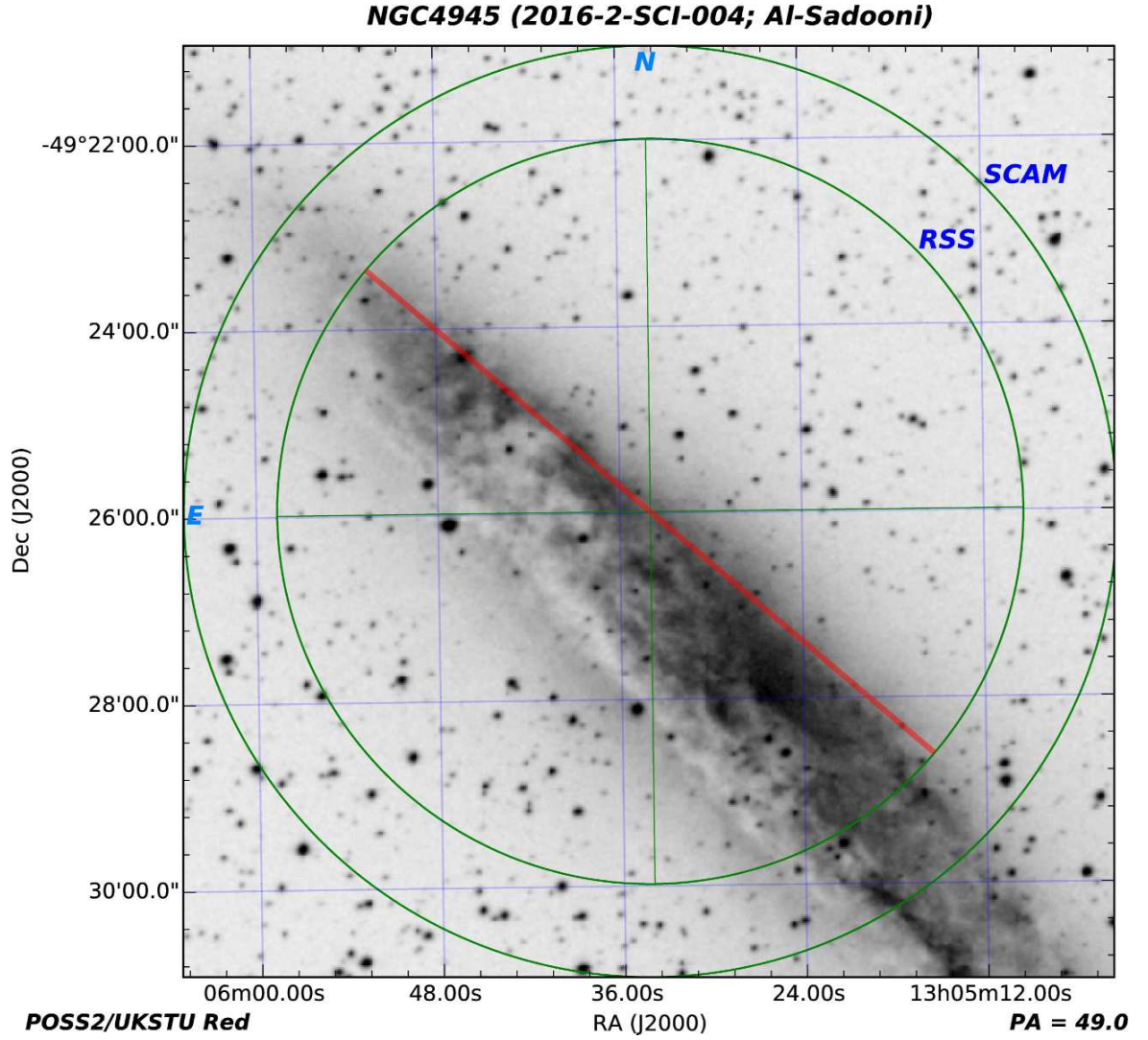


Figure A.9: As Figure A.6, but for  $PA = 49^\circ$  and the centre of the slit (LS4 in Figure 4.1) at (RA:  $13^h 5^m 34^s$ , Dec:  $-49^\circ 25' 59''.4$ ).

## B Spectra of different objects in NGC 300

Examples spectra of different observed objects in NGC 300 are shown in the following Figures.

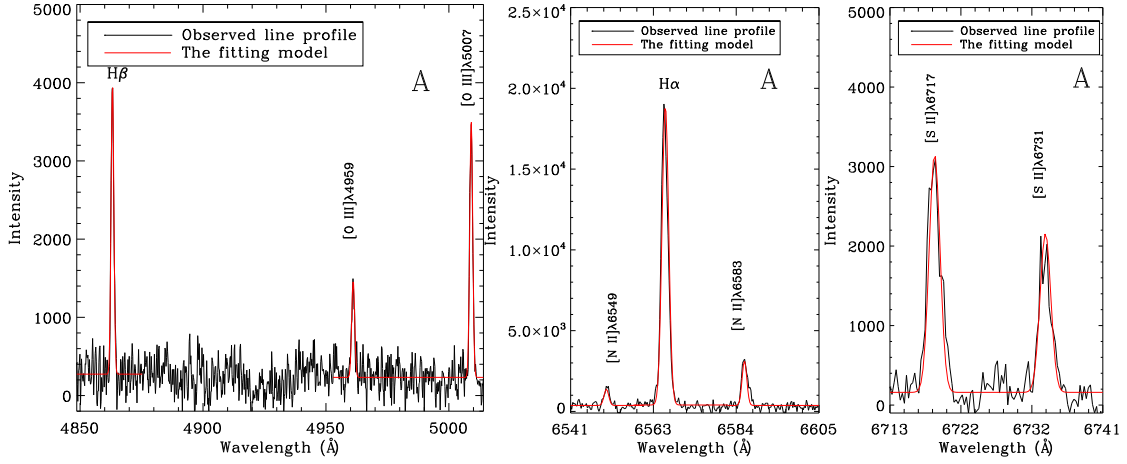


Figure B.1: Optical emission lines from object A. The left panel displays H $\beta$  and forbidden [O III] $\lambda\lambda$ 4959,5007; the middle panel covers H $\alpha$  and forbidden [N II] $\lambda\lambda$ 6549,6583; the right panel shows forbidden [S II] $\lambda\lambda$ 6717,6731 lines. The resolution is 0.75 Å and the long-slit was oriented with PA = 44°.

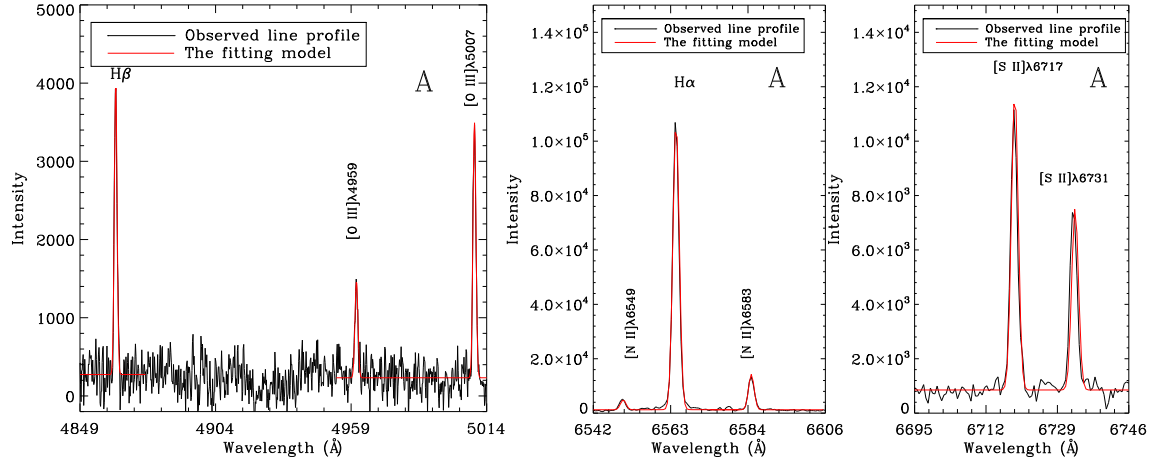


Figure B.2: As Figure B.1, but now the long-slit was oriented with PA = 155°.

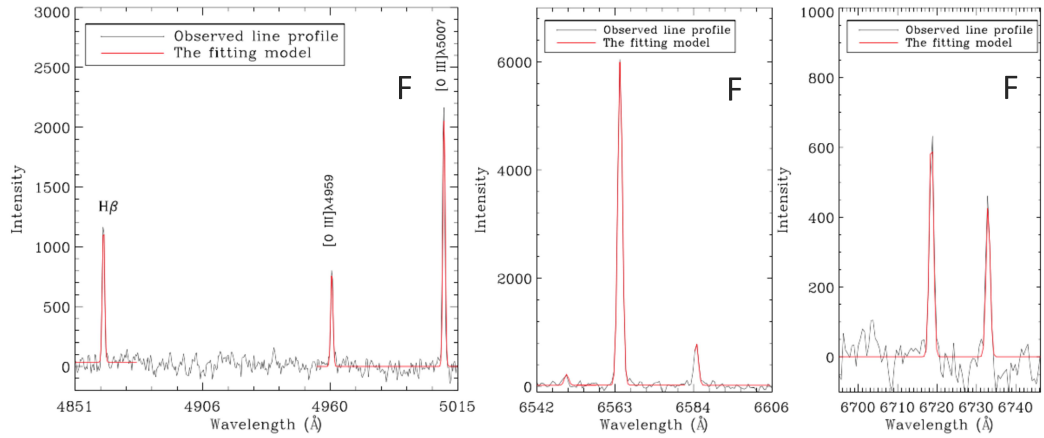


Figure B.3: As Figure B.2, but for object F.

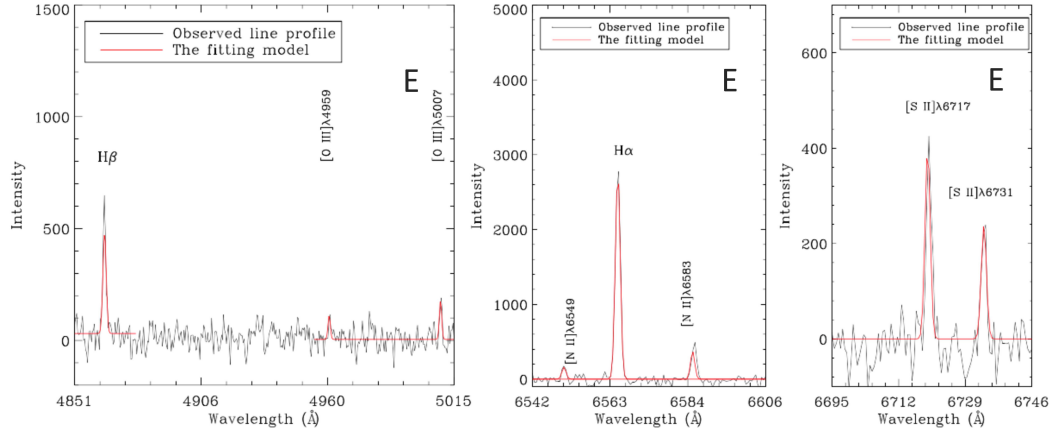


Figure B.4: As Figure B.3, but for object E.

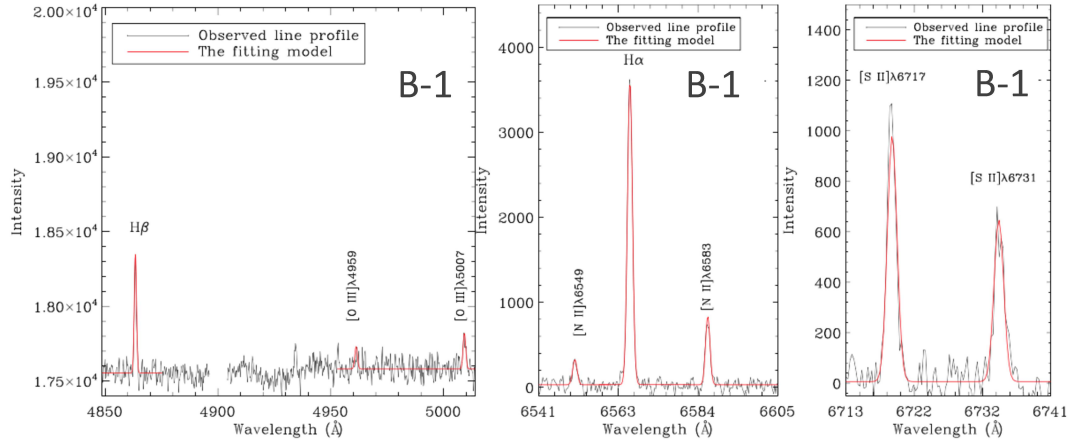


Figure B.5: Optical emission lines from object B-1. The left panel displays H $\beta$  and forbidden [O III] $\lambda\lambda 4959, 5007$ ; The middle panel covers H $\alpha$  and forbidden [N II] $\lambda\lambda 6549, 6583$ ; the right panel shows forbidden [S II] $\lambda\lambda 6717, 6731$ . The resolution is  $0.75 \text{ \AA}$  and the long-slit was oriented with PA =  $44^\circ$ .

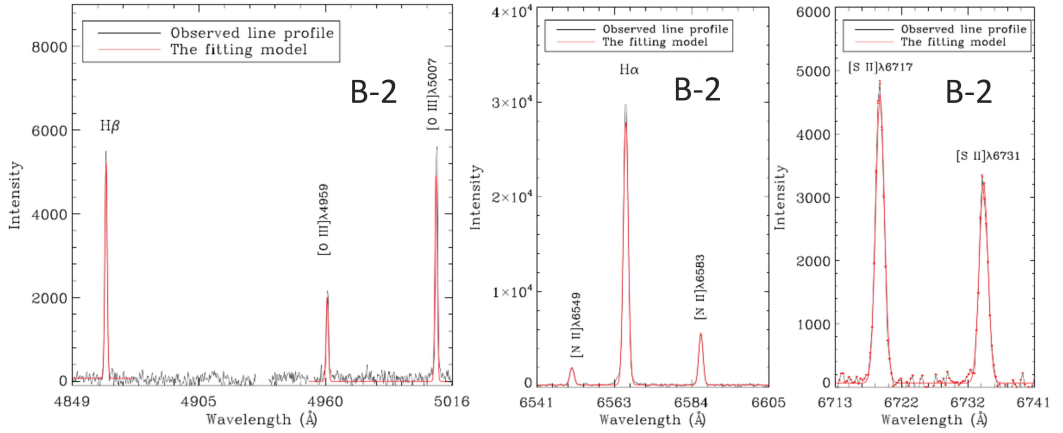


Figure B.6: As Figure B.5, but for object B-2.

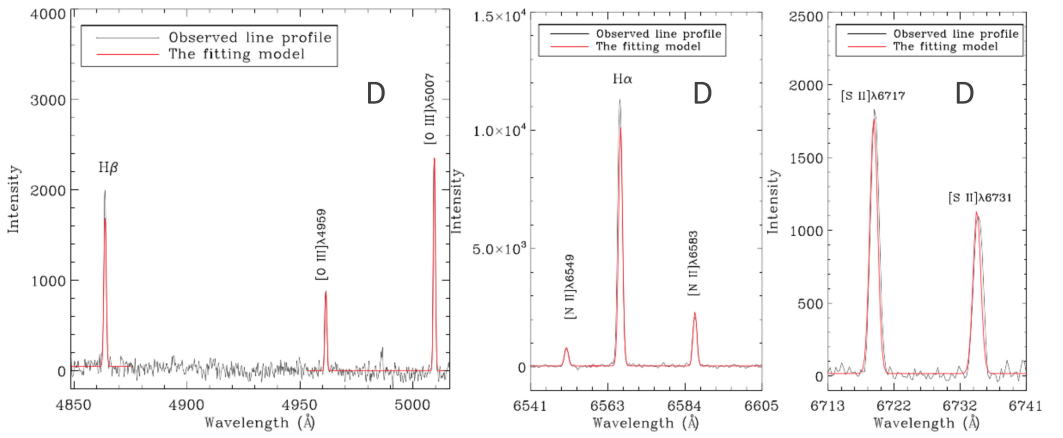


Figure B.7: As Figure B.6, but for object D.

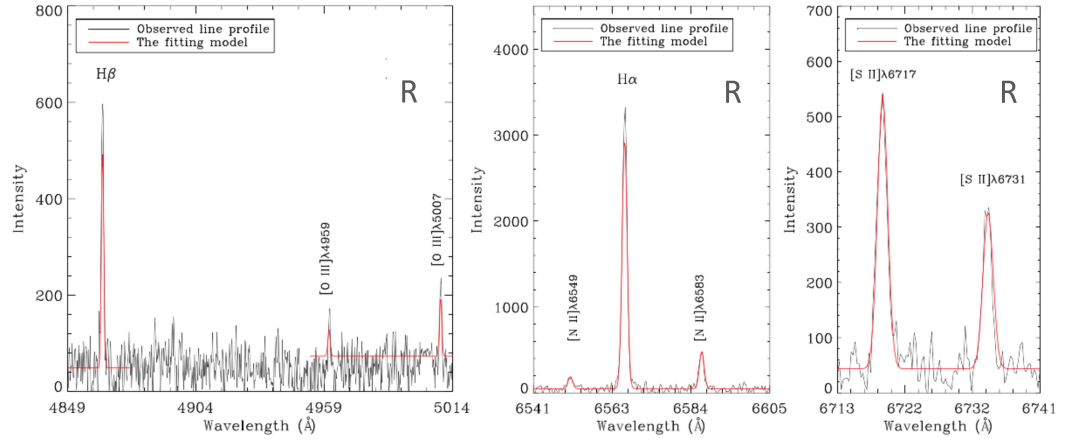


Figure B.8: As Figure B.7, but for object R.

## C Profiles were marked onto the object B in Figure 3.15.

The extracted profiles of  $H\alpha$  from the labelled areas in Figure 3.15.

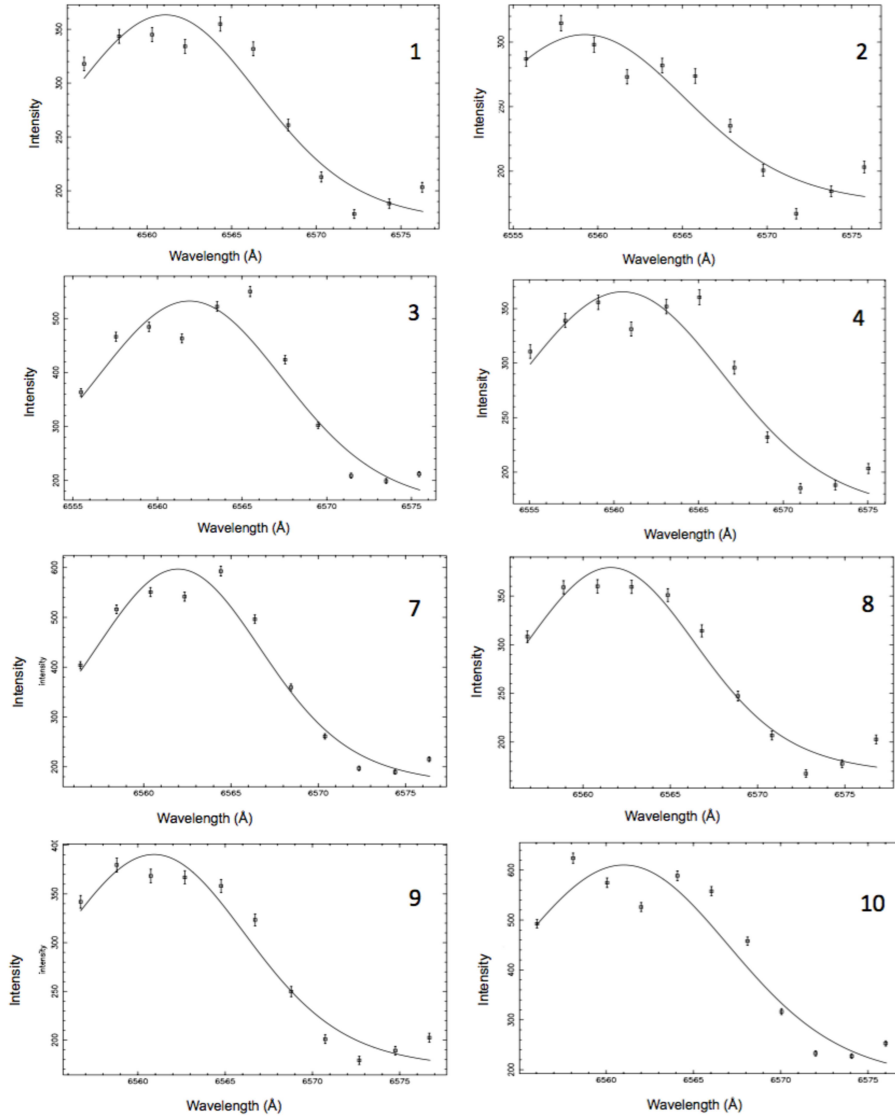


Figure C.1: The  $H\alpha$  profiles in various regions in object B, which are marked onto the map in the bottom right panel in Figure 3.15.

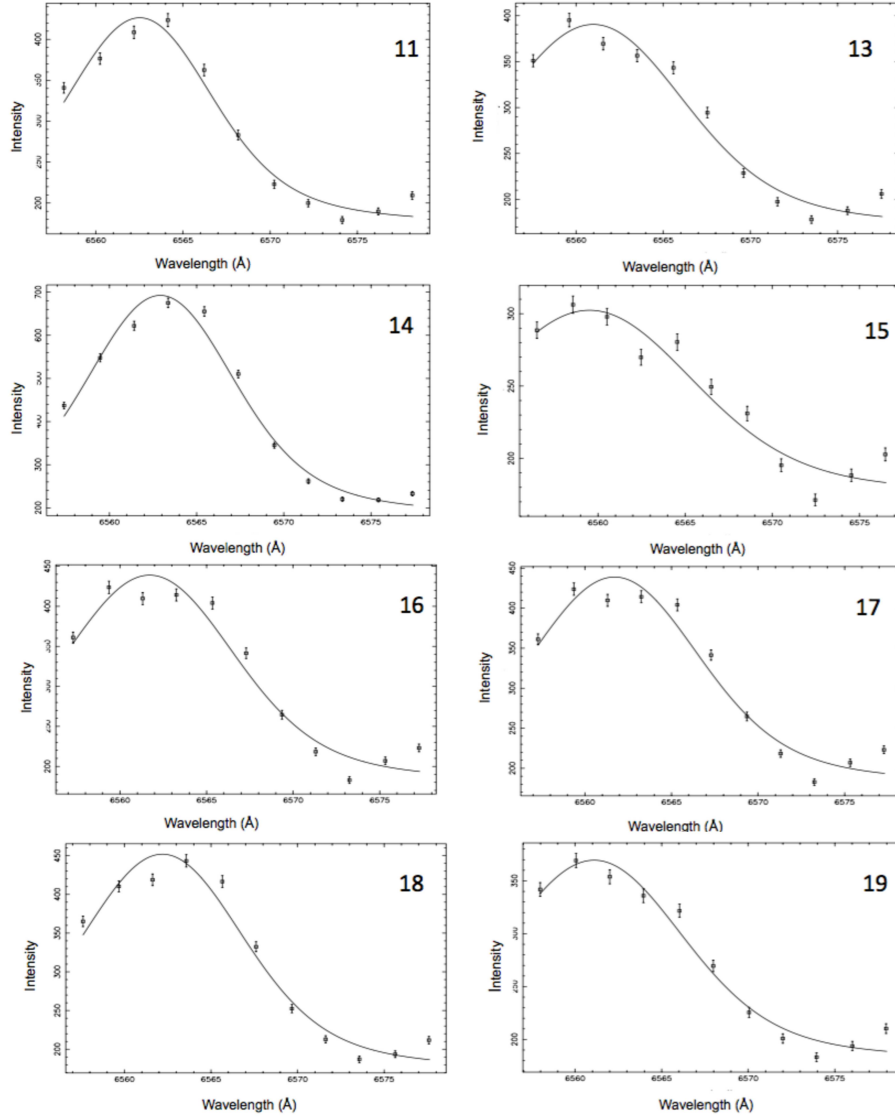


Figure C.2: Continuation of Figure C.1.

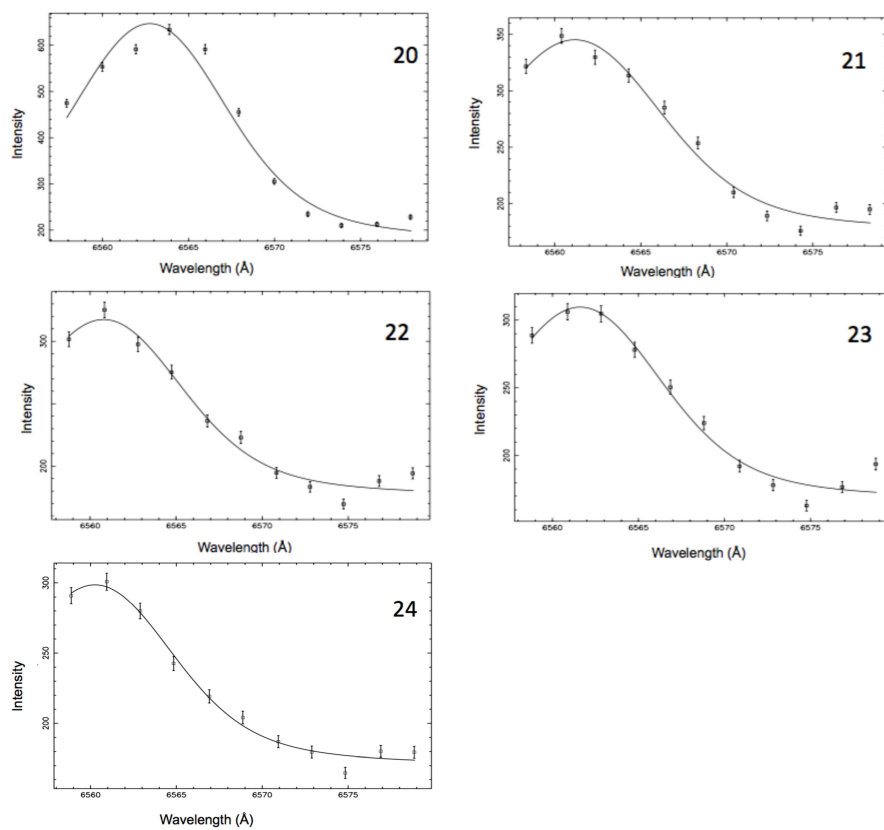


Figure C.3: Continuation of Figure C.1.

## D An example of input file used in CLOUDY model

The following Table shows the input file used with the CLOUDY code showing the commands that used for the predicted model in Chapter 3.

Table D.1: An example of an input file used in Chapter 2.4.4.3.

input	comment
Blackbody, temp = 20000 K	specifies spectrum of illuminating star, and temp if BB
Luminosity total 35.08	log luminosity of illuminating star, in $\text{erg s}^{-1}$
Distance 1.9 linear Mpc	
Print line flux at Earth	
Abundances H II	there is an inbuilt H II abundance list in CLOUDY so you should specify (note the space) abundances H II region
Radius 14.3	log radius of emitting gas, in cm
Hden 3.0	log H density, in $\text{cm}^{-3}$
Iterate 6	number of iterations
Print line sort wavelength [range 4000 Å to 7300 Å]	restricts the output of lines to the range specified
Print line column linear	linear, rather than log, fluxes
print last	this specifies that CLOUDY just outputs the last last iteration only (rather than all 6 of them)
Sphere	specifies geometry of emitting gas

# E Table for the full sample of galaxies included in the optical and radio survey

The following table lists basic information of 36 galaxies selected in the optical and radio survey presented in chapter 5.

Table E.1: Basic information for 36 disc galaxies included in the optical and radio survey.

Name	RA (J2000) h m s	Dec (J2000) ° ' "	Morphological type	Radial velocity km s <sup>-1</sup>
ESO 416-G25	02 48 41	-31 32 11	Scd	4782
IC 1963	03 35 31	-34 26 50	Sab	1638
NGC 1381	03 36 32	-35 17 43	S0	
ESO 201-G22	04 09 00	-48 43 37	Sc	3799
IC 2058	04 17 54	-55 55 58	Sc	
ESO 202-G35	04 32 16	-49 40 33	Sc	1601
NGC 1886	05 21 48	-23 48 37	Sb	
ESO 33-G22	05 31 41	-73 45 05	Sc	4080
ESO 311-G12	07 47 34	-41 27 08	Sa	893
ESO 564-G27	09 11 55	-20 07 01	Sd	
ESO 435-G14	09 57 48	-28 30 24	Sc	2505
IC 2531	09 59 56	-29 37 04	Sc	
ESO 435-G50	10 10 50	-30 25 26	Sc	2553
ESO 263-G15	10 12 20	-47 17 42	Sc	2302
NGC 3390	10 48 04	-31 32 00	S0a	
ESO 377-G7	11 06 26	-36 41 48	Sc	2579
ESO 505-G3	12 01 07	-24 34 05	Sc	1497
ESO 321-G10	12 11 43	-38 32 56	Sb	2988
ESO 506-G2	12 20 10	-26 04 00	Sb	3896
NGC 4672	12 46 16	-41 42 21	Sa	3289
ESO 322-G87	12 48 03	-40 49 07	Sb	3429
ESO 269-G15	12 57 13	-46 22 29	Sc	3211
ESO 575-G61	13 08 16	-21 00 08	Sc	1588
ESO 444-G21	13 23 31	-30 06 51	Sc	4166

Table E.2: Continuation to Table E.1.

Name	RA (J2000) h m s	Dec (J2000) ° ' "	Morphological type	Radial velocity km s <sup>-1</sup>
ESO 383-G5	13 29 24	-34 16 17	S	3485
ESO 446-G18	14 08 38	-29 34 19	Sc	4684
IC 4393	14 17 49	-31 20 57	Sc	
IC 4484	14 47 44	-73 18 21	Sc	
ESO 138-G14	17 07 00	-62 05 04	Sc	1298
IC 4819	19 07 07	-59 28 01	Sc	
IC 4871	19 35 42	-57 31 09	Sc	
ESO 460-G31	19 44 22	-27 24 25	Sb	5729
ESO 340-G8	20 17 12	-40 55 25	Sd	2697
ESO 340-G9	20 17 20	-38 40 25	Sc/Ir	2460
ESO 531-G22	21 40 29	-26 31 41	Sc	3300
ESO 240-G11	23 37 50	-47 43 39	Sc	2656

# Bibliography

- Ables J. G., Forster J. R., Manchester R. N., Rayner P. T., Whiteoak J. B., Mathewson D. S., Kalnajs A. J., Peters W. L., Wehner H., 1987, MNRAS
- Abramson A., Kenney J. D. P., Crowl H. H., Chung A., van Gorkom J. H., Vollmer B., Schiminovich D., 2011, AJ, 141, 164
- Afflerbach A., Churchwell E., Werner M. W., 1997, ApJ, 478, 190
- Alloin D., Collin-Souffrin S., Joly M., Vigroux L., 1979, A&A, 78, 200
- Amorín R. O., Pérez-Montero E., Vílchez J. M., 2010, ApJL, 715, L128
- Anders E., Grevesse N., 1989, GeoCoA, 53, 197
- Aoyama S., Hou K.-C., Shimizu I., Hirashita H., Todoroki K., Choi J.-H., Nagamine K., 2017, MNRAS, 466, 105
- Arribas S., Colina L., Bellocchi E., Maiolino R., Villar-Martín M., 2014, A&A, 568, A14
- Bae H.-J., Woo J.-H., Karouzos M., Gallo E., Flohic H., Shen Y., Yoon S.-J., 2017, ArXiv e-prints
- Baldwin J. A., Phillips M. M., Terlevich R., 1981, PASP, 93, 5
- Barbieri C. V., Fraternali F., Oosterloo T., Bertin G., Boomsma R., Sancisi R., 2005, A&A, 439, 947
- Battaglia G., Helmi A., Morrison H., Harding P., Olszewski E. W., Mateo M., Freeman K. C., Norris J., Shtetman S. A., 2005, MNRAS, 364, 433
- Bayliss M. B., Ashby M. L. N., Ruel J., Brodwin M., Aird K. A., Bautz M. W., Benson B. A., Bleem L. E., Bocquet S., Carlstrom J. E., Chang C. L., Cho H. M., Clocchiatti A., Crawford T. M., Crites A. T., Desai S., Dobbs M. A., Dudley J. P., Foley R. J., Forman W. R., George E. M., Gettings D., Gladders M. D., Gonzalez A. H., de Haan T., Halverson N. W., High F. W., Holder G. P., Holzappel W. L., Hoover S., Hrubes J. D., Jones C., Joy M., Keisler R., Knox L., Lee A. T., Leitch E. M., Liu J., Lueker M., Luong-Van D., Mantz A., Marrone D. P., Mawatari K., McDonald M., McMahon J. J., Mehl J., Meyer S. S., Miller E. D., Mocanu L., Mohr J. J., Montroy T. E., Murray S. S., Padin S., Plagge T., Pryke C., Reichardt C. L., Rest A., Ruhl J. E., Saliwanchik B. R., Saro A., Sayre J. T., Schaffer K. K., Shirokoff E., Song J., Stalder B., Šuhada R., Spieler H. G., Stanford S. A.,

- Staniszewski Z., Stark A. A., Story K., Stubbs C. W., van Engelen A., Vanderlinde K., Vieira J. D., Vikhlinin A., Williamson R., Zahn O., Zenteno A., 2014, *ApJ*, 794, 12
- Bell E. F., de Jong R. S., 2001, *ApJ*, 550, 212
- Bell E. F., Wolf C., Meisenheimer K., Rix H.-W., Borch A., Dye S., Kleinheinrich M., Wisotzki L., McIntosh D. H., 2004, *ApJ*, 608, 752
- Bendo G. J., Henkel C., D’Cruze M. J., Dickinson C., Fuller G. A., Karim A., 2016, *MNRAS*, 463, 252
- Bernard E. J., Ferguson A. M. N., Barker M. K., Hidalgo S. L., Ibata R. A., Irwin M. J., Lewis G. F., McConnachie A. W., Monelli M., Chapman S. C., 2012, *MNRAS*, 420, 2625
- Bertola F., Corsini E. M., 2000, in Combes F., Mamon G. A., Charmandaris V., eds, *Dynamics of Galaxies: from the Early Universe to the Present*, Astronomical Society of the Pacific Conference Series Vol. 197, p. 115
- Bizyaev D., Walterbos R. A. M., Yoachim P., Riffel R. A., Fernández-Trincado J. G., Pan K., Diamond-Stanic A. M., Jones A., Thomas D., Cleary J., Brinkmann J., 2017, *ApJ*, 839, 87
- Blair W. P., Long K. S., 1997, *ApJS*, 108, 261
- Bland J., Tully R. B., 1989, *AJ*, 98, 723
- Breitschwerdt D., McKenzie J. F., Voelk H. J., 1991, *A&A*, 245, 79
- Bresolin F., Gieren W., Kudritzki R.-P., Pietrzyński G., Urbaneja M. A., Carraro G., 2009a, *ApJ*, 700, 309
- Bresolin F., Gieren W., Kudritzki R.-P., Pietrzyński G., Urbaneja M. A., Carraro G., 2009b, *ApJ*, 700, 309
- Bresolin F., Stasińska G., Vílchez J. M., Simon J. D., Rosolowsky E., 2010, *MNRAS*, 404, 1679
- Breysacher J., Azzopardi M., Testor G., Muratorio G., 1997, *A&A*, 326, 976
- Buisson H., Fabry C., Bourget H., 1914, *ApJ*, 40
- Camps-Fariña A., Beckman J. E., Font J., Borlaff A., Zaragoza-Cardiel J., Amram P., 2016, *MNRAS*, 461, L87

- Camps-Fariña A., Zaragoza-Cardiel J., Beckman J. E., Font J., Velázquez P. F., Rodríguez-González A., Rosado M., 2017, *MNRAS*, 468, 4134
- Caplan J., Deharveng L., 1986, *A&A*, 155, 297
- Carignan C., 1985, *ApJS*, 58, 107
- Castor J., McCray R., Weaver R., 1975, *ApJL*, 200, L107
- Cazzoli S., Arribas S., Colina L., Piqueras-López J., Bellocchi E., Emonts B., Maiolino R., 2014, *A&A*, 569, A14
- Chen B.-Q., Liu X.-W., Yuan H.-B., Huang Y., Xiang M.-S., 2015, *MNRAS*, 448, 2187
- Chevalier R. A., Clegg A. W., 1985, *Nature*, 317, 44
- Chomiuk L., Wilcots E. M., 2009, *ApJ*, 703, 370
- Corbin M. R., Baldwin J. A., Wilson A. S., 1988, *ApJ*, 334, 584
- Corwin, Jr. H. G., de Vaucouleurs A., de Vaucouleurs G., 1978, *AJ*, 83, 1566
- Côté S., Freeman K. C., Carignan C., Quinn P. J., 1997, *AJ*, 114, 1313
- Cunningham M. R., Whiteoak J. B., 2005, *MNRAS*, 364, 37
- Dahlem M., Golla G., Whiteoak J. B., Wielebinski R., Huettmeister S., Henkel C., 1993, *A&A*, 270, 29
- Danehkar A., Karovska M., Maksym W. P., Montez, Jr R., 2017, *ArXiv e-prints*
- Davies R. L., Groves B., Kewley L. J., Dopita M. A., Hampton E. J., Shastri P., Scharwächter J., Sutherland R., Kharb P., Bhatt H., Jin C., Banfield J., Zaw I., James B., Juneau S., Srivastava S., 2016, *MNRAS*, 462, 1616
- de Vaucouleurs G., 1964, *ApJ*, 139, 899
- Deharveng L., Caplan J., Lequeux J., Azzopardi M., Breysacher J., Tarengi M., Westerlund B., 1988, *A&AS*, 73, 407
- Denicoló G., Terlevich R., Terlevich E., 2002, *MNRAS*, 330, 69
- D’Odorico S., Rosa M., Wampler E. J., 1983, *A&AS*, 53, 97
- Domínguez A., Siana B., Henry A. L., Scarlata C., Bedregal A. G., Malkan M., Atek H., Ross N. R., Colbert J. W., Teplitz H. I., Rafelski M., McCarthy P., Bunker A., Hathi N. P., Dressler A., Martin C. L., Masters D., 2013, *ApJ*, 763, 145

- Done C., Madejski G. M., Smith D. A., 1996, *ApJL*, 463, L63
- Dopita M. A., Sutherland R. S., 1995, *ApJ*, 455, 468
- Dopita M. A., Sutherland R. S., 2003, *Astrophysics of the diffuse universe*
- Falc3n-Barroso J., Knapen J., 2013, *Canary Islands Winter School of Astrophysics, Secular Evolution of Galaxies*, Cambridge University Press
- Ferland G. J., 1996, *Hazy, A Brief Introduction to Cloudy* 90
- Ferland G. J., Porter R. L., van Hoof P. A. M., Williams R. J. R., Abel N. P., Lykins M. L., Shaw G., Henney W. J., Stancil P. C., 2013, *RMxAA*, 49, 137
- Ferreras I., 2015, *IAU General Assembly*, 22, 2221587
- Floch E. L., Cosmos Collaboration, 2011, in Wang W., Lu J., Luo Z., Yang Z., Hua H., Chen Z., eds, *Galaxy Evolution: Infrared to Millimeter Wavelength Perspective*, *Astronomical Society of the Pacific Conference Series Vol. 446*, p. 185
- Fraternali F., Binney J. J., 2006, *MNRAS*, 366, 449
- Fraternali F., Oosterloo T. A., Sancisi R., Swaters R., 2005, in Braun R., ed., *Extra-Planar Gas*, *Astronomical Society of the Pacific Conference Series Vol. 331*, p. 239
- Frye B., Broadhurst T., Benítez N., 2002, *ApJ*, 568, 558
- Gallimore J. F., Baum S. A., O’Dea C. P., Pedlar A., Brinks E., 1999, *ApJ*, 524, 684
- Garnett D. R., 2002, *ApJ*, 581, 1019
- Gelderman R., Woodgate B. E., Brown L. W., 1995, in Comte G., Marcelin M., eds, *IAU Colloq. 149: Tridimensional Optical Spectroscopic Methods in Astrophysics*, *Astronomical Society of the Pacific Conference Series Vol. 71*, p. 89
- George R. D., Ivison R. J., Smail I., Swinbank A. M., Hopwood R., Stanley F., Swinyard B. M., Valtchanov I., Werf P. P. v. d., 2014, *MNRAS*, 442, 1877
- Gibson S. J., Taylor A. R., Higgs L. A., Dewdney P. E., 2000, *ApJ*, 540, 851
- Gieren W., Pietrzyński G., Soszyński I., Bresolin F., Kudritzki R.-P., Minniti D., Storm J., 2005a, *ApJ*, 628, 695
- Gieren W., Pietrzyński G., Soszyński I., Bresolin F., Kudritzki R.-P., Minniti D., Storm J., 2005b, *ApJ*, 628, 695

- Glazebrook K., Blake C., Economou F., Lilly S., Colless M., 1999, MNRAS, 306, 843
- Gonçalves D. R., Mampaso A., Corradi R. L. M., Perinotto M., Riera A., López-Martín L., 2004, MNRAS, 355, 37
- Gruppioni C., Pozzi F., Rodighiero G., Delvecchio I., Berta S., Pozzetti L., Zamorani G., Andreani P., Cimatti A., Ilbert O., Le Floch E., Lutz D., Magnelli B., Marchetti L., Monaco P., Nordon R., Oliver S., Popesso P., Riguccini L., Roseboom I., Rosario D. J., Sargent M., Vaccari M., Altieri B., Aussel H., Bongiovanni A., Cepa J., Daddi E., Domínguez-Sánchez H., Elbaz D., Förster Schreiber N., Genzel R., Iribarrem A., Magliocchetti M., Maiolino R., Poglitsch A., Pérez García A., Sanchez-Portal M., Sturm E., Tacconi L., Valtchanov I., Amblard A., Arumugam V., Bethermin M., Bock J., Boselli A., Buat V., Burgarella D., Castro-Rodríguez N., Cava A., Chanical P., Clements D. L., Conley A., Cooray A., Dowell C. D., Dwek E., Eales S., Franceschini A., Glenn J., Griffin M., Hatziminaoglou E., Ibar E., Isaak K., Ivison R. J., Lagache G., Levenson L., Lu N., Madden S., Maffei B., Mainetti G., Nguyen H. T., O'Halloran B., Page M. J., Panuzzo P., Papageorgiou A., Pearson C. P., Pérez-Fournon I., Pohlen M., Rigopoulou D., Rowan-Robinson M., Schulz B., Scott D., Seymour N., Shupe D. L., Smith A. J., Stevens J. A., Symeonidis M., Trichas M., Tugwell K. E., Vigroux L., Wang L., Wright G., Xu C. K., Zemcov M., Bardelli S., Carollo M., Contini T., Le Fèvre O., Lilly S., Mainieri V., Renzini A., Scodreggio M., Zucca E., 2013, MNRAS, 432, 23
- Guainazzi M., Matt G., Brandt W. N., Antonelli L. A., Barr P., Bassani L., 2000, A&A, 356, 463
- Guijarro A., Peletier R. F., Battaner E., Jiménez-Vicente J., de Grijs R., Florido E., 2010, A&A, 519, A53
- Hamuy M., Walker A. R., Suntzeff N. B., Gigoux P., Heathcote S. R., Phillips M. M., 1992, PASP, 104, 533
- Hamuy M., Suntzeff N. B., Heathcote S. R., Walker A. R., Gigoux P., Phillips M. M., 1994, PASP, 106, 566
- Hartigan P., Raymond J., Hartmann L., 1987, ApJ, 316, 323
- Heald G. H., Rand R. J., Benjamin R. A., Bershadsky M. A., 2007, ApJ, 663, 933
- Heckman T. M., Armus L., Miley G. K., 1990, ApJS, 74, 833
- Helou G., Roussel H., Appleton P., Frayer D., Stolovy S., Storrie-Lombardi L., Hurt R., Lowrance P., Makovoz D., Masci F., Surace J., Gordon K. D., Alonso-Herrero

- A., Engelbracht C. W., Misselt K., Rieke G., Rieke M., Willner S. P., Pahre M., Ashby M. L. N., Fazio G. G., Smith H. A., 2004, *ApJS*, 154, 253
- Henkel C., Muehle S., Bendo G., Jozsa G. I. G., Gong Y., Viti S., Aalto S., Combes F., Garcia-Burillo S., Hunt L. K., Mangum J., Martin S., Muller S., Ott J., van der Werf P., Malawi A. A., Ismail H., Alkhuja F., Asiri H. M., Aladro R., Alves F., Ao Y., Baan W. A., Costagliola F., Fuller G., Greene J., Impellizzeri C. M. V., Kamali F., Klessen R. S., Mauersberger R., Tang X. D., Tristram K., Wang M., Zhang J. S., 2018, *ArXiv e-prints*
- Henry R. B. C., Worthey G., 1999, *PASP*, 111, 919
- Henry R. B. C., Kwitter K. B., Bates J. A., 2000, *ApJ*, 531, 928
- Hlavacek-Larrondo J., Marcelin M., Epinat B., Carignan C., de Denus-Baillargeon M.-M., Daigle O., Hernandez O., 2011, *MNRAS*, 416, 509
- Hoopes C. G., Walterbos R. A. M., 2003, *ApJ*, 586, 902
- Hoopes C. G., Walterbos R. A. M., Greenwalt B. E., 1996, *AJ*, 112, 1429
- Hopkins P. F., Hernquist L., Cox T. J., Kereš D., 2008, *ApJS*, 175, 356
- Hopkins P. F., Quataert E., Murray N., 2012, *MNRAS*, 421, 3522
- Howk J. C., Savage B. D., 1999a, *AJ*, 117, 2077
- Howk J. C., Savage B. D., 1999b, *ApJ*, 517, 746
- Howk J. C., Rueff K. M., Lehner N., Wotta C. B., Croxall K., Savage B. D., 2018, *ApJ*, 856, 167
- Hubble E. P., 1926, *ApJ*, 64
- Iwasawa K., Koyama K., Awaki H., Kunieda H., Makishima K., Tsuru T., Ohashi T., Nakai N., 1993, *ApJ*, 409, 155
- Izotov Y. I., Thuan T. X., 1999, *ApJ*, 511, 639
- Jerjen H., Freeman K. C., Binggeli B., 1998, *AJ*, 116, 2873
- Jo Y.-S., Seon K.-i., Shinn J.-H., Yang Y., Lee D., Min K.-W., 2018, *ArXiv e-prints*
- Jones A., Kauffmann G., D'Souza R., Bizyaev D., Law D., Haffner L., Bahé Y., Andrews B., Bershadsky M., Brownstein J., Bundy K., Cherinka B., Diamond-Stanic A., Drory N., Riffel R. A., Sánchez S. F., Thomas D., Wake D., Yan R., Zhang K., 2017, *A&A*, 599, A141

- Jones A. P., Tielens A. G. G. M., Hollenbach D. J., 1996, *ApJ*, 469, 740
- Kang X., Zhang F., Chang R., Wang L., Cheng L., 2016, *A&A*, 585, A20
- Karachentsev I. D., Kaisina E. I., 2013, *AJ*, 146, 46
- Kauffmann G., Heckman T. M., Tremonti C., Brinchmann J., Charlot S., White S. D. M., Ridgway S. E., Brinkmann J., Fukugita M., Hall P. B., Ivezić Ž., Richards G. T., Schneider D. P., 2003, *MNRAS*, 346, 1055
- Kauffmann G., White S. D. M., Guiderdoni B., 1993, *MNRAS*, 264, 201
- Kennicutt, Jr. R. C., 1998, *ARA&A*, 36, 189
- Kereš D., Katz N., Weinberg D. H., Davé R., 2005, *MNRAS*, 363, 2
- Kewley L. J., Ellison S. L., 2008, *ApJ*, 681, 1183
- Kewley L. J., Dopita M. A., Sutherland R. S., Heisler C. A., Trevena J., 2001, *ApJ*, 556, 121
- Kim S. C., Sung H., Lee M. G., 2002, *Journal of Korean Astronomical Society*, 35, 9
- King A., Pounds K., 2015, *ARA&A*, 53, 115
- Köppen J., Hensler G., 2005, *A&A*, 434, 531
- Kormendy J., Kennicutt, Jr. R. C., 2004, *ARA&A*, 42, 603
- Kruegel E., Tutukov A., Loose H., 1983, *A&A*, 124, 89
- Kulkarni S. R., Heiles C., 1987, in Hollenbach D. J., Thronson, Jr. H. A., eds, *Interstellar Processes, Astrophysics and Space Science Library Vol. 134*, p. 87
- Lagache G., Haffner L. M., Reynolds R. J., Tufte S. L., 2000, *A&A*, 354, 247
- Lagrois D., Joncas G., Drissen L., 2012, *MNRAS*, 420, 2280
- Lakićević M., van Loon J. T., Meixner M., Gordon K., Bot C., Roman-Duval J., Babler B., Bolatto A., Engelbracht C., Filipović M., Hony S., Indebetouw R., Misselt K., Montiel E., Okumura K., Panuzzo P., Patat F., Sauvage M., Seale J., Sonneborn G., Temim T., Urošević D., Zanardo G., 2015, *ApJ*, 799, 50
- Lauberts A., Valentijn E. A., 1989, *The surface photometry catalogue of the ESO-Uppsala galaxies*
- Leisy P., Dennefeld M., 2006, *A&A*, 456, 451

- Lenc E., Tingay S. J., 2009a, *AJ*, 137, 537
- Lenc E., Tingay S. J., 2009b, *AJ*, 137, 537
- Lequeux J., 2005, *The Interstellar Medium*
- Lintott C. J., Schawinski K., Slosar A., Land K., Bamford S., Thomas D., Raddick M. J., Nichol R. C., Szalay A., Andreescu D., Murray P., Vandenberg J., 2008, *MNRAS*, 389, 1179
- Lípari S., Tsvetanov Z., Macchetto F., 1997, *ApJS*, 111, 369
- Lockman F. J., Benjamin R. A., Heroux A. J., Langston G. I., 2008, *ApJL*, 679, L21
- López-Cobá C., Sánchez S. F., Moiseev A. V., Oparin D. V., Bitsakis T., Cruz-González I., Morisset C., Galbany L., Bland-Hawthorn J., Roth M. M., Dettmar R.-J., Bomans D. J., González Delgado R. M., Cano-Díaz M., Marino R. A., Kehrig C., Monreal Ibero A., Abril-Melgarejo V., 2016, *MNRAS*
- López-Cobá C., Sánchez S. F., Moiseev A. V., Oparin D. V., Bitsakis T., Cruz-González I., Morisset C., Galbany L., Bland-Hawthorn J., Roth M. M., Dettmar R.-J., Bomans D. J., González Delgado R. M., Cano-Díaz M., Marino R. A., Kehrig C., Monreal Ibero A., Abril-Melgarejo V., 2017, *MNRAS*, 467, 4951
- Maiolino R., Gallerani S., Neri R., Cicone C., Ferrara A., Genzel R., Lutz D., Sturm E., Tacconi L. J., Walter F., Feruglio C., Fiore F., Piconcelli E., 2012, *MNRAS*, 425, L66
- Marcelin M., Boulesteix J., Georgelin Y. P., 1985, *A&A*, 151, 144
- Marconi A., Moorwood A. F. M., Origlia L., Oliva E., 1994, *The Messenger*, 78, 20
- Marconi A., Oliva E., van der Werf P. P., Maiolino R., Schreier E. J., Macchetto F., Moorwood A. F. M., 2000, *A&A*, 357, 24
- Marino R. A., Rosales-Ortega F. F., Sánchez S. F., Gil de Paz A., Vílchez J., Miralles-Caballero D., Kehrig C., Pérez-Montero E., Stanishev V., Iglesias-Páramo J., Díaz A. I., Castillo-Morales A., Kennicutt R., López-Sánchez A. R., Galbany L., García-Benito R., Mast D., Mendez-Abreu J., Monreal-Ibero A., Husemann B., Walcher C. J., García-Lorenzo B., Masegosa J., Del Olmo Orozco A., Mourão A. M., Ziegler B., Mollá M., Papaderos P., Sánchez-Blázquez P., González Delgado R. M., Falcón-Barroso J., Roth M. M., van de Ven G., Califa Team, 2013, *A&A*, 559, A114
- Martín-Fernández P., Jiménez-Vicente J., Zurita A., Mediavilla E., Castillo-Morales Á., 2016, *MNRAS*

- Martínez-González S., Wünsch R., Palouš J., 2017, *ApJ*, 843, 95
- Mathewson D. S., Clarke J. N., 1973, *ApJ*, 180, 725
- Matsubayashi K., Sugai H., Hattori T., Kawai A., Ozaki S., Kosugi G., Ishigaki T., Shimono A., 2009, *ApJ*, 701, 1636
- Matsuura M., Dwek E., Barlow M. J., Babler B., Baes M., Meixner M., Cernicharo J., Clayton G. C., Dunne L., Fransson C., Fritz J., Gear W., Gomez H. L., Groenewegen M. A. T., Indebetouw R., Ivison R. J., Jerkstrand A., Leboutteiller V., Lim T. L., Lundqvist P., Pearson C. P., Roman-Duval J., Royer P., Staveley-Smith L., Swinyard B. M., van Hoof P. A. M., van Loon J. T., Verstappen J., Wesson R., Zandano G., Blommaert J. A. D. L., Decin L., Reach W. T., Sonneborn G., Van de Steene G. C., Yates J. A., 2015, *ApJ*, 800, 50
- McCall M. L., 1984, *MNRAS*, 208, 253
- McClure-Griffiths N. M., Dickey J. M., Gaensler B. M., Green A. J., 2002, *ApJ*, 578, 176
- McCormick A., Veilleux S., Rupke D. S. N., 2013, *ApJ*, 774, 126
- McKee C. F., Ostriker J. P., 1977, *ApJ*, 218, 148
- Merritt D., Ferrarese L., 2001, *ApJ*, 547, 140
- Mihalas D., 1978, *Stellar atmospheres /2nd edition/*
- Mitchell C. J., Williams T. B., Spekkens K., Lee-Waddell K., Kuzio de Naray R., Sellwood J. A., 2015, *AJ*, 149, 116
- Mitchell C. J., Sellwood J. A., Williams T. B., Spekkens K., Kuzio de Naray R., Bixel A., 2018, *AJ*, 155, 123
- Moiseev A. V., 2002, *Bulletin of the Special Astrophysics Observatory*, 54, 74
- Moore B., Lake G., Katz N., 1998, *ApJ*, 495, 139
- Moorwood A. F. M., Glass I. S., 1984, *A&A*, 135, 281
- Moorwood A. F. M., Oliva E., 1994, *ApJ*, 429, 602
- Moorwood A. F. M., van der Werf P. P., Kotilainen J. K., Marconi A., Oliva E., 1996, *A&A*, 308, L1
- Morisset C., Delgado-Inglada G., Sánchez S. F., Galbany L., García-Benito R., Husemann B., Marino R. A., Mast D., Roth M. M., 2016, *A&A*, 594, A37

- Mouhcine M., Ferguson H. C., Rich R. M., Brown T. M., Smith T. E., 2005, *ApJ*, 633, 810
- Mutch S. J., Croton D. J., Poole G. B., 2011, *ApJ*, 736, 84
- Nakai N., 1989a, *PASJ*, 41, 1107
- Nakai N., 1989b, *PASJ*, 41, 1107
- Nesvadba N. P. H., Lehnert M. D., Eisenhauer F., Gilbert A., Tecza M., Abuter R., 2006, *ApJ*, 650, 693
- Norman C. A., Ikeuchi S., 1989, *ApJ*, 345, 372
- Odegard N., Arendt R. G., Dwek E., Haffner L. M., Hauser M. G., Reynolds R. J., 2007, *ApJ*, 667, 11
- Oliveira C. M., Dupuis J., Chayer P., Moos H. W., 2005, *ApJ*, 625, 232
- Oort J. H., 1970, *A&A*, 7, 381
- Osterbrock D. E., Ferland G. J., 2006, *Astrophysics of gaseous nebulae and active galactic nuclei*
- Osterbrock D., Flather E., 1959, *ApJ*, 129, 26
- Osterbrock D. E., 1989, *Astrophysics of gaseous nebulae and active galactic nuclei*
- Osterbrock D. E., Fulbright J. P., Martel A. R., Keane M. J., Trager S. C., Basri G., 1996, *PASP*, 108, 277
- Osterbrock D. E., Tran H. D., Veilleux S., 1992, *ApJ*, 389, 305
- Pagel B. E. J., Edmunds M. G., Blackwell D. E., Chun M. S., Smith G., 1979, *MNRAS*, 189, 95
- Paron S., Celis Peña M., Ortega M. E., Fariña C., Petriella A., Rubio M., Ashley R. P., 2017, *MNRAS*, 470, 4662
- Payne J. L., Filipović M. D., Pannuti T. G., Jones P. A., Duric N., White G. L., Carpano S., 2004, *A&A*, 425, 443
- Peimbert M., 1975, *ARA&A*, 13, 113
- Pérez-Beaupuits J. P., Spoon H. W. W., Spaans M., Smith J. D., 2011, *A&A*, 533, A56
- Pérez-Montero E., Contini T., 2009, *MNRAS*, 398, 949

- Phillips J. P., Cuesta L., 1999, *AJ*, 118, 2919
- Pogge R. W., Atwood B., Byard P. L., O'Brien T. P., Peterson B. M., Lame N. J., Baldwin J. A., 1995, *PASP*, 107, 1226
- Rand R. J., 1996, *ApJ*, 462, 712
- Rand R. J., 2000, *ApJL*, 537, L13
- Rangwala N., Williams T. B., Pietraszewski C., Joseph C. L., 2008, *AJ*, 135, 1825
- Relaño M., Kennicutt, Jr. R. C., 2009, *ApJ*, 699, 1125
- Relaño M., Lisenfeld U., Vilchez J. M., Battaner E., 2006, *A&A*, 452, 413
- Reynolds R. J., 1990, in Bowyer S., Leinert C., eds, *The Galactic and Extragalactic Background Radiation*, IAU Symposium Vol. 139, p. 157
- Robitaille T. P., Rossa J., Bomans D. J., van der Marel R. P., 2007, *A&A*, 464, 541
- Rogstad D. H., Wright M. C. H., Lockhart I. A., 1976, *ApJ*, 204, 703
- Rossa J., Dettmar R.-J., 2000, *A&A*, 359, 433
- Rossa J., Dettmar R.-J., 2003, *A&A*, 406, 493
- Rossa J., Dahlem M., Dettmar R.-J., van der Marel R. P., 2008, *ArXiv e-prints*
- Roussel H., Gil de Paz A., Seibert M., Helou G., Madore B. F., Martin C., 2005, *ApJ*, 632, 227
- Roy A. L., Oosterloo T., Goss W. M., Anantharamaiah K. R., 2010, *A&A*, 517, A82
- Rubin R. H., Simpson J. P., Haas M. R., Erickson E. F., 1991, *ApJ*, 374, 564
- Rueff K. M., Howk J. C., Pitterle M., Hirschauer A. S., Fox A. J., Savage B. D., 2013, *AJ*, 145, 62
- Ryder S. D., Sun Y.-S., Ashley M. C. B., Burton M. G., Allen L. E., Storey J. W. V., 1998, *PASA*, 15, 228
- Sabbadin F., Minello S., Bianchini A., 1977, *A&A*, 60, 147
- Sadler E. M., Slee O. B., Reynolds J. E., Roy A. L., 1995, *MNRAS*, 276, 1373
- Sánchez Almeida J., Caon N., Muñoz-Tuñón C., Filho M., Cerviño M., 2018, *MNRAS*, 476, 4765

- Sancisi R., Fraternali F., Oosterloo T., van der Hulst T., 2008a, *A&A Rv*, 15, 189
- Sancisi R., Fraternali F., Oosterloo T., van der Hulst T., 2008b, *A&A Rv*, 15, 189
- Sarzi M., Corsini E. M., Cappellari M., Pizzella A., Vega Beltrán J. C., Funes J. G., Bertola F., 2000, in Combes F., Mamon G. A., Charmandaris V., eds, *Dynamics of Galaxies: from the Early Universe to the Present*, *Astronomical Society of the Pacific Conference Series Vol. 197*, p. 139
- Schawinski K., Urry C. M., Simmons B. D., Fortson L., Kaviraj S., Keel W. C., Lintott C. J., Masters K. L., Nichol R. C., Sarzi M., Skibba R., Treister E., Willett K. W., Wong O. I., Yi S. K., 2014, *MNRAS*, 440, 889
- Schild H., Crowther P. A., Abbott J. B., Schmutz W., 2003, *A&A*, 397, 859
- Schurch N. J., Roberts T. P., Warwick R. S., 2002, *MNRAS*, 335, 241
- Searle L., 1971, *ApJ*, 168, 327
- Sembach K. R., Savage B. D., 1996, *ApJ*, 457, 211
- Sembach K. R., Howk J. C., Ryans R. S. I., Keenan F. P., 2000, *ApJ*, 528, 310
- Sérsic J. L., 1966, *ZA*, 64, 212
- Shapiro P. R., Field G. B., 1976, *ApJ*, 205, 762
- Shaver P. A., McGee R. X., Newton L. M., Danks A. C., Pottasch S. R., 1983, *MNRAS*, 204, 53
- Shields G. A., 1974, *ApJ*, 193, 335
- Shopbell P. L., Bland-Hawthorn J., 1998, *ApJ*, 493, 129
- Silk J., Mamon G. A., 2012, *Research in Astronomy and Astrophysics*, 12, 917
- Sparre M., Springel V., 2017, *MNRAS*, 470, 3946
- Stanchev O., Nedialkov P., Georgiev T., 2004, *Comptes Rendus de l'Academie Bulgare des Sciences*, 57(7), 7:5
- Stasińska G., Peña M., Bresolin F., Tsamis Y. G., 2013, *A&A*, 552, A12
- Stein Y., Bomans D. J., Ferguson A. M. N., Dettmar R.-J., 2017, *A&A*, 605, A5
- Storchi-Bergmann T., Calzetti D., Kinney A. L., 1994, *ApJ*, 429, 572

- Strickland D. K., Heckman T. M., Colbert E. J. M., Hoopes C. G., Weaver K. A., 2004, *ApJS*, 151, 193
- Sugai H., Davies R. I., Ward M. J., 2003, *ApJL*, 584, L9
- Tamura Y., Oguri M., Iono D., Hatsukade B., Matsuda Y., Hayashi M., 2015, *PASJ*, 67, 72
- Taniguchi Y., Kawara K., Nishida M., Tamura S., Nishida M. T., 1988, *AJ*, 95, 1378
- Temim T., Slane P., Kolb C., Blondin J., Hughes J. P., Bucciantini N., 2015, *ApJ*, 808, 100
- Tomisaka K., Ikeuchi S., 1988, *ApJ*, 330, 695
- Toomre A., 1977, in Tinsley B. M., Larson, D. Campbell R. B. G., eds, *Evolution of Galaxies and Stellar Populations*, p. 401
- Tüllmann R., Breitschwerdt D., Rossa J., Pietsch W., Dettmar R.-J., 2006, *A&A*, 457, 779
- Tully R. B., Shaya E. J., Karachentsev I. D., Courtois H. M., Kocevski D. D., Rizzi L., Peel A., 2008, *ApJ*, 676, 184
- Veilleux S., Osterbrock D. E., 1987, *ApJS*, 63, 295
- Veilleux S., Cecil G., Bland-Hawthorn J., 2005, *ARA&A*, 43, 769
- Veilleux S., Shopbell P. L., Rupke D. S., Bland-Hawthorn J., Cecil G., 2003, *AJ*, 126, 2185
- Venturi G., Marconi A., Mingozzi M., Carniani S., Cresci G., Risaliti G., Mannucci F., 2017, *Frontiers in Astronomy and Space Sciences*, 4, 46
- Vila-Costas M. B., Edmunds M. G., 1992a, *MNRAS*, 259, 121
- Vila-Costas M. B., Edmunds M. G., 1992b, *MNRAS*, 259, 121
- Villar V. A., Berger E., Chornock R., Margutti R., Laskar T., Brown P. J., Blanchard P. K., Czekala I., Lunnan R., Reynolds M. T., 2016, *ApJ*, 830, 11
- Vincenzo F., Belfiore F., Maiolino R., Matteucci F., Ventura P., 2016, *MNRAS*, 458, 3466
- Vogel M., 2017, *Contemporary Physics*, 58, 193
- Weaver R., McCray R., Castor J., Shapiro P., Moore R., 1977, *ApJ*, 218, 377

- Webster B. L., Smith M. G., 1983, *MNRAS*, 204, 743
- Westmeier T., Braun R., Koribalski B. S., 2011, *MNRAS*, 410, 2217
- Whiteoak J. B., Gardner F. F., 1977, *Australian Journal of Physics*, 30, 187
- Whiteoak J. B., Gardner F. F., 1979, *Proceedings of the Astronomical Society of Australia*, 3, 319
- Whiteoak J. B., Wilson W. E., 1990, *MNRAS*, 245, 665
- Wiegert T., English J., 2014, *NewA*, 26, 40
- Wild V., Rosales-Ortega F., Falcón-Barroso J., García-Benito R., Gallazzi A., González Delgado R. M., Bekeraité S., Pasquali A., Johansson P. H., García Lorenzo B., van de Ven G., Pawlik M., Pérez E., Monreal-Ibero A., Lyubenova M., Cid Fernandes R., Méndez-Abreu J., Barrera-Ballesteros J., Kehrig C., Iglesias-Páramo J., Bomans D. J., Márquez I., Johnson B. D., Kennicutt R. C., Husemann B., Mast D., Sánchez S. F., Walcher C. J., Alves J., Aguerri A. L., Alonso Herrero A., Bland-Hawthorn J., Catalán-Torrecilla C., Florido E., Gomes J. M., Jahnke K., López-Sánchez Á. R., de Lorenzo-Cáceres A., Marino R. A., Mármol-Queraltó E., Olden P., del Olmo A., Papaderos P., Quirrenbach A., Vílchez J. M., Ziegler B., 2014, *A&A*, 567, A132
- Wolfire M. G., 2010, *Highlights of Astronomy*, 15, 409
- Wolfire M. G., McKee C. F., Hollenbach D., Tielens A. G. G. M., 2003, *ApJ*, 587, 278
- Wolfire M. G., Hollenbach D., McKee C. F., 2010, *ApJ*, 716, 1191
- Wu H., Cao C., Hao C.-N., Liu F.-S., Wang J.-L., Xia X.-Y., Deng Z.-G., Young C. K.-S., 2005, *ApJL*, 632, L79
- Wuyts S., Förster Schreiber N. M., van der Wel A., Magnelli B., Guo Y., Genzel R., Lutz D., Aussel H., Barro G., Berta S., Cava A., Graciá-Carpio J., Hathi N. P., Huang K.-H., Kocevski D. D., Koekemoer A. M., Lee K.-S., Le Floc'h E., McGrath E. J., Nordon R., Popesso P., Pozzi F., Riguccini L., Rodighiero G., Saintonge A., Tacconi L., 2011, *ApJ*, 742, 96
- Xiao L., Stanway E., Eldridge J. J., 2018, *ArXiv e-prints*
- Zhang C.-P., Li G.-X., Wyrowski F., Wang J.-J., Yuan J.-H., Xu J.-L., Gong Y., Yeh C. C., Menten K. M., 2016, *A&A*, 585, A117
- Zurita A., Bresolin F., 2012, *MNRAS*, 427, 1463